Spin squeezing and spin dynamics in a trapped-atom clock

Meng-Zi Huang

THÈSE DE DOCTORAT
DE SORBONNE UNIVERSITÉ

Spécialité : Physique

École doctorale nº564 : Physique en Île-de-France

réalisée au

Laboratoire Systèmes de Référence Temps-Espace
et Laboratoire Kastler Brossel

présentée par

HUANG Meng-Zi
黄梦梓

pour obtenir le grade de

DOCTEUR DE SORBONNE UNIVERSITÉ

Sujet de la thèse :

Spin squeezing and spin dynamics in a trapped-atom clock

soutenue le 17 septembre 2019

devant le jury composé de

M^{me}	Monika SCHLEIER-SMITH	Rapporteur
M.	Morgan MITCHELL	Rapporteur
M.	Ludovic PRICOUPENKO	Examinateur
M.	Rodolphe BOUDOT	Examinateur
M.	Jakob REICHEL	Directeur de thèse
M.	Carlos L. GARRIDO ALZAR	Membre invité

Abstract

Atomic sensors are among the best devices for precision measurements of time, electric and magnetic fields, and inertial forces. However, all atomic sensors that utilise uncorrelated particles are ultimately limited by quantum projection noise (QPN), as is already the case for state-of-the-art atomic clocks. This so-called standard quantum limit (SQL) can be overcome by employing entanglement, a prime example being the spin-squeezed states. Spin squeezing can be produced in a quantum non-demolition (QND) measurement of the collective spin, particularly with cavity quantum electrodynamical (QED) interactions.

In this thesis, I present the second-generation trapped-atom clock on a chip (TACC) experiment, where we combine a metrology-grade compact clock with a miniature cavity-QED platform to test quantum metrology protocols at a metrologically-relevant precision level. In a standard Ramsey spectroscopy, the stability of the apparatus is confirmed by a fractional frequency Allan deviation of 6×10^{-13} at 1 s. We demonstrate spin squeezing by cavity QND measurement, reaching 8(1) dB for 1.7×10^4 atoms, currently limited by decoherence due to technical noise. Applying these spin-squeezed states in the clock measurement is within reach.

Cold collisions between atoms play an important role at this level of precision, leading to rich spin dynamics. Here we find that the interplay between cavity measurements and collisional spin dynamics manifests itself in a quantum amplification effect of the cavity measurement. A simple model is proposed, and is confirmed by initial measurements. New experiments in this direction may shed light on the surprising many-body physics in this sytem of interacting cold atoms.

To my parents

Acknowledgement

This thesis would not have been possible without the contributions and support from many people, to whom I would like to express my sincere gratitude.

My thesis advisor Jakob Reichel receives my first and foremost thanks. He has been inspiring me ever since my first visit to the group, with his enthusiasm and rigour as a true physicist. After my daily work has moved to l'Observatoire, the weekly lunches with him have become so precious, as they are always filled with lively discussions about anything from physics to language, to music and to politics. There are so many things I need to learn in a different culture, but I am glad that I have had a good teacher. I am also indebted to Carlos Garrido Alzar, my supervisor at l'Observatoire de Paris, for his guidance and support. His kindness and humour have also been a great company for the lab work.

Half of the presented work is due to my dear colleague, Tommaso Mazzoni, whose patience and cheerfulness well compensated my melancholy. We worked together seamlessly for two years from the first day of the new setup, to the verge of our squeezing results. This substantial period of my PhD would not have been so enjoyable without him.

This work would also have been impossible without the work laid down by Konstantin Ott, who designed the new atom chip and established the methods for its realisation. He trained me as we worked on the chip fabrication and cavity assembly. I have even burdened him, during his stressful time of writing, with a half-finished but almost destroyed sample, which he courageously saved. I am also glad to have two-year overlap with Théo Laudat. He handed us the old setup and the know-how and helped us to dismantle it for the new generation, probably with intricate sentiments. His shared enthusiasm with Tommaso for cinema has also been an amusement decorating numerous lunches. I had a good time while three of us were teamed up.

I am grateful to all my teammates in the atom chips group at l'ENS, for all the great discussions and enjoyment accompanied by the cult of coffee brewing in S1. During my first year at l'ENS building our cavities, Romain Long and Francesco Ferri have been a superb company and support, building their cavity in curious synchronisation. I appreciate the strong link we kept after I have been working at l'Observatoire, thanks to the not-always-regular group seminars, and occasional lunches in the garden of "irlandais" under the sunshine.

My fellow PhDs and colleagues in the IACI group at SYRTE certainly made me feel home at l'Observatoire. I thank them deeply for their help in the lab and stimulating discussions in our "café les deux machines".

As I have been lucky to benefit from two great labs, LKB and SYRTE, I am obviously indebted to numerous colleagues and staffs. I had the great help from the administration and secretaries in both labs, from the mechanical workshops, from the MUTA team at

SYRTE on vacuum installation and from the electronic workshop at SYRTE. Their works are indispensable for me.

I thank our theory collaborators, Alice Sinatra, Jean-Noël Fuchs, Frédéric Piéchon and Franck Laloë, for the helpful and on-going discussions. My special thanks to Jean-Noël, who helped me patiently with the numerical simulations using his code.

I apologise to all friends and colleagues whose names are not mentioned explicitly. I had the fear that my feeble words would overshadow what they deserve.

My circle outside the lab remained regretfully small, but full of love and care from my dear friends. I appreciated the jokes around the dinner table, and the serious collective "research" of good Chinese food. I especially thank my roommate Zhihao Duan for his understanding and collaboration for three years in a tiny apartment. He always motivates me with his diligence.

Living in France is not always easy, but every time I imagined doing my PhD elsewhere, I would appreciate the opportunity I had to learn a beautiful language, to buy piles of old books that I am not able to read, and to wander in Paris in a lively solitude. I probably will not escape the "curse" of Hemingway, that this moveable feast is with me.

In the end, as from the bottom of my heart, I thank the endless love from my parents. This thesis is dedicated to them.

Contents

Introduction **ix**

1 Spin squeezing for metrology **1**
1.1 Atomic clocks and clock stability . . . 1
1.1.1 Basic notions . . . 2
1.1.2 Trapped-atom clocks and TACC . . . 5
1.1.3 Clock stability . . . 9
1.2 Concepts of spin squeezing . . . 12
1.2.1 Surpassing SQL with spin-squeezed state . . . 12
1.2.2 Overview of spin-squeezing generation . . . 14
1.3 Spin squeezing in cavity-quantum electrodynamics . . . 16
1.3.1 Real-world cavities . . . 17
1.3.2 Cavity-QED in the dispersive regime . . . 18
1.3.3 Squeezing by QND measurement . . . 22
1.3.4 Squeezing by cavity feedback . . . 25

2 Experimental methods **29**
2.1 Setup . . . 29
2.1.1 Atom chip assembly . . . 29
2.1.2 Vacuum system . . . 31
2.1.3 Optical system . . . 33
2.1.4 Magnetic fields . . . 38
2.2 Cold atom preparation and interrogation . . . 40
2.2.1 Laser cooling and optical pumping . . . 40
2.2.2 On-chip transport of atoms . . . 41
2.2.3 Evaporative cooling . . . 45
2.2.4 The clock trap . . . 46
2.2.5 Interrogation photons . . . 48
2.2.6 Interrogation pulse tuning . . . 53
2.2.7 Absorption imaging . . . 56
2.3 Cavity probing and stabilisation . . . 60
2.3.1 Cavity parameters . . . 60
2.3.2 Laser scheme and setup . . . 63
2.3.3 PDH lock with minimum intra-cavity power . . . 66
2.3.4 Digital filter cancelling mechanical resonances . . . 70

2.3.5 Feed-forward targeting the thermal drift . . . 74
2.3.6 Locking "without" light . . . 75

3 A highly stable cavity-QED platform 79
3.1 Clock stability analysis . . . 79
3.1.1 Detection noise . . . 80
3.1.2 Dick effect . . . 81
3.1.3 Atom number fluctuation . . . 82
3.1.4 Magnetic and temperature fluctuations . . . 85
3.1.5 Ramsey Contrast . . . 88
3.1.6 Preliminary stability results . . . 89
3.1.7 Prospects with spin-squeezed states . . . 90
3.2 Characterisation of the atom-cavity coupling . . . 91
3.2.1 Vacuum-Rabi splitting . . . 91
3.2.2 Cavity shift in the dispersive regime . . . 95
3.2.3 Atom-cavity alignment . . . 98
3.2.4 Intra-cavity optical lattice . . . 100

4 Spin squeezing by measurement 105
4.1 Inhomogeneous coupling and decoherence . . . 105
4.1.1 Phase shift by cavity probe . . . 106
4.1.2 Monte-Carlo simulations . . . 107
4.1.3 Contrast and phase measurements . . . 107
4.2 Composite measurements . . . 109
4.2.1 Spin echo . . . 109
4.2.2 Composite π pulse . . . 111
4.2.3 Coherence measurements . . . 114
4.3 Conditional spin squeezing . . . 116
4.3.1 Measurement uncertainty . . . 117
4.3.2 Spin noise estimation . . . 120
4.4 Squeezing by cavity feedback . . . 121
4.5 Outlook . . . 122
4.5.1 Squeezing lifetime . . . 122
4.5.2 Alternative inhomogeneous-light-shift compensation . . . 122

5 Quantum amplification by ISRE 125
5.1 Identical spin rotation effect (ISRE) . . . 125
5.1.1 Basic principles . . . 125
5.1.2 An intuitive picture with atoms in two energy classes . . . 127
5.1.3 Experimental signatures . . . 128
5.1.4 Mean-field kinetic equation . . . 129
5.1.5 Observation of ISRE via motional energy . . . 132
5.2 Interplay between ISRE and cavity measurements . . . 133
5.2.1 Origin: inhomogeneous coupling . . . 134
5.2.2 Cavity shift in a continuous probing . . . 135
5.2.3 ISRE triggered by a probe pulse . . . 136

5.2.4 Dynamics in motional energy sensed by cavity shift 137
5.3 Amplification of quantum fluctuations 139
5.3.1 Experimental observations 139
5.3.2 Simple model with two energy classes 143
5.3.3 Simulation using classical spins 145
5.3.4 Circumventing the amplification 146
5.3.5 Future work 146

Conclusion and outlook **149**

A PDH error signal **151**

B Alternative light shift compensation **154**

C Résumé en français **158**

List of Figures **164**

Bibliography **167**

Introduction

The redefinition of the international system of units (SI) – a revolutionary endeavour that redefines all base units based on the constants of nature [1, 2] [1] – has come into effect this very year. Finally realising the spirit of "à tous les temps, à tous les peuples", the new SI is not only elegant, but will also foster future technological innovations. Historically, precision measurements and standards have been crucial for scientific discoveries, which led to improvements in technology and instrumentation, again enabling measurements at a higher precision level.

As a prime example, time (frequency) measurement is at the very heart of the SI. Although the SI second is not redefined this time – it has been based on a constant of nature, the Caesium hyperfine transition, since 1967 [3][2] – frequency measurement is by far the most precise measurement, and it is also closely related to the realisation (mises en pratique) of other base units like length and electric voltage.

Centuries ago, navigation over seas was enabled by the best clocks at the time, transforming the landscape of humanity. In the last fifty years, ever since clocks entered the atomic era, the precision of frequency measurement has been improved by 6 orders of magnitude, forming the basis of e.g. the global positioning systems (GPS) and high-speed telecommunication – technologies that we might take for granted today. Nowadays, atomic clocks based on optical transitions have reached a precision of 10^{-18} [5, 6] – an error less than a second in the age of the universe. The ever increasing precision not only promises future applications such as cm-level geodesic measurements, including positioning and gravity field [7]; but will also shed light on some of the most fundamental questions in physics, such as the test of fundamental constants and general relativity, as well as the search for new forces and matter [8].

Atoms are not only perfect frequency standards for timekeeping – as nature provides us with infinite numbers of identical copies[3] – we also realised that atoms' internal state is susceptible to the environment, which allows us to use atoms as sensors for external fields and forces. Atomic sensors have shown great promises, achieving state-of-the-art precision in measuring magnetic field [10], electric field [11], gravity [12], gravity gradient [13] and rotations [14]. Similar to clocks, extreme precision enables new horizons for fundamental physics studies [15].

In a broader sense, atomic sensors (including clocks) are attracting more and more interest and efforts to bring them out of the laboratory. At the forefront of applications are the developments of second-generation compact clocks (compared to e.g. those used in GPS

[1] Precisely speaking, fixing the numerical values of the constants based on received physical laws.
[2] New definition based on optical transitions is underway [4].
[3] An idea that dates back to Maxwell and Lord Kelvin [9]

satellites) [16, 17, 18, 19], and chip-scale atomic devices [20]. Commercial solutions have also emerged [21, 22].

The standard quantum limit However, all atomic sensors are ultimately limited by a fundamental noise source – the quantum projection noise (QPN). Generally, atoms are prepared in a quantum superposition state to probe the quantities to be measured, e.g. in the simplest form of a qubit $\alpha|0\rangle + \beta|1\rangle$, where $|0\rangle$ and $|1\rangle$ are the basis states and the measured quantities are encoded in complex numbers α and β ($|\alpha|^2 + |\beta|^2 = 1$). But atoms are finally detected projectively in the eigenstates $|0\rangle$ and $|1\rangle$, leading to the QPN – we are measuring a continuous variable (e.g. $|\beta|^2$) with digital outcomes. The QPN is then given by a binomial distribution that limits the measurement precision to $1/\sqrt{N}$, if we have N independent atoms to measure at a time. This limit, the best one can do with uncorrelated atoms (or classical states), is called the standard quantum limit (SQL).

The SQL is a limit for a given resource (atom number), which is in reality always finite and maybe expensive. In fact, state-of-the-art primary frequency standards – atomic fountain clocks – are already limited by the QPN [23], while optical clocks [6] and magnetometers [24] are coming near. As a fundamental limit, the SQL will eventually be the dominant noise for many other atomic sensors in the near future as technical noise being reduced.

Spin squeezing and QND measurement It turns out that with N quantum objects (atoms) at hand the ultimate limit is the Heisenberg limit (error $\sim 1/N$). The SQL, despite its name, is a classical limit and can be overcome with non-classical states [25] or non-trivial protocols [26]. For the former, atoms are entangled such that we can gain more information (Fisher information) for the measured quantitiy compared to classical states. Notably, employing non-classical states and protocols for sensing and metrology – quantum sensing – is a major theme of the emerging quantum technologies, as reflected in the recently launched European quantum flagship [27].

Among the metrologically useful non-classical states, one example, arguably the most practical one, is the spin-squeezed state. Like the photonic forerunner, squeezed states in general, redistribute the uncertainty in two conjugate observables (as opposed to an even distribution for independent particles) to have a "squeezed" uncertainty for one observable, which can be eventually used for measurements beyond the SQL [28, 29]. Applications of squeezed state in sensing have been demonstrated in various systems: squeezed light improves the gravitational wave detectors [30] and biological measurements of living cells [31]; spin-squeezing has been demonstrated in trapped ions [32] and with ensemble of neutral atoms in the context of atomic clock, which is the focus of this thesis.

Generating spin-squeezed states in atomic ensembles relies on entangling the atoms through either direct (collisional) interactions or light-mediated interactions. The former has been achieved in Bose-Einstein condensates (BECs) [33, 34] and applied to magnetometry [35, 36]; the latter has been extensively explored with optical quantum non-demolition (QND) measurements [37]. A QND measurement in this context only measures the collective atomic state without projecting each atom. A measurement with sub-QPN precision then effectively squeezes the atomic state as the uncertainty of the latter is reduced to that of the measurement. It can be implemented via the optical response of an atomic transition. Dispersively coupled photons experience the atomic-state-dependent refractive index, leading to a phase shift or polarisation rotation.

QND measurements have long been explored with free-space probes in optical magnetometry, and spin squeezing has been demonstrated to improve the sensor sensitivity [24, 38]. While in the context of atomic clocks (two-level systems), the first spin-squeezed state is also demonstrated with a free-space Mach-Zehnder interferometer [39]. One challenge of the QND measurements is to protect the atoms from decoherence induced by the light, characterised by the optical depth or the ratio between coherent photon scatterings which entangle the atoms and incoherent ones that project individual atoms.

The employment of optical cavities for interfacing the atoms can greatly increase the optical depth, entering the realm of the so-called cavity-quantum electrodynamics (cavity-QED) [40]. After the first spin squeezing demonstration in cavity-QED systems [41], squeezing records have been rapidly refreshed. A remarkable 100 times noise reduction below the SQL has been recently demonstrated [42]. Moreover, cavity feedback can also efficiently produce spin-squeezed states [43, 44, 45].

A few spin squeezing experiments based on cavity-QED have also demonstrated clock operations [46, 42], showing up to 10 dB improvement below the SQL. However, these experiments remain at the proof-of-principle level – in terms of clock stability, they cannot even match a good quartz oscillator. Applying spin squeezing in real atomic clocks remains experimentally challenging. To bring the successful demonstrations to a metrologically relevant level is precisely the major motivation of this thesis.

TACC-2: a test bed for quantum metrology In this thesis, I present the second-generation Trapped-Atom Clock on a Chip (TACC-2) experiment and the first results. The first-generation setup is conceived as one of the possible future compact clocks [47] and as a test bed for atomic interactions that are important for trapped-atom clocks [48, 49]. A metrologically-relevant performance has been demonstrated [50]. TACC-2 aims at applying spin squeezing and other quantum technologies to this metrology-grade clock by upgrading it with on-chip fibre-based Fabry-Pérot cavities. This cavity-QED system in principle allows up to 20 dB measurement-based squeezing for $\sim 5 \times 10^4$ atoms (see Ch. 1). We realised this new setup and achieved preliminary results showing 8 dB conditional spin squeezing for 1.7×10^4 atoms, currently limited by decoherence due to technical noise. At the same time, we confirmed that the new setup remains "metrology-grade", reaching a fractional frequency instability of $\sim 6 \times 10^{-13}$ at 1 s in a standard clock operation. Spin squeezed states are readily applicable to a real atomic clock.

At this stability level and with long coherence time, unexplored physics may become relevant to the spin-squeezing interaction. For example, cold collisions among the atoms - well known for trapped-atom systems – lead to non-trivial spin dynamics. A particular effect, the identical spin rotation effect (ISRE) can correlate an atom's external and internal degrees of freedom [51], entangling the atoms in a different way. Similar effects originated from cold collisions are also seen in the state-of-the-art fermionic optical lattice clocks [52, 53], showing relevance to the ultimate clock precision and the study of many-body physics. Combining spin dynamics and entangling interactions from the cavity, QND measurements or cavity feedback, may lead to unexplored non-classical states. As a first manifestation, we observed a quantum amplification effect of the QND measurement, similar to the interaction-based readout schemes using one-axis-twisting interactions [54, 55].

Another motivation of TACC-2, more specific to clocks, is to employ QND measurements as a technical advantage to reduce the dead time of the clock cycle, hence alleviating the clock

degradation by the phase noise of the local oscillator (so-called Dick effect) [56]. The Dick effect is a major noise source for atomic clocks, particularly relevant to compact clocks which have stringent requirements on the weight, size, and power consumption. For example, QND measurements allow to reuse the atoms in several short Ramsey cycles, permitting the use of moderate local oscillators without compromising the clock duty cycle. TACC-2 allows to test these quantum technologies that are relevant to broader applications at a metrologically relevant stability level.

Structure of the manuscript

- We start with an introduction to atomic clocks, focusing on TACC and its major noise sources of clock instability. I will introduce spin squeezing more formally and discuss in detail squeezing generations in a cavity-QED system, either by QND measurement or by cavity feedback.
- Chapter Two describes the experimental setup for preparing and manipulating cold atoms. I dedicate a section to the techniques for stabilising the on-chip fibre Fabry-Pérot cavities.
- Chapter Three presents the characterisation of our stable cavity-QED system. After a detailed assessment of clock stability in the standard configuration, we proceed to characterise atom-light interactions, through the iconic vacuum Rabi splitting, and in the dispersive regime where spin squeezing will be performed.
- Due to inhomogeneous coupling, spin echo needs to be applied to preserve the coherence after a cavity measurement. The careful implementation of spin-echoed measurements allows a demonstration of 8 dB conditional squeezing, presented in Chapter Four.
- Chapter Five demonstrates the observation of quantum amplification of cavity measurements induced by ISRE. I briefly review the ISRE and give an intuitive picture to understand the observations. Preliminary numerical simulations are also presented.
- Finally I discuss further improvements of the presented work, as well as future experiments.

Chapter 1

Spin squeezing for metrology

This thesis aims to apply spin squeezing to an atomic clock at a metrologically relevant level. This chapter gives a brief introduction to both aspects: atomic clocks and their stabilities on one hand, and spin squeezing of neutral atoms in cavity-QED systems on the other. The experimental setting of the thesis is introduced in a metrological context, and we will discuss the prospects of this new apparatus in terms of achievable squeezing.

1.1 Atomic clocks and clock stability

Generally, the extreme sensitivity of atomic sensors is commonly achieved in interferometers: the measured quantity is mapped to a phase shift between two modes (two atomic states) and is read out using interferometric techniques (Fig. 1.1). For example, certain types of atomic clocks are interferometers with two internal states ($|\uparrow\rangle$ and $|\downarrow\rangle$) whose transition frequency serves as a frequency standard. The interferometer phase shift is set by the frequency of the electromagnetic field that composes the interferometer, realising an ultra sensitive frequency measurement. Another prime example is atomic inertial sensors measuring gravity (gravimeter), AC acceleration (accelerometer), or rotations (gyroscope). They are matter-wave interferometers: the atomic wave packets are spatially separated (two modes of momentum states) and then recombined such that the phase difference between the states in different trajectories is sensitive to inertial forces.

In practice, the most common working scheme of atomic clocks is a servo loop to lock a *local oscillator* (LO) – a continuously running clock signal – on the atomic transition frequency. The frequency of the LO is repeatedly compared with the atomic transition by "interrogating" an atomic sample and is subsequently corrected. The spectroscopic measurement of the local oscillator can be performed in various ways, all based on the coherent evolution of the clock states under a driving field, which will be explained in this section.

While this interrogation scheme is known as "passive", an "active" scheme also exists such that a clock signal is directly generated from the atomic transition through a resonant cavity. The most important example would be the active hydrogen maser [57], which plays an important role in timekeeping and dissemination of time reference.

In this section, I will be focusing on atomic clocks based on two-mode interferometer. After some basic formalism in the language of pseudo-spin (spin-1/2 or N spin-1/2), we discuss the figures of merit of clocks in a context relevant to our experiment – trapped-atom

clocks, among which are some of the state-of-the-art apparatuses.

1.1.1 Basic notions

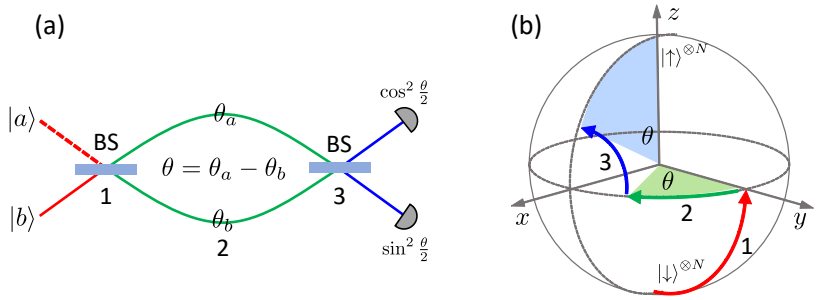

Figure 1.1 Two-mode Mach-Zehnder interferometer (a) and Ramsey interferometer in the Bloch sphere representation (b). The interferometers can be separated into three steps: 1) a prepared mode is split into superposition by a beamsplitter (BS), or a $\pi/2$ rotation on the Bloch sphere; 2) a phase θ is accumulated between the two paths or the two internal states; 3) the final BS or $\pi/2$ rotation transforms the phase shift into a probability difference of detection in the two eigenmodes.

1.1.1.1 The Bloch sphere representation

A pure quantum state of a two-level system (spin-1/2 or qubit) can be written as $|\psi\rangle = \cos\frac{\vartheta}{2}|\uparrow\rangle + e^{i\varphi}\sin\frac{\vartheta}{2}|\downarrow\rangle$, therefore pictorially represented as a "spin vector" $\boldsymbol{s}$ of unity length forming the so-called Bloch sphere, with the two eigenstates $|\uparrow\rangle$ and $|\downarrow\rangle$ on the poles, $0 \leq \vartheta \leq \pi$ and $0 \leq \varphi \leq 2\pi$ the polar and azimuthal angles, respectively. The projections in the Cartesian coordinates, $\boldsymbol{s} = (\sin\vartheta\cos\varphi, \sin\vartheta\sin\varphi, \cos\vartheta)$, are the expectation values of the Pauli matrices $\boldsymbol{s} = \langle\hat{\boldsymbol{\sigma}}\rangle = (\langle\hat{\sigma}_x\rangle, \langle\hat{\sigma}_y\rangle, \langle\hat{\sigma}_z\rangle)$. More generally, a mixed state can be depicted with a reduced spin length $|\boldsymbol{s}| < 1$.

Any unitary transformation of a qubit can be represented as a rotation on the Bloch sphere, $e^{-i\theta\hat{\sigma}_{\boldsymbol{n}}/2}$, where $\boldsymbol{n}$ is the rotation axis such that $\hat{\sigma}_{\boldsymbol{n}} = \boldsymbol{n}\cdot(\hat{\sigma}_x, \hat{\sigma}_y, \hat{\sigma}_z)$ and θ the rotation angle.

For an ensemble of N *distinguishable* qubits, one can define the collective spin vector $\hat{\boldsymbol{S}} = (\hat{S}_x, \hat{S}_y, \hat{S}_z)$, where

$$\hat{S}_x = \frac{1}{2}\sum_{l=1}^{N}\hat{\sigma}_x^{(l)}, \quad \hat{S}_y = \frac{1}{2}\sum_{l=1}^{N}\hat{\sigma}_y^{(l)}, \quad \hat{S}_z = \frac{1}{2}\sum_{l=1}^{N}\hat{\sigma}_z^{(l)} \tag{1.1}$$

with $\hat{\sigma}_{x,y,z}^{(l)}$ the Pauli vector of the lth qubit. These operators satisfy the commutation relations:

$$[\hat{S}_x, \hat{S}_y] = i\hat{S}_z, \quad [\hat{S}_y, \hat{S}_z] = i\hat{S}_x, \quad [\hat{S}_z, \hat{S}_x] = i\hat{S}_y. \tag{1.2}$$

The 2^N dimensional Hilbert space has the well-known angular momentum basis $|S, S_z\rangle$, satisfying $\hat{\boldsymbol{S}}^2|S,S_z\rangle = S(S+1)|S,S_z\rangle$ and $\hat{S}_z|S,S_z\rangle = S_z|S,S_z\rangle$, with the eigenvalues $0 \leq S \in \{N/2, N/2-1, \ldots\}$ and $S_z \in \{-S, -S+1, \ldots, +S\}$.

We shall introduce the coherent spin state (CSS), constructed from the product of N qubits all aligned in the same spin state along $\boldsymbol{s}$:

$$|\theta, \phi, N\rangle = \bigotimes_{l=1}^{N} \left(\cos\frac{\theta}{2} |\uparrow\rangle_l + e^{i\phi} \sin\frac{\theta}{2} |\downarrow\rangle_l \right) \tag{1.3}$$

It is the eigenstate of $\hat{S}_{\boldsymbol{s}}$ with the maximum eigenvalue $S = N/2$, and it remains in a subspace with maximum spin $S = N/2$ under a collective rotation $\otimes_{l=1}^{N} e^{-i\theta\hat{\sigma}_{\boldsymbol{n}}/2} = e^{-i\theta\hat{S}_{\boldsymbol{n}}}$.

This particular subspace with maximum $S = N/2$ is spanned by the states symmetric under particle exchange, with dimension $N + 1$. Angular momentum operators can be transformed to bosonic creation and annihilation operators in the two modes $|\uparrow\rangle$ and $|\downarrow\rangle$ [58]. Briefly speaking, one finds a basis formed by the eigenstates of $\hat{S}_z$ (also eigenstates of $\hat{\boldsymbol{S}}^2$), the so-called Dicke states:

$$|n\rangle_z = \left| S = \frac{N}{2}, S_z = -\frac{N}{2} + n \right\rangle \tag{1.4}$$

where $n \in \{0, 1, \ldots, N\}$ corresponds to the number of "excitations" from mode $|\downarrow\rangle$ to $|\uparrow\rangle$. It can be visualised as the "circles of latitude" on the Bloch sphere with a specific S_z, but has no information in S_x and S_y, The Dicke states are therefore highly entangled states.

The Dicke states of $\hat{S}_z$, $|n\rangle_z$, can be extended to any spin projection $\hat{S}_{\boldsymbol{n}} = \boldsymbol{n}\cdot\hat{\boldsymbol{S}}$. The eigenstates $|n\rangle_{\boldsymbol{n}}$ of $\hat{S}_{\boldsymbol{n}}$ result from a collective rotation of $|n\rangle_z$: for example, $|n\rangle_x = e^{-i(\pi/2)\hat{S}_y} |n\rangle_z$. Remarkably, the CSS can be written as a superposition of the Dicke states [58]: – a product state is decomposed in the highly entangled basis states.

1.1.1.2 Rabi rotation

In the following, our discussion of an ensemble of N qubits will be limited to a CSS under the idealised collective rotations, since a CSS resembles a single qubit and is very close to what we prepare in the lab. For simplicity I will continue in the notion of a single qubit, but bearing in mind the collective nature of the experimental realisations.

Let us consider how a spin rotation results from the interaction between the qubit and a LO driving field. The LO field couples $|\uparrow\rangle$ and $|\downarrow\rangle$, like e.g. the coupling of an electric dipole to an electric field, or that of a magnetic dipole to a magnetic field. The system Hamiltonian can be written as

$$\begin{aligned}\hat{\mathcal{H}} &= \frac{\hbar\omega_{\mathrm{at}}}{2}\hat{\sigma}_z + \hbar\Omega_{\mathrm{R}} f(t)\cos(\omega_{\mathrm{LO}}t + \phi)\hat{\sigma}_x \\ &= \frac{\hbar\omega_{\mathrm{at}}}{2}\hat{\sigma}_z + \frac{\hbar\Omega_{\mathrm{R}}}{2} f(t)(e^{i\omega_{\mathrm{LO}}t+\phi} + e^{-i\omega_{\mathrm{LO}}t-\phi})(\hat{\sigma}_+ + \hat{\sigma}_-)\end{aligned}$$

where $\hat{\sigma}_\pm = \frac{1}{2}(\hat{\sigma}_x \pm i\hat{\sigma}_y)$. Ω_{R} quantifies the coupling between the qubit and the field. We also introduced $f(t)$ as a slow-varying envelope function of the interaction. In the rotating frame of the LO, and under rotating wave approximation (RWA), we can ignore the term oscillating at $2\omega_{\mathrm{LO}}$ as long as $\Omega_{\mathrm{R}}, \Delta_{\mathrm{LO}} \ll \omega_{\mathrm{at}}$, with $\Delta_{\mathrm{LO}} = \omega_{\mathrm{LO}} - \omega_{\mathrm{at}}$. the Hamiltonian becomes

$$\begin{aligned}\hat{\mathcal{H}} &= -\frac{\hbar\Delta_{\mathrm{LO}}}{2}\hat{\sigma}_z + \frac{\hbar\Omega_{\mathrm{R}}}{2} f(t)(e^{i\phi}\hat{\sigma}_+ + e^{-i\phi}\hat{\sigma}_-) \\ &= \frac{\hbar}{2}\boldsymbol{\Omega}\cdot\hat{\boldsymbol{\sigma}}\end{aligned} \tag{1.5}$$

where

$$\boldsymbol{\Omega} = \begin{pmatrix} \Omega_{\mathrm{R}} f(t) \cos\phi \\ -\Omega_{\mathrm{R}} f(t) \sin\phi \\ -\Delta_{\mathrm{LO}} \end{pmatrix} \tag{1.6}$$

will be referred to as the Rabi vector. We can see for a constant field $f(t) = 1$, the state evolves as $|\psi(t)\rangle = e^{-i(\Omega t/2)\boldsymbol{n}_{\mathrm{R}}\cdot\hat{\boldsymbol{\sigma}}} |\psi(0)\rangle$. It is a rotation with angle Ωt around the axis $\boldsymbol{n}_{\mathrm{R}}$, where we call $\Omega \equiv |\boldsymbol{\Omega}| = \sqrt{\Omega_{\mathrm{R}}^2 + \Delta_{\mathrm{LO}}^2}$ the Rabi frequency, and $\boldsymbol{n}_{\mathrm{R}} = \boldsymbol{\Omega}/\Omega$.

Under a near-resonant field, the rotation axis lies on the equator. One transfers the population between the eigenstates $|\downarrow\rangle$ and $|\uparrow\rangle$. Starting from $|\downarrow\rangle$ for instance, the transition probability in eigenstate $|\uparrow\rangle$, $P_\uparrow$ (or particles numbers for many qubits under collective rotation) results in the so-called Rabi oscillation:

$$\begin{aligned} P_\uparrow &= \left| \langle\uparrow| e^{-i(\Omega t/2)\boldsymbol{n}_{\mathrm{R}}\cdot\hat{\boldsymbol{\sigma}}} |\downarrow\rangle \right|^2 \\ &= \left| \langle\uparrow| \cos\frac{\Omega t}{2}\boldsymbol{I} - i\sin\frac{\Omega t}{2}\boldsymbol{n}_{\mathrm{R}}\cdot\hat{\boldsymbol{\sigma}} |\downarrow\rangle \right|^2 \\ &= \frac{\Omega_{\mathrm{R}}^2}{\Omega^2}\sin^2\left(\frac{\Omega t}{2}\right) \end{aligned} \tag{1.7}$$

In the laboratory, the LO field is pulsed to interrogate the atoms. For example, a simple square pulse of duration τ, with $\Omega_{\mathrm{R}}\tau = \pi$ implements a so-called π pulse. The Δ_{LO} dependence of $P_\uparrow$ allows to perform the Rabi spectroscopy to determine the LO frequency with respect to the atomic transition. The spectrum exhibits a "sinc"-like shape due to the convolution with a square pulse (window), therefore the linewidth is Fourier limited to the inverse pulse length $\sim 2\pi/\tau$.

The maximum sensitivity of the transition probability to the LO detuning $\mathrm{d}P_\uparrow/\mathrm{d}\Delta_{\mathrm{LO}}$ can be obtained close to the half-maximum of the spectrum. However, as we can see intuitively, this sensitivity is not constant during the pulse as the spin rotates, and it is also not optimum. In addition, the longer interrogation pulse required for higher sensitivity is in general experimentally difficult, especially when the atoms are moving.

1.1.1.3 Ramsey spectroscopy

The Ramsey spectroscopy is a two-pulse sequence, implementing a two-mode interferometer with the internal states [57]. Prepared in an eigenstate, the first $\pi/2$ pulse (or a beam splitter) puts the qubit into a superposition state, which is maximally sensitive to the LO frequency noise; a phase θ is accumulated between the two states, in proportion to the LO detuning Δ_{LO} and the free evolution time T_{R} (dubbed the Ramsey time); a final $\pi/2$ pulse closes the interferometer arms, transforming the phase θ into a measurable population difference in the final particle-counting detection (Fig. 1.1(b)).

The state evolution during a Ramsey sequence can be written down as (assuming LO phase $\phi = 0$):

$$\begin{aligned} \hat{R} &= \exp\left[-i\Omega\tau_p\frac{\hat{\sigma}_x}{2} - i\Delta_{\mathrm{LO}}\tau_p\frac{\hat{\sigma}_z}{2}\right]\exp\left[i\Delta_{\mathrm{LO}}T_{\mathrm{R}}\frac{\hat{\sigma}_z}{2}\right]\exp\left[-i\Omega\tau_p\frac{\hat{\sigma}_x}{2} - i\Delta_{\mathrm{LO}}\tau_p\frac{\hat{\sigma}_z}{2}\right] \\ &\overset{\Delta_{\mathrm{LO}}\ll\Omega}{\simeq} \exp\left[-i\frac{\pi}{2}\frac{\hat{\sigma}_x}{2}\right]\exp\left[i\theta\frac{\hat{\sigma}_z}{2}\right]\exp\left[-i\frac{\pi}{2}\frac{\hat{\sigma}_x}{2}\right] \end{aligned}$$

where $\tau_p = \pi/(2\Omega_\mathrm{R})$ is the duration of the pulse, and the phase $\theta = \Delta_\mathrm{LO} T_\mathrm{R}$. For small detuning compared to the Rabi frequency as we developed in the second line, the $\pi/2$ pulses are almost perfect, and the first pulse transfers $|\downarrow\rangle$ to $(|\uparrow\rangle + i\,|\downarrow\rangle)/\sqrt{2}$, which evolves into $(|\uparrow\rangle + ie^{-\theta}\,|\downarrow\rangle)/\sqrt{2}$ after Ramsey time T_R and the second pulse produces the final state $\cos(\theta/2)\,|\uparrow\rangle + \sin(\theta/2)\,|\downarrow\rangle$ to be detected. The transition probability in $|\uparrow\rangle$ then reads

$$P_\uparrow = \cos^2\frac{\theta}{2} = \frac{1}{2} + \frac{\cos(\Delta_\mathrm{LO} T_\mathrm{R})}{2} \tag{1.8}$$

This shows the "central fringes" of the Ramsey spectrum, with its linewidth limited by the inverse Ramsey time π/T_R. It's worth noting that these narrow fringes are under a broad envelope similar to the Rabi spectrum (when $\Delta_\mathrm{LO} \ll \Omega$ breaks down), with a width again set by the pulse duration $2\pi/\tau_p$.

The maximum sensitivity to the LO detuning for spectroscopy is again at the half-maximum of the central fringe with $\Delta_\mathrm{LO} = \pm\pi/2T_\mathrm{R}$:

$$\left.\frac{\mathrm{d}P_\uparrow}{\mathrm{d}\Delta_\mathrm{LO}}\right|_\mathrm{max} = \pm\frac{T_\mathrm{R}}{2} = \frac{\pi}{2\omega_\mathrm{at}} Q_c \tag{1.9}$$

where we have referred to the quality factor Q_c of the clock – clock frequency divided by the full-width-at-half-maximum (FWHM) of the central fringe – which is sometimes useful for comparing oscillators.

The Ramsey interferometer offers superior sensitivity compared to the Rabi spectroscopy. The pulses can be performed in short time, while the quality factor of the clock is only limited by the free evolution time, during which the atoms are free from the interrogation field.

It is appreciably at the heart of the ingenious design of atomic fountain clocks, where cold atoms are launched upwards in a parabolic flight and traverse a microwave cavity twice, implementing the two $\pi/2$ pulses of the Ramsey interferometer. The Ramsey free evolution time is then determined by the height of the trajectory, limited by the size of the apparatus.

Many atomic inertial sensors are also based on the atomic fountain configuration. Similarly, the sensitivity to inertial forces scales with the interferometer time which is determined by the size of the trajectories [59]. To achieve higher sensitivities, one has to enlarge the apparatus, but also to fight against the free expansion of the cloud, requiring colder samples. An extreme example is the pico-Kelvin temperature required in a 10 m tall atomic fountain interferometer [60].

1.1.2 Trapped-atom clocks and TACC

With trapped atoms, limitations of the free-falling and expanding atoms can be alleviated. Long Ramsey evolution times and at the same time a compact setup make trapped-atom clocks extremely attractive. Similarly, trapped-atom inertial sensors, or with atoms in a "waveguide" for guided matter-wave interferometry, are promising for various applications [61].

However, trapping the atoms might seem contradictory to metrology that measures an unperturbed transition *by definition*. A trap is an inhomogeneous energy potential, which is in general different for the two clock states. The trap can then induce shift on the clock transition frequency that compromises the clock accuracy and stability. The inhomogeneous shift also deteriorates the coherence in the spectroscopic measurement. Luckily, "magic"

traps are found in various systems, in which the two clock states are perturbed equally such that the clock transition is unaffected. As a prime example, the discovery and realisation of "magic wavelengths" for various narrow-line optical transitions lead to the rapid development of optical lattice clocks, reducing the uncertainty by two orders of magnitude in merely a decade [62, 63].

Atomic clocks suffer not only from *single-atom* uncertainties, such as the perturbations from the trap, but also from the *ensemble* uncertainties from collisional interactions among atoms, leading to density dependent frequency shift. The latter has been a major issue of trapped-atom clocks in which the atomic density is generally high.

In fermionic optical lattice clocks, strong interactions contrarily suppress collisional shift [64], leading to the recent development of 3D lattice clocks with degenerate Fermi gases [65]. But this is not the case for microwave clocks with Rb or Cs atoms, which are currently closer to broader applications. Then the QPN is harder to mitigate as increasing the atom number has a price to pay. In this context, spin-squeezing beyond the SQL is particularly relevant for trapped-atom clocks.

We will from now on focus on our experiment – trapped-atom clock on a chip (TACC) at SYRTE. It is a microwave clock using magnetically trapped, ultra-cold ^{87}Rb atoms. TACC has been a unique realisation of metrology-grade trapped-atom clock based on atom chip technologies.

1.1.2.1 Atom chips

Since their invention eighteen years ago, atom chips [66] have enabled experiments from fast preparation of BECs to the zero-g experiments in a drop-tower [67]. Atom chips continue to attract tremendous efforts with the prospects not only as compact and robust platforms for atomic sensors and clocks, but also allowing to trap molecules, charged particles and Rydberg atoms for the study of quantum technologies and fundamental physics. A recent review can be found in [68].

Like conventional magnetic traps, atom chips create magnetic field minima (static or dynamic) that can trap atoms with positive magnetic moment (low-field seekers). Various types of traps can be generated by a combination of bias fields and electric currents running on the chip in various geometries. Here, I shall only mention two common types of static traps concerned in this thesis.

Quadrupole traps Commonly generated simply by a pair of anti-Helmholtz coils, quadrupole traps can provide tight confinement, due to non-vanishing field gradient at the trap centre. However, zero-field at the trap centre leads to spin-flip losses (Majorana losses) [69], more significant for the colder atoms.

For atom chips, the building block of micro-traps is the 2D quadrupole trap created by a single wire and a homogeneous bias field perpendicular to it [66]. Confinement in the third dimension while maintaining a finite field gradient at the trap centre can be achieved by bending the wire in a U-shape. This is widely used for the magneto-optical trap (MOT) in atom chip experiments. A pedagogical demonstration can be found in [70].

Ioffe-Pritchard traps The Ioffe-Pritchard traps alleviate the Majorana losses by having a finite B-field at the minimum (field gradient also vanishes). The trap potential near

the trap centre then approximates a harmonic potential. Ioffe-Pritchard traps are realised on atom chips by a Z-shape wire, or more versatilely by dimple traps – two wires cross perpendicularly. The latter is commonplace for ultra-cold atoms and is predominantly used in TACC experiment.

1.1.2.2 A pseudo-magic trap for TACC

In the ^{87}Rb ground state manifold, states $|1,-1\rangle$, $|2,1\rangle$ and $|2,2\rangle$ are magnetically trappable. Luckily, The energy difference between $|1,-1\rangle$ and $|2,1\rangle$ – a function of magnetic field – exhibits a minimum at a "magic field" $B_m \simeq 3.229$ G, where the transition frequency is first-order insensitive to the magnetic field. $|1,-1\rangle \to |\downarrow\rangle$ and $|2,1\rangle \to |\uparrow\rangle$ are then used as the clock states, with the Zeeman shift near B_m given by

$$\Delta\nu_B = b(B - B_m)^2 \equiv b\Delta B^2 \tag{1.10}$$

where $b \simeq 431.356$ Hz/G^2 [71].

We will consider an atomic cloud trapped in a harmonic trap. We shall see that a pseudo-magic trap can be found, in which the inhomogeneity in the transition frequency can be largely cancelled, resulting in very long coherence times.

Zeeman shift In a harmonic trap with trapping frequencies ω_x, ω_y and ω_z, the Zeeman shift (Eq. 1.10) is position dependent ($\boldsymbol{r} = (x, y, z)$) [47]:

$$\Delta\nu_B(\boldsymbol{r}) = \frac{bm^2}{\mu_\mathrm{B}^2}\left(\omega_x^2 x^2 + \omega_z^2\left(y^2 + z^2\right) - 2gz + \Delta B\frac{\mu_\mathrm{B}}{m}\right)^2 \tag{1.11}$$

where m is the atomic mass , g the gravitational acceleration, and μ_B the Bohr magneton. The gravity shifts the cloud away from the trap centre, the so-called "gravitational sag". It has a considerable influence which will become clear later. The curvature of the shift at the trap centre can have different signs depending on the bias field ΔB.

Collisional shift On the other hand, with (cold) thermal cloud, we consider that the ensemble can be treated classically and the atomic density is given by the Maxwell-Boltzmann distribution at temperature T:

$$n(\boldsymbol{r}) = \frac{N}{(2\pi)^{3/2}x_T y_T z_T}\exp\left[-\frac{x^2}{2x_T^2}\right]\exp\left[-\frac{y^2}{2y_T^2}\right]\exp\left[-\frac{z^2}{2z_T^2}\right] \tag{1.12}$$

where N is the number of atoms, k_B the Boltzmann constant, and $x_T = \sqrt{k_\mathrm{B}T/(m\omega_x^2)}$ (similar for y_T and z_T).

The collisional interactions induce a frequency shift that depends on the density. It can be described in a mean-field manner [71]:

$$\Delta\nu_\mathrm{mf}(\boldsymbol{r}) = \frac{2\hbar}{m}n(\boldsymbol{r})\left[(a_{\uparrow\uparrow} - a_{\downarrow\downarrow}) + f\left(2a_{\uparrow\downarrow} - a_{\downarrow\downarrow} - a_{\uparrow\uparrow}\right)\right] \tag{1.13}$$

where a_{ij}, $i,j \in \{\uparrow,\downarrow\}$ are the s-wave scattering lengths. $f = (n_\downarrow(\boldsymbol{r}) - n_\uparrow(\boldsymbol{r}))/n(\boldsymbol{r})$ is the population imbalance. We will consider $f = 0$ for a standard Ramsey sequence. For ^{87}Rb, $a_{\downarrow\downarrow} = 100.44a_0$, $a_{\uparrow\uparrow} = 95.47a_0$ and $a_{\uparrow\downarrow} = 98.09a_0$ with $a_0 = 0.529$ Å [71]. So $\Delta\nu_\mathrm{mf}$ is negative. We will also refer to the collisional shift as density shift later.

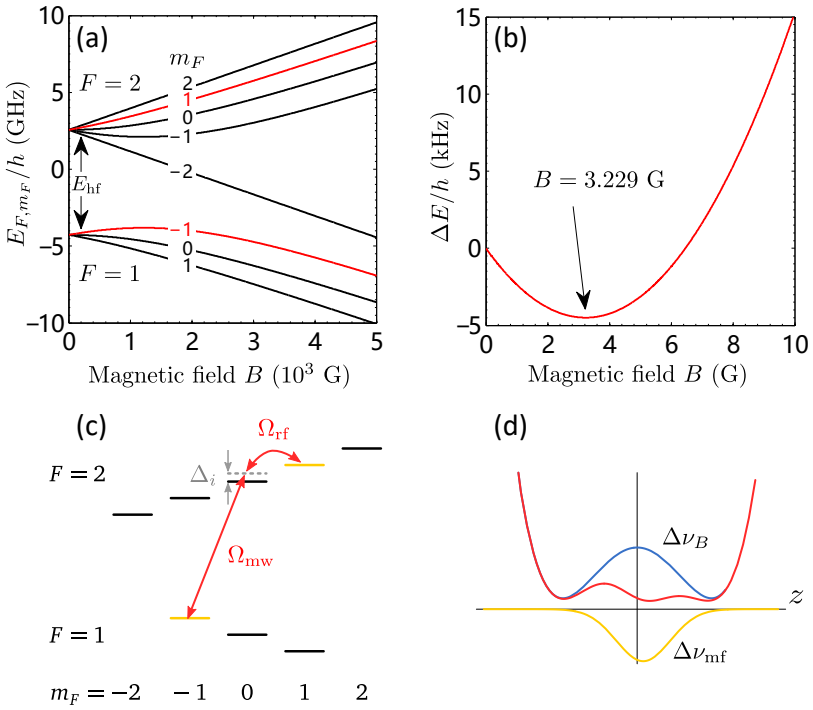

Figure 1.2 The clock transition and pseudo-magic trap in TACC, Adapted from [72]. (a) Energy of the $5^2S_{1/2}$ hyperfine ground states of ^{87}Rb in magnetic field, calculated using the Breit-Rabi formula [73]. (b) Energy difference between the clock states $|1,-1\rangle$ and $|2,1\rangle$ showing a magic field at $B_m \simeq 3.229$ G. (c) Two-photon transition implemented in TACC, with $\Delta_i \approx 500$ kHz. (d) Mutual compensation between the inhomogeneous Zeeman shift $\Delta\nu_B$ and the mean-field collisional shift $\Delta\nu_{\rm mf}$, at bottom field slightly lower than B_m ($\Delta B < 0$). The compensation is slightly compromised due to gravitational sag that shifts the cloud away from the trap centre.

Spatial inhomogeneity compensation While the collisional shift is stronger towards the cloud centre (a positive curvature), the Zeeman shift can be tuned ($\Delta B < 0$) to have the opposite curvature that almost cancels the inhomogeneity close to the trap centre. The imperfections are twofold: different forms of the magnetic potential (quadratic) and the density (Gaussian); and the fact that gravitational sag displaces the centre of the density profile away from that of the magnetic potential (Fig. 1.2(c)). Nevertheless, this mutual compensation between the two inhomogeneity sources allows a coherence time of a few seconds in TACC [47].

Two-photon transition To drive the clock transition, two photons are needed via an intermediate state $|1,0\rangle$ or $|2,0\rangle$. In the experiment we use a microwave (MW) field $\sim$ 6.834 GHz and a radio-frequency (RF) field ~ 1.7 MHz with Rabi frequencies $\Omega_{\rm mw}$ and $\Omega_{\rm rf}$ respectively, with a detuning $\Delta_{\rm i}/(2\pi) \sim 500$ kHz to the intermediate $|2,0\rangle$. The two-photon Rabi frequency is given by

$$\Omega_{\rm R} = \frac{\Omega_{\rm mw}\Omega_{\rm rf}}{2\Delta_{\rm i}} \tag{1.14}$$

under the assumption $\Omega_{\mathrm{mw}}, \Omega_{\mathrm{rf}} \ll \Delta_{\mathrm{i}}$ for a negligible population of the intermediate state.

An AC-Zeeman shift (or light shift) arises as (considering only a 3-level system) [70]:

$$\delta\omega_{\mathrm{AC}} = \frac{\Omega_{\mathrm{rf}}^2 - \Omega_{\mathrm{mw}}^2}{4\Delta_{\mathrm{i}}} \tag{1.15}$$

rendering the clock frequency sensitive to the power fluctuations in the excitation fields. Taking into account all Zeeman sublevels in the ground state manifold, and assuming an equal mixture of σ^+ and σ^- polarisations of the excitation field, Ω_{rf} vanishes [70]. But in reality it persists and actually allows to compensate the shift induced by the MW (if they have opposite signs). However, this compensation does not eliminate the sensitivity to differential power fluctuations in the MW and RF fields. More theoretical discussions about the clock trap in TACC can be found in [70, 72].

1.1.3 Clock stability

In this subsection, after a general introduction to the metrics of evaluating a clock, we will briefly discuss some common noise sources of our clock. A detailed analysis of the TACC-2 stability is given in Sec. 3.1.

1.1.3.1 Figures of merit

In general, locking the LO to the atomic transition realises a clock signal

$$\nu_{\mathrm{clk}}(t) = \nu_{\mathrm{at}}^0(1 + \epsilon + y(t)) \tag{1.16}$$

where ν_{at}^0 denotes the unperturbed atomic frequency. We will use frequencies in Hz for convenience. We identify two terms that are commonly used for evaluating clocks.

Accuracy ϵ denotes a systematic shift from the unperturbed atomic frequency. It depends on the particular realisation and its uncertainty quantifies the *accuracy* of the clock. It is less of a concern for secondary standards for applications, as long as the systematic inaccuracies can be calibrated with the primary standards. However, the uncertainty of the systematic error cannot be distinguished from the random error of a measurement, therefore also contributes to the clock instability. The clock accuracy is not studied in this thesis.

Stability $y(t)$ is the fractional frequency fluctuation and quantifies the stability of the clock. More specifically, one also distinguishes short-term (seconds) and long-term (hours, days) stability, depending on the application. The noise mechanisms and limits are also very different. In this thesis, we focus on the applications of quantum technologies, which target on improving the short-term stability.

Allan variance The Allan variance is the standard way to characterise the clock stability. It resolves the problem that the standard variance is not well defined at low frequencies if the clock signal has flicker noise or drift. Specifically, the Allan variance (AVAR) is defined as [74]:

$$\sigma_y^2(\tau) = \frac{1}{2(M-1)} \sum_{i=1}^{M-1} (\bar{y}_{i+1} - \bar{y}_i)^2 \tag{1.17}$$

It is the expectation value of the two-sample variance, where $\bar{y}_i(\tau)$'s are contiguous samples averaged over time τ:[1]

$$\bar{y}_i(\tau) = \frac{1}{\tau}\int_{(i-1)\tau}^{i\tau} y(t)\mathrm{d}t \tag{1.18}$$

which reveals the noise at different time scales.

If we consider the noise spectrum (a function of the Fourier frequency), the Allan variance can be understood as a bandpass filter near the frequency $1/(2\tau)$. The scaling of $\sigma_y^2(\tau)$ as a function of τ then reflects different noise sources in the power spectrum of the clock signal [75]. For example, white frequency noise, which usually dominates in timescales between seconds to hours, scales as τ^{-1}. The flicker frequency noise appears flat in σ_y^2 versus τ, and random walk frequency noise diverges as $\sim \tau$.

We will be later using the Allan deviation which is the square root of the Allan variance. We assume that the clock has white frequency noise in the timescale of interest such that

$$\sigma_y(\tau) = \sigma_{y,\mathrm{shot}}\sqrt{\frac{T_c}{\tau}} \tag{1.19}$$

where $\sigma_{y,\mathrm{shot}}$ is the Allan deviation of one clock cycle, with cycle time T_c.

In each clock cycle, the atomic frequency is only probed by the LO during the Ramsey time. The frequency difference is affected by the sensitivity function $g(t)$ of the Ramsey sequence [76]:

$$\Delta\nu = \frac{\int_0^{T_c}\left(\nu_{\mathrm{at}}(t) - \nu_{\mathrm{LO}}(t)\right)g(t)\mathrm{d}t}{\int_0^{T_c} g(t)\mathrm{d}t} \tag{1.20}$$

with

$$g(t) = \begin{cases} a\sin\Omega t & \text{if } 0 \le t < \tau_p \\ a\sin\Omega\tau_p & \text{if } \tau_p \le t < \tau_p + T_{\mathrm{R}} \\ a\sin\Omega(T_{\mathrm{R}} + 2\tau_p - t) & \text{if } \tau_p + T_{\mathrm{R}} \le t < T_{\mathrm{R}} + 2\tau_p \\ 0 & \text{otherwise} \end{cases} \tag{1.21}$$

A normal Ramsey sequence $\Omega\tau_p = \pi/2$ operating at half fringe gives $a = 1$. Here $\nu_{\mathrm{at}}(t)$ includes shift of the ensemble atomic frequency that is subject to fluctuations, contributing to clock instability. Overall, the uncertainty of a clock measurement (one cycle) is given by the uncertainty of $\Delta\nu$, $\sigma_{\Delta\nu}$, and the uncertainty in the detection (of $P_\uparrow$), $\sigma_{P_\uparrow}$:

$$\sigma_{y,\mathrm{shot}} = \sqrt{\left(\frac{\sigma_{\Delta\nu}}{\nu_{\mathrm{at}}}\right)^2 + \left(\frac{2\sigma_{P_\uparrow}}{\pi Q_c}\right)^2} \tag{1.22}$$

where Q_c is the clock quality factor (Eq. 1.9). We will briefly discuss some major noise sources in the following.

1.1.3.2 Noise in $P_\uparrow$ measurement

Uncertainties in determining $P_\uparrow$ originate from different mechanisms:

[1] In practice, for limited clock measurement samples, one uses the overlapping Allan variance or Total variance [74].

Quantum projection noise As we have already discussed in the introduction, projective measurements of uncorrelated atoms lead to the binomial distribution of the outcome. Operating at mid-fringe with $P_\uparrow = \frac{1}{2}$, the variance of $N_\uparrow$ from measuring N atoms reads: $\mathrm{Var}(N_\uparrow) = P_\uparrow(1 - P_\uparrow)N = N/4$. Hence the noise in $P_\uparrow$ due to QPN reads $\sigma_{P_\uparrow} = 1/(2\sqrt{N})$. One can only fight with it by increasing the atom number in an unfavourable scaling $N^{-1/2}$. Moreover, density-related frequency shift and technical difficulties also limit this approach, as we will see in particular for TACC (Sec. 3.1).

Detection noise The error in counting atoms in the two states also leads to an uncertainty in $P_\uparrow$. It is usually of technical origin and is subject to the experimental methods. It may also boil down to some form of shot noise: for example, the photon shot noise of the imaging beam or the fluorescence. In TACC, the primary detection is absorption imaging. The detection noise is nearly limited by the photon shot noise.

Other technical noise In a Ramsey sequence, we assume two $\pi/2$ pulses. However, noise in the pulse area of the $\pi/2$ pulses due to e.g. power fluctuations of the LO field directly leads to error in the final $P_\uparrow$.[2] Apart from technical improvements, slow variations can be rejected by e.g. probing alternately on both sides of the Ramsey fringe and only extracting the frequency from the differential signal.

1.1.3.3 Local oscillator noise

Most naively, as a phase modulo π is measured in a Ramsey scheme, the phase is subject to an ambiguity when its deviation might exceed π. Moreover, a large frequency deviation reduces the sensitivity of the Ramsey spectroscopy (cf. Eq. 1.9, with $P_\uparrow$ different from 1/2). In other words, the clock has a fairly narrow bandwidth in correcting the LO frequency.

More profoundly, as we can see from Eq. 1.20, how precisely the LO frequency is measured is also determined by the sensitivity function. The clock is blind to the LO noise outside the Ramsey time. With the T_R only a small fraction of the cycle time T_c, the clock resembles a discrete data acquisition that periodically samples the LO frequency and its fluctuations, suffering from aliasing such that high frequency LO noise (multiples of the sampling frequency $1/T_c$) can further degrade the clock stability.

This is known as the Dick effect, which has been one of the most important noise sources for optical clocks today. The Cs fountain clock at SYRTE is supported by a cryogenic sapphire oscillator, which is not accessible for broader metrological applications. In fact, the Dick effect can be the most prominent limit for compact devices where only a quartz crystal is affordable.

This also motivates new techniques such as non-destructive measurements to use the same atoms in multiple clock measurements [56]. In the case where the excess LO noise limits the Ramsey time, multiple short Ramsey sequences sharing a single phase of atom preparation effectively improve the clock duty cycle (T_R/T_c), alleviating the Dick effect.

In TACC, the Dick effect is a major contribution to clock instability. Although recycling atoms with non-destructive measurements has not been studied in this thesis, it is one of the two major objectives of TACC-2 and experiments will be carried out in the near future.

[2] Although in principle errors in the preparation also influence the collisional shift during the Ramsey sequence, see e.g. [77].

1.1.3.4 Collisional shift

As introduced in Eq. 1.13, the collisional shift is one of the most important systematic effects in atomic fountains and has a major contribution to the uncertainty [78, 79]. The situation is much severer for trapped-atom clocks in which the density can be 4 orders of magnitude higher.

Correction to the systematic error can be applied shot-to-shot based on the measurement of the total atom number which determines the atomic density. However, this correction is compromised by the detection noise in the atom number. Furthermore, in the presence of atom loss, only the final atom number is known. The statistical nature of atom loss imposes an uncertainty in the average atom number during the interrogation time, hence in the collisional shift. In fact, as we will see, for TACC-2 the uncertainty of this correction can be an important source of clock instability, if a large part of the atoms is lost.

1.1.3.5 Other instabilities in TACC

There are other technical fluctuations which deteriorate the clock stability in TACC. Here I only take an overview and a detailed analysis will be given in Sec. 3.1.

Magnetic field fluctuations As I mentioned, the pseudo-magic trap for TACC requires a bias field slightly lower than the magic field. In this case, however, the Zeeman shift is more sensitive to magnetic field variations. Further is the bias field away from the magic field, the bigger the contribution from the magnetic field fluctuation. As we will see, this is one of the major noise sources in TACC.

Atom temperature and its fluctuations Both the Zeeman shift and the density shift depend on the atom temperature, but an optimum field exists at which the total shift is first-order insensitive to temperature fluctuations. However, this optimum field differs from the magic field hence the insensitivity to the temperature fluctuation and that to the magnetic field fluctuation can not reconcile. The overall optimum bias field inevitably suffers from noise both in magnetic field and in atom temperature.

1.2 Concepts of spin squeezing

1.2.1 Surpassing SQL with spin-squeezed state

We resume from section 1.1 and consider the quantum uncertainties in the collective spin in a theoretical setting. A Heisenberg uncertainty relation between the spin operators directly results from the commutation relations (Eq. 1.2):

$$\Delta S_{\boldsymbol{n}} \Delta S_{\perp} \geq |\langle \hat{S}_{\boldsymbol{s}} \rangle|/2 \tag{1.23}$$

where $\boldsymbol{n}$ is an axis perpendicular to the mean spin direction $\boldsymbol{s}$, and $\perp$ is orthogonal to both $\boldsymbol{n}$ and $\boldsymbol{s}$. $\Delta S_{\boldsymbol{n}} = \sqrt{\langle \hat{S}_{\boldsymbol{n}}^2 \rangle - \langle \hat{S}_{\boldsymbol{n}} \rangle^2}$ denotes the standard deviation of an ensemble of measurements of $\hat{S}_{\boldsymbol{n}}$.

For the CSS, $|\theta, \phi, N\rangle$, a projective measurement along any direction $\perp$ orthogonal to $\boldsymbol{s}$ will project each qubit into the two eigenstates with equal probability. Therefore $\langle \hat{S}_{\perp} \rangle = 0$

and the variance of the measurement $(\Delta S_\perp)^2 = N/4$, coming from the sum of all qubits. This can be seen for example from

$$(\Delta S_z)^2 = \frac{1}{4}\sum_{i=1}^{N}\langle x|\hat{\sigma}_z^2|x\rangle_i = \frac{N}{4}$$

where $|x\rangle = (|\uparrow\rangle + |\downarrow\rangle)/\sqrt{2}$, and knowing that $\langle x|\hat{\sigma}_z|x\rangle_i = 0$.

It can be shown that the CSS is the optimal separable state for metrology [25], as it saturates the Heisenberg inequality. It exhibits an equal distribution of the uncertainty $\Delta S_{\boldsymbol{n}} = \Delta S_\perp = \sqrt{N}/2$. This isotropic minimum uncertainty is known as the standard quantum limit (SQL), which leads to the QPN in the clock measurements. In terms of a phase measurement, we are interested in the angular resolution on the Bloch sphere:

$$\Delta\theta_{\mathrm{SQL}} = \frac{\Delta S_{\perp,\mathrm{CSS}}}{|\langle\hat{\boldsymbol{S}}_{\boldsymbol{s}}\rangle|} = \frac{1}{\sqrt{N}}, \tag{1.24}$$

Nevertheless, the isotropic uncertainty distribution originates from the separable state, but the uncertainty relations do not prevent a single projection from being more precise than the SQL. It turns out that entanglement between particles can lead to such "redistribution" of the uncertainty, resulting in a "squeezed" state, namely $\Delta S_\perp < \sqrt{N}/2$. Using the squeezed quadrature therefore enables measurement precisions beyond the SQL.

Certainly, many other entangled states exhibit metrological gain, generally described using Quantum Fisher information (see e.g. [25]), which is beyond the scope of this thesis.

Squeezing measures Without knowing the details of the entanglement, spin squeezing can be simply assessed by the standard uncertainty. The minimum uncertainty normalised to the SQL,

$$\xi_{\mathrm{N}}^2 = \left(\frac{\Delta S_{\perp,\mathrm{min}}}{\Delta S_{\perp,\mathrm{CSS}}}\right)^2 = \frac{4(\Delta S_{\perp,\mathrm{min}})^2}{N} \tag{1.25}$$

is sometimes referred to as the number squeezing if $\xi_{\mathrm{N}}^2 < 1$ [28]. It is more metrologically relevant to assess the angular resolution $\Delta\theta$, in which the length of the spin $|\langle\hat{\boldsymbol{S}}_{\boldsymbol{s}}\rangle|$ measures the "resource" in a practical squeezing process – taking into account the coherence, or the contrast of the Ramsey fringes. This metric, known as the Wineland criterion for spin squeezing [29], is defined as

$$\xi^2 = \left(\frac{\Delta\theta_{\perp,\mathrm{min}}}{\Delta\theta_{\mathrm{SQL}}}\right)^2 = \frac{N(\Delta S_{\perp,\mathrm{min}})^2}{|\langle\hat{\boldsymbol{S}}_{\boldsymbol{s}}\rangle|^2} \tag{1.26}$$

$\xi^2 < 1$ signals a metrological spin squeezing, it is shown to be a sufficient condition of certain types of entanglement [80]. ξ^{-2} is commonly reported in dB, as it shows the effective gain in atom number to achieve the same resolution.

While as the noise distribution is squeezed in one axis, the other quadrature is necessarily anti-squeezed to satisfy the Heisenberg uncertainty relation (Eq. 1.23). But the latter is not always saturated. Squeezed states that saturate the uncertainty are called minimum uncertainly states or optimal squeezed states. A lower bound of ξ^2 can be found for these states [25]:

$$\xi^2 \geq \frac{2}{N+2} \tag{1.27}$$

which is essentially the ultimate Heisenberg limit. For a detailed review of many other squeezing measures, see for example [81, 25].

Motivations for trapped-atom clocks As we know, the SQL is not a remote theoretical limit. The state-of-the-art atomic fountains have long reached a short-term stability limited by the QPN [23]. Here I would like to emphasise that spin squeezing surpassing the SQL is particularly relevant for trapped-atom clocks:

- For trapped-atom clocks in which the collisional shift can impose a large uncertainty due to high density, the number of atoms is often limited. Employing spin-squeezed states can mitigate the severe SQL.
- In recently developed 3D lattice clocks in which collisional interactions are suppressed by keeping a single atom per lattice site [65], increasing atom number becomes technically difficult and the QPN limit is expected to be approached soon.
- More generally, squeezed states can benefit compact applications where the number of atoms is limited, either technically or fundamentally.

1.2.2 Overview of spin-squeezing generation

With all these prospects, there have been tremendous experimental efforts over a decade to demonstrate and study spin squeezing in atomic systems. Here I give a brief summary of the most studied methods for squeezing generation.

As a particular type of entanglement, spin squeezing correlates the local spin observables of the atoms. Let us distinguish two categories of entanglement creation, namely by dynamics due to interactions between atoms or by a partial projection of the collective state.

1.2.2.1 Squeezing by inter-atomic interactions

Described in terms of collective spin operators, entanglement requires non-linearity. A benchmark model is the so-called one-axis twisting (OAT) Hamiltonian, with the simplest non-linearity:

$$\hat{\mathcal{H}}_{\mathrm{OAT}} = \hbar\chi\hat{S}_z^2 \tag{1.28}$$

The collective operator $\hat{S}_z^2$ actually means that each atom interacts with all others. But it also gives a very intuitive picture: the precession rate is itself proportional to S_z, distorting the Bloch sphere (Fig. 1.3(b)). The initially isotropic noise distribution is twisted under the dynamics. It can be shown that the process almost preserves the minimum uncertainty area and exhibits squeezing along a certain axis [28]. The dynamics reaches a maximum squeezing parameter around $t_{\max} \sim \chi^{-1}N^{-2/3}$ and later loses the squeezing as the state wraps around the Bloch sphere, but the entanglement keeps increasing, and the assessment of which requires more complex measures like the nonlinear squeezing [82]. The maximum squeezing at $t_{\max}$ scales with $\xi^2 \sim N^{-2/3}$.

Collisional interactions in BECs As widely explored, collisional interactions in a BEC lead to an OAT Hamiltonian, in which χ depends on the scattering lengths and the overlap of the wavefunctions of the condensate modes. By controlling the scattering lengths via

Feshbach resonances [33, 36] or modifying the wavefunction overlap via state-dependent potentials [34, 35], substantial spin squeezing has been achieved. However, strong interactions in a BEC generally limit their application for clocks.

Cavity feedback As will be detailed below, light-mediated interactions between atoms in an optical cavity can also produce an effective OAT Hamiltonian [43, 44]. The χ term now depends on the dispersive coupling between atoms and cavity photons, and can be very large in a strong-coupling cavity-QED system. However, there is usually excessive noise enhancement in the anti-squeezed quadrature that far exceeds the squeezing due to cavity decay. This so-called non-unitary anti-squeezing compromises possible metrological gain in clock applications [83], but recent progress has approached near unitary squeezing [84, 45].

Beyond OAT A few other schemes show metrological advantages compared to the OAT, including the "twist-and-turn" [85] and two-axis-counter-twisting (TACT) [28]. The former has been demonstrated in a BEC [86], while the TACT, despite extensive theoretical studies, remains experimentally challenging. Ideally, the TACT, described by a Hamiltonian $\hat{\mathcal{H}}_{\mathrm{TACT}} = \hbar\alpha(\hat{S}_\theta^2 - \hat{S}_{\theta+\pi/2}^2)$ can achieve maximum squeezing at the Heisenberg limit $\xi^2 \sim 1/N$, and it squeezes faster compared to OAT ($\xi^2 \sim N^{-2/3}$). However, the benefits can be lost in the presence of decoherence [87].

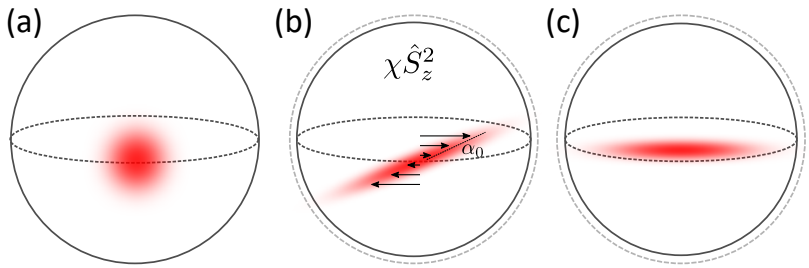

Figure 1.3 Conceptual representation of squeezing by QND measurement and by OAT dynamics. (a) depicts a CSS prepared on the equator with its spin uncertainty. (b) illustrates the OAT dynamics: the precession rate depends on S_z. The twisted noise distribution exhibits minimum uncertainty along the axis of $\vec{z}$ rotated by α_0. (c) shows the squeezing by QND measurement. $\langle\hat{S}_z\rangle$ after each measurement depends on the measurement result, which itself fluctuates as the SQL, but ΔS_z is deterministically reduced after the measurement, limited by the measurement uncertainty. The squeezing is revealed by ΔS_z conditioned on the measurement outcome unless feedback correction is applied. In both (b) and (c), the dashed outer spheres indicate the possible coherence loss due to the squeezing process.

1.2.2.2 Squeezing by quantum non-demolition measurement

A QND measurement is a measurement that preserves the measured observable. For example, if the Hamiltonian of the measurement process satisfies $[\hat{S}_z, \hat{\mathcal{H}}_{\mathrm{QND}}] = 0$, meaning that S_z is a constant of motion, measuring an observable in $\hat{\mathcal{H}}_{\mathrm{QND}}$ (that couples to $\hat{S}_z$) can realise a QND measurement of $\hat{S}_z$.

The measurement projects the collective spin $\hat{S}_z$ but not individual atoms. In fact, this partial projection leads to entanglement that can modify the noise distribution, e.g. ΔS_z. In another point of view, the collective observable ($\hat{S}_z$) is known to the limit of the measurement uncertainty, which can be more precise than the SQL.

Since the squeezed state after the measurement (e.g. S_z) depends on the measurement result, the squeezing is "conditional" if one looks at the measurement outcomes. But after each measurement, ΔS_z is deterministically reduced. Unconditional squeezed can be achieved by correcting S_z after each measurement using the information of the measurement result [88, 89].

QND measurements of atomic systems are generally realised by atom-light interactions. The measurement uncertainty is then limited by the photon shot noise (PSN) of the probe light, before reaching the maximum achievable squeezing that is set by non-ideal effects such as decoherence due to photon scattering and Raman spin-flip processes.

Free-space QND measurements can be implemented in free-space, based on i) the phase shift induced by the dispersive coupling, as shown in one of the first demonstrations of spin squeezing [39]; ii) and the Faraday rotation of light [90, 38, 91], a promising candidate for quantum-enhanced magnetometry. Nevertheless, high level of squeezing is generally difficult due to weak coupling (optical depth) in a single-pass geometry.

Cavity-QED The optical depth of the atoms is strongly enhanced in an optical cavity as each photon travels many round-trips interacting with the atoms, entering the realm of (collective) strong coupling. Since the early demonstration of conditional spin-squeezing based on cavity measurements [41], squeezing records have been quickly updated [92, 89], and reached lately almost 20 dB [42]. These include atom-light coupling both in the dispersive regime [41, 42] and in the resonant regime [93, 89].

We will discuss the cavity measurement scheme in more detail. The squeezing results in this thesis are conditional squeezing by cavity measurement, which belongs to this category.

QND measurements for clocks On the other hand, QND measurements in their on right are of great interest for clocks. Here even a coherence-non-preserving quantum non-destructive measurement can be employed to perform multiple Ramsey cycles reusing the same atoms, which will improve the duty cycle of the clock. It is particularly interesting for clocks suffering from Dick effect such as many current optical clocks [94, 95], and compact clocks (like ours). For true QND measurements, atoms are not only recycled but also stay in coherence. For example, (weak) QND measurements only lock the LO (in presence of phase noise) roughly in phase with the atoms to ensure the phase sensitivity. It has been demonstrated that QND measurements outperform uncorrelated Ramsey sequences with recycled atoms [96, 56], opening ways to improving clocks and interferometer-based sensors.

1.3 Spin squeezing in cavity-quantum electrodynamics

In this section, We briefly review some basic concepts in cavity-QED and the realisation of spin squeezing. After introducing some general properties of the coupled system, I will focus

on the far-detuned dispersive regime in which our experiments are performed. I also briefly discuss the limits to achievable squeezing in general and in our system.

1.3.1 Real-world cavities

We focus here on Fabry-Pérot (F-P) cavities, formed by two highly reflective mirrors separated by length L. The resonance condition gives equally spaced resonances in frequency domain separated by $\nu_{\rm fsr} = c/2L$ – the free spectral range (FSR) – where c is the speed of light. It is also the inverse of the round trip time.

The cavity enhancement for atom-light interactions comes from the amount of round-trips a photon travels before it leaves the cavity. This is precisely the cavity *finesse* $\mathcal{F}$, which is defined as the ratio between photon lifetime (the inverse of loss rate κ) and the time for one round-trip:

$$\mathcal{F} = \frac{2\pi\nu_{\rm fsr}}{\kappa} = \frac{2\pi}{\mathcal{L}_{\rm tot}} \simeq \frac{\pi}{\mathcal{T}+\mathcal{L}} \tag{1.29}$$

where the total loss $\mathcal{L}_{\rm tot}$ is assumed to consist of the transmission $\mathcal{T}$ and loss $\mathcal{L}$ in each of the two identical mirrors. $\mathcal{F}$ is effectively the quality factor of the resonator. For high finesse cavities, $\mathcal{L}$, including scattering and absorption, can be comparable to $\mathcal{T}$, significantly limiting the maximum power transmitted on resonance:

$$T_{\rm max} = \frac{\mathcal{T}^2}{(\mathcal{T}+\mathcal{L})^2} \tag{1.30}$$

One can find the spectral response of a F-P cavity, to an incoming field at ω_p with detuning $\delta_p = \omega_p - \omega_0 \ll 2\pi\nu_{\rm fsr}$, where ω_0 is the cavity resonance:

$$T = \left(\frac{\kappa_t}{\kappa}\right)^2 \frac{1}{1+\left(\frac{\delta_p}{\kappa/2}\right)^2} \tag{1.31}$$

$$R = \frac{\left(\frac{\kappa_l}{\kappa}\right)^2 + \left(\frac{\delta_p}{\kappa/2}\right)^2}{1+\left(\frac{\delta_p}{\kappa/2}\right)^2} \tag{1.32}$$

where κ_t and κ_l denote the decay rates due to transmission and loss, respectively:

$$\frac{\kappa_t}{\kappa} \simeq \frac{\mathcal{T}}{\mathcal{T}+\mathcal{L}}, \quad \frac{\kappa_l}{\kappa} \simeq \frac{\mathcal{L}}{\mathcal{T}+\mathcal{L}} \tag{1.33}$$

We recognise the Lorentzian shape of the spectrum, with linewidth κ ($2\pi\times$FWHM in frequency). The phases of the transmitted and reflected light, with respect to the input field read

$$\tan\phi_t = \frac{\delta_p}{\kappa/2}, \quad \tan\phi_r = \frac{\kappa_t}{\kappa_l}\frac{\delta_p}{\kappa/2} \tag{1.34}$$

In the end, coherent interaction between the photon and an atomic transition should compete with the decay rate of the atomic transition Γ and that of the cavity κ.

Detection limit The cavity frequency can be generally determined by measuring the cavity response to a probe field. Information is contained in the photons that leave the cavity, both in transmission and reflection. If one uses coherent field, as in most experiments, the measurement is ultimately limited by the quantum fluctuation of the field, or the PSN of the detected photons.

A general measurement can be viewed as performed on the phase, e.g. in the phase of the transmitted light ϕ_t. The PSN limit on this phase is $\Delta\phi_t = 1/(2\sqrt{n_d})$, where Δ stands for standard deviation and n_d is the average detected photon number. The uncertainty in knowing the cavity resonance is therefore

$$\Delta\delta_{\mathrm{PSN}} = \frac{\mathrm{d}\delta_p}{\mathrm{d}\phi_t}\Delta\phi_t = \frac{\kappa}{2}(\sec\phi_t)^2\Delta\phi_t = \frac{\kappa}{4\eta_d\sqrt{n_d}} \tag{1.35}$$

where we have defined the detection sensitivity $\eta_d = 1/(1+(2\delta_p/\kappa)^2)$. As a comparison, a homodyne detection measuring the imaginary part of the signal near resonance, $\delta_p \simeq 0$, gives a maximum sensitivity $\eta_d = 1$. However, this maximum sensitivity is obtained only when the phase of the signal is almost known.

A heterodyne detection, sampling both the real and imaginary part, is therefore more robust to an unknown signal [97]. But the overall sensitivity is reduced to 1/2.

One can also simply measure the transmitted photon number at $\delta_p = \kappa/2$. This gives a sensitivity of 1/2, same to that of the heterodyne detection. This can also be seen from the Lorentzian transmission profile:

$$\Delta n_d = \Delta\delta_p \left|\frac{\partial}{\partial\delta_p}\left(\frac{2n_d}{1+(2\delta_p/\kappa)^2}\right)\right|_{\delta_p=\kappa/2} = \frac{2n_d}{\kappa}\Delta\delta_p \tag{1.36}$$

$$\text{PSN:}\quad \Delta n_d = \sqrt{n_d}$$

$$\Rightarrow \Delta\delta_{\mathrm{PSN}} = \frac{\kappa}{2\sqrt{n_d}} \tag{1.37}$$

In addition, the detector efficiency plays a crucial rule, as no remedy exists to the loss of information.

1.3.2 Cavity-QED in the dispersive regime

1.3.2.1 Jaynes-Cummings model

Similar to Eq. 1.5, but with a well-defined cavity mode, we can describe the interaction between a single atom and cavity photons by the famous Jaynes-Cummings Hamiltonian [98]. In the RWA, with the coupling rate $g \ll \omega_a, \omega_c$, it reads

$$\hat{\mathcal{H}}_{\mathrm{JC}}/\hbar = \omega_a \left|\mathrm{e}\right\rangle\!\left\langle\mathrm{e}\right| + \omega_c\hat{c}^\dagger\hat{c} + g(\left|\mathrm{e}\right\rangle\!\left\langle\mathrm{g}\right|\hat{c} + \left|\mathrm{g}\right\rangle\!\left\langle\mathrm{e}\right|\hat{c}^\dagger) \tag{1.38}$$

where ω_a and ω_c are frequencies of the atomic transition and of the cavity, respectively. Here we consider an electronic transition between ground state $|\mathrm{g}\rangle$ and excited state $|\mathrm{e}\rangle$, with a decay rate Γ of the excited state. $\hat{c}^\dagger$ ($\hat{c}$) is the creation (annihilation) operator of photons in the cavity mode.

This can be extended to N atoms, resulting in the Tavis-Cummings Hamiltonian [99]. Assuming the same g for all atoms, the system resembles that of a single atom with the

collective coupling $\mathcal{G} = g\sqrt{N}$. In the manifold of a single excitation, the eigenfrequencies of the coupled system is given by

$$\omega_\pm - \omega_a = \frac{\Delta_c \pm \sqrt{\Delta_c^2 + 4\mathcal{G}^2}}{2} = \frac{\Delta_c \pm \sqrt{\Delta_c^2 + 4g^2N}}{2} \tag{1.39}$$

where $\Delta_c = \omega_c - \omega_a$ is the cavity detuning. This gives the so-called Vacuum-Rabi splitting of $2\mathcal{G}$ at $\Delta_c = 0$. At far detuning, the bare-cavity frequency feels a shift, linear to the atom number N: $\omega_- \simeq \omega_c + g^2N/\Delta_c$. It is precisely this dependence on N that is utilised to perform QND measurements of the atomic population.

Note that the eigenstates of the system are superpositions of photonic and atomic state. The linewidth of the eigenmodes,

$$\kappa'_\pm = \frac{\kappa + \left(\frac{\mathcal{G}}{\omega_\pm - \omega_a}\right)^2 \Gamma}{1 + \left(\frac{\mathcal{G}}{\omega_\pm - \omega_a}\right)^2} \tag{1.40}$$

is determined by both decay channels. We find that in the good cavity limit $\kappa \ll \Gamma$, the natural linewidth of the atomic transition will set the limit of the system decay.

1.3.2.2 Collective QND measurement

Probing the eigenfrequency of the system through the cavity provides a measurement of the collective coupling which depends on N. This is the basis of spin-squeezing by measurement in cavity-QED systems.

A cavity measurement can be arbitrarily precise with more photons, but it is never perfectly QND and the imperfections, which generally scale with the number of photons, will eventually limit the squeezing by measurement. From an information point of view, measuring the atomic state relies on the fact that atoms reveal their states through scattering probe photons, but only the coherent scattering into the cavity mode ensures the QND character on the collective state, without distinguishing individual atoms. In practice, only these photons can be collected. The scattering into free space either collapses an atom or changes its state, leading to loss of coherence or spin flip errors.

Therefore, squeezing by measurement is ultimately limited by the number of scattered photons (into free space) n_s per atom. One figure of merit in cavity-QED systems is the cooperativity $C = \frac{(2g)^2}{\kappa\Gamma}$, which characterises the coherent interaction strength with respect to the decay channels. $C > 1$ marks the *strong coupling regime*. In fact, for a measurement of the collective state, it is the collective cooperativity NC that determines the measurement precision.

In reality, the coupling g, an electric dipole coupling, depends on the field strength. The maximum coupling g_0 at the anti-node at the center of the cavity is quantified as

$$g_0 = \sqrt{\frac{\omega_a}{2\hbar\epsilon_0 V_m}} \cdot \mu \tag{1.41}$$

where μ is the dipole matrix element for the particular transition. V_m is the mode volume of the photon. For a Gaussian mode in a cavity, $V_m = \pi w_0^2 L/4$, where L is the cavity length and w_0 the waist. We see here the coupling is only determined by the atomic properties

and the cavity geometry. Increasing g_0 by reducing V_m brings the advantages of fibre-based micro-cavities [100].

QND measurements for spin squeezing can be implemented at different cavity detunings Δ_c, which do not solely determine the squeezing limit. In general, the optimum choice of detuning depends on the cavity linewidth. For example, in the bad cavity limit $\kappa \gg \Gamma$, to achieve a cavity measurement precision that reveals the QPN of the atoms (a good benchmark), n_s doesn't depend on Δ_c. The resonant regime may be beneficial due to the reduced technical requirements [97]. However, in the good cavity limit $\kappa \ll \Gamma$, it is desirable to go to the far-detuned regime. The squeezing is eventually limited by the atomic level structure (for hyperfine states as clock states).

In the following, we will focus on the far-detuned regime, namely the maximum detuning in a hyperfine ground-state manifold. More details about the resonant regime can be found in the experiments from the Thompson group at JILA (see for example [101, 89]). I will also give further discussions in the context of vacuum-Rabi splitting experiments in Sec. 3.2.1.

1.3.2.3 Effective spin model in the alkali ground state manifold

In the context of atomic clocks with alkali atoms (^{87}Rb in particular), the qubit states are two hyperfine ground states with transition frequency $\omega_{\text{at}}/2\pi$ (~ 6.8 GHz). For simplicity, the hyperfine manifold of the excited states (e.g. of the D2 transition) can be regarded as a common excited state. We shall consider both ground states $|\uparrow\rangle$ and $|\downarrow\rangle$ in the coupled system with the cavity (cf Eq. 1.38):

$$\hat{\mathcal{H}}_s/\hbar = \omega_c \hat{c}^\dagger \hat{c} + \sum_{i=1}^{N} \left[\frac{\omega_{\text{at}}}{2} \hat{\sigma}_z^{(i)} + \omega_a \left|\text{e}\right\rangle_i \langle \text{e}|_i + g \left(c \left|\text{e}\right\rangle_i \langle \uparrow|_i + c \left|\text{e}\right\rangle_i \langle \downarrow|_i + \text{h.c.} \right) \right] \tag{1.42}$$

where we consider N atoms and assume an equal coupling g for both transitions and for all atoms. In the far-detuned regime, the optimal cavity detuning is an equal detuning from either ground state: $\Delta_c = \omega_{\text{at}}/2$. If the intra-cavity photon number is very low $\langle \hat{c}^\dagger \hat{c} \rangle \ll (\Delta_c/g)^2$, the excited state can be adiabatically eliminated, resulting in an effective Hamiltonian [102]:

$$\begin{aligned} \hat{\mathcal{H}}_s/\hbar &= \omega_c \hat{c}^\dagger \hat{c} + \sum_{i=1}^{N} \left[\left(\frac{\omega_{\text{at}}}{2} + \frac{g^2}{\Delta_c} \hat{c}^\dagger \hat{c} \right) \hat{\sigma}_z^{(i)} \right] \\ &= \omega_c \hat{c}^\dagger \hat{c} + \frac{2g^2}{\Delta_c} \hat{c}^\dagger \hat{c} \hat{S}_z + \omega_{\text{at}} \hat{S}_z \end{aligned} \tag{1.43}$$

The second term describes the dispersive interaction between the spin and the cavity. Grouping it with the first term, we see that the cavity experiences a frequency shift proportional to $\hat{S}_z$:

$$\delta\omega_c = \frac{2g^2}{\Delta_c} S_z \tag{1.44}$$

while grouping it with the third term, we find the AC Stark shift experienced by the atom:

$$\delta\omega_{\text{at}} = \frac{2g^2}{\Delta_c} \langle \hat{c}^\dagger \hat{c} \rangle \tag{1.45}$$

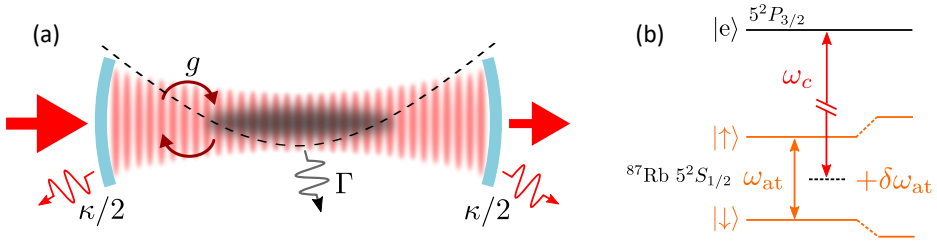

Figure 1.4 Schematics of the cavity-QED system in TACC-2. (a) The cavity-QED system with cavity decay rate κ, atomic decay rate Γ, and atom-light interaction at rate g. The dashed curve indicates that atoms are trapped magnetically in a shallow trap elongated along the cavity axis. (b) The energy diagram of the dispersive coupling. The cavity is equally detuned from the clock states – two hyperfine ground states of ^{87}Rb. An AC Stark shift $\delta\omega_{\mathrm{at}}$ is experienced by the atoms in the presence of a cavity photon.

1.3.2.4 Inhomogeneous coupling

As g is position dependent, the coupling for N atoms in a thermal distribution is inhomogeneous. The real collective observable therefore differs from $\hat{S}_z$, and is instead a weighted sum of $\hat{\sigma}_z^{(i)}$ depending on the coupling:

$$\hat{\mathcal{S}}_z = \frac{1}{2Z}\sum_{i=1}^{N}\eta_i\hat{\sigma}_z^{(i)} \tag{1.46}$$

where $\eta_i \leq 1$ and Z some normalisation factor. It can be shown that this observable is equivalent to a symmetric spin operator (homogeneous coupled) with a reduced length $\mathcal{S}$ [103], once the normalisation factor is chosen properly to preserve the commutation relations (Eq. 1.2). Specifically, the variance is given by the SQL:

$$(\Delta\mathcal{S}_z)^2 = \mathcal{S}/2 = \mathcal{S}_{z,\max}/2 \tag{1.47}$$

$$\frac{1}{4Z^2}\sum_{i=1}^{N}\eta_i^2 = \frac{1}{2}\cdot\frac{N}{2Z}\sum_{i=1}^{N}\eta_i \tag{1.48}$$

we have

$$Z = \frac{\sum_{i=1}^{N}\eta_i^2}{\sum_{i=1}^{N}\eta_i} \tag{1.49}$$

We can find an effective coupling for this effective spin, such that the cavity shift is properly produced:

$$\delta\omega_c = \sum_{i=1}^{N}\frac{g_i^2}{\Delta_c}\hat{\sigma}_z^{(i)} = \frac{2Zg_0}{\Delta_c}\left(\frac{1}{2Z}\sum_{i=1}^{N}\eta_i\hat{\sigma}_z^{(i)}\right) = \frac{2g_{\mathrm{eff}}^2}{\Delta_c}\hat{\mathcal{S}}_z \tag{1.50}$$

where we let $\eta_i = g_i^2/g_0^2$, and

$$g_{\mathrm{eff}}^2 = g_0^2\frac{\sum_{i=1}^{N}\eta_i^2}{\sum_{i=1}^{N}\eta_i} = \frac{\sum_{i=1}^{N}g_i^4}{\sum_{i=1}^{N}g_i^2} \tag{1.51}$$

This homogeneously coupled spin $\mathcal{S}$ has an effective atom number

$$N_{\text{eff}} = 2\mathcal{S} = N\frac{(\sum_{i=1}^{N}\eta_i)^2}{\sum_{i=1}^{N}\eta_i^2} = N\frac{(\sum_{i=1}^{N}g_i^2)^2}{\sum_{i=1}^{N}g_i^4} \tag{1.52}$$

In the following, we will nevertheless assume homogeneous coupling and continue to use S_z and S for simplicity.

1.3.3 Squeezing by QND measurement

1.3.3.1 Scattering, phase shift, and PSN

As the cavity frequency is determined by $\hat{S}_z$, which appears as a constant of motion in the effective Hamiltonian (Eq. 1.42), a cavity measurement with weak photonic excitation qualifies as a QND measurement of $\hat{S}_z$.

Starting with an initial CSS along x ($\langle S_z\rangle = 0$) The uncertainty of S_z after a cavity measurement is determined by the uncertainty of the measurement. However, it is crucial to consider the incoherent scattering of the off-resonant cavity photons. The detrimental scattering rate per atom is given by

$$\Gamma_s = \langle\hat{c}^\dagger\hat{c}\rangle\frac{g^2}{\Delta_c^2}\Gamma \tag{1.53}$$

As these photons are eventually lost, we can define a decay rate due to the scattering

$$\kappa_s = \frac{N\Gamma_s}{n_c} = N\frac{g^2}{\Delta_c^2}\Gamma = NC\left(\frac{\Gamma}{\omega_{\text{at}}}\right)^2\kappa \tag{1.54}$$

where n_c is the average intra-cavity photon number, and we have set $\Delta_c = \omega_{\text{at}}/2$ and used the cooperativity C. The cavity now decays at a rate $\kappa' = \kappa + \kappa_s$. We find similarities in Eq. 1.40. Note that despite the far detuning, the cavity linewidth can be significantly modified if NC approaches $(\omega_{\text{at}}/\Gamma)^2$.

For a collective measurement, the scattered photon per atom is an important benchmark:

$$n_s = \int \mathrm{d}t\ \Gamma_s = \frac{\Gamma}{2\Delta_c}\frac{2g^2}{\Delta_c}\int \mathrm{d}t\ n_c = \phi_{\text{ac}}\frac{\Gamma}{\omega_{\text{at}}} \tag{1.55}$$

which is totally determined by the accumulated phase due to the AC Stark shift

$$\phi_{\text{ac}} = \frac{2g^2}{\Delta_c}\int \mathrm{d}t\ n_c \tag{1.56}$$

It also serves as a good measure of the measurement strength.

The detected photon in transmission (half of the total decay) can be related to ϕ_{ac} as

$$n_d = \frac{q_d\kappa_t}{2}\int \mathrm{d}t\ n_c = \frac{q_d\kappa_t}{2\kappa C}\frac{\omega_{\text{at}}}{\Gamma}\phi_{\text{ac}} \tag{1.57}$$

where q_d denotes the detector efficiency, including all technical losses.

Recall that we have derived the uncertainty in determining the cavity frequency by n_d detected photons, but now the cavity decay rate is modified to κ' (Eq. 1.37):

$$\Delta\delta_{\mathrm{PSN}} = \frac{\kappa'}{4\eta_d\sqrt{n_d}}, \quad \text{with} \quad \eta_d = \frac{1}{1+(2\delta_p/\kappa')^2} \tag{1.58}$$

From the cavity shift per atom (Eq. 1.44), we obtain the uncertainty on spin projection S_z:

$$\Delta S_{z,\mathrm{PSN}} = \Delta\delta_{\mathrm{PSN}} \Big/ \left(\frac{2g^2}{\Delta_c}\right) = \frac{\kappa + \kappa NC\left(\Gamma/\omega_{\mathrm{at}}\right)^2}{4g^2/\omega_{\mathrm{at}}\cdot 4\eta_d\sqrt{n_d}} = \frac{1+NC\left(\Gamma/\omega_{\mathrm{at}}\right)^2}{4\eta_d C(\Gamma/\omega_{\mathrm{at}})\sqrt{n_d}} \tag{1.59}$$

$$= \frac{1+NC\left(\Gamma/\omega_{\mathrm{at}}\right)^2}{\sqrt{8\epsilon_c C(\Gamma/\omega_{\mathrm{at}})}}\frac{1}{\sqrt{\phi_{\mathrm{ac}}}} \tag{1.60}$$

where we also express it in term of ϕ_{ac} with $\epsilon_c \equiv \eta_d^2 q_d(\kappa_t/\kappa)$. Note that here we assumed collecting only the transmitted photon (or only the reflection). A factor of 2 can be gained in n_d (or ϕ_{ac}) if one collects all outgoing photons. We also see the advantage of a homodyne detection, as a factor of 2 can be gained in η_d.

While the measurement precision can be improved by more probe photons, PSN limited spin uncertainty is eventually superseded by the adverse effect of the scattered photons, as we shall see below.

1.3.3.2 Conditional spin uncertainty

I shall point out that Eq. 1.60 is the uncertainty in the measurement of S_z, better noted as $\Delta M|_{S_z}$, with M the unbiased estimator $\langle M\rangle|_{S_z} = S_z$. The conditional uncertainty of S_z on M can be inferred from $\Delta M|_{S_z}$, through the general relation [104]:

$$(\Delta S_z)^2|_M = \frac{\mathrm{Var}(S_z)}{\mathrm{Var}(M)}(\Delta M)^2|_{S_z} \tag{1.61}$$

where $\mathrm{Var}(\cdot)$ denotes the unconditional variance. Therefore

$$(\Delta S_z)^2|_M = \frac{\mathrm{Var}(S_z)(\Delta M)^2|_{S_z}}{\mathrm{Var}(S_z) + (\Delta M)^2|_{S_z}} \tag{1.62}$$

We realise that for a CSS, $\mathrm{Var}(S_z) = S/2$, the conditional variance will remain unchanged for an imprecise measurement $(\Delta M)^2|_{S_z} \gg S/2$, while for a precise measurement below the SQL, $(\Delta M)^2|_{S_z} \ll S/2$, it approaches (but smaller than) the uncertainty of the measurement. The unintuitive reduction comes from the information of the initial CSS.

We shall assume a precise measurement in the following, such that $(\Delta S_z)^2|_M \simeq (\Delta M)^2|_{S_z}$. We then obtain the squeezing parameter for the conditional spin (assuming no coherence loss):

$$\xi^2 \simeq \frac{(\Delta S_z)^2|_M}{\mathrm{Var}(S_z)} = \frac{\left(1+NC\left(\Gamma/\omega_{\mathrm{at}}\right)^2\right)^2}{2\epsilon_c NC(\Gamma/\omega_{\mathrm{at}})}\frac{1}{\phi_{\mathrm{ac}}} \tag{1.63}$$

1.3.3.3 Limits

The back-action of the scattered photons is twofold: a scattering event causes an atom to collapse, as the scattering process is in principle distinguishable. The atom will no longer be in the CSS, causing a reduction in the total spin S (or loss of contrast $\mathcal{C}$ of the interferometer fringes); on the other hand, a Raman process that flips the spin may happen following a scattering event, bringing additional uncertainty in S_z after the measurement.

Contrast decay Theoretically, the contrast is reduced by

$$\mathcal{C} = \mathcal{C}_0 e^{-n_s} \tag{1.64}$$

with initial contrast $\mathcal{C}_0$. It appears to be insignificant compared to the limit imposed by the Raman flip [97]. Nevertheless, if we assume that the back-action is limited by the contrast loss, the squeezing parameter becomes (writing Eq. 1.63 in terms of n_s)

$$\xi^2 \simeq \frac{(\Delta S_z)^2|_M}{\mathrm{Var}(S_z)\mathcal{C}^2} = \frac{\left(1 + NC\left(\Gamma/\omega_{\mathrm{at}}\right)^2\right)^2}{2\epsilon_c NC} \frac{e^{2n_s}}{n_s} \tag{1.65}$$

where we set $\mathcal{C}_0 = 1$. A minimum is reached with $n_s = 1/2$ when the contrast is reduced to $\sim 61\%$:

$$\xi^2_{\mathrm{opt},\mathcal{C}} \simeq \frac{\left(1 + NC\left(\Gamma/\omega_{\mathrm{at}}\right)^2\right)^2}{2\epsilon_c NC} \frac{e}{n_s} \tag{1.66}$$

Raman flip In a simple model, we assume that an atom that scattered a photon may return to the opposite spin state with a probability p. This gives rise to a random walk of S_z, with a variance

$$(\Delta S_{z,\mathrm{flip}})^2 = Npn_s = Np\frac{\Gamma}{\omega_{\mathrm{at}}}\phi_{\mathrm{ac}} = \frac{2pNC}{q_d(\kappa_t/\kappa)}\left(\frac{\Gamma}{\omega_{\mathrm{at}}}\right)^2 n_d \tag{1.67}$$

For ^{87}Rb, p can take 1/6 [97]. Precisely, for the clock states of TACC ($|1,-1\rangle$ and $|2,1\rangle$), the probability of a real spin flip is 1/40, while $|2,1\rangle$ can be lost to $|2,2\rangle$ with a probability of 1/6. The latter is also trappable but will not contribute to the interferometer.

Combining Eq. 1.67 with Eq. 1.60, we have the total spin uncertainty

$$(\Delta S_z)^2|_M \simeq (\Delta S_{z,\mathrm{PSN}})^2 + (\Delta S_{z,\mathrm{flip}})^2 \tag{1.68}$$

$$\simeq \frac{\left(1 + NC\left(\Gamma/\omega_{\mathrm{at}}\right)^2\right)^2}{8\epsilon_c C(\Gamma/\omega_{\mathrm{at}})}\frac{1}{\phi_{\mathrm{ac}}} + Np\frac{\Gamma}{\omega_{\mathrm{at}}}\phi_{\mathrm{ac}} \tag{1.69}$$

which has a minimum:

$$(\Delta S_{z,\mathrm{opt}})^2|_M = \sqrt{\frac{Np}{2\epsilon_c C}}\left(1 + NC\left(\Gamma/\omega_{\mathrm{at}}\right)^2\right) \tag{1.70}$$

at the optimal measurement strength

$$\phi_{\mathrm{ac,opt}} = \frac{1 + NC\left(\Gamma/\omega_{\mathrm{at}}\right)^2}{\sqrt{8\epsilon_c NCp}(\Gamma/\omega_{\mathrm{at}})} \tag{1.71}$$

We obtain the optimal squeezing parameter for the conditional spin (assuming no coherence loss)

$$\xi^2 \simeq \frac{(\Delta S_{z,\mathrm{opt}})^2|_M}{N/4} \simeq \sqrt{\frac{8p}{\epsilon_c NC}}\left(1 + NC\,(\Gamma/\omega_{\mathrm{at}})^2\right) \tag{1.72}$$

We can identify two regimes: one with low atom number such that $NC \ll (\omega_{\mathrm{at}}/\Gamma)^2$. The squeezing ξ^{-2} grows as $\sim \sqrt{NC}$; while the squeezing will saturate $\sim \sqrt{8p\epsilon_c}(\omega_{\mathrm{at}}/\Gamma)$ as the atom number reaches an optimum $N_{\mathrm{opt}} = (\omega_{\mathrm{at}}/\Gamma)^2 C$. This is the fundamental limit of the dispersive scheme where the maximum detuning is set by the atomic structure.

Anti-squeezing It can be shown that the anti-squeezing in ΔS_y is enhanced above the minimum uncertainty area due to free-space scattering and optical losses [105]:

$$\Delta S_y \Delta S_z = \frac{N}{4}\frac{1}{\sqrt{\epsilon_c \kappa/\kappa'}} \tag{1.73}$$

In practice, the measurable anti-squeezing is usually higher than this prediction due to technical noise. The consequence of the excess anti-squeezing can be twofold: first, the anti-squeezing leads to an reduction in total spin length (coherence) due to the finite Bloch sphere curvature. However, this effect is negligible for a reasonably large atom number. Second, also due to the Bloch sphere curvature, the uncertainty in S_y can leak into S_z if the final state is not precisely at $S_z = 0$. After all, a clock is meant to measure such a deviation. In fact, the record demonstration of 20 dB squeezing has an increase in the uncertainty area of 19 dB, which can completely lose its metrological advantage in a realistic context of clocks [83].

1.3.3.4 Prospective squeezing in TACC-2

Here I give an estimate of achievable squeezing in the TACC-2 experiment based on typical parameters that are detailed in the following chapters. For a typical thermal cloud at 200 nK, the average cooperativity is about $C = 0.42$. We currently probe the cavity through transmission with the probe laser detuned at $\delta_p = \kappa/2$ and a total detection efficiency of 0.5 is realistic. Fig. 1.5(a) shows the calculated squeezing parameter as a function of the measurement strength for 2×10^4 atoms (a typical number for clock measurements), using Eq. 1.69. The situation of optimum detection is also plotted for comparison. The squeezing reaches a maximum of 18 dB for the realistic case, while the ideal detection can give 23 dB. We also plot this optimum squeezing as a function of atom number (Fig. 1.5(b)), showing that it is not limited by the atomic structure for the current setup.

1.3.4 Squeezing by cavity feedback

Recalling the effective Hamiltonian of the system (Eq. 1.42), we note that the interaction terms $\sim \hat{c}^\dagger \hat{c} \hat{S}_z$ can result in the OAT Hamiltonian if the intra-cavity photon number $\hat{c}^\dagger \hat{c}$ is engineered to be correlated with S_z. In fact, as S_z determines the cavity frequency, probing the cavity with a detuning correlates the transmitted photon number (which determines $\hat{c}^\dagger \hat{c}$) with the cavity frequency, hence with S_z.

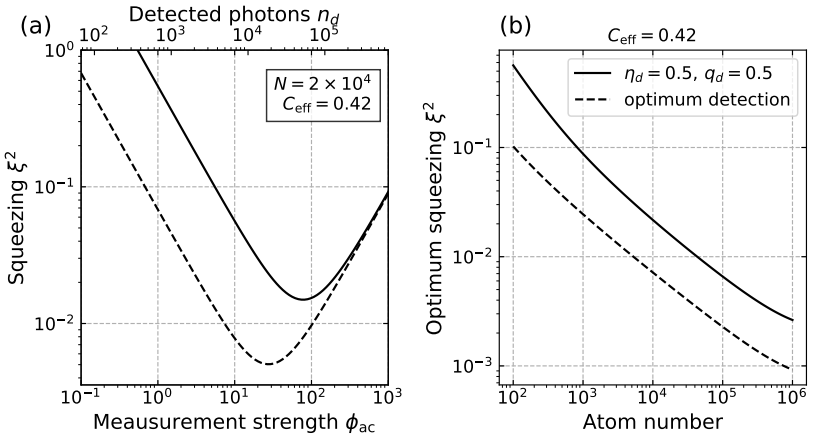

Figure 1.5 Achievable squeezing in TACC-2. In both panels, we assume an average cooperativity $C_{\rm eff} = 0.42$, which is typical for the experiment. We assume, for the solid curves, measurements by cavity transmission with probe detuning $\kappa/2$ ($\eta_d = 1/2$) and a detector efficiency of $q_d = 0.5$ which is close to the current setting, while the dashed curves assume perfect detection with homodyne method ($\eta_d = q_d = 1$, still collecting half of the exiting light), representing almost the theoretical limit of the setup. In (a) we plot the squeezing parameter as a function of $\phi_{\rm ac}$ (and n_d) for 2×10^4 atoms. We identify on the left the PSN limit and on the right the Raman flip limit (we set $p = 1/40$ for our clock states). (b) The optimum squeezing as a function of atom number. We see that ultimate limit $NC \sim (\omega_{\rm at}/\Gamma)^2$ is rather remote for the current experiment.

Formally, the system Hamiltonian is treated in an open quantum system with an input coherent field $|\beta\rangle$ and decay channels into free space. The evolution of the spin distribution can be described through the evolution of the moments of spin operators in the Heisenberg picture, with the cavity field traced out [43]. We will assume a detuning of $\kappa/2$ to have a near maximum correlation between S_z and cavity transmission.

Since S_z is a constant of motion, $\langle S_z\rangle$ and ΔS_z are conserved. But the cavity field induces correlation between S_y and S_z. Most practically, one evaluates the evolution of the raising operator $\hat{S}_+ = \hat{S}_x + i\hat{S}_y$. Following [43], it can be shown that for small $\phi_{\rm ac}$ per photon, the lowest moments read

$$\langle \tilde{S}_+ \rangle_\beta = e^{-\frac{Q}{2S}} e^{i\frac{Q}{S}S_z} S_+(0) \tag{1.74}$$

$$\langle \tilde{S}_+^2 \rangle_\beta = e^{-\frac{2Q}{S}} e^{i\frac{Q}{S}(2S_z-1)} S_+^2(0) \tag{1.75}$$

where $\langle\ \rangle_\beta$ denotes the partial trace over the cavity field, $\tilde{S}_+$ denotes $\hat{S}_+(t)$ after the evolution time t, and we have defined a dimensionless shearing strength

$$Q \equiv S n_t \left(\frac{4g^2}{\Delta_c \kappa}\right)^2 \tag{1.76}$$

with $n_t = |\beta|^2\kappa t/2 = n_d/q_d$ the average transmitted photon number during the evolution. We notice that the precession rate of $\hat{S}_+$ is indeed proportional to S_z. The correlation between S_y and S_z is given by

$$\langle \tilde{S}_y S_z + S_z \tilde{S}_y \rangle = (2S-1) S e^{-\frac{Q}{2S}} \sin\left(\frac{Q}{2S}\right) \cos^{2S-1}\left(\frac{Q}{2S}\right) \tag{1.77}$$

and the increased uncertainty in $\hat{S}_y$ due to the OAT reads:

$$(\Delta\tilde{S}_y)^2 = \frac{S}{4}(2S+1) - \frac{S}{4}(2S-1)e^{-\frac{2Q}{S}}\cos^{2S-1}\left(\frac{Q}{S}\right) \tag{1.78}$$

$$\approx \frac{S}{2}(1+2Q+Q^2) \tag{1.79}$$

where the approximation is $S \gg 1$ and $|QS_z/S| \ll 1$. We identify the initial noise of the CSS in the first term, the noise from the cavity photon shot noise ($Q \propto n_t \propto t$) in the second, and the cavity feedback ($\propto t^2$) in the third. It is the last term that allows the OAT squeezing in the open quantum system [43], at a price of stretching the uncertainty region beyond the minimum uncertainty area for $Q > 1$.

We also have the spin variance after a rotation along $\boldsymbol{S}$ with an angle $-\alpha$ to verify the squeezing

$$\Delta S_\alpha^2 = \frac{1}{2}\left(V_+ - \sqrt{V_-^2 + W^2}\cos(2\alpha - 2\alpha_0)\right) \tag{1.80}$$

where $V_\pm = (\Delta S_y)^2 \pm (\Delta S_z)^2$, $W = \langle \tilde{S}_y S_z + S_z \tilde{S}_y \rangle$ and $\tan 2\alpha_0 = W/V_-$.

The minimum (at angle α_0) and maximum (at $\alpha_0 + \pi/2$) uncertainties, in terms of the squeezing parameter, approximately scale as $\xi_{\alpha_0} \sim 2/Q$ and $\xi'_{\alpha_0+\pi/2} \sim Q^2$. The noise reduction is limited by PSN as for squeezing by QND measurement. But the anti-squeezing grows more quickly – the back-action of measuring S_z through the cavity feedback. This increase of the total uncertainty area ($\sqrt{2Q}$) can in principle be recovered by detecting the light leaking out of the cavity, basically performing a cavity measurement.

Limits The anti-squeezing imposes a severer limit due to the curvature of the Bloch sphere. More precisely, the squeezing scales as [43, 104]

$$\xi_{\alpha_0}^2 \approx \frac{2}{Q} + \frac{Q^4}{24S^2} \tag{1.81}$$

where the second term is attributed to the Bloch sphere curvature. This gives an optimum squeezing $\xi^2_{\text{curv}} \approx 1.5 \cdot S^{-2/5}$ (see also [106]). Nevertheless, it is shown more recently that the excess anti-squeezing can be suppressed by far detuning the probe laser with respect to the cavity resonance, essentially performing a weak measurement [84].

On the other hand, photon scattering into free space is always detrimental. Scattering induced Raman flip leads to similar squeezing limit as for QND-measurement based squeezing (Eq. 1.72). However, these are insignificant compared to the curvature limit, already for a moderate cooperativity $C \sim 1$.

Chapter 2

Experimental methods

The TACC-2 experiment is built on the know-how of the first generation (later referred to as TACC-1), which was designed and built under metrological requirements [70, 107]. Major upgrades have been carried out to reach our new objectives, including a new atom chip assembly, a new vacuum system to embed a 2D-magneto-optical trap (MOT), and the laser setup for probing the cavities.

In the first part, I will describe the experimental setup of TACC-2, recalling also some remarks from the assembling of the experiment. In the second part, I further detail the procedures for cold atom preparation, manipulation, interrogation and detection. The final part is dedicated to the stabilisation of our fibre cavities, for which novel techniques have been employed to realise a unique cavity-QED platform.

2.1 Setup

2.1.1 Atom chip assembly

At the core of our apparatus is a new atom chip that combines conventional elements for trapping and manipulating atoms with on-chip fibre cavities (Fig. 2.1). The atom chip is a bonded two-layer structure. Both the *base chip* and the *science chip* are on aluminium nitride substrate with electroplated gold conductors patterned by photo lithography. The design and fabrication of the chip assembly have been carefully described in the thesis of K. Ott [108], here I only give an overview and a few remarks.

Cavity assembly Two fibre cavities are mounted on chip, targeting different regimes of cavity-QED coupling. They are mounted side by side closely on the same pair of piezoelectric stacks, having a single control of cavity length (detailed properties in Sec. 2.3.1).

The cavity mount that holds the piezo stacks and fibres resembles a "bridge" (Fig. 2.2(a)). It is glued on one "abutment" to the chip (to avoid excess strain on the bridge), hanging the cavities very close to the chip surface ($\sim 400\ \mu$m). Another part of the chip is dedicated to the capture of atoms in a mirror-MOT [109]. Although designed in a small size to minimise the obstruction of optical access for the MOT, the bridge still requires a distance of 9 mm between the MOT site and the cavities, a distance that is bridged by on-chip atom transport via the central circular "Omega" wire (Section 2.2.2).

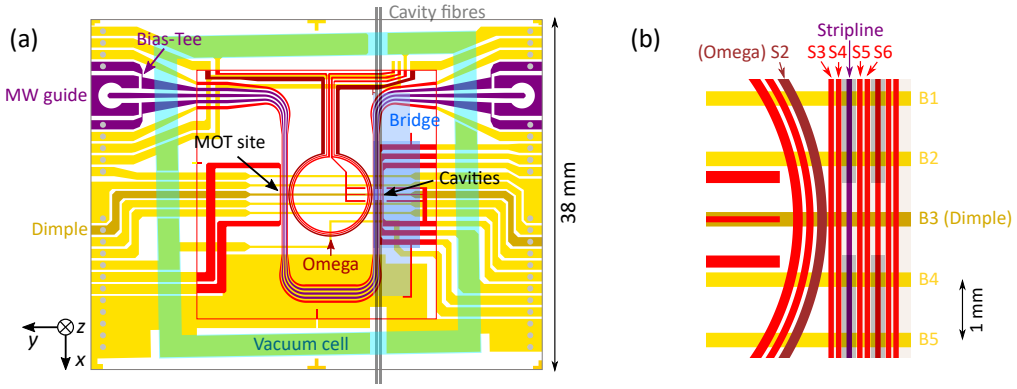

Figure 2.1 (a) atom chip layout. Red patterns are on the science chip, on top of the yellow patterns of the base chip (apart from those elements high-lighted by other colours). (b) Zoom-in of the cavity region.

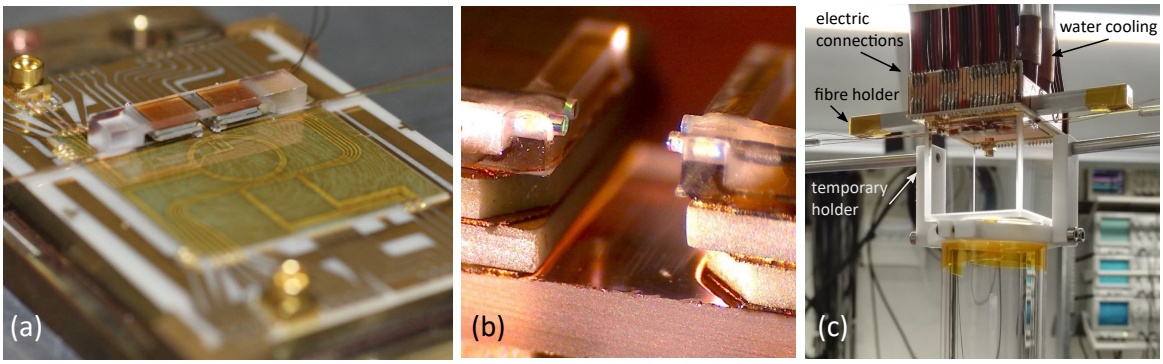

Figure 2.2 Photograph of the chip assembly before gluing the cell (a), close-in photo of the cavities (b) and the assembled vacuum cell (c). We can also see the electric connections and the copper block backing the chip in (c).

Coplanar waveguide (CPW) The key structure on the chip for clock operation is a coplanar waveguide to deliver microwave (MW) photons (in the evanescent field) to the atoms. Its central conductor (later referred to as the *stripline*) also provides a DC current for the principal confinement of the trap. This design has been tested with success in the previous chip. In the new chip we are also able to run currents in the "ground" conductors of the CPW thanks to an on-chip bias-tee (see [108] 5.2.5), indispensable for manipulating the traps for the atom transport. The CPW is also curved to form crossings with the base-chip wires both at the MOT site and on top of one fibre cavity.

We measured an attenuation of 13 dB across the waveguide (including two cables on both sides), much higher than the 9 dB loss in the previous chip.[1] The on-chip bias-tee may be responsible for this excess loss.

Electric connections Due to the spatial constraints, we adopted the same method of electric connections to the chip wires as in TACC-1. Copper conductors on an "adapter"

[1] 9 dB including cables reported in the thesis of Reinhard [70] 5.1.1

printed circuit board are connected to the chip via silver wires (bonded to the chip conductors using silver-filled conductive glue and soldered to copper). On the other side they are soldered to standard ribbon wires (Fig. 2.2(c)).

As in the first generation, the chip is backed by a copper block containing a U-shape conductor (Macro-U), a bended copper wire (Macro-I) parallel to the stripline at the MOT site, and conduit for water cooling. The geometry is depicted in Fig. 2.5. This copper block is installed after the vacuum is set, using a room-temperature-curing thermal glue.[2] Due to the high viscosity of the glue, the thickness of the glue layer is poorly controlled, setting the limit of thermal conductance for the temperature stabilisation of the chip.

2.1.2 Vacuum system

Vacuum cell and fibre feed-through The "principal" vacuum chamber, following our traditional design, is simply formed by the chip replacing one wall of a cubic glass cell.[3] The opposite wall has a home-drilled hole, and is glued to a commercial "glass-metal transition" with a standard CF-40 flange (Fig. 2.2(c)).

The new challenge is to let through our fibres, which involve fragile photonic crystal fibres. We had to cut two relatively large trenches (1 mm^2) on the cell wall, and sealed them with UHV-compatible glue, the same glue for the chip-cell interface (EPO-TEK 353ND).[4]

A separate 2D-MOT chamber The vacuum system (Fig. 2.3) is separated by an in-line valve into two parts – the upper part designed to be compatible with the previous setup, and the lower part for the 2D-MOT [110]. The 2D-MOT chamber is home made from titanium alloy with indium sealed windows. An orifice in this chamber allows a differential pumping between the two chambers. The science chamber is pumped by a 100 l/s getter pumper and a 5 l/s ion pump (Nextorr D 100-5), and a later added 20 l/s ion pump (Varian StarCell). The 2D-MOT chamber is pumped by a 50 l/s getter (SEAS GP-50) and a 2 l/s ion pump (Varian).

The Rb source attached to the 2D-MOT is pure metal sealed in a glass cell, tightly fitted in a bespoke titanium tube, which can be deformed to break the cell and release rubidium when the vacuum is set.[5]

The idea of adding a 2D-MOT with differential pumping is to shorten the MOT loading time by a strong, pre-cooled, and well-aligned atomic flux, while keeping a good vacuum in the science chamber. The clock would also benefit from a longer trap lifetime in a better vacuum. Unfortunately, unsolved vacuum issues eliminate the second benefit.

Vacuum problems Apart from unfortunate malfunctioning and replacement of a few components, we encountered a mysterious phenomenon after the bake-out. The commercial parts have been baked properly before the installation of the chip assembly and achieved a pressure of 1×10^{-10} mbar. The bake-out with the chip assembly, however, is limited to

[2] Loctite® ABLESTIK 2151

[3] (outside) AR coated Pyrex

[4] The first attempt to fill the trenches, when the cell was glued to the chip, was not successful, as small leaks opened up in the feed-through after curing. It was after a second attempt, placing each glue barrier horizontally and forcing new glue to flow into the leak under gravity for hours, did we pass the leak test.

[5] However, this design has a few records of unsuccessful release of Rb, including this experiment. The remedy was unfortunately replacing the source tube and crossing fingers.

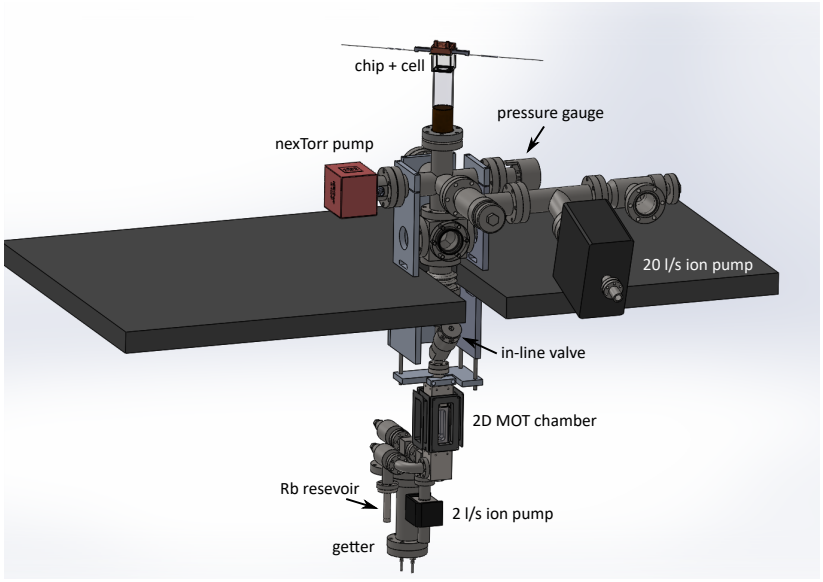

Figure 2.3 Schematics of the vacuum system.

120 ℃, by various materials in use (notably the glue to seal the vacuum). We still achieved a pressure of 3×10^{-10} mbar when the chamber was just cooled down to room temperature after a one-week bake-out. But the pressure started to increase, not stopping even after days. The same phenomenon occurred after another bake-out for two weeks (Fig. 2.4(a)). After pressure rose above 1×10^{-9} mbar in one month, we added another ion pump but only to see 10% improvement, almost proportional to the added pumping power.[6]

We fail to understand this slow pressure rise after bake-out. A possible explanation is some diffusion through the glue layer, notably of Helium. However, this contradicts with the poor improvement from the added StarCell pump, which would have increased the pumping speed for noble gases considerably. There could also be trapped minuscule air bubbles in the various glues (due to imperfection in their preparation or curing) that slowly outgas into the vacuum, although this could hardly explain the long timescale to reach equilibrium. Nevertheless, we do know that the dominant outgassing source is located around the chip, as shown in a strong dependence of the vacuum on the the chip temperature, also seen in the cold atom lifetime below.

Trap lifetime As a consequence of the vacuum problem, the atom lifetime in the trap is limited to $2 \sim 3$ s (Fig. 2.4(b)), even worse than the previous setup (~ 5.7 s). This is surprising since the vacuum levels measured by the same type of gauge (Leybold IONIVAC) are comparable in the two setups, around 1.5×10^{-9} mbar. But the real pressure close to the chip surface can indeed be much higher than what the gauge measures if the main outgassing source is the chip itself.

The short lifetime limits us in various aspects. It is then necessary to have a faster (but maybe compromised) evaporative cooling and faster transport. The achievable Ramsey time

[6] We added about 10 l/s due to the limited conductance, compared to the existing 100 l/s getter pump. However, this specified pumping speed is only for nitrogen under certain pressure. The real increased pumping power is hard to quantify.

is also reduced, as analysed in the next chapter.

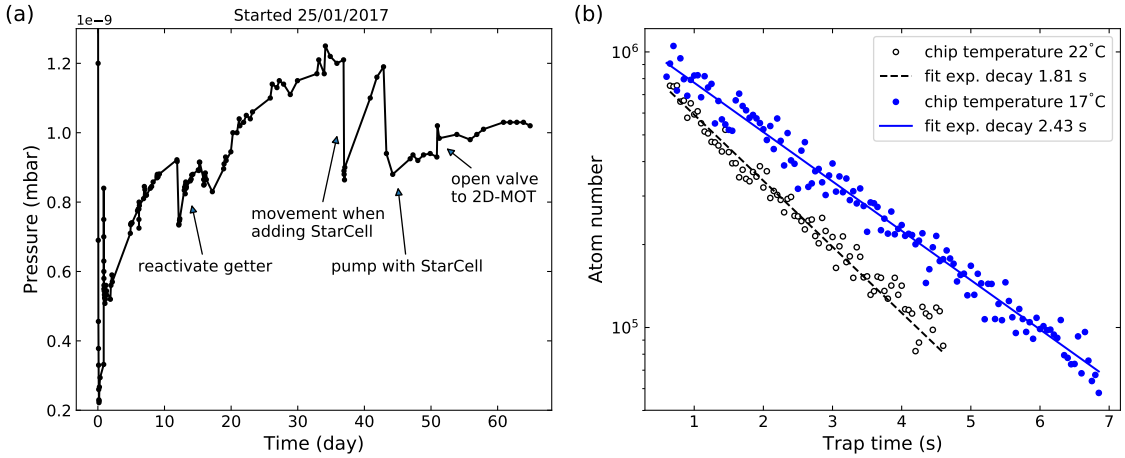

Figure 2.4 (a) The pressure log of the vacuum chamber after bake-out (readout of a gauge). The pressure eventually rose to $\sim 1.5 \times 10^{-9}$ mbar after a few months. (b) Cold atom lifetime in the clock trap, with the atom chip at different temperatures, controlled by water-cooling circuit. Clear correlation with the temperature suggests that the out-gassing of some chip components limits the vacuum level hence the atom lifetime.

2.1.3 Optical system

Here I summarise the optical setup for cooling, pumping and imaging the atoms. The optical setup for the fibre cavities is described later in the dedicated section.

2.1.3.1 Geometry of fields

Let me start with an overview of the geometry of all relevant optical and magnetic fields, shown in Fig. 2.5, to facilitate the perception of the experimental details. The reference frame is consistent with that shown in Fig. 2.1, which we will use throughout the thesis.

The current sources used in TACC-1 are all unipolar, rendering the directions of fields and polarisations of laser beams almost uniquely determined. In TACC-2, the transport of atoms, achieved by a rotation of the magnetic trap (see Sec.2.2.2), requires at least one bias B-field to change sign. In fact, later we found it necessary to switch the directions of multiple fields, and we do have some freedom in choosing the field configuration in the end.

To illustrate the determination of field directions, I give one example of the optical pumping. To prepare a pure state in one of our clock states $|1,-1\rangle$ and $|2,1\rangle$ (we will note the ground state manifold as $|F,m_F\rangle$), only the former is directly accessible through optical pumping. Therefore the pumping beam is fixed to σ^- polarisation and can only be delivered through the detection beam path along $\vec{x}$, due to limited optical access along $\vec{y}$. The layout of the optics (Fig. 2.8) determines that the MOT cooling beams along $\vec{x}$ can only have the orthogonal polarisation. Therefore the MOT B-fields are also determined, et cetera.

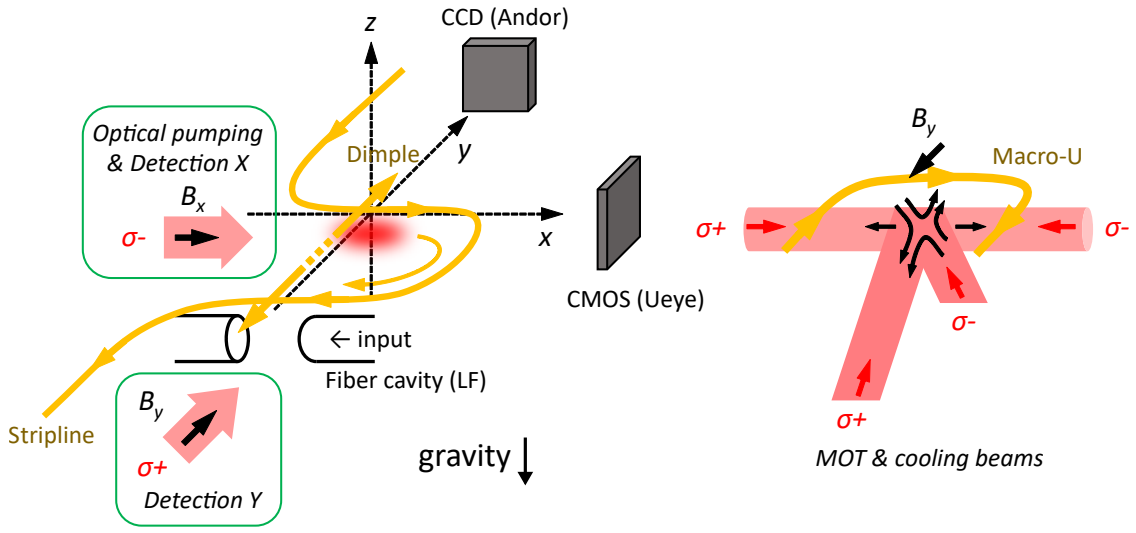

Figure 2.5 Geometry of fields. On the left, the stripline, dimple wire, and the fibre cavity is sketched in our reference frame. Dimple current is inverted for the traps either on the MOT site or on the cavity site. The reason is explained in Sec. 2.2.6.3. On the right, cooling beams and B-fields for the MOT are depicted. For clarity, Macro-I is not depicted, but its current is locally the same as the Macro-U at the MOT site. Note that the polarisations are defined with respect to the coordinates, except that for the 45° beams, the polarisation is defined with respect to the propagation direction. LF: low finesse or the science cavity, detailed in Sec. 2.3.1. Andor and Ueye are two cameras.

2.1.3.2 Lasers

The optical table and the associated electronics are barely modified from the previous setup [107]. Two SYRTE-made extended-cavity diode lasers (ECDLs) and a slave diode provide the four frequencies and all six laser beams needed (as depicted in Fig. 2.5).

Frequency generation The frequency diagram of the lasers and their generations are sketched in Fig. 2.6. All frequencies are referenced through the repumper laser to a standard saturated absorption spectroscopy (SAS). The repumper is locked in between $|F = 1\rangle \rightarrow |F' = 1\rangle$(1-1) and 1-2 transitions to easily access either transition for pumping and repumping, respectively. The master laser (master in the sense for the slave diode) is locked to the repumper by beat-note, hence more widely tunable, to generate either the cooling beams near 2-3 transition, or the pumping beam at 2-2 transition. The layout of the optical table is shown in Fig. 2.7(a).

Optical power The four cooling beams are powered by the slave diode and can deliver ~ 10 mW power each. But as an ECDL has only 30 mW output power, for optical pumping and detection, power is not ample. It is worth noting that the two optical pumping beams are combined with the detection beams with polarising beam splitters (PBSs) before coupling into the detection fibres (Fig. 2.7(a)). Therefore the powers of optical pumping and detection are mutually exclusive in each direction: if all the detection power goes to $\vec{x}$, then all the pumping power will be in $\vec{y}$. It may lead to power shortage in certain imaging configurations.

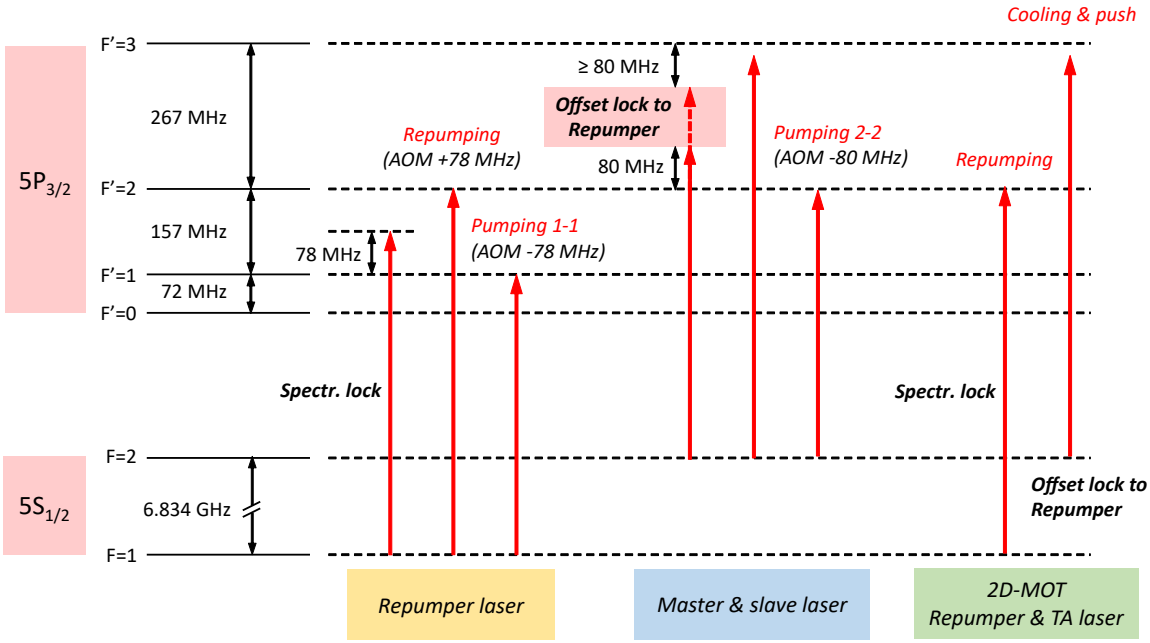

Figure 2.6 Diagram of laser frequency generation, including that of the 2D-MOT. AOM: acousto-optic modulator

Repumper for detection The repumper is previously only present in the 45° beams, so that it does not enter the camera if used during the imaging. Otherwise it would compromise the atom number estimation. In the new setup, imaging the atoms inside the cavity with this repumper wouldn't work since the 45° beams don't enter the cavity. We have to send repumper colinear with detection beam in $\vec{y}$. To couple some repumper into the detection fibres without losing too much power, it is first combined with the master pump beam line with orthogonal polarisation (Fig. 2.7(a)), therefore mutually exclusive in their powers. This temporary solution might also limit the available power in certain cases.

2D-MOT The existing laser bench has neither extra space nor power to feed the additional cooling and repumper beams for the 2D-MOT. A small breadboard is set to have a minimalist but stand-alone module to power the 2D-MOT. The layout is shown in Fig. 2.7(b).

Due to the relaxed requirement on the frequency or amplitude noise for the 2D-MOT lasers, we implemented a simpler SAS to lock the repumper ECDL, by directly modulating the diode current at 70 kHz. The cooling laser is a self-seeded tapered amplifier (TA) laser (TAL-780-1000)[111], frequency locked by beating with the repumper. The small extended cavity at the back side of the TA chip is of a cat-eye design. The spectral linewidth and the output mode are worse than a standard ECDL, while sufficient for our 2D-MOT.

For simplicity, the push beam is split from the cooling beam, incapable of independent frequency tuning. While a detuning might be optimal (see for example [112]), it works well for us in this simple configuration. It turned out to be important though to focus the push beam onto the 2D-MOT, which increases the flux reaching the 3D-MOT by a factor of 10 compared to a collimated push beam. Due to the long distance ($\sim$ 0.7 m) between the 2D-MOT and the atom chip, the MOT loading is very sensitive to the push beam power,

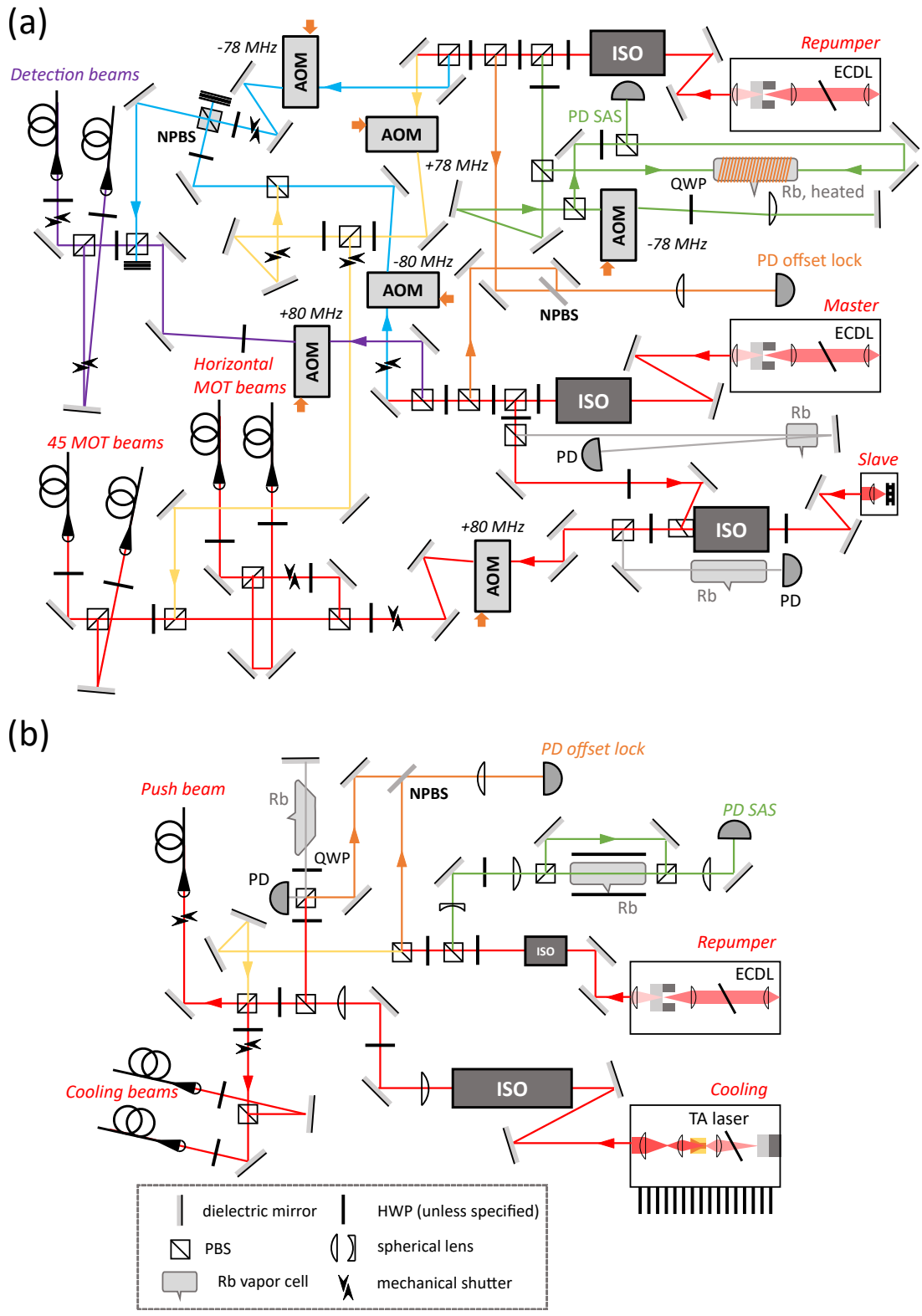

Figure 2.7 Layout of the optical table. (a) the main bench for cooling, pumping and detection. (b) the 2D-MOT module. Laser beams are coloured by functionalities: green: SAS; orange: offset lock; yellow: repumping; blue: optical pumping; purple: imaging; grey: monitoring; red: cooling and others. ISO: optical isolator; HWP: half waveplate; QWP: quarter waveplate; (N)PBS: (non-)polarising beam splitter; PD: photodiode.

exhibiting a clear optimum.

The characteristics of the atomic beam out of the 2D-MOT have not been rigorously examined. But loading the mirror-MOT works reasonably well so that 10^7 atoms can bee loaded in the MOT within 0.5 s, sufficient for our experiments.

2.1.3.3 "Optical hat"

The optical components around the vacuum cell and inside the μ-metal shield are home-made to meet the spatial constraints and non-magnetic requirement, mostly inherited from the previous setup. In the elegant design of our predecessors, components were pre-aligned on an aluminium plate to be put around the vacuum cell as a hat. In our new situation with the fragile fibres in place, the "hat" can only be assembled around the cell with great caution.

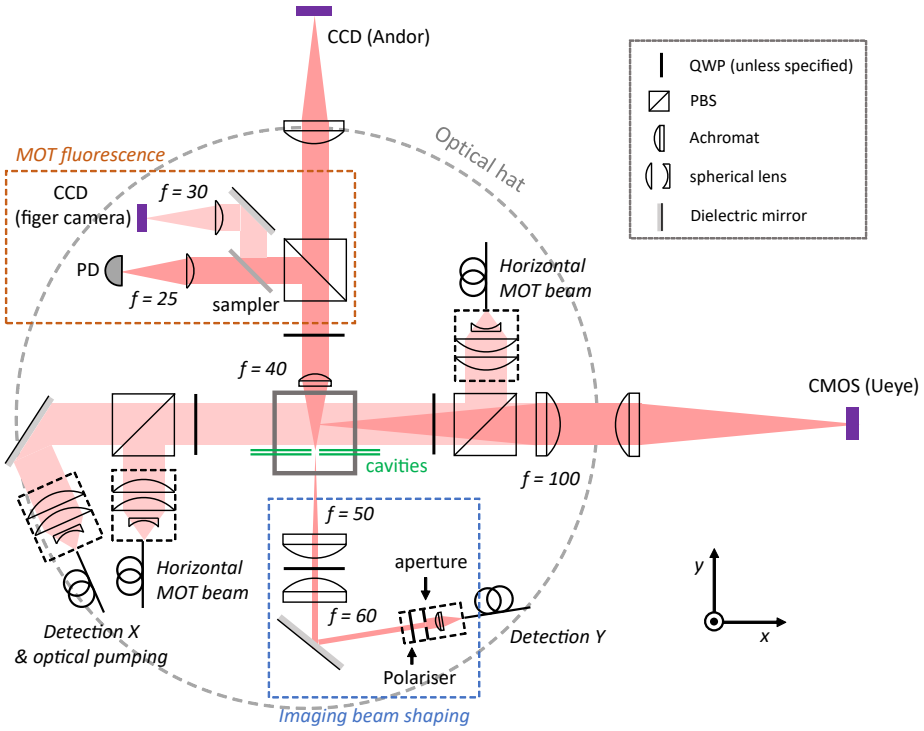

Figure 2.8 Schematics of the optics on the optical hat. The magnification in either direction can be easily modified by changing the last lens (therefore not specified).

Imaging through cavity The layout of the optics has been adapted to the presence of the cavity. The imaging beam along $\vec{y}$ axis, i.e. through the cavity, needs to be shaped to avoid scattering on the fibres or the bridge. Beam shaping is done by imaging an aperture (which properly cuts a collimated beam) to the atoms' plane in the cavity. This plane is again imaged to the CCD camera, completing the absorption imaging. At the same time, however, atoms at the MOT site cannot be properly imaged with this camera. The imaging scheme and other optics on the optical hat are sketched in Fig. 2.8.

MOT fluorescence Having a real-time monitor of the MOT[7] has been an omnipresent and indispensable tool in many cold-atom labs. We managed to fit on the optical hat a "finger" camera and a photodiode, to obtain a MOT image together with a fluorescence signal on the photodiode during the MOT phase. This signal allows us to perform feedback control of the MOT loading time, obtaining a more stable atom number in the molasses phase.

2.1.4 Magnetic fields

The magnetic field stability in the trap centre is obviously crucial to the magnetically-trapped atomic clocks. The optimal B-field differs from the magic field due to gravity and the density shift, rendering the clock frequency even first-order sensitive to B-field fluctuations. The fluctuation comes from the background field and the trapping field. For the former, magnetic shielding and a careful control of materials present inside the shield are necessary. For the latter, one requires highly stable current sources to generate the trap.

Shielding The two-layer μ-metal shields provide at least an attenuation of 3000 of the ambient field, sufficient to bring the background fluctuation below a few μG, which can be neglected at our target stability level. The design and characterisation of the shields have been reported in Reinhard's thesis [70] 4.5.

Magnetic materials Materials inside the shield will directly contribute to the magnetic fluctuation. They also experience strong field variations from the coils that generate the trap. Therefore ferromagnetic materials should be avoided as their hysteric response to the field can compromise the B-field stability.

The TACC team has been meticulous about putting things inside the μ-metal, such as designing all mirror mounts without springs, and measuring each screw with a gaussmeter. But we noticed that in the previous setup several magnetic materials did escape the scrutiny, including specially ordered (non-magnetic specified) but still magnetic fibre connectors (Diamond E-2000), and some nickel-containing thermistors. The residual magnetic field of the E-2000 is from the spring that holds the mechanism, and can reach ~ 100 mG in the vicinity. But since the fibre connectors are relatively far from the atoms, we kept the springs for their mechanical stability.

The thermistors pose a bigger problem as some are mounted on the copper block on the chip, close to the atoms. Seemingly harmless when they are new, they can be magnetised up to 1 G in their vicinity. Unfortunately, we initially installed this type of thermistors in TACC-2, then suffered from a large residual field of ~ 80 mG and a gradient of ~ 50 mG/cm in the molasses phase, with a slow decay. After discovering their evil effect and replacing them with non-magnetic platinum-film thermistors, we reduced the residual field to 1.6 mG (Fig. 2.9).

In the previous experiment a similar slow decay of B-field in the molasses phase was observed, which was attributed to eddy currents in the shield. Compensation fields had to be applied to get sufficiently cold molasses. I think the magnetic thermistors could be another explanation.

[7] usually on an old-fashioned CRT monitor

The biggest surprise was our custom-made piezo stacks for the cavity. After the fibre cavities were assembled, we realised that they contain nickel due to manufacturer's mistake. We measured a field up to 20 mG in the vicinity of another sample, frightening us with the possibility that the clock might never work. The relief came almost two years later when we achieved a reasonable clock stability (see Sec. 3.1). It could be that magnetic hysteresis of the piezo stacks is not so strong as to compromise the stability of the residual field.

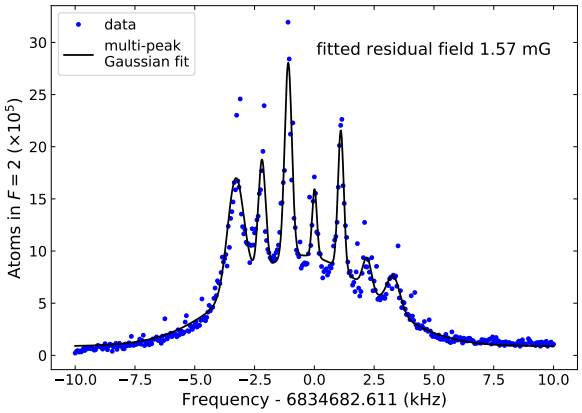

Figure 2.9 Residual magnetic field measured by MW spectroscopy after replacing the nickel-containing thermistors.

Current sources For critical currents to generate the clock trap, we employ the SYRTE-made low-noise current sources that are developed for TACC-1 in the PhD of F. Reinhard. They can deliver up to 3 A, and have a relative rms noise (bandwidth from 20 Hz to 100 kHz) below 4×10^{-6}, with a long-term drift about 10^{-5} [70]. Therefore in the experiment, the current stability is more likely to be limited by the digital control signal from a National Instrument card with 16-bit resolution (1.5×10^{-5}).

The B-field fluctuation in the clock trap may well be contributed from all four currents that form the trap, but the dominant contribution is most likely the dimple current, which runs only about 20 mA, while the same source is required to reach 3 A in other phases. The relative noise can be as high as 2×10^{-3} during the clock trap (due to the digital control signal). Nevertheless, this can be easily improved in the future by another source dedicated to low current for the clock trap.

In addition, we added home-made switches to almost all current sources to be able to invert the polarity. The effect of these switches on the current stability remains to be studied.

2.2 Cold atom preparation and interrogation

In this section I will describe some key steps in an experimental sequence and their optimisation. A typical cycle is pictorially sketched in Fig. 2.10, and key parameters of different magnetic traps are summarised in Tab. 2.1.

2.2.1 Laser cooling and optical pumping

Like other cold-atom experiments, the atom preparation starts with loading the 3D-MOT, with the 2D-MOT illuminated simultaneously.

Then follows the compressed MOT, in which additional confinement is quickly turned on to compress the cloud and bring it closer to the chip. This also determines the position and size of the molasses. Further cooling in the molasses therefore allows more gain in the phase-space density. The cloud can reach about 5 μK in the molasses, while being rather close to the chip to facilitate loading into a magnetic trap.

At the end of the molasses short optical pumping is performed. As I mentioned, the optical pumping beams at 1-1 and 2-2 transitions are in σ^- polarisation. However, pumping into the clock state $|1,-1\rangle$ cannot be 100% efficient, as the state $|2,-2\rangle$ is also a dark state for the pumping beams and will be populated. Nevertheless, $|2,-2\rangle$ is not magnetically trappable and is immediately lost in the first magnetic trap.

In principle, one should ensure a good purity of the polarisation for the optical pumping to work. That means not only well-defined optical polarisations but also a well-defined bias field (along $\vec{x}$, i.e. B_x). Mysteriously, our predecessors have found a better pumping efficiency with an impure polarisation. Let me go one step further and then return to the explanation.

After the optical pumping the atoms are loaded into the first magnetic trap. It can be shown that an optimal loading, in terms of preserving the phase space density, can be found for a harmonic trap with the same characteristic size and temperature as the molasses (see [70] 2.3), and of course, with the trap centre well aligned with the molasses. Ideally it should also be formed instantly to avoid adding entropy.

In practice, this trap (a dimple trap) is found with the maximum available currents since the molasses is still far from the chip (about 1 mm). Turning on the B-fields and chip currents requires some time (milliseconds) to avoid oscillations, due to the high currents and limited bandwidth of the sources.

The obvious procedure is to first turn on B_x for optical pumping, after which we turn on B_y and the two chip currents for the magnetic trap. However, strange as it may sound, it turns out that turning on both B-fields simultaneously during the optical pumping phase gives not only better loading due to shorter delay, but also higher efficiency of the optical pumping. The impure polarisation due to the existence of B-fields in both $\vec{x}$ and $\vec{y}$ somehow reduces the number of atoms ending up in $|2,-2\rangle$. As a result, we do find a slight leakage in the trappable states $|2,1\rangle$ and $|2,2\rangle$. But the overall loading efficiency is much better.

After the first magnetic trap, if we were in TACC-1, we should then quickly tighten the magnetic trap to perform evaporative cooling. And later ramp the trap into a shallow form for clock interrogation. These are all carried out at roughly the same position, with the principal confinement always provided by the stripline.

For TACC-2, the *experiment* is carried out in the cavity, which is 1 cm away from the first magnetic trap. I will focus on this transport procedure in the following.

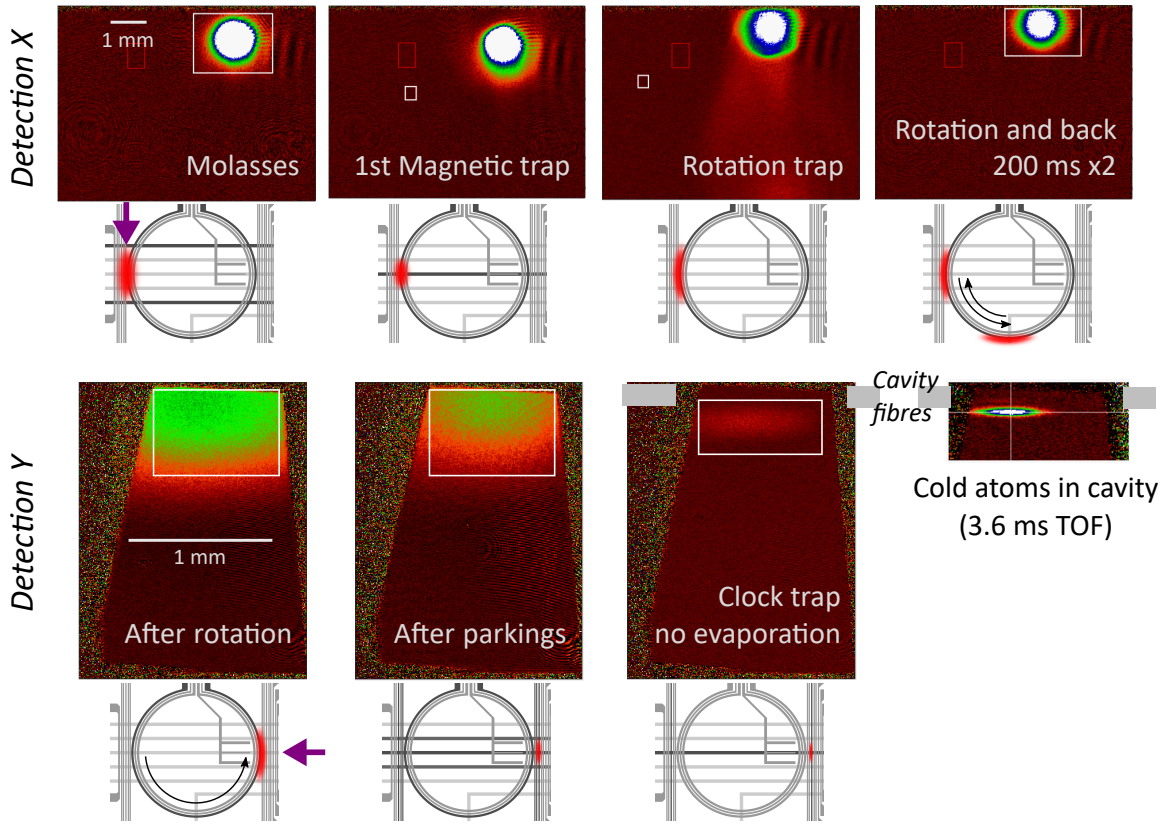

Figure 2.10 Images taken in various steps during the transport, with corresponding conceptual bottom views below. Images in the first row are taken along $\vec{x}$ and in the second row along $\vec{y}$ through the cavity. The shaded boxes in the last two images indicate the fibre mirrors (not visible in the images). The purple arrows indicate the imaging axes.

2.2.2 On-chip transport of atoms

2.2.2.1 The first magnetic trap

The first magnetic trap deserves a few more words, as it determines the available atom number and phase-space density for later manipulation in magnetic traps. As I mentioned, the first magnetic trap should be a harmonic trap, which is most easily realised by a dimple trap. We use the maximum current in the crossed wires (stripline and dimple) together with high current in the macro-I, trying to form the biggest possible trap. A dimple trap is by design anisotropic (elongated in $\vec{x}$). We can in principle increase the longitudinal ($\vec{x}$) confinement by employing more wires parallel to the dimple, but the potential improvement is marginal as they are also far apart.

In practice, the accessible dimple trap cannot perfectly match the molasses and its formation cannot be instantaneous. Therefore the molasses is inevitably perturbed, and some oscillatory dynamics can be observed if we hold it longer in this trap. It turned out better to immediately modify the trap for the next step.

As will be detailed in the next section, the trap for the main transport is formed by the central circular wire (dubbed Omega). To simplify the sequence and to gain in overall

Table 2.1 Sequence of magnetic traps. Δt: duration of the step, I_{strip} and I_{dim}: stripline and dimple current, B_y and B_x: bias field in $\vec{y}$ and $\vec{x}$, d_0: distance from trap centre to chip surface, $\omega_{x,y,z}$: trap frequencies, B_0: magnetic field at trap bottom

Steps	Δt (ms)	I_{strip} (A)	I_{dim} (A)	B_y (G)	B_x (G)	d_0 (μm)	ω_x /2π (Hz)	ω_y /2π (Hz)	ω_z /2π (Hz)	B_0 (G)
1st MTrap[†]	3	2.9	2.5	16.5	10.5	630	22	67	64	5.8
ramp	20	↘	↘	∼	↘					
rotation	200	2	0	15	0	240	3.4[*]	61[*]	60[*]	0
paral. park.	20[‡]	2	1.5	15	10	240	45	285	276	4.8
ramp	200	↘	↗	↗	↗					
evaporation	1250	1.5	3	29	15	93	96	2.5k	2.5k	4.6
ramp	50	↗	∼	↘	↘					
inter. trap	1	2.4	3	15.7	10	280	50	560	550	1.0
ramp	600	↘	↘	↘	↘					
clock trap	-	2.03	25m	9.25	3.36	420	4	110	120	3.2

[†] The first magnetic trap also requires a marco-I current of 14 A
[*] For this quadrupole trap, field gradients are instead shown in G/mm
[‡] Time for each parallel park

efficiency, we directly form the first magnetic trap with the Omega wire, which is parallel to and locally resembles the stripline at the MOT site. With a strong confinement along $\vec{x}$, it can form a dimple trap with a negligible effect from the curvature. It suffices to modify a bit the compressed-MOT to form the molasses aligned with the Omega.

Current ramp-up From an experimental point of view, even for the ideally instantaneous first magnetic trap, it is practically better to ramp the fields in the presence of electric inductance. Any change in current too abruptly should be avoided, to minimise residual oscillations and risks in high transient fields. A linear ramp is generally not optimal as the second derivative at the beginning and the end of the ramp is still "infinite".

We most often utilise a "turnOn" function, the lowest order polynomial function with vanishing first and second order derivatives at the beginning and at the end. That is, from $t = 0$ to the end of the ramp $t = T$, the field A varies as

$$A(\tau) = A_i + (A_f - A_i) \cdot (6\tau^5 - 15\tau^4 + 10\tau^3) \tag{2.1}$$

with $\tau = t/T$ between 0 and 1. A_i and A_f are the initial and final values, respectively.

I shall note that without special notice, all transitions between different traps are realised by ramping consisting fields in this "turnOn" manner. It is possible that the intermediate properties of the trap are not optimal, but it turned out to work well in most situations.

Atom number stability The first magnetic trap is also crucial for obtaining a stable number of atoms. The loading efficiency is strongly affected by the spatial overlap between the trap and the molasses, while the latter is determined by the power balance of the cooling beams. In the long term, power drift of the cooling beams slowly changes the molasses position and hence the loading efficiency, which directly results in a reduction in the final atom number. Therefore in practice it is often the beam balance that is tuned to optimise the final atom number, especially in a daily or weekly practice.

In short term (shot-to-shot) however, the origin of the position fluctuation of molasses is more complicated and its effect on the final atom number more subtle. We haven't yet thoroughly studied this issue. Another major source of atom number fluctuation comes from the MOT loading. We observe a strong atom number fluctuation in the molasses (up to 10% peak-to-peak), most often related to the temperature in the lab. Luckily, the atom number in the molasses is perfectly correlated with the fluorescence signal at the end of the MOT, which allows us to control the MOT loading time to obtain a stable fluorescence. However, for the atom number in the final magnetic trap, correlation with the fluorescence persists but is not perfect, most likely due to the intervention of the position fluctuation of the molasses.

In the end, the shot-to-shot fluctuation in the final atom number remains considerable (typically $4 \sim 5\%$ in standard deviation) and cannot be improved by the fluorescence feedback. This is worse than TACC-1, but we suspect that it is due to the 2D-MOT loading scheme and the increased complexity in the first magnetic trap.

2.2.2.2 Rotation in a quadrupole trap

The main transport, bridging 1 cm distance between the MOT site and the cavity, is done by trapping and moving the cloud along the circumference of the Omega. Current in the Omega plus a bias field forms a quadruple trap, which can be understood by regarding the Omega as a deformed U. The trap centre is close to the point on the circle to which the bias field direction is perpendicular. One can therefore move the trap along the circle by turning the bias field. A rotation angle θ is achieved by varying B_x and B_y as

$$B_x = -B_0 \sin\theta, \quad B_y = B_0 \cos\theta \tag{2.2}$$

where B_0 is some field amplitude. Concerning the dynamics, θ is varied in time using the turnOn function (Eq. 2.1). It turns out to be important to have no angular velocity and acceleration at the beginning and the end of the rotation.

Between quadrupole and dimple To switch from the first magnetic trap (a dimple trap), to the quadrupole trap for rotation, one needs to ramp off the dimple current and B_x, because the rotation trap has no bias field in $\vec{x}$ in its initial position (otherwise it will simply rotate). However, during the transition, before B_x is completely off, the trap centre is displaced along $\vec{x}$ (imagine a quadruple trap experiencing a rotation of the total bias field). We can observe centre-of-mass oscillations of the cloud along $\vec{x}$ after the transition.

This is also true when the rotation trap is transformed back into dimple, on the cavity side. It might be possible to find an optimal ramp of the B-field that minimises this "rotation" effect. But in the end, we adopted another approach:

- From the first magnetic trap to the rotation trap, we ramp off B_x and dimple as quickly as possible. It turned out that the residual oscillation is smaller for a faster ramp.
- After the rotation to the cavity side, instead of transforming the quadrupole trap to a dimple trap on the Omega, we first move the trap to the adjacent wire (S3), but we keep it quadrupole using two perpendicular wires (B2 and B4). There is no B_x during the process. Now as S3 is not bended, it is straight forward to ramp into a dimple trap.

Cloud temperature According to calculations [108], the tangential confinement of the rotation trap is determined by the curvature of the wire and by the bias field. With our accessible bias field, the tangential trap depth is about 500 μK. One does have to consider the initial temperature of the cloud to prevent excessive loss during the transport.

One strategy is to do some evaporative cooling before the transport. But we abandoned this approach after realising that performing two evaporations will cost too many atoms and too much time. Therefore we had a guideline that is to perform the transport as quickly as possible. The initial temperature once loaded in the rotation trap, about 50 μK, also turned out not to suffer from high losses.

2.2.2.3 "Parallel parking"

As we can see from the chip layout (Fig. 2.1), between the Omega and the stripline there are S3 and S4 in parallel, symmetric on both sides. The cloud is elongated along these wires, therefore moving the cloud sideways was dubbed parallel parking. It is the principal confinement of the trap that is switched between adjacent wires. It turned out to be sufficient to ramp down and up the current in the adjacent wires simultaneously in a "turnOn" manner. As there is a small variation in $\vec{z}$ of the trap centre during the transition, residual oscillation along $\vec{z}$ occurs and depends on the ramping speed. A small delay between the ramp-down and ramp-up can be tuned to minimise this oscillation. The longitudinal (dimple) confinement is kept constant and sufficiently large. The parallel parking is almost lossless between two dimple traps.

However, as I pointed out earlier, these parkings after the rotation from the Omega to the stripline need to be tailored for the transition between quadrupole and dimple. Specifically, we have the first parking from Omega (S2) to S3 in quadrupole traps, simply ramping up current in S3 and B2+B4 (a U-type trap). The second parking to S4 transforms the quadrupole trap to a dimple trap by ramping up the dimple current. Finally the last parking to the stripline is done in dimple traps.

Once the cloud is trapped on the stripline we start the evaporation process, in which the trap is strongly compressed. However, the efficiency of this compression is hard to directly assess in terms of atom loss and adiabaticity, since the atoms in this trap are too hot to be imaged with the time-of-flight (TOF) technique. Therefore, we optimise the compression by measuring the atom number when the cloud is again decompressed into the clock trap. We also observe that the efficiency of the evaporative cooling (assessing the atom number and temperature in the clock trap) depends on the trap of the parallel parking, especially on the longitudinal confinement (dimple current and B_x).

2.2.2.4 Summary and future improvements

In summary, I give an example of the overall transport efficiency in Table 2.2. There is still room for improvement, notably in the initial loading into the rotation trap, and in the parallel parking process. For the latter, we are in a compromise because a tighter longitudinal confinement seems to be better for the pre-evaporation compression, while a weaker confinement works better for the transition between quadrupole and dimple traps, but a better clever trap ramp is certainly possible.

Table 2.2 A summary of transport efficiencies

Steps or conditions	duration (ms)	final atom number (a good example)
MOT + molasses	~ 1500	2.9×10^7
1st MTrap	3	2.6×10^7 *
ramp to rotation trap	15	1.6×10^7
(hold in the rotation trap)	200	1.1×10^7
rotation	200	9.1×10^6 **
park to S3 (quadrupole)	20	7.2×10^6
park to S4 (dimple)	20	6.7×10^6
park to stripline	20	6.6×10^6

* This is the number instantly after trap formation, still containing some atoms that are not trappable and later expelled.
** This is an underestimation. It is actually measured after a 90° rotation and back taking in total 400 ms.

2.2.3 Evaporative cooling

With atoms in the highly-compressed evaporation trap, we perform forced evaporative cooling to reach ultracold temperatures, even to BEC. The key is to achieve high collision rate for thermalisation and a well adapted RF radiation to remove the hot atoms in time. With atoms in $|1,-1\rangle$, the RF radiation is blue-detuned from the Zeeman splitting between $|1,-1\rangle$ and the untrappable $|1,0\rangle$, capable of expelling atoms with higher energies, effectively reducing the trap depth.

By sweeping the RF frequency closer to the Zeeman splitting, while allowing sufficient time for the atoms left in the trap to reach thermal equilibrium, the atoms are cooled down. It can be shown that the optimal frequency sweep is very close to an exponential function in time [113]. In addition, the power of the RF radiation is ramped down at the end of the frequency ramp. Previous optimisations arrived at a two-step linear ramp-down of the RF power. The RF radiation is provided by a SRS DS345, using its internal exponential frequency sweep (external trigger) and analogue amplitude modulation to control the power.

In TACC-2, due the reduced lifetime, we tried to further increase the collision rate by using an even tighter evaporation trap (typical trap frequencies $\{\omega_x, \omega_y, \omega_z\} \sim 2\pi \cdot \{0.08, 1.8, 1.8\}\,\mathrm{kHz}$), reducing the evaporation time from previously 3 s to 1.25 s. The final atom number and temperature are not too much compromised.

Dependence of the final temperature on initial atom number We noticed clear dependence of the final atom temperature on the initial atom number, though it is not reported by our predecessors. In other words, the evaporation is sensitive to the initial condition (most likely density). Fig. 2.11(a) shows a similar dependence for different final frequencies of the RF sweep (i.e. final temperature). It is however not due to the fact that we are doing the evaporation faster, as this dependence persists for longer evaporation (Fig. 2.11(b)).

In more recent data (not shown), this atom number dependence seems to be weaker. It deserves further investigation as it renders the clock stability more sensitive to technical noise.

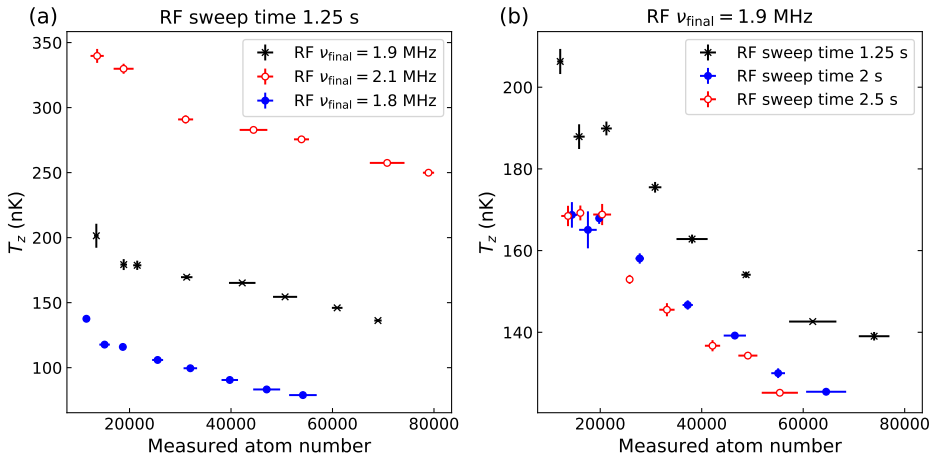

Figure 2.11 Atom number dependence of the atom temperature after evaporation. The final frequency of the RF sweep is varied in (a), while the sweep time is varied in (b). the near-linear dependence on the atom number has prevailed.

2.2.4 The clock trap

As analysed in Sec. 3.1.4.1, the optimal clock trap is a compromise between strong confinement along $\vec{z}$ to compensate the gravitational sag, and low atomic density to minimise the density shift. We arrived at an extremely elongated trap, eventually constrained by the cavity geometry.

The position of the cavity imposes further constraints. The relatively long distance ($\sim 420\,\mu$m) from the chip surface limits the achievable transverse confinement. The clock traps used in this thesis have trap frequencies $\{\omega_x, \omega_y, \omega_z\} \sim 2\pi \cdot \{4, 120, 110\}$ Hz. ω_z is slightly lower than ω_y due to the gravitational sag.

2.2.4.1 Displacing the trap

In principle, as a normal dimple trap, the clock trap only employs currents in the stripline and the dimple, with bias fields B_y and B_x. However, properly aligning the cloud with the cavity mode requires additional complexity of the clock trap. For instance, B_z is needed to displace the trap along $\vec{y}$.[8] The optimisation of the trap position using the atom-light interaction will be shown in Sec. 3.2.3.

In addition, the trap position in $\vec{x}$ exhibits an asymmetry due to imperfections in the bias fields (mostly in B_y). The displacement with respect to the dimple wire (hence the cavity centre) can reach hundreds of μm, when the dimple confinement becomes extremely weak. It prevents us from exploiting the most shallow trap along $\vec{x}$ accommodable in the cavity. In order to centre the trap along $\vec{x}$, we have to employ another base-chip wire (B2) crossing the stripline, with current running in the same direction as in the dimple. The magnetic simulation is not accurate enough, and the current is experimentally tuned.

[8] Unluckily, the B_z needed is in the opposite direction as for the MOT, requiring to invert B_z as well.

2.2.4.2 Residual oscillations

At the end of the evaporation, the trap is decompressed into the shallow clock trap. This decompression should be adiabatic to avoid excitation. For a linear decompression of a harmonic trap of frequency $\omega/2\pi$, the adiabaticity condition can be formulated as $\dot{\omega} \ll \omega^2$ [114].

In our case, the decompression is also associated with a displacement of the trap position (about 330 μm in $\vec{z}$ moving away from the chip, and about 200 μm in $\vec{x}$ due to asymmetry mentioned above). This makes the adiabaticity criterion difficult to fulfil, especially for the trap displacement when very low trap frequencies are approached.

In practice, we assess the residual centre-of-mass oscillations in the clock trap to optimise the decompression. These oscillations should be minimised as they contribute to the inhomogeneity-related decoherence.

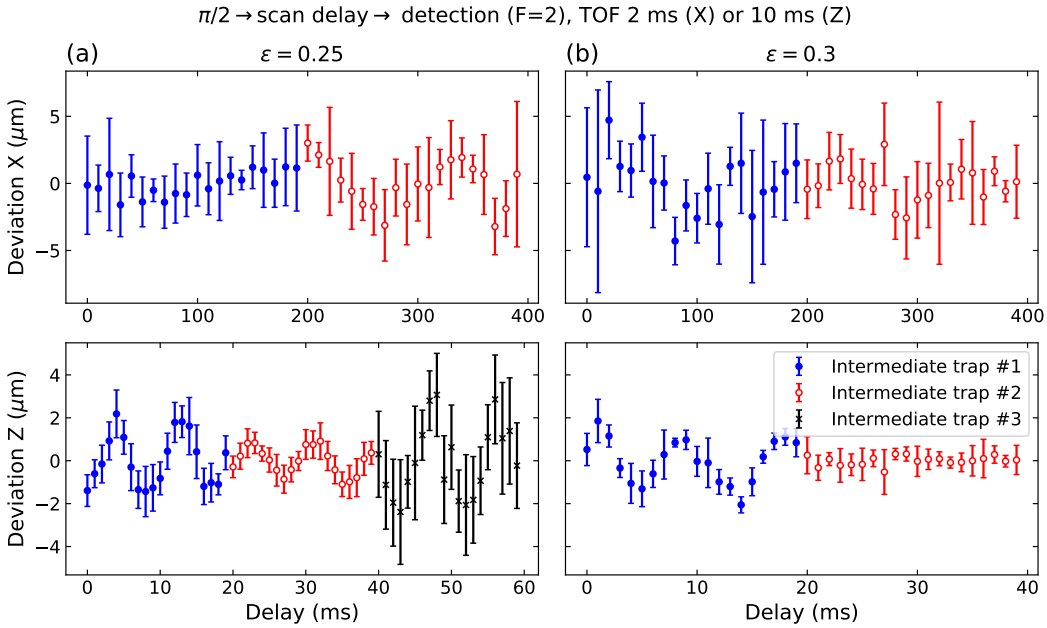

Figure 2.12 Residual oscillations in the clock trap. A $\pi/2$ pulse is applied once the decompression is finished to mimic a typical experimental cycle, but only $|F = 2\rangle$ is detected after a variable trap time (to avoid using ARP (Sec. 2.2.7.1)). Oscillations in $\vec{x}$ (first row) and $\vec{z}$ (second row) are measured in different timescales and with different TOFs (2 ms and 10 ms, respectively). We compare mainly two intermediate traps: the one used in TACC-1 (#1, trap frequencies {50 Hz, 550 Hz, 550 Hz}) and a tighter one (#2, {55 Hz, 1040 Hz, 1040 Hz}) that has a large displacement in the second step. The tightest trap (#3) aligned with the clock trap ({38 Hz, 200 Hz, 200 Hz}) seems not tight enough, causing larger oscillations. We also vary the ramp of the second step by changing ϵ, clearly for $\epsilon = 0.25$ (a) the ramp is too fast at the beginning, causing a larger oscillation compared to $\epsilon = 0.3$ (b). Oscillations in $\vec{x}$ is not so strong. Data are shifted in the horizontal axis intentionally for visual clarity.

Two-step decompression In TACC-1 this issue is addressed by ramping the trap in two steps. The first step, rather short, ideally displaces the trap centre to its final position while

keeping the trap tight. This intermediate trap has frequencies $\{50, 550, 550\}$ Hz. The second step performs pure trap decompression, and the decompression has to be slower and slower as the trap being opened. The only problem at the time was the residual displacement of trap centre along $\vec{x}$ in the second step, which results in oscillations in $\vec{x}$ (see Dugrain's thesis [115] 2.4).

The adiabaticity is ensured by ramping the trap in a modified form of the integrated Blackman profile [116]:

$$A(\tau) = A_i + (A_f - A_i) \cdot \left(\tau^\epsilon - \frac{25}{42\pi} \sin(2\pi\tau^\epsilon) + \frac{1}{21\pi} \sin(4\pi\tau^\epsilon) \right) \quad (0 \leq \tau \leq 1) \tag{2.3}$$

where again $\tau = t/T$ is the normalised time of a ramp duration T. The exponent $\epsilon = 0.3$ basically rescales the time in a power law, implementing a ramp that slows down.

In TACC-2, we started with the old intermediate trap of TACC-1, which is not expected to be optimum since it is not aligned any more with the final trap, which is further away from the chip surface (~ 420 μm instead of ~ 300 μm). A large displacement along $\vec{z}$ takes place in the second step of slow decompression. We indeed observe visible centre-of-mass oscillations along $\vec{z}$ (Fig. 2.12, trap #1).

However, following the idea of the two-step ramp, even the tightest trap available at the cavity position is not tight enough to keep the process adiabatic (trap #3 in Fig. 2.12), causing even bigger oscillations. Slowing down the first step doesn't help as it somehow only turns the centre-of-mass oscillations into shot-to-shot fluctuations of cloud position, without reducing the magnitude.

With some trial and error, we found it better to have a tighter intermediate trap even it would be further away from the final trap, showing that it was the first step that was the major cause of the oscillation in $\vec{z}$ (trap #2 in Fig. 2.12). The second step should then be improved as there is now a large displacement in $\vec{z}$. Increasing the exponent to $\epsilon = 0.3$ further reduces the oscillation, meaning that the initial ramp of the second step was too fast. This modification makes the ramp slower at the beginning but faster in the end (compared to $\epsilon = 0.25$). Luckily we haven't observed bigger oscillations in $\vec{x}$.

2.2.5 Interrogation photons

As outlined in Sec. 1.1.2.2, the clock transition between the clock states $|\downarrow\rangle \equiv |1, -1\rangle$ and $|\uparrow\rangle \equiv |2, 1\rangle$ requires two photons in σ^+ polarisation, via an off-resonant intermediate state ($|2, 0\rangle$). Therefore one photon close to the hyperfine splitting (about 6.834 GHz) and the other close to the Zeeman splitting in RF, generated by a home-made frequency chain and a direct digital synthesizer (DDS), respectively. The detuning to the intermediate state is about 500 kHz, which sets an upper bound for the Rabi frequency between the clock states.

2.2.5.1 Microwave chain

As shown in Sec. 1.1.3.3, the LO phase noise is crucial to reach metrological level of precision. The challenge is predominantly on the MW source, since it is up-converted from a low-frequency reference, and the phase noise simply scales up.

Our MW source is a home-made low noise synthesiser, referenced to the stable 100 MHz reference available at SYRTE [117]. The architecture is presented in Fig. 2.13. The principle

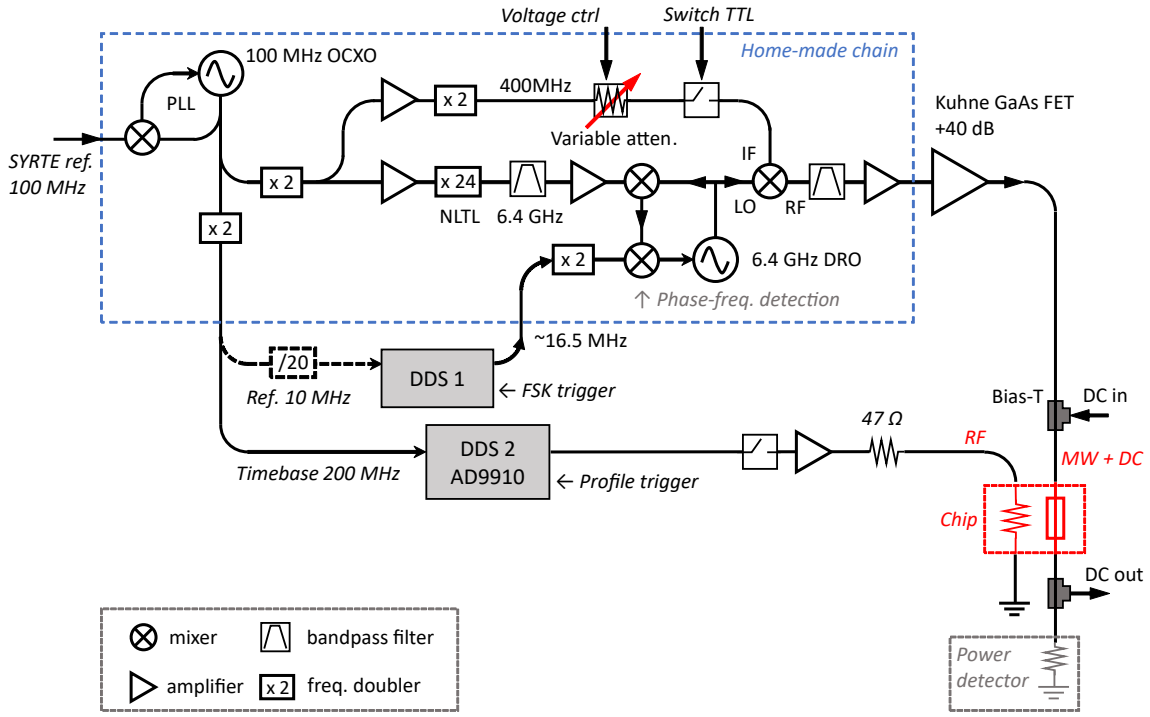

Figure 2.13 Schematics of the generation of MW and RF photons. Only a simplified scheme of the MW chain is shown. The DDS1 is temporally a Rigol DG1032Z, with frequency-shift keying (FSK) functionality. DDS2 is based on AD9910, allowing faster switching between 8 stored output profiles. OCXO: oven-controlled crystal oscillator; NLTL: non-linear transmission line.

is to phase lock a dielectric resonator oscillator (DRO) running at 6.434 GHz to the 100 MHz SYRTE reference, buffered by a phase-locked quartz oscillator. A stable 6.4 GHz signal is generated by the quartz reference through non-linear process to lock the DRO, with a tunable offset about 34 MHz provided by a DDS. The stabilised DRO then drives the output mixer (LO port), and another 400 MHz signal (also derived from the quartz oscillator) powers (IF port) the final output at the clock frequency.

Phase noise and upgrade The phase noise of the chain has been measured previously by beating two quasi-identical copies. The Dick effect in TACC is most sensitive to LO phase noise at sub-Hertz level (see Sec. 3.1.2), where the phase noise of the SYRTE reference signal dominates over the noise added by the chain [50]. I shall note that this reference is stable in long term as it is a Hydrogen maser locked to the atomic fountain clock, but suffers from higher frequency noise during the transmission. The local quartz (Wenzel 501-04516D) is locked to the SYRTE reference up to 100 Hz, since its phase noise outperforms the reference above this frequency.

Improving the LO can obviously alleviate the Dick effect. We have recently replaced the original quartz with a new one from NEL frequency controls Inc., a 100 MHz oscillator internally multiplied from a 10 MHz crystal.[9] It has a lower phase noise than the SYRTE

[9] 10 MHz crystals generally have better close-in phase noise than 100 MHz crystals.

reference from about a few Hz. Therefore we can slightly improve the MW phase noise by locking the chain to the SYRTE reference with a lower bandwidth. However, it turned out that we have to keep a locking bandwidth of 10 Hz, then the slight improvement in phase noise above 10 Hz will have a negligible effect on the Dick effect.

Amplitude dependence of the MW phase We encountered a mysterious phase shift when performing a Ramsey sequence with two $\pi/2$ pulses in different powers (i.e. Rabi frequencies). For example, two $\pi/2$'s supposedly phase continuous, don't bring atoms from $|\downarrow\rangle$ all to $|\uparrow\rangle$, and it turned out to be a pure phase shift between the two pulses (Fig. 2.14(a)). One does not encounter this problem using the same power for the two $\pi/2$ pulses.

We later realised that the phase of the MW chain output depends on the output power. As shown in Fig. 2.13, the power control of the output is achieved by controlling the power of the 400 MHz arriving at the IF port of the final mixer. This is again done with a voltage variable attenuator (Minicircuits TFAS-1SM+). This device, however, introduces strong phase imbalance depending on the control current (Fig. 2.14(b)). We did not perform a full calibration of this dependence as we would not need to vary the power arbitrarily. But one has to keep this in mind and find the phase offset at the particular power setting.

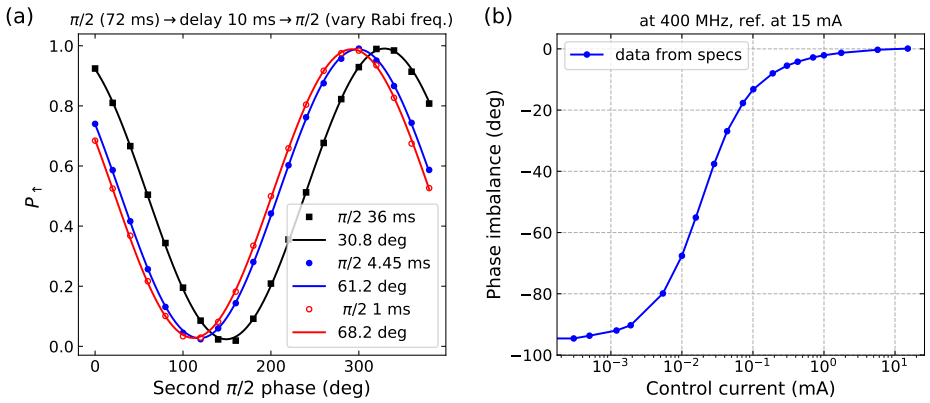

Figure 2.14 Amplitude dependence of the MW phase. (a) Ramsey fringes with the first $\pi/2$ pulse of duration 72 ms, while the second $\pi/2$ pulse at a different Rabi frequency (varying power). There is a clear phase shift for pulses with different powers. (b) The phase shift of the variable attenuator (TFAS-1SM+) as a function of control current, data taken from the datasheet.[10]

2.2.5.2 RF photon

Fine control of the clock LO frequency and phase is more easily achieved via the RF photon, which is generated directly by a DDS. The phase noise of the DDS is negligible as the frequency is down-converted from the stabilised 100 MHz reference.

Fast phase shifting TACC-1 has been exclusively using SRS DS345, with a timebase of 40 MHz derived from the chain. These devices, despite their excellent phase noise, do

[10] datasheet from https://ww2.minicircuits.com/pdfs/TFAS-1SM+.pdf

not have the capabilities of switching or modulation of frequency and phase with external control, except through GPIB communication which is very slow.

In TACC-2 we have been exploring sequences more complicated than the constant interrogation pulses, requiring fast control of frequency, phase and amplitude. We therefore utilise a DDS AD9910, which can store 8 output profiles (independent frequency, phase and amplitude) that can be selected in real time. The switching is phase continuous, and stabilises within 1.5 μs (at 1.7 MHz output). A home-made controller allows to toggle between these profiles with a single trigger. It adds a delay of 100 ns, negligible for our application.

2.2.5.3 Field inhomogeneity

The excitation fields delivered by the chip wires are intrinsically inhomogeneous, as the field strength decays away from the conductor. We can have simple estimations of the major inhomogeneities. Let us first recall the two-photon Rabi frequency (Eq. 1.14)

$$\Omega_{\mathrm{R}}(\boldsymbol{r}) = \frac{\Omega_{\mathrm{mw}}(\boldsymbol{r})\Omega_{\mathrm{rf}}(\boldsymbol{r})}{2\Delta_i(\boldsymbol{r})} \tag{2.4}$$

where now the Rabi frequencies of the MW (Ω_{mw}) and RF (Ω_{rf}) field, and the detuning to $|2,0\rangle$ are all position dependent. $\Delta_i(\boldsymbol{r})$ arises from the linear Zeeman shift of states $|\downarrow\rangle$ and $|\uparrow\rangle$ with respect to the magnetically-insensitive intermediate state. The Zeeman shift is inhomogeneous due to the trapping potential, which has a variation (rms) of $\sigma_{\Delta_B} \approx \frac{k_{\mathrm{B}}T}{2\hbar} \approx 2\pi \cdot 2$ kHz for our typical temperature $T = 200$ nK. The variation of the Rabi frequency for $\Delta_i \approx 2\pi \cdot 500$ kHz is

$$\frac{\sigma_\Omega}{\Omega_{\mathrm{R}}} \approx \frac{\sigma_{\Delta_B}}{\Delta_i} \approx 4 \times 10^{-3} \tag{2.5}$$

This inhomogeneity is symmetric about the trap centre in all directions (temperatures can be different).

Let us then consider the RF field. Delivered through a nearby wire (S6) parallel to the stripline, the inhomogeneity in the longitudinal direction $\vec{x}$ can be neglected since the wavelength is extremely long. Transversely, the inhomogeneity can be estimated simply by using the Biot-Savart law of an infinite-long thin wire. The B-field magnitude is

$$B_{\mathrm{rf}} \approx \frac{\mu_0}{2\pi}\frac{I_{\mathrm{rf}}}{r'_0} \tag{2.6}$$

where I_{rf} is the current of the RF. We define $\boldsymbol{r}'$ as the direction from S6 to the cloud, and $r'_0 = \sqrt{z_0^2 + d_{\mathrm{S6}}^2} \approx 520$ μm with z_0 the distance from the cloud to the chip surface (or to the stripline) and $d_{\mathrm{S6}} = 300$ μm the distance between the stripline and S6. The gradient of the B-field determines the gradient of the Rabi frequency Ω_{rf} (along $\boldsymbol{r}'$):

$$\partial_{r'} B_{\mathrm{rf}} = -\frac{\mu_0}{2\pi}\frac{I_{\mathrm{rf}}}{(r'_0)^2} = -\frac{B_{\mathrm{rf}}}{r'_0} \Rightarrow \partial_{\boldsymbol{r}'}\Omega_{\mathrm{rf}} \propto \frac{\Omega_{\mathrm{rf}}}{r'_0} \tag{2.7}$$

Therefore the inhomogeneity of the Rabi frequency across the cloud width (thermal distribution with $\sigma_z \approx \sigma_y$ transversely) reads:

$$\left.\frac{\sigma_\Omega}{\Omega_{\mathrm{rf}}}\right|_{\boldsymbol{r}'} \approx \frac{\sigma_z}{r'_0} \approx \frac{7}{520} = 1.3 \times 10^{-2} \tag{2.8}$$

where we have assumed a cloud of 200 nK with trap frequency $\omega_z = 2\pi \cdot 110$ Hz.

For the MW, the field is determined by the transverse mode of the CPW. We can nevertheless estimate it by the field of three infinite-long thin wires, with I_{mw} in the stripline and $-I_{\mathrm{mw}}/2$ in the two ground wires ($d = 170$ μm from the stripline). Due to symmetry, at the trap position (z_0 above the stripline), the field vanishes in $\vec{z}$, so does the field gradient in $\vec{y}$. Therefore we can consider the field strength along $\vec{y}$ only:

$$B_{\mathrm{mw}} \approx \frac{\mu_0 I_{\mathrm{mw}}}{2\pi}\left(\frac{1}{z_0} - \frac{z_0}{z_0^2 + d^2}\right) \tag{2.9}$$

and the gradient along $\vec{z}$:

$$\partial_z B_{\mathrm{mw}} = -\frac{\mu_0 I_{\mathrm{mw}}}{2\pi}\frac{d^2(3z_0^2 + d^2)}{z_0^2(z_0^2 + d^2)^2} = -B_{\mathrm{mw}}\frac{3z_0^2 + d^2}{z(z_0^2 + d^2)} \tag{2.10}$$

Similarly, we have the inhomogeneity across the cloud:

$$\left.\frac{\sigma_\Omega}{\Omega_{\mathrm{mw}}}\right|_z \approx \frac{\sigma_z}{z_0}\frac{3z_0^2 + d^2}{z_0^2 + d^2} \approx 4.5 \times 10^{-2} \tag{2.11}$$

In $\vec{x}$, the situation is more uncertain. We know that there can be a standing wave in the CPW, and in the worst case, the cloud sits in between a node and an anti-node. The variation would be

$$\left.\frac{\sigma_\Omega}{\Omega_{\mathrm{mw}}}\right|_x = \frac{2\pi\sigma_x}{\lambda_{\mathrm{mw}}/2} \approx \frac{2\pi \cdot 120\ \mu\mathrm{m}}{0.5 \cdot 4.38\ \mathrm{cm}} = 3.5 \times 10^{-2} \tag{2.12}$$

where λ_{mw} is the wavelength of the MW and σ_x the thermal width along $\vec{x}$. A trap frequency $\omega_x = 2\pi \cdot 4$ Hz and a different temperature $T_x \sim 100$ nK are assumed. Note that this only gives an upper bound. Apparently, the MW inhomogeneity along $\vec{z}$ is dominant. We shall see below its consequences in the experiment.

Experimental evidence We have observed evidence of the field inhomogeneity. We apply a π pulse after preparing the atoms on the equator of the Bloch sphere, where the transition probability $P_\uparrow$ is more sensitive to the pulse error of the π pulse. Consider a strongly inhomogeneous field and a short pulse such that the atoms are static during the pulse. For a pulse area π *on average*, atoms closer to the chip experience a larger pulse area, therefore are driven below the equator, contributing more to the atoms detected in $|\downarrow\rangle$. As a result, the average position of the detected atoms in $|\downarrow\rangle$ will be closer to the chip, compared to those detected in $|\uparrow\rangle$. So we expect to measure a separation in the average position of the two states. As the atoms are actually oscillating in the trap, measuring their average position over time should reveal an "oscillation", out-of-phase for the two states.

We indeed observe these apparent oscillations of the two states, when the π pulse lasts only a fraction of the oscillation period along $\vec{z}$ (Fig. 2.15(b)). Note that this is not real centre-of-mass oscillation but position-dependent spin polarisation across the cloud. This effect is absent when the pulse is sufficiently long or a multiple of the oscillation period (Fig. 2.15(c)), as the oscillation of the atoms averages out the field inhomogeneity.

It's worth noting that this spatiotemporal oscillation of spin polarisation has been used previously in TACC-1 to study spin waves and collisional frequency shift [49]. However, to achieve homogeneous excitations, we learn that the oscillation period along $\vec{z}$ sets the minimum timescale for the MW pulses.

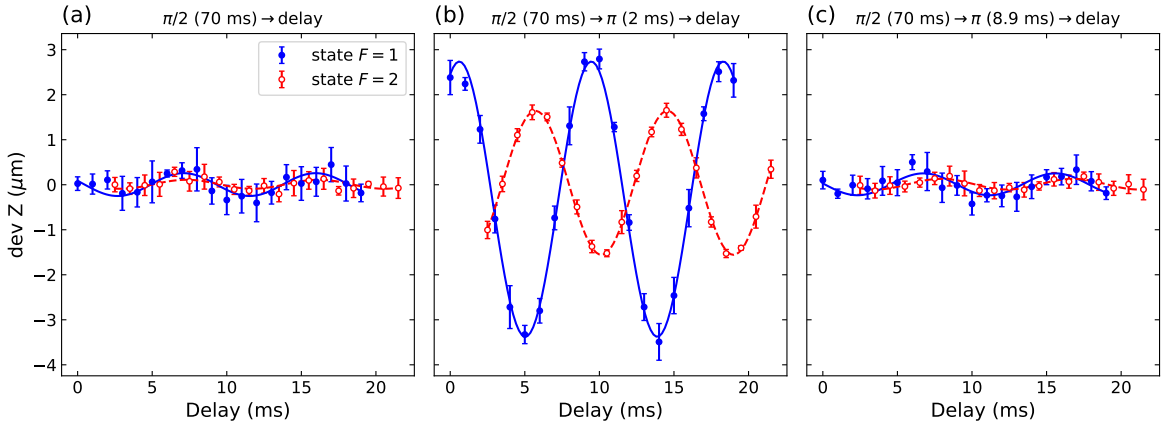

Figure 2.15 Evidence of the inhomogeneous excitation field. We prepare the atoms on the equator of the Bloch sphere by a 70 ms $\pi/2$ pulse, resulting in small centre-of-mass oscillations (a). The data of state $|\uparrow\rangle$ are shifted horizontally by 2.5 ms to account for the time delay between the release of the two states. Strong "oscillations" appear if we apply a short π pulse (b). These oscillations are in fact position-dependent spin distribution due to the π pulse inhomogeneity. The "oscillations" of the two states are not completely out-of-phase, possibly due to residual centre-of-mass oscillations. (c) If we instead apply a π pulse with the duration of 8.9 ms, which is exactly a trap period (in $\vec{z}$), the oscillations disappear. The curves are sinus fits to guide the eye.

2.2.6 Interrogation pulse tuning

Here I briefly describe the basic tuning procedures of the interrogation pulse, normally to realise a $\pi/2$, a π or any arbitrary rotation. A rotation is determined by the frequency, phase, and area of the pulse, where the area means the integration of amplitude over the pulse duration. As detailed in the following, the amplitudes of both the MW and RF have to be individually tuned, while the frequency and phase tunings are done only in the RF.

2.2.6.1 Magic field

The magic field can be easily found by fitting the quadratic relation between the transition frequency and the applied bias field B_x (Eq. 1.10, Fig. 2.16(a)). A series of simple Rabi spectroscopy suffice as long as the pulse length is not completely wrong. The π-pulse duration (π/Ω_{R} where Ω_{R} is the Rabi frequency) does have an approximately linear relation with the B_x (Fig. 2.16(b)). The reason is that as we fix the MW frequency but only vary the RF frequency, the detuning to the intermediate state varies linearly as a function of the bottom field due to the Zeeman shift of the clock states. Ω_{R} is hence inversely proportional to B_x, so is the π-pulse length proportional to B_x. However, this relation is not precise as the bias field also affects the trap position with respect to the chip surface.

Finding the magic field also helps to identify the two-photon light shift (see below), since we know from theory the clock transition at the magic field. A coarse tuning of the light shift compensation would be simply to approach the resonance of the Rabi spectroscopy to the theoretical value, if one starts from scratch.

2.2.6.2 Detuning and pulse length

At a given bias field, and with the coarsely found clock frequency, we can observe Rabi oscillations by varying the pulse duration. By fitting the oscillations we determine the duration for a π pulse or any other pulse. We can then perform a Ramsey spectroscopy to determine the resonance frequency more precisely.

However, the frequency we found can be still perturbed by the two-photon light shift. We can compensate the light shift by the balance of the amplitudes of RF and MW fields (see below). Once the light shift compensated, can the frequency and pulse duration be tuned definitively. Multiple iterations might be needed if one starts far from optimum.

For a very short pulse, the thermal motion in the trap need to be respected, due to the MW inhomogeneity (Sec. 2.2.5.3). This means that we lose the freedom to tune the pulse area by fine tuning the pulse duration. On the contrary, the pulse duration is fixed to a multiple of oscillation period in $\vec{z}$, while the pulse area is tuned via the amplitude.

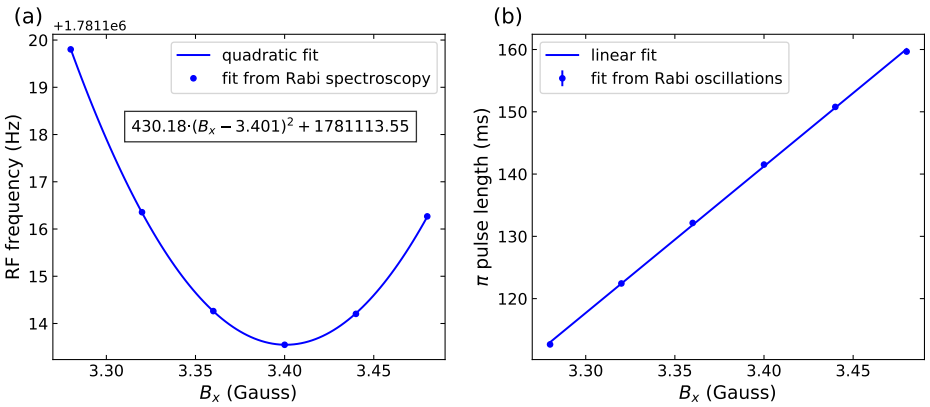

Figure 2.16 Typical data of RF pulse tuning procedure. (a) Transition frequencies found by Rabi spectroscopy, as a function of the bottom field (B_x). A quadratic fit reveals the magic field (experimental value). (b) π-pulse lengths measured through Rabi oscillations, as a function of B_x. They roughly follow a linear relation.

Amplitude transient In determining the pulse duration by fitting Rabi oscillations, we assume a constant Rabi frequency. Obviously the more oscillations, the better can we determine the Rabi frequency. However, there is transient variation both in the MW and RF fields after switching on, probably due to thermal effects in the RF switch and in other components. It is observed as a slow increase in amplitude, about 0.6% in amplitude for the RF, but can be as large as 2.5% in amplitude for the MW for a short but strong pulse.

This transient not only compromises the pulse-length tuning, as it introduces a systematic error if we use multiple Rabi oscillations to fit the Rabi frequency, but also renders the composite pulse imperfect (Sec. 4.2.2), as the constituent pulses will be intrinsically different in amplitude. In the future, we can apply feedback to stabilise the MW power, although a fast feedback during the pulse might be challenging.

2.2.6.3 Amplitude: two-photon light shift

Both the MW and RF fields induce light shift on the clock states. In theory, assuming an equal composition of σ^+ and σ^- polarisations in the driving fields, the RF photon produces no net light shift on the clock transition (see [70] 3.1.3). But in practice, the polarisation of the field is not ideal and the RF field does induce a light shift, actually allowing to compensate the light shift induced by the MW, if they have opposite signs. The sign of the RF light shift, is determined by the polarisation. Without in-depth understanding, we discovered that delivering the RF photon through a chip wire on different sides of the stripline, induces light shift of opposite signs. One simply has to choose the correct wire.

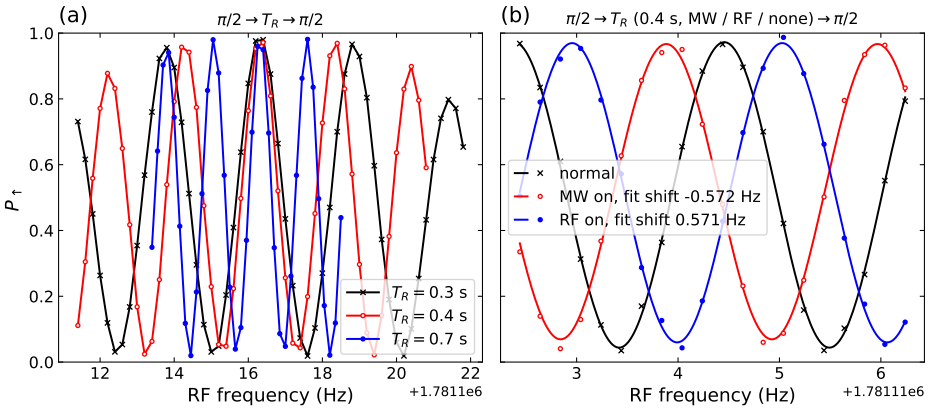

Figure 2.17 Typical data of two-photon light shift compensation, by varying T_R (a), or by letting RF or MW field on during T_R (b).

Note that this light shift compensation is not like those called "magic" (such that the light shift would be first-order insensitive to the fluctuation of the field amplitude). It is simply the crossing of two linear dependences, so that the light shift of either field is still linearly sensitive to amplitude fluctuations.

The two-photon light shift can be identified by performing Ramsey spectroscopy with different Ramsey times (T_R). For example, if the atomic transition is not perturbed during the pulse, the central Ramsey fringes for different T_R should all align, since it is simply the true atomic transition (Fig. 2.17(a)). Otherwise, the LO is only on resonance with the perturbed clock transition (as we "calibrated" the pulse), while the atoms will evolve at the unperturbed frequency during the Ramsey time, acquiring a phase depending on T_R. Therefore the central fringes for different Ramsey times generally do not align.

One can therefore tune the amplitude ratio of the RF and MW while preserving their product (hence Ω_R), until the central Ramsey fringes align for any Ramsey time.[11] Or more precisely, we can determine the light shift of the RF or the MW separately, by comparing a normal Ramsey sequence with one keeping either the RF or the MW field on during the Ramsey time, respectively. As the $\pi/2$ pulses are in common, the difference between the central fringes directly indicates the frequency shift during the Ramsey time. By running three Ramsey spectroscopy sequences (normal, RF on during T_R, and MW on during T_R),

[11] Precisely speaking, even without light shift, the central fringes still differ slightly for different T_R, due to the density shift and the atom loss during the sequence.

we obtain the ratio between the RF and MW light shifts, which can be then immediately balanced (Fig. 2.17(b)).

2.2.7 Absorption imaging

At the end of the sequence, the trap is switched off, and the atoms (in $|F = 2\rangle$) are imaged by a detection beam resonant on the $F = 2 \rightarrow F' = 3$ cycling transition. A second image (bright frame) is subsequently taken with the atoms removed. Two frames combined obtain the absorption image of the atomic cloud. The absorption is governed by the atomic density n integrated over the imaging axis (column density), as e.g. imaging along $\vec{y}$:

$$\frac{\mathrm{d}I}{I} = -n(x, y, z)\sigma(I) \cdot \mathrm{d}y \tag{2.13}$$

where I is the intensity of the imaging beam. $\sigma(I)$ is the absorption cross-section of the cycling transition, dependent on the saturation and detuning δ of the imaging beam

$$\sigma(I) = \frac{\sigma_0}{1 + I/I_{\mathrm{sat}} + (2\delta/\Gamma)^2} \tag{2.14}$$

where Γ is the natural linewidth of the transition, $I_{\mathrm{sat}} = \hbar\omega\Gamma/2\sigma_0$ the saturation intensity, and $\sigma_0 = 3\lambda^2/2\pi$. We obtain the column density in a unit area knowing the intensity I_{br} before the absorption (bright frame) and after the atoms I_{im} (image frame):

$$\begin{aligned} n(x, z) &= \int n(x, y, z)\mathrm{d}y = \int_{I_{\mathrm{br}}}^{I_{\mathrm{im}}} \frac{\mathrm{d}I}{\sigma I} \\ &= \frac{1 + (2\delta/\Gamma)^2}{\sigma_0} \ln\left(\frac{I_{\mathrm{br}}}{I_{\mathrm{im}}}\right) + \frac{1}{\sigma_0 I_{\mathrm{sat}}}(I_{\mathrm{br}} - I_{\mathrm{im}}) \end{aligned} \tag{2.15}$$

where the second term accounts for the transparency due to saturation at higher intensities. We shall work in a regime $I \sim I_{\mathrm{sat}}$ where the contributions from the two terms are comparable. It has the advantage to achieve high signal-to-noise ratio (SNR) even for a high optical depth [118]. We see later that the detection noise due to PSN is also minimised in this regime. Applying Eq. 2.15 to an area A of a pixel allows to obtain the atom number per pixel from the camera counts N_{cc}, which is related to the intensity as

$$N_{\mathrm{cc}} = GN_{\mathrm{e}} = G\eta N_{\mathrm{ph}} = G\eta\frac{IA\tau_d}{\hbar\omega} \tag{2.16}$$

where N_{ph} and N_{e} are the number of photons and photoelectrons, respectively. G denotes the electronic gain of the sensor and η is the overall conversion that includes optical losses and the quantum efficiency (QE) of the sensor. τ_d is the duration of the imaging pulse. Therefore, the atom number from a particular pixel reads ($\delta = 0$):

$$N = \frac{A}{\sigma_0'} \ln\left(\frac{N_{\mathrm{br}}^*}{N_{\mathrm{im}}^*}\right) + \frac{2}{G\eta\tau_d\Gamma}(N_{\mathrm{br}}^* - N_{\mathrm{im}}^*) \tag{2.17}$$

Here N_{im}^* and N_{br}^* denotes the "corrected" counts of this pixel in the image and bright frame respectively, namely removing the dark counts[12] and normalising the overall power of the imaging beam in the two frames (using a region containing no atom). Note that the cross-section σ_0' differs from the theoretical value due to imperfect polarisation and wrong transitions (from the cycling transition) that the atoms initially see.

[12] Dark current of a CCD, while negligible for a CMOS

Cameras As depicted in Fig. 2.5, we can perform absorption imaging along $\vec{x}$ for atoms at the MOT site and along $\vec{y}$ for atoms in the cavity. The imaging along $\vec{x}$ serves only for characterisations, hence we use an economic industrial camera (IDS uEye® UI-3070CP), which has a CMOS sensor (Sony IMX252) with high resolution (3 MP), high dynamic range (71 dB, not reached due to the 12-bit ADC), high frame rate (120 fps), and reasonable QE at 780 nm (32%). Although it cannot perform fast frame transfer[13] nor interline frame transfer[14] compared to other high-end CCD cameras that are commonly employed for absorption imaging, the fast frame rate of CMOS still allows to obtain good absorption images (see Fig. 2.10, first row).

Imaging along $\vec{y}$ requires low-noise detection for clock operations in the cavity. We use the same camera as in TACC-1 (Andor iKon M934-BRDD) which has been thoroughly calibrated previously [72]. The CCD has a QE $\sim 95\%$ and is operating at $-60\,^{\circ}\mathrm{C}$ to reduce electronic noise and dark current, such that the noise is dominated by PSN. It can perform fast frame transfer, allowing us to take two images with ~ 5 ms delay.

Due to the limited NA of the imaging lens (and half obstructed by the atom chip), we have to let the cloud expand for a sufficient TOF before imaging, to avoid fringes due to diffraction. For a thermal cloud the minimum TOF is about 1 ms, while for a BEC, diffraction fringes are visible until about 5 ms TOF.

2.2.7.1 Double detection and adiabatic rapid passage (ARP)

To detect the two clock states separately, one traditionally performs a "double detection" scheme. $|F = 2\rangle$ is first detected, while during the bright frame, repumper is added to detect $|F = 1\rangle$. The two states are spatially separated due to the free fall during the time delay between the two images. Therefore, the second image still provides a bright frame for $|F = 2\rangle$ while the first image provides the bright frame for $|F = 1\rangle$.

The drawbacks of the double detection include the vulnerability to power and frequency fluctuations between the two images. Furthermore, the detectivity of $|F = 1\rangle$ is different from that of $|F = 2\rangle$ due to the process of repumping, especially apparent for a short detection pulse or in a dense cloud. All these contribute to the uncertainty in determining $P_{\uparrow}$.

Another state-resolved detection method developed in TACC-1 is the ARP that quickly transfers all atoms in $|\downarrow\rangle$ into $|2, 0\rangle$, starting to fall subsequently. Atoms in $|\uparrow\rangle$ stay trapped and are released later such that they are spatially separated from the atoms in the other state. The image frame then contains both clouds simultaneously. Technical noise between the image and bright frames is common to both states. The difference in detectivity of $|\uparrow\rangle$ and $|2, 0\rangle$ are negligible as they are both quickly pumped to the cycling states. For a quantitative comparison between double detection and ARP, see [119] 3.4.1.

The adiabatic transfer is ensured by a strong MW through the CPW, sweeping adiabatically through the transition. In practice we sweep the transition frequency instead, by varying the bottom field (Zeeman shift) in an integrated Blackman profile. The power of the MW is also ramped in a Blackman profile. We achieve 100% efficiency with uncertainty limited by the detection noise.

It's worth noting that one should also make sure that all atoms are removed before the

[13] Electrons in half of the sensor can be quickly transferred to the other half, as a temporal storage. It allows obtaining two images using half of the sensor area with very short delay.

[14] Each pixel contains a masked well that can store one image. Two images can be acquired consecutively.

bright frame, either by a sufficiently strong imaging pulse or by a dedicated push beam. Otherwise atoms in $|\uparrow\rangle$ that are not removed may coincidentally falls into the region where the atoms in $|2,0\rangle$ were, introducing an error in atom number.

In TACC-2, however, we are restricted to ARP for a precise atom number measurement in the cavity. As mentioned in Sec. 2.1.3.2, using repumper in detection along $\vec{y}$ causes problems since the repumper also enters the CCD. In double detection, the optical powers in the image and bright frames are drastically different. The power of the repumper is not precisely known in each shot, so it cannot be removed from the calculation to obtain an accurate atom number. Hence, we will only use the double detection scheme when ARP is not accessible. On the other hand, our ARP scheme involves a sweep of bottom field which perturbs the magnetic trap. This affects e.g. the measurement of temperature in $\vec{x}$ through TOF. We shall use the double detection for these types of measurement where a precise atom number is not crucial. Alternatively, one can implement a MW frequency sweep for the ARP to avoid such imperfection.

2.2.7.2 Detection noise

Here I briefly discuss the detection noise of the imaging system. The primary noise source, for the Andor camera working at $-60\,^{\circ}\mathrm{C}$, is the PSN. Precisely speaking, it is the shot noise of the photoelectrons – $\sigma^2(N_\mathrm{e}) = \langle N_\mathrm{e}\rangle$ – that corresponds to fluctuations in the intensity

$$\sigma^2(I) = \frac{\hbar\omega}{\eta A\tau_d}\langle I\rangle \tag{2.18}$$

We can have an estimate of the PSN through Eq. 2.15:

$$\sigma^2(n(x,z)) = \frac{\hbar\omega}{\eta A\tau_d\sigma_0}\left(\frac{I_\mathrm{br}+I_\mathrm{im}}{I_\mathrm{br}I_\mathrm{im}} + \frac{4}{I_\mathrm{sat}} + \frac{I_\mathrm{br}+I_\mathrm{im}}{I_\mathrm{sat}^2}\right) \tag{2.19}$$

which reaches a minimum when

$$I_\mathrm{br} = \frac{I_\mathrm{sat}}{\sqrt{1-a}}, \quad \text{with } 1-a = \frac{I_\mathrm{im}}{I_\mathrm{br}} \tag{2.20}$$

This suggests that it is always preferable to work with $I \gtrsim I_\mathrm{sat}$, even for a small optical depth. We also see that the area A of the pixel, or practically the magnification of the imaging, also influences the PSN. The practical limit is the saturation of the CCD. It is also preferable to work close to the saturation of the sensor to exploit the full dynamic range.

In practice, there is not so much room to play. With the current magnification of 1.875 (detection $\vec{y}$), we can barely achieve I_sat for a 10 μs imaging pulse. It is also not practical to optimise the detection through the optical depth of the cloud. In the end, the detection noise from the PSN is about 2 atoms per pixel at I_sat [119], which gives typically a detection noise of 60 atoms for 1000 counted pixels. A calibration with QPN of the atoms is given in Sec. 3.1.1.

Cloud compression Given that the intensity is always close to I_sat, the PSN scales with the amount of collected light, which is determined by the real size of the cloud. Imaging transversely through the cavity, the cloud is quite extended along $\vec{x}$, requiring a large number of pixels to be counted, giving a large noise.

Nevertheless, as we only care about the atom number in each state (at least for the clock operation), one can compress the cloud into a smaller size. Therefore, we increase the confinement along $\vec{x}$ (a ramp-up of dimple current for 15 ms) before the ARP phase. But the cloud will not be stationary after the ramp-up, so the ramp-up duration is experimentally optimised to minimise the cloud size at the detection time. However, I shall note that $|\downarrow\rangle$ is released first while $|\uparrow\rangle$ stays in the trap for a longer time. The two clouds undergo different dynamics and the optimisation depends on the TOF and the delay before releasing $|\uparrow\rangle$. With this simple scheme, we are able to reduce the necessary number of pixels to about 400 instead of 1000 for each cloud.

Another obvious defect is the fact that we select a rectangular region to count the atom number while the cloud is mostly elliptical. We always suffer from the noise from 22% of the pixels that do not contain atoms! This should be improved in the near future.

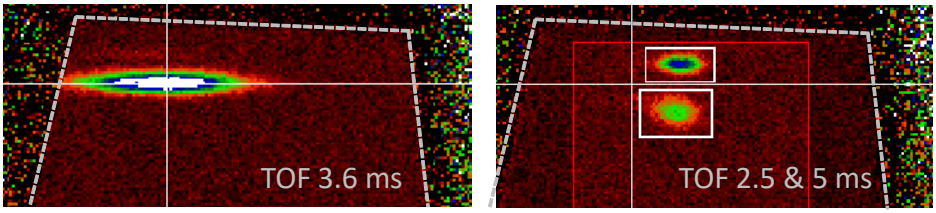

Figure 2.18 (a) Typical absorption image through the cavity, the cloud is shifted from the cavity centre (approximately the centre of the aperture) due to imperfection of the bias fields. (b) Image of the two clock states with ARP and cloud compression. The region outlined by the red rectangle is the region of bright frame recomposition. In these images no fringe is clearly visible. The recomposed region only appears to have a better normalised background. The dashed lines indicate the aperture of the imaging beam.

Fringe cancellation The next major noise source is caused by optical fringes, due to vibrations or frequency fluctuation between the two frames. We routinely apply a post-processing of the images to remove optical fringes, by reconstructing a bright frame that perfectly matches the image frame (in the region excluding the atoms) from a basis of previously taken images. In theory, the optimum noise reduction can be a factor of $\sqrt{2}$ since there is only one image instead of two. The efficiency of the fringe recomposition has been analysed in [119].

I shall point out that with the ARP detection and the bright frame recomposition, the bright frame is in principle not needed. Therefore the camera is not required to perform fast frame transfer.

2.3 Cavity probing and stabilisation

Despite the compact and robust nature of fibre cavities, there are many challenges in our system for achieving a stable cavity resonance. This section is dedicated to the setup and techniques for the cavity probing and stabilisation.

2.3.1 Cavity parameters

I shall emphasise again the uniqueness of our cavity system. In order to accommodate a thermal cloud with tens of thousands of atoms in a shallow clock trap, the cavity length extends to 1.2 mm, which is close to the longest fibre cavity ever reported [120]. The most prominent technical challenge was to machine fibre mirrors of large radii of curvature (ROC), overcome by a multi-shot technique [108, 121, 120]. Another challenge was the poor input mode-matching from a single-mode fibre, since for long cavities, the cavity mode size on the mirrors can be considerably bigger than that of a conventional single-mode fibre. Therefore we use a large-mode photonic crystal (PC) fibre (LMA-20) at the input to improve the mode-matching to potentially 60% (see [108] 4.1.5 for more details). The PC fibre is also "endlessly" single mode at 780 nm and 1560 nm for our dual-wavelength scheme (detailed below). The output fibre employs a multi-mode (MM) fibre to ensure maximum collection of the output photons. I shall note that recent developments allow 90% mode-matching efficiency using spliced graded-index (GRIN) fibres [122].

The two cavities mainly differ in the finesses of the 780 nm modes, one with low finesse (LF) of about 2700 and the other high finesse (HF) of about 38000, targeting different atom-cavity coupling regimes. The 1560 nm modes both have high finesse and serve for cavity locking or forming an optical lattice to trap the atoms. Throughout this thesis, we use the LF cavity as the science cavity for the atoms, and the HF cavity as an auxiliary.

Cavity parameters are summarised in Table 2.3. Mirrors are characterised by optical profilometry after the CO_2 machining [121, 120]. The cavity linewidth is measured by calibrated sidebands in the transmission spectrum (obtained by scanning the cavity length). The cavity finesse is hence deduced. The main uncertainty comes from the determination of the cavity length, which is measured from a high resolution photograph of the cavity.

Commensurate wavelengths In many previous cavity-QED experiments with atoms trapped in intra-cavity optical lattice, the mode of the probe light does not overlap spatially with the trapping field, causing inhomogeneous coupling. Using lattices at commensurate wavelengths has gain interests in recent experiments using rubidium, thanks to the dipole transition at 780 nm, twice of which comfortably lies within the Telecom standard. Unfortunately, 1560 nm is quite close to other transitions ($5P_{3/2}$ to $4D_{3/2}$ and $4D_{5/2}$), causing strong light shift on the excited state ($5P_{3/2}$). Nevertheless, advantages in optimal cavity coupling may out-weight the inconvenience of this perturbation [123, 124].

It's worth noting that for short fibre cavities, an exact double-wavelength doesn't provide the optimum mode overlap due to the Gouy phase. For example, for a cavity of length 200 μm, the optimum lattice wavelength is rather 1559 nm [124].

Moreover, to ensure the anti-nodes of the two modes overlap instead of the opposite case (at least at the cavity centre), the phase shift from the mirror reflection has to be properly engineered for both wavelengths (by engineering the penetration depth into the

Bragg reflector). In fact, for short cavities, only at a particular design length can the two modes be resonant simultaneously.

In TACC-2, atoms should be trapped magnetically so the commensurate wavelength is not essential for a squeezed clock. We adopted this scheme for technical convenience, and also for having the possibility to explore intra-cavity lattice experiments with optimum coupling.

However, the mirror phase shift is only correctly engineered for the LF cavity. For the HF cavity, the 780 nm mode and the exact-double-wavelength 1560 nm mode are not resonant at the same time, but with a detuning of 25 GHz (of the 1560 nm mode).

	Unit	**Low Finesse (LF)**		**High Finesse (HF)**	
Length L	μm	1215 ± 20		1275 ± 20	
$\mathrm{ROC_{MM}}$	μm	1612/1523		1494/1416	
$\mathrm{ROC_{PCF}}$	μm	1559/1468		1513/1437	
$\mathrm{ROC_{eff}}$	μm	1560/1520		1490/1430	
z_R	μm	745/761		711/737	
collapse L_{col}	μm	60 ± 5		50 ± 5	
FSR ν_{fsr}	GHz	123 ± 2		118 ± 2	
		780 nm	**1560 nm**	**780 nm**	**1560 nm**
waist w_0	μm	13.6/13.7	19.2/19.4	13.3/13.5	18.8/19.1
w_m	μm	17.5/17.6	24.8/24.9	17.8/17.9	25.2/25.3
$\kappa/(2\pi)$	MHz	45.8 ± 0.6	5.35 ± 0.08	3.08 ± 0.08	2.02 ± 0.06
$\mathcal{F}$	$\times 10^3$	2.69 ± 0.1	23.06 ± 0.8	38.2 ± 2.1	58.2 ± 3.6
bir. split. $\Delta_{\mathrm{bir}}/\kappa$		-	-	1.1	0.7
$T_{\mathrm{FFP}}(\delta = 0)$ †		25.8%	10.8%	3.2%	7.9%
$R_{\mathrm{FFP}}(\delta \gg \kappa)$ †		42.1%	65.0%	42.9%	71.4%
$R_{\mathrm{FFP}}(\delta = 0)$ †		10.4%	40.8%	30.9%	48.3%
ϵ_1 ‡		0.36	0.31	0.27	0.27
$\lvert\eta\rvert$ ‡		0.45	0.76	0.53	0.79
ϕ_η ‡	π	0.01	-0.18	0.01	0.01
$g_0/(2\pi)$	MHz	10.9	-	10.9	-
$C_0 = 4g_0^2/\kappa\Gamma$		1.90	-	25.44	-
$\delta\omega_c^0/(2\pi)$	kHz	34.9	-	34.8	-
C_{eff}		0.42	-	6.07	-
$\delta\omega_{\mathrm{eff}}/(2\pi)$	kHz	8.55	-	8.30	-

Table 2.3 Cavity parameters of both cavities at 780 and 1560 nm, updated from [108]. $\mathrm{ROC_{eff}}$ are deduced from the higher-order mode spectra [108] 4.2.5. w_m is the $1/e$ radius of the mode on the mirrors. The birefringent splitting is not measurable for the LF cavity. $\kappa/2\pi$ is FWHM. g_0, C_0 and $\delta\omega_c^0 = 4g_0^2/\omega_{\mathrm{at}}$ use the D2 dipole matrix elements summed over all sublevels, namely $\frac{1}{2} \cdot |\langle J = \frac{1}{2} || e\boldsymbol{r} || J' = \frac{3}{2} \rangle|^2$, and $\Gamma/2\pi = 6.07$ MHz (FWHM) [73]. The effective values, however, use the σ^+ transitions relevant in the experiment, and assume a cloud at $T = 200$ nK in the trap with $\omega_z = 2\pi \cdot 110$ Hz.
† These values are taken after the integration of the vacuum cell, prior to bake-out. Bending loss in the input PC fibre is included, which is extremely sensitive to stress, especially for 780 nm. The bending loss in the final setup is higher.
‡ These are estimated with the transmission and reflection listed (not the full spectra), containing the input bending loss, only to give the order of magnitude.

Transmission and reflection From transmission and reflection spectra, one can evaluate the mode-matching (to TEM(0,0) mode) of the fibre Fabry-Pérot (FFP) cavities. Based on the basic notions in Sec. 1.3.1, and the model developed in [121] (see also [125]), we have the transmission of the FFP cavity:

$$T_{\mathrm{FFP}}(\delta) = \frac{P_{\mathrm{tran}}}{P_{\mathrm{in}}} = \epsilon_1\epsilon_2 T(\delta) \tag{2.21}$$

where ϵ_1 is the input mode-matching coefficient, and ϵ_2 is that for the output. The general expression of the reflection reads [121]:

$$\begin{aligned} R_{\mathrm{FFP}}(\delta) = \frac{P_{\mathrm{refl}}}{P_{\mathrm{in}}} &= R(\delta)\epsilon_1^2 + (1-\epsilon_1)^2\,|\eta|^2 + \\ &+ 2\epsilon_1(1-\epsilon_1)\,|\eta|\left[\cos\phi_\eta\left(1-\frac{\kappa}{\kappa_t}T(\delta)\right) + \sin\phi_\eta\frac{\kappa_t}{\kappa}\frac{2\delta/\kappa}{1+(2\delta/\kappa)^2}\right] \end{aligned} \tag{2.22}$$

where the complex coefficient $\eta = |\eta|\,e^{i\phi_\eta} = \frac{1}{1-\epsilon_1}\sum_{m,n\neq 0}|C_{m,n}|^2\,e^{i(\phi_{m,n}-\phi_{0,0})}$. This comes from decomposing the mode of the input fibre $|\mathrm{f}\rangle$ into the TEM eigenmodes of the cavity as $|\mathrm{f}\rangle = \sum_{m,n} C_{m,n}\,|(m,n)\rangle$, with $\sum_{m,n}|C_{m,n}|^2 = 1$. Then $\epsilon_1 = |C_{0,0}|^2$. Note that the reflection introduces only phase shifts $\phi_{m,n}$ on the high-order modes as they are off-resonant. Their values depend on the Gouy phase of each mode.

Experimentally, we shall assume $\epsilon_2 \approx 1$ because of the MM fibre. Then from the resonant transmission $\epsilon_1\frac{\mathcal{T}^2}{(\mathcal{T}+\mathcal{L})^2}$, we can estimate the mode matching coefficient ϵ_1. From the two extreme cases of the reflection we can estimate $|\eta|$ and the phase ϕ_η. For the LF cavity, $\mathcal{L} \ll \mathcal{T}$, we arrive at simpler expressions:

$$R_{\mathrm{FFP}}(\delta = 0) = (1-\epsilon_1)^2|\eta|^2 \tag{2.23}$$

$$R_{\mathrm{FFP}}(\delta \gg \kappa) = (\epsilon_1^2 + (1-\epsilon_1^2)\,|\eta|^2 + 2\epsilon_1(1-\epsilon_1)\,|\eta|\cos\phi_\eta) \tag{2.24}$$

The estimated values are listed in Tab. 2.3. A fit with the full spectra is shown in Fig. 2.19.

Changes in finesse Several previous experiments have reported changes in cavity finesse due to rubidium contamination. In Tab. 2.4, I summarise measured cavity finesse after certain events. After a year of operation with rubidium, the finesse of the science cavity (LF) has reduced. Unfortunately, we missed an important data point after the bake-out, so the existing data do not allow us to draw any conclusion. It will become clearer some time later.

Table 2.4 Finesse changes after various events and a year of operation

Events	LF cavity ($\times 10^3$)		HF cavity ($\times 10^3$)	
	780 nm	**1560 nm**	**780 nm**	**1560 nm**
Glued	2.44	22.4	30.0	54.4
Heat cured	2.92	23.5	39.2	62.5
Few days later	2.94	23.2	36.5	54.9
Mounted on chip & cell	2.98	23.4	38.2	58.2
A year's operation with Rb	2.69	23.1		

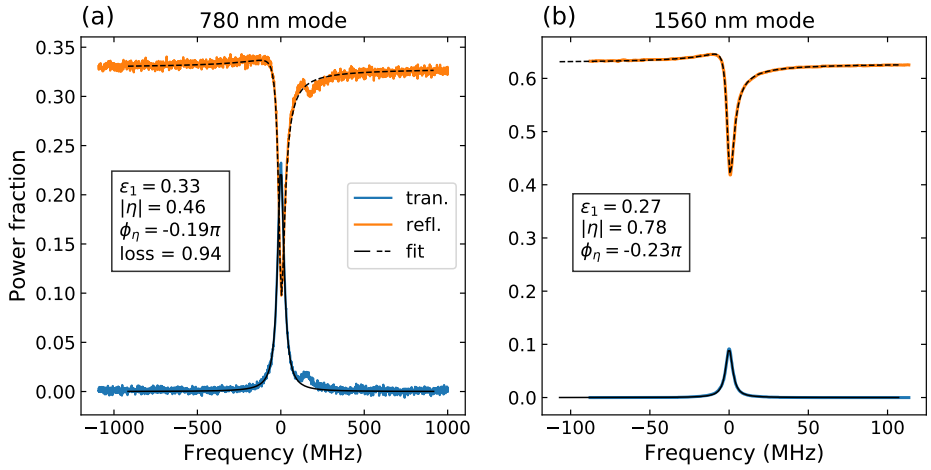

Figure 2.19 Transmission and reflection spectra of the 780 nm mode (a) and the 1560 nm mode (b) in the science cavity. Data are taken in the final setup. We fit the spectra with Eq. 2.21 and 2.22 to obtain the mode-coupling coefficients, while for the 780 nm mode (a) we added a loss term in the input fibre to account for the bending loss in the final setup. A High-order mode close to the fundamental mode in 780 nm is visible (a).

2.3.2 Laser scheme and setup

2.3.2.1 Overview

Based on the commensurate-wavelength design, the probe laser at 780 nm can be generated from frequency doubling of a 1560 nm source laser, ensuring inherent frequency locking of the two lasers. Thanks to mature Telecom photonic technologies, powerful and reliable lasers are readily available at 1560 nm. In fact, Telecom based 780 nm laser sources for cold-atom applications have been developed and met success (e.g. muQuans and MenloSystems) due to the robustness of an all-fibre setup.

Our setup[15] also exploits fibre-based 1560 nm laser, laser amplifier, and components (Fig. 2.22). A fibre injected periodically-poled lithium niobate (PPLN) crystal generates frequency-doubled 780 nm laser into free-space, one part to reference the source laser via a modulation transfer spectroscopy (MTS) [126, 127] on Rb vapour.[16] The two wavelengths are finally combined in free-space to be injected into the science cavity. For the auxiliary cavity, for now we only inject 1560 nm laser through direct fibre mating.

One feature of the cavity assembly is that the two cavities are mounted as close as possible on the same pair of piezo stacks, such that the thermal and mechanical perturbations to the cavity length are largely in common. One can envisage that by stabilising one cavity, the other is also stabilised. In other words, we could have a stabilised science cavity with only 1560 nm light in the auxiliary cavity. We shall discuss the feasibility later, but in general, a combination of locking both cavities is necessary, as outlined in Fig. 2.20.

[15] Mostly built by Ralf Kohlhaas

[16] The MTS resembles a standard SAS but gives a zero-background error signal, which is dominated by the cycling transitions.

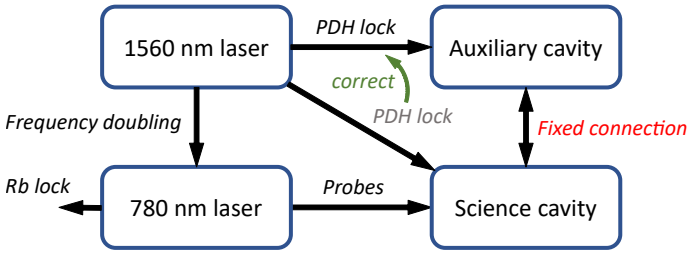

Figure 2.20 Schematics of lasers and cavity stabilisation for cavity-QED experiments. The fixed connection between the two cavities is subject to residual thermal drift, which can be overcome by a "two-cavity interlock" (Sec. 2.3.6).

2.3.2.2 Laser frequencies

Frequency reference To implement QND measurements of S_z in the dispersive regime, the cavity resonance is detuned in between the transitions $5S_{1/2}(F = 1) \rightarrow 5P_{3/2}$ and $5S_{1/2}(F = 2) \rightarrow 5P_{3/2}$, where we have ignored the smaller hyperfine splittings of the excited state. As the detuning determines the atom-cavity coupling for the two clock states, a precise and stable adjustment of the cavity frequency is required. The probe laser frequency should also be independently tunable, to vary the detuning to the cavity mode. As none of these frequencies is close to a particular transition of ^{87}Rb, we instead lock the laser to the cycling transition of ^{85}Rb ($F = 3 \rightarrow F' = 4$), which is close to our target. At the same time, possible leakage resonant with the atomic transitions is avoided.

The frequency relations of the double-wavelength system are better depicted as a function of the cavity length, as shown in Fig. 2.21. For the science cavity, our target mode is ~ 2 GHz away from the ^{85}Rb reference at 780 nm. At the same time, it is about 800 MHz away from the laser at 1560 nm.[17] The probe laser is generated by an electro-optical modulator (EOM), with the unwanted carrier and red sideband being sufficiently filtered by the cavity. Its power and frequency are hence easily tunable. To stabilise the cavity at the target, we employ standard Pound-Drever-Hall (PDH) techniques using the 1560 nm mode.

PDH scheme for the science cavity We can directly apply PDH modulation at 800 MHz and lock the cavity to the blue sideband. In fact, this is the only choice for satisfying another crucial requirement of the experiment: the 1560 nm locking light has to be weak enough to have negligible trapping effect. Only by sending a weak sideband into the cavity could we minimise the intra-cavity power while retaining a workable PDH signal. The noise limit of the setup is analysed below.

PDH scheme for the auxiliary cavity Since the two cavities are not independently tunable, the resonance frequencies are determined (within one FSR) when they are glued, which was not fully controllable. In our case, the resonance frequency of the 1560 nm modes differ by about 35 GHz. Therefore, to stabilised the science cavity with the auxiliary cavity, the offset of the latter need to bridged.

[17] Half of 2 GHz, plus 170 MHz offset due to the fact that the cavity is not simultaneously resonant at 780 nm and its precise double wavelength.

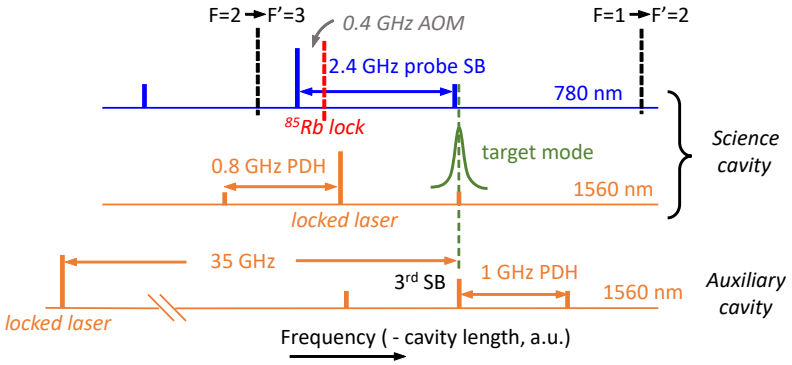

Figure 2.21 Cavity probing frequencies of the two cavities. The frequency scales are different by a factor of 2 for 780 nm and for 1560 nm in the horizontal axis, but correspond to the same change in cavity length.

As shown in Fig. 2.21, we generate a 35 GHz sideband (third order sideband from a strong drive at 15 GHz by an EOM) to bridge the frequency offset. Another modulation at about 1 GHz is added for the PDH lock. Since now we can lock to the "carrier" (the third sideband of the laser), the PDH modulation frequency is not constrained. In practice we tune this frequency to tune the phase of the PDH error signal (about 1 GHz).

This PDH lock serves as a complementary stabilisation method. Certainly, we can lock the science cavity with its own 1560 nm mode, which is more reliable. However, despite the effort to minimise the locking light power, the atoms will always be perturbed by it. Alternatively, we can rely on locking the auxiliary cavity, while the stabilisation is subject to residual drift between the two cavities. This latter scheme will be discussed in detail in Sec. 2.3.6.

2.3.2.3 RAM of fibre EOMs and temperature stabilisation

We utilise fibre EOMs for large modulation depth and bandwidth. However, they generally suffer more from residual amplitude modulation (RAM) compared to free-space models. One well known cause is the interference effect between phase-modulated light (polarised along the e-axis of the crystal) and the un-modulated light (polarised along the o-axis). This can happen if the input polarisation is not perfectly aligned with the crystal e-axis[18] [128], which is generally the case in a fibre EOM pre-aligned by the manufacturer. Normally this misalignment can no longer be corrected.

Upon demodulation of the detected reflection, RAM contributes a DC offset to the PDH signal. Fluctuation in the RAM amplitude is directly translated into a fluctuating offset that shifts the locking point. In the case of a large offset compared to the signal itself, the lock can be even rendered unstable. Nevertheless, as an interference effect, the RAM also depends on the phase shift ϕ_{eo} between the e- and o-light in the crystal, which is affected by many parameters. It can be shown in a simple model that the RAM vanishes when $\phi_{eo} = 0$. Experimentally it can be achieved by adjusting the temperature of the crystal or by applying

[18] In a simple theoretical model, the RAM occurs after a final polariser. However, we observe RAM directly at the output fibre of the EOM. More complicated processes (e.g. polarisation dependent loss) might have taken place.

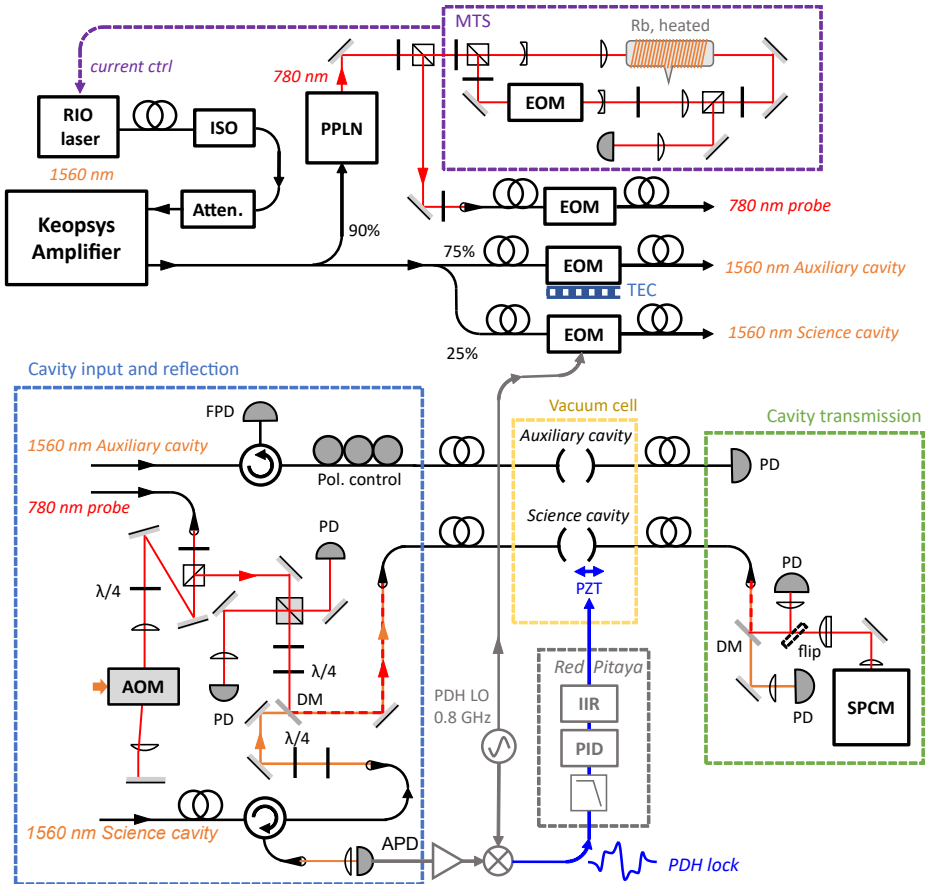

Figure 2.22 Schematics of the complete laser setup for cavity probing and stabilisation. Here we show direct PDH locking of the science cavity. Electronics are shown in grey. APD: avalanche photodiode; DM: dichroic mirror; FPD: fast photodiode; PZT: piezoelectric stack; SPCM: single photon counting module; TEC: thermoelectric cooler.

a DC electric field [128, 129].

In our setup, one of the EOMs (EOSPACE PM-5V5-UV) exhibits a very strong RAM. ~ 0.1℃ change can render the RAM from maximum to minimum. As one simple solution, we have implemented passive temperature control of the EOM. The stability of our temperature control limits the fluctuation in RAM to an acceptable level (~ 0.01 V for a signal of ~ 0.4 V).

2.3.3 PDH lock with minimum intra-cavity power

To lock the science cavity with its 1560 nm mode, the intensity should be minimised to avoid trapping the atoms in the standing-wave potential, also to minimise light shift on the clock transition which deteriorates the clock stability and induces dephasing due to the inhomogeneity in the intensity. Fig. 2.23 shows theoretical calculations of the light shift, including both D1 and D2 transitions. Only a few tens of nW input power is tolerable, making the PDH lock challenging. But it is worth noting that for the science cavity, the probe mode (780 nm) has a much larger linewidth than the 1560 nm mode for PDH lock. This slightly alleviates the requirement on the locked stability in terms of linewidth fractions

of the 1560 nm mode.

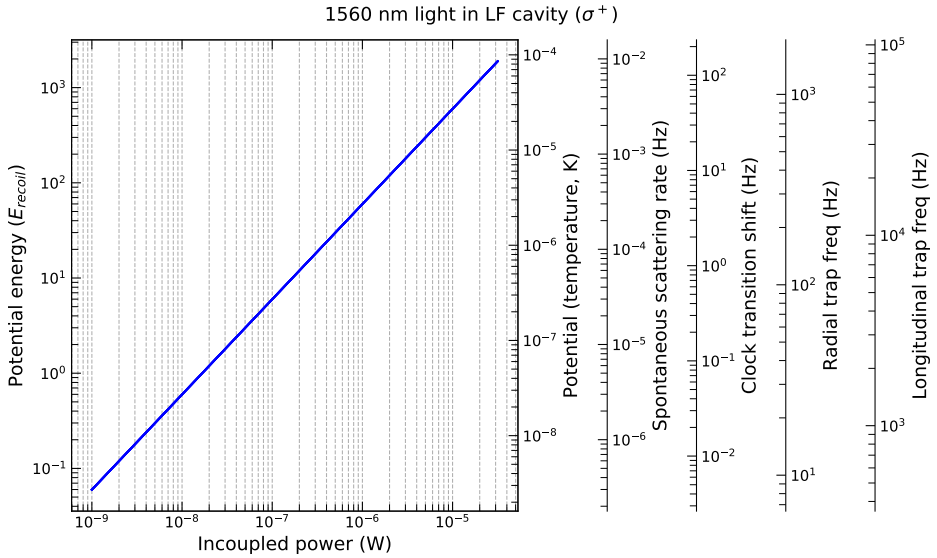

Figure 2.23 Calculated trapping potential (in recoil energy E_{recoil} and temperature), scattering rate and light shift induced by the 1560 nm locking light. All values correspond to the peak intensity at the cavity centre. We have assumed a σ^+ polarisation because σ^- gives a slightly larger light shift, not quite visible in this scale.

2.3.3.1 Limitations

PSN Fundamentally, with minimum intra-cavity power, the measurement of the cavity frequency would be limited by the PSN of the collected photons in the sideband, which contains the phase information of the cavity. The signal is amplified by the carrier (heterodyne) to be detectable. A strong carrier is therefore needed to overcome the detector's electronic noise. More quantitatively, the PSN in the PDH error signal has a white spectral density [130] (a derivation is given in Appendix A):

$$S_e \simeq \sqrt{2\frac{hc}{\lambda}P_r} \approx 16\sqrt{P_r/\mathrm{mW}} \quad (\mathrm{pW/Hz^{1/2}}) \tag{2.25}$$

where λ is the laser wavelength, h the Planck constant, and c the speed of light. P_r is the reflected power (in mW for the numerical expression). This shall be compared with the noise equivalent power (NEP) of the photodetector. If the detector is PSN limited, namely NEP$< S_e$, the PSN gives a fundamental limit of the frequency noise:

$$S_f = \sqrt{\frac{hc}{8\lambda}}\frac{(\Delta\nu_{1560})}{\sqrt{P_s}} \approx \frac{21}{\sqrt{P_s/\mathrm{nW}}} \quad (\mathrm{Hz/Hz^{1/2}}) \tag{2.26}$$

where $\Delta\nu_{1560} = 5.35$ MHz is the linewidth of the 1560 nm mode. We see that it only explicitly depends on the sideband power P_s (in nW for the numerical expression). This fundamental limit from the PSN is difficult to reach in practice.

Detection efficiency An important practical limitation is the detection efficiency of the reflected light, due to limited mode-matching between the cavity mode and the fibre mode (~ 0.27 from Fig. 2.19(b)). The bending loss in the PC fibres is not so prominent at 1560 nm. We use a fibre circulator to make maximum use of the available power, while the collection efficiency of the reflection about 56% is not optimum (compared to e.g. a 90:10 beam splitter). The collimation lens we use to inject both 780 nm and 1560 nm light into the science cavity has VIS-NIR coating in order to optimise the transmission for the probe, but has only 88.7% transmission at 1560 nm. It turns out that for our current experiment, it would have been better to use coating optimised for 1560 nm. We would gain 11% in the signal with the same intra-cavity power for such a modification in the future.

Following Sec. 2.3.1, we shall distinguish the reflection coefficient for the resonant blue sideband, $\epsilon_1 \approx 0.27$ and that of the off-resonant carrier and red sideband, $R_{\mathrm{FFP}}(\delta \gg \kappa) \approx 0.65$. The common collection efficiency into the photodiode is about 0.89 (coating)$\times$0.56 (circulator)≈ 0.5.

Detectors In practice, PSN-limited detection is not always achievable. The carrier power cannot be arbitrarily high to increase the signal, limited by the saturation of the detector, the available power, and leakage of the carrier into the cavity.

We have two good photodetectors available in the experiment, APD310 and FPD310, both from MenloSystems. From the specifications,[19] FPD310 simply cannot be PSN-limited before reaching saturation, while APD310 can in principle achieve a PSN-limited detection. The latter requires less in-coupled power to achieve the same SNR, compared to the former (a theoretical analysis is given in Appendix A). However, in practice we realised that FPD310 (fibre-coupled) gives a higher SNR than the APD310 (free-space), given the same reflected light. The reason is under investigation.

2.3.3.2 Calibration of the locking light

With the APD310, we are able to obtain a lockable PDH signal with 10 nW input power which should have a negligible effect according to the theoretical calculation (Fig. 2.23). In terms of the frequency noise, it turns out that it is limited by other experimental challenges detailed in the following subsections.

We start by calibrating the locking light power. This is done by extrapolation since the expected transmission of tens of nW is not easy to directly measure. As the sideband is generated by phase modulation, its power scales linearly with the modulation power at low modulation depths (Fig. 2.24). We do observe the deviation from linear scaling at high modulation power, which allows us to fit the V_π of the EOM.

We then evaluate the light shift on the clock transition by Ramsey spectroscopy. By varying the power of the locking light, we measure the average frequency shift from the Ramsey fringes. Despite that we ignore the trapping effect, and the transmission efficiency is not precisely known, the data agree well with the theoretical calculations (Fig. 2.25). The result confirms that we could safely work with this amount of locking light until we are limited by uncertainties at tens of mHz level.

[19] APD310: gain 2.5×10^4 V/W, NEP (calculated) 2 pW/$\sqrt{\mathrm{Hz}}$;
FPD310: gain 5×10^3 V/W, NEP (calculated) 15.7 pW/$\sqrt{\mathrm{Hz}}$

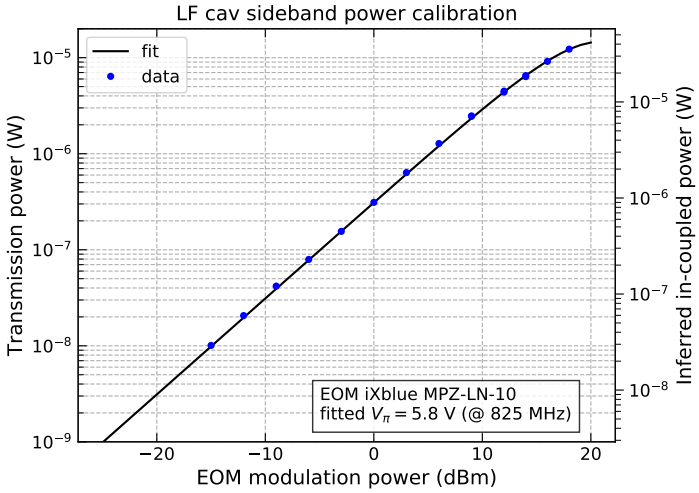

Figure 2.24 Calibration of the locking light power as a function of the EOM modulation power. By fitting the "saturation" by the Bessel function we can get the V_π of the EOM, which is not provided at all modulation frequencies. The calibration allows to obtain the input power at modulation power below -20 dBm by extrapolation, at which the lock will be operating. For example, locking at -20 dBm, the corresponding in-coupled power is 9.0 nW.

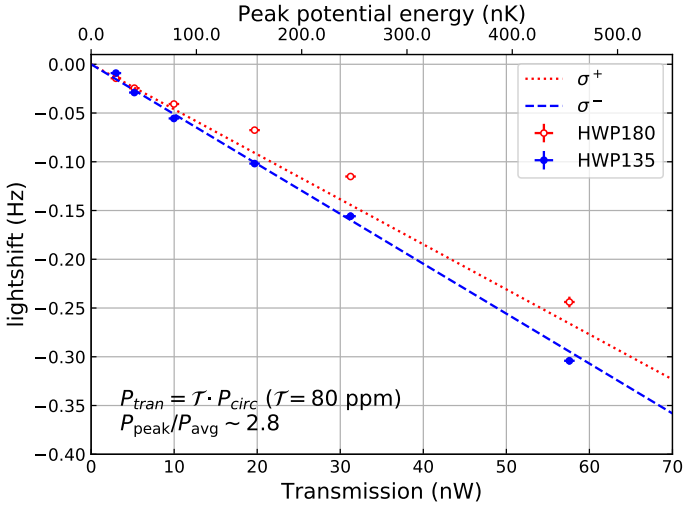

Figure 2.25 Frequency shift measured by Ramsey spectroscopy at different locking light powers. They agree well with the calculation assuming the designed mirror transmission (80 ppm) and perfect collection efficiency. As the Ramsey fringes measure an average frequency shift of the ensemble, we calculate the ensemble averaging of a thermal cloud at 200 nK which gives the factor 2.8 (averaging the standing wave simply gives a factor of 2, cf. Sec. 4.1). The two sets of data (blue and red circles) have orthogonal polarisations corresponding to the maximum and the minimum induced light shift, But the exact polarisation is not well known. For these input powers, the trapping effect is not yet strong such that the linear scaling is still dominant.

On the other hand, we do observe an influence of the locking light on the cloud compression (Sec. 2.2.7.2). Specifically, with the locking light, the final cloud size after the compression appears to be bigger. In this thesis, most of the cavity data are taken with the science cavity locked with minimum intensity (9 nW in-coupled power). But given the possibility to lock with the auxiliary cavity, we constantly verify that there is no measurable effect of the locking light.

2.3.4 Digital filter cancelling mechanical resonances

2.3.4.1 Feedback model

Having a good PDH signal is only the very first step. The lock is achieved by feeding back the error signal to the piezo actuators through a proportional–integral–derivative (PID) controller. Let us start with a general model of the feedback control. As shown in Fig. 2.26, the control signal (r) is applied to the system through the piezo driver (C), and the system P ("Plant") responds in cavity length x (what we aim to control). P includes the piezo actuation and other mechanical responses. Disturbance d from the environment can enter at this stage, notably vibrations. The cavity length x, however, is not directly accessible. We sense it through the PDH stage S, where measurement noise n can enter. For our discussion below, we shall assume that S does not introduce any delay, but it may be a nonlinear function. We send our error signal x' to the lockbox F and close the feedback loop.

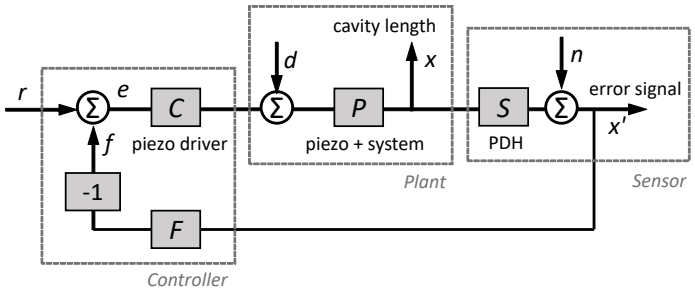

Figure 2.26 Feedback control model.

The closed-loop cavity response x or error signal x' are given by

$$x = \frac{CP}{1+CPSF}r + \frac{P}{1+CPSF}d - \frac{SFCP}{1+CPSF}n \tag{2.27}$$

$$x' = \frac{CPS}{1+CPSF}r + \frac{PS}{1+CPSF}d + \frac{1}{1+CPSF}n \tag{2.28}$$

For simplicity, we will ignore the measurement noise n in the following discussion, so the error signal x' is equivalent to the cavity displacement x up to only a conversion factor S. We shall consider the transfer function (TF) of the plant $\frac{x'}{r} = \frac{CPS}{1+CPSF}$, and the sensitivity function to disturbance $\frac{x'}{d} = \frac{PS}{1+CPSF}$.

The zeros of the denominator $1+CPSF$ determine the stability of the system. Intuitively, unless the gain is sufficiently small, a phase delay of CPF close to π would render the feedback unstable (oscillate). In fact, a resonance in the system P can give such a π phase shift. With a normal PID controller as the lockbox F, the gain has to be attenuated sufficiently before

reaching the very first resonance, meaning a lock bandwidth much lower than the resonance frequency. An ideal solution would be to add a filter in F that perfectly cancels the zeros and poles in P. This cancellation requires a precise determination of P (zeros and poles) and an accurate implementation of the complementary filter.

2.3.4.2 Mechanical resonances of the bridge

An optical cavity generally exhibits resonances of mechanical origin, which can limit lock bandwidth to rather low frequencies. For example, our piezo stacks have a resonance at about 70 kHz. More severely, since the bridge is fixed to the chip at only one end, it basically forms a cantilever, whose flexure modes can be at very low frequencies.

These resonances appear in the power spectrum of the error signal when the cavity is locked. We had to limit the lock bandwidth below 100 Hz by adding low-pass filters to avoid oscillations. So the cavity is essentially free-running above 100 Hz, and the noise power spectrum reflects the magnitude of PS.

But to determine the zeros and poles of P we need the full response. To do this, we use a network analyser: sinusoidal modulations are applied to the piezo (r in Fig. 2.26), and the PDH error signal x' is compared with the modulation. We do have to keep the cavity near resonance to have a meaningful error signal, by applying a slow correction signal to the other piezo. We could only faithfully obtain the open-loop TF of CPS above the bandwidth of this slow lock, which is about 10 Hz. This poses no problem as we are interested in the resonances at kHz frequencies.

As shown in Fig. 2.27, we identify many mechanical resonances, appearing in resonance-antiresonance pairs. Finite elements simulation of the bridge structure confirms that the lowest resonances (2.6 kHz and 10 kHz) indeed originate from the lowest order flexure modes of the bridge (Fig. 2.28). The small resonance at 5.5 kHz is likely due to the fundamental flexure mode in the horizontal direction (simulation not shown). The first resonance at 2.6 kHz has actually very low damping, with its phase shift reaching a full π. It is then not surprising that with a simple PID the bandwidth has to be limited to about only 100 Hz. Nevertheless, by applying a proper filter to compensate the resonances, the lock bandwidth can be greatly improved.

2.3.4.3 IIR filter implemented on Red Pitaya

The resonances and antiresonances can be modelled by poles and zeros in the TF. A filter can be implemented to precisely cancel the zeros with poles of the same values and vice versa. From the measured open-loop TF of CPS, we fit each resonance-antiresonance pair with a complex zero-pole pair (Fig. 2.27). The fit is only perform on the phase, since unlike the magnitude, it is not affected by the nonlinear sensitivity of the PDH error signal (in S). We also verify that the piezo driver[20] (C) is responsible for the overall 2π phase delay (4 poles). Therefore we determine P fairly precisely, which also determines the desired filter.

We are limited to 13 zero-pole pairs due to the hardware (see below). The four poles are not included in the filter.[21] Although these poles limit the feedback to only tens of kHz, it turns out to make the lock more stable, since they filter the un-compensated high-frequency

[20] Piezomechanik SVR 150bip/3

[21] A filter with diverging gain at high frequency is also not desirable.

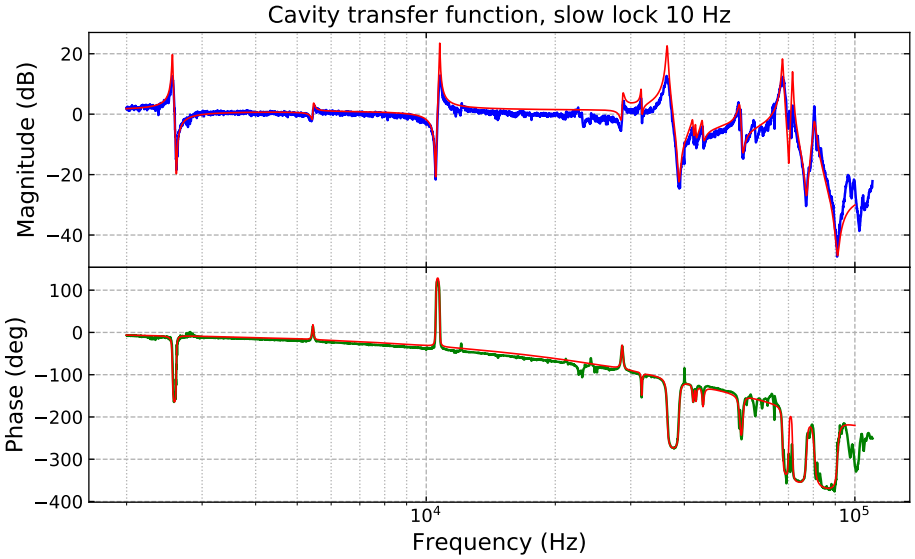

Figure 2.27 Bode plot of cavity response, measured with the network analyser module in Red Pitaya. We have not plotted below 2 kHz since there is no feature and we rather see the loop response of the slow lock. The fitting is performed only on the phase data. The magnitude data has been normalised to meet the model (zero at DC). The model includes 13 complex zero-pole pairs, and 4 real poles to account for the low-pass response of the piezo driver.

resonances which in any case limit the lock bandwidth. In practice, such a highly complex filter can only be implemented digitally. But luckily, an affordable tool has been recently developed.

Red Pitaya and PyRPL package The STEMlab® Red Pitaya is a low-cost field-programmable gate array (FPGA) board with integrated micro-processor as well as ADCs and DACs for fast analog inputs and outputs. It can implement digital oscilloscopes, network analysers, PIDs, filters and other digital signal processing (DSP).

Based on this hardware, a python-package – Python Red Pitaya Lockbox (PyRPL)[22] – has been developed by L. Neuhaus at LKB (and later joined by many others). This platform

[22] https://pyrpl.readthedocs.io/

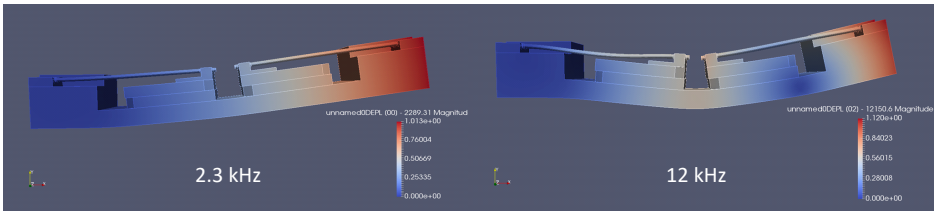

Figure 2.28 Finite elements simulation of the bridge. Shown are two lowest eigenmodes at 2.3 kHz (left) and 12 kHz (right). They most likely correspond to two prominent resonances at 2.6 kHz and 10.5 kHz respectively.

integrates multiple DSP modules (function generators, oscilloscopes, network analysers, IQ modulators, PIDs, filters) that can be interconnected. It is initially designed precisely for PDH locking of optical cavities: an infinite impulse response (IIR) filter is implemented to tackle resonances in the TF. More details about the Red Pitaya hardware and PyRPL architecture can be found in [131].

The IIR filter module simply takes the values of the complex zero-pole pairs obtained from the fit of the TF (limited to 13 zero-pole pairs). It implements a filter (TF with the role of zeros and poles inverted), which can be inserted in the feedback loop, before a normal PID and some low-pass filters.

I shall note that in contrast to IIR filters, finite impulse response (FIR) filters can also implement an arbitrary filter TF. The latter is in principle more versatile and stable, but suffers from a compromise between filter frequency resolution and delay due to the limited FPGA resource. Prior to PyRPL, FIR filters have been implemented using Red Pitaya for cavity locking [132], with a limited bandwidth of 2.8 kHz. The same resource allows to implement IIR filters with sampling frequency up to MHz. A theoretical comparison and the implementation of the IIR filters in the FPGA can also be found in [131].

Lock improvement Finally, the lock is greatly improved with the IIR filter. The power spectral density (PSD) of the closed-loop PDH signal shows reduced noise up to 20 kHz, compared to the system with a slow lock. The latter represents the free running noise above tens of Hz (Fig. 2.29). We shall conclude that the lock bandwidth reaches about 20 kHz, which is almost an order of magnitude above the first resonance. This bandwidth is limited by the maximum 13 zero-pole pairs available in the FPGA. Future improvement in the hardware (e.g. reallocation of resources) should be able to further extend the bandwidth.

We have also tried adding the derivative (usually not used) of the PID and adding a high frequency lock (with a high-pass filter) to lock the laser frequency to the cavity. However, the improvement after some attempts is marginal.

2.3.4.4 Mechanical isolation

After all, all the mechanical resonances show up because they are more susceptible to the mechanical noise from the environment. it is always favourable to reduce noise from its source, through passive noise isolation.

Acoustic noise through air We have identified that the mechanical modes of the cavity are indeed sensitive to sound, by applying a weak audio source at 2.6 kHz and 10 kHz pointing to particular parts of the setup. It turns out that the vacuum system acts as a good antenna (or horn) of acoustic noise: pointing the noise source close to any vacuum part can clearly excite the corresponding mechanical mode of the cavity. Other parts in direct contact with the chip – electric connections and water-cooling hoses – are not clearly susceptible to sound.

Therefore, the acoustic noise in the lab is obviously a noise source, notably the ventilation of numerous instruments and the hum of the air-conditioning. We added an enclosure of the vacuum setup, with partially sound-proof panels and partially PVC curtains (5 mm thick). This also improves the temperature stability of the setup. There is a clear improvement

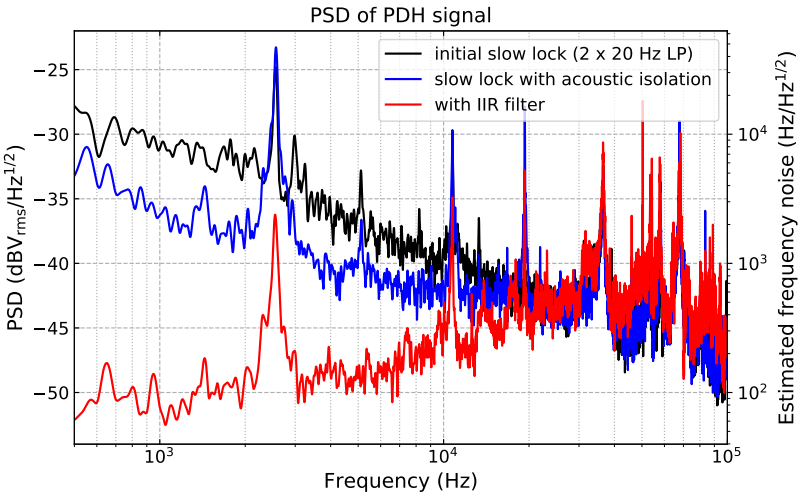

Figure 2.29 Lock improvement with IIR filter. We compare the power spectra of the PDH error signal using a slow lock (black) and a faster one with the IIR filter (red). There is clear improvement up to 20 kHz, showing that the lock bandwidth is extended by one order of magnitude above the first resonance. We also show the noise reduction after the installation of acoustic isolation (blue) with the same slow lock.

with this enclosure (blue over black in Fig. 2.29), although unexpectedly the PSD of the mechanical resonances remains unchanged. This suggests that they are probably not primarily excited by acoustic noise through air.

Vibrations via physical contact Unfortunately, our optical table – three aluminium breadboard stacked – is not good at damping vibrations. One of the remaining vibration source – a ventilation fan in the Andor camera – can in principle propagate noise to the vacuum system through the optical table, although we have not seen a clear impact of this vibration on the noise PSD. This fan can in principle be replaced by water cooling, which could be less noisy.

Another concern is the mechanical shutter of the Andor camera. The shock is so strong that the execution can immediately unlock the cavity. We have to abandon the shutter (keep it open) throughout the experimental cycle.

The water cooling of the chip (through the macro-U block) poses another issue. In fact, we can excite the 2.6 kHz resonance by increasing the water cooling pump speed, hence the flow speed. Luckily, we do not see a clear difference when the pump speed is below 1900 rpm.

2.3.5 Feed-forward targeting the thermal drift

When the experiment is running, the DC currents generating the trap have a strong thermal impact, perturbing the cavity length way beyond the capture range of the lock. The major impact is from the stripline, which runs directly above the bridge. In fact, in a typical experimental cycle, the thermal drift of the cavity resonance, is about 1600 times the cavity linewidth (1560 nm mode).

Nevertheless, this thermal cycle of cavity drift, after running for a few minutes, is

rather reproducible, meaning that we can apply a calibrated feed-forward to compensate it. Fig. 2.30(a) shows the measured cavity drift during one experimental cycle, where we can clearly identify different phases of the sequence. The measurement is done by scanning the cavity length in large range continuously and finding the resonance (transmission peak) with respect to the piezo voltage in each scan. Due to limited time and frequency resolution of the measurement, we perform an interpolation of the data to obtain a smooth feed-forward signal. It turns out that it is more important to avoid abrupt changes in the feed-forward rather than a precise compensation. Because the lock itself can capture some drift but abrupt feed-forward would make the lock oscillate.

With the feed-forward, the residual cavity drift is kept within $\sim$ 20 cavity linewidths, which can be followed by the PDH lock. The cavities can remain locked throughout the sequence, except that the lock is sometimes rendered oscillating for a short period after the sudden switch-off of the stripline current at the beginning of TOF. As the cavity interaction is already over, this brief period of oscillation is not an issue.

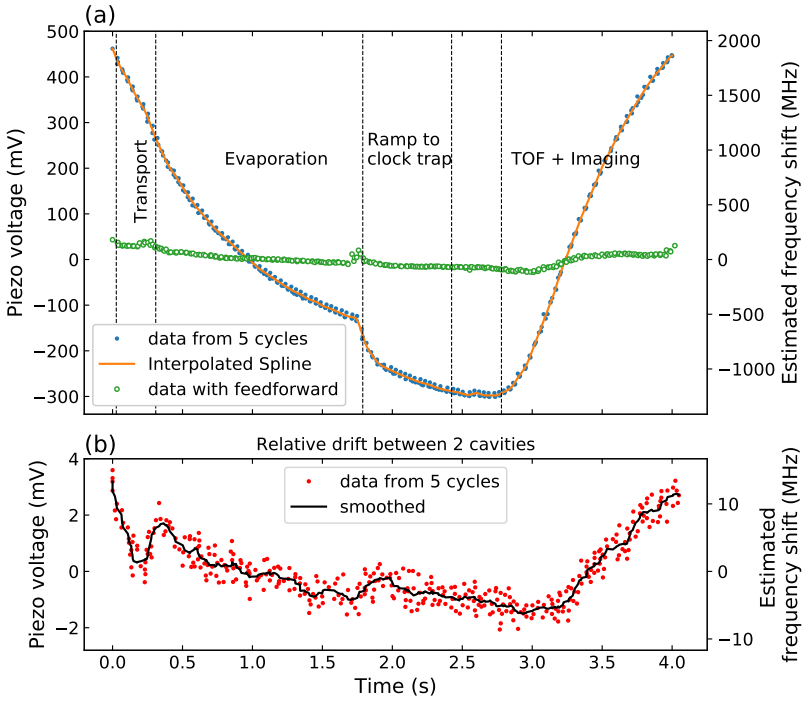

Figure 2.30 (a) Thermal drift of the cavity frequency in one experimental cycle, exceeding $\sim$ 1600$\times$ cavity linewidth. Different phases of the sequence can be clearly identified. With the feed-forward applied, the residual drift (open green circles) is reduced to $\sim$ 20$\times$ cavity linewidth. (b) Relative drift between the two cavities.

2.3.6 Locking "without" light

Relative frequency drift As explained earlier, we have the possibility to stabilise the science cavity by locking only the auxiliary. Although the fix connection works fine at high frequencies, low frequency relative drift in cavity lengths is inevitable.

One can simply imagine that if the two cavities are not perfectly parallel, a given piezo displacement results in a different change in cavity lengths. This is naturally correlated with the thermal deformation of the bridge, as the piezo displaces accordingly to keep the cavity length locked. In a similar measurement, we record both cavity resonances while scanning the piezo in a experimental cycle. The relative drift between the two cavities also follows the thermal cycle of a single cavity (Fig. 2.30(b)). Though seemingly reproducible, a simple feed-forward correction of this relative drift is not sufficient. In fact, there is a slow random drift over $\sim$ 10 MHz in a few seconds, on top of the more deterministic thermal cycle. We do need to correct the cavity length locked through the auxiliary cavity. This is achieved through an additional frequency lock.

Two-cavity "interlock" Let us first recall how the cavities are locked. The PDH signal of the science cavity locks the cavity length to the 1560 nm laser, which is referenced to an absolute frequency. At this particular cavity length (of the science cavity), the auxiliary cavity is detuned 35 GHz from the 1560 nm laser. We use a third-order sideband to bridge this gap.

The relative drift between the two cavities can be corrected via this 35 GHz sideband. More concretely, we can lock both PDH signals of the two cavities simultaneously (Fig. 2.31(a)): the piezo is controlled by the PDH lock of the auxiliary cavity, whose resonance frequency (via the 35 GHz sideband) is controlled by the PDH signal of the science cavity, such that the latter has the correct frequency.

In practice, a precise tuning of about 40 MHz is required on the 35 GHz sideband. While a direct frequency modulation (FM) is not available, we instead reference the synthesiser externally (10 MHz) with a signal from a DDS that can perform analog FM. The PDH error signal of the science cavity then drives this analog FM after a digital PI controller (Fig. 2.31(b)).

With this two-cavity interlock, the PDH signal of the science cavity serves as a "frequency lock" of the auxiliary cavity. We can keep the auxiliary cavity always locked, but turn off the locking light in the science cavity while keeping the frequency lock at the last locked value (via a sample-and-hold circuit, an example is shown in Fig. 2.32). This is a practical scheme for locking the science cavity "without light".

Additional feedback Once the frequency lock is turned off, the science cavity is again subject to the relative drift. But at least we start from the right place. In practice, we would be interested in turning off the locking light only during the critical Ramsey time, to minimise the light shift from the locking light. In fact, with the two-cavity interlock, the relative drift can be precisely assessed by opening the frequency lock but keep tracking of the PDH signal of the science cavity. We observe that during the Ramsey sequence of the experimental cycle, the relative drift is a few MHz in 100 ms.

Nevertheless, we realise that the relative drift is also correlated with the correction applied to the piezo (by the PDH lock of the auxiliary cavity). This can be understood again in the picture with non-parallel cavities: the relative length change is directly related to the piezo displacement. The correction signal to the piezo therefore provides additional information about the drift. We add the piezo correction signal (PDH of the auxiliary cavity) to the correction signal for the frequency lock (PDH of the science cavity) with a properly tuned

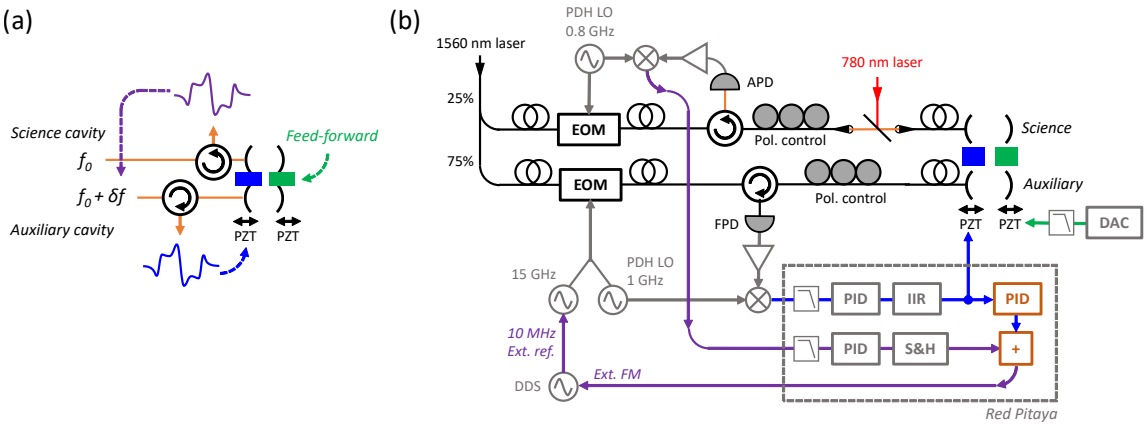

Figure 2.31 Two-cavity interlock setup. (a) shows the simplified schematics of the two-cavity interlock. (b) shows the detailed setup (only the lock part). Electronics are shown in grey, while the PDH signals are in the same colours as in (a). Most of the signal processing is performed by the Red Pitaya board. The additional feedback explained in the text is indicated in orange.

gain (block diagram shown in Fig. 2.31(b)). Note that it plays no role when the two-cavity interlock is on, but starts to correct the relative drift after the frequency lock is open (Fig. 2.32).

The final residual relative drift is in the order of 1 MHz in 100 ms, and appears rather reproducible. In principle this could be further improved by additional feed-forward or calibration.

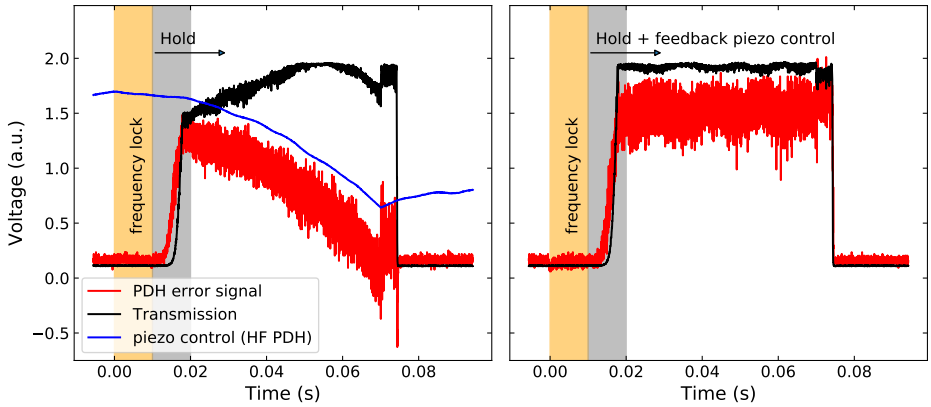

Figure 2.32 Demonstration of additional feedback of the piezo correction signal to the frequency lock. It is actually a sequence used to load atoms in the intra-cavity lattice (Sec. 3.2.4). Here the cavities are locked with the auxiliary cavity and we plot the transmission and the PDH error signal of the science cavity, as well as the piezo control signal – output of the PDH lock of the auxiliary cavity (HF). The two-cavity interlock is active in the orange region for 10 ms, then the frequency lock holds the last value (left panel). After the grey region (during which the 1560 nm power in the science cavity is being ramped up), we see the relative drift from the PDH error signal (red) and the transmission (black). Clearly, the piezo control signal is correlated with the residual drift, meaning that it could be used to correct the drift. With this additional signal applied to the frequency lock (right panel), the residual drift is clearly reduced. While at this timecale (50 ms) the correction seems perfect, we can see residual drift at longer timescale of hundreds of ms. The final kink in the signals is due to a perturbation in the sequence.

Chapter 3

A highly stable cavity-QED platform

TACC-2 is designed to explore spin squeezing at a metrologically relevant level of precision, bridging the gap between the proof-of-principle experiments and real metrological applications. It requires firstly a good clock that reaches or approaches the SQL, and secondly well controlled atom-cavity interactions that generate spin-squeezed states.

In this chapter I will present characterisations of the TACC-2 setup in both aspects. In the first part, we evaluate the clock stability in standard configurations. I will show that we reach a clock instability of $\sim 6 \times 10^{-13}\tau^{-1/2}$ and that QPN contributes a major part. In contrast to a proof-of-principle experiment, our clock at this level already strives (in terms of operation conditions: atom number, Ramsey time, trap parameters, etc.) to balance different noise sources, fundamental and technical, for an optimum stability. In fact, the benefits of using squeezed states not only concern the QPN. They also allow to explore a larger parameter space that would otherwise be barred by the QPN. I will briefly discuss the possible improvement of clock stability using squeezed states.

In the second part, we characterise the atom-cavity interactions from different aspects, starting in the strong-coupling vacuum-Rabi splitting regime. We then focus on the dispersive coupling that realises our cavity measurements of S_z. I also show preliminary results with atoms trapped in the intra-cavity lattice.

3.1 Clock stability analysis

In the context of today's microwave clocks for potential applications, we aim at a short-term stability of few parts 10^{-13}. The previous setup reached a fractional frequency stability of 5.8×10^{-13} at 1 s [50]. TACC-2 differs from its predecessor in several respects. While the dead time is reduced by the 2D-MOT, the trap lifetime is shortened (cf. Fig. 2.4). The added elements on the chip (piezos in particular) are potential sources of stray fields and the more complicated transport scheme may impact atom number and trap stability. Luckily, by understanding the contributions from different noise sources, we managed to find operation conditions that achieve a stability $\sim 6 \times 10^{-13}$.

In this section, we evaluate the clock stability using standard Ramsey sequence with CSSs, but in the situation very close to a future squeezed clock, namely with atoms placed inside the cavity but without cavity interactions. As in [50], I will start with some well-understood noise sources including the detection noise, QPN, the Dick effect and atom

losses. We then discuss the modelling of two of the dominant noise sources – magnetic field and atom temperature – which have complex influences on the choice of trap parameters, temperatures and bottom field. I will be using the Allan deviation (Sec. 1.1.3.1) to quantify the noise throughout this section.

In view of using squeezed states that suppress the QPN, and using cavity detection that reduces the detection noise, I will discuss how the parameter space (e.g. Ramey time) can be further expanded compared to the classical situation.

3.1.1 Detection noise

In the detection of a clock sequence, the transition probability $P_\uparrow \equiv N_\uparrow/(N_\uparrow+N_\downarrow)$ is measured to obtain the clock frequency. The determination of $P_\uparrow$ is degraded by the detection noise of absorption imaging and the QPN. As we know, the QPN contributes to the noise in $P_\uparrow$ (standard deviation $\sigma_{P_\uparrow}$) as $\sigma_{P_\uparrow,\mathrm{qpn}} = 1/(2\sqrt{N})$, where $N = N_\uparrow + N_\downarrow$.

As discussed in Sec. 2.2.7.2, the detection noise of absorption imaging is limited by optical fringes and shot noise of the photoelectrons. For a given imaging intensity $\sim I_{\mathrm{sat}}$, the detection noise is roughly a compromise between the minimum number of pixels and the saturation of the CCD. We define the detection noise σ_{det} as the standard deviation in atom number of each state, assuming the same for $N_\uparrow$ and $N_\downarrow$. This gives a noise in $P_\uparrow$:

$$\sigma_{P_\uparrow,\mathrm{det}} = \frac{\sigma_{\mathrm{det}}}{\sqrt{2}N} \tag{3.1}$$

$P_\uparrow$ is also affected by the technical noise in the state preparation (e.g. the power fluctuation of the MW) or in the detection (e.g. the fluctuation in detection efficiencies of the two states). In a calibration measurement where we detect right after a $\pi/2$ pulse, the three noise sources can be separately quantified as they have different scalings as a function of the atom number. Shown in Fig. 3.1(c), we fit the data by

$$\sigma^2_{P_\uparrow} = \frac{\sigma^2_{\mathrm{det}}}{2N^2} + \frac{1}{4N} + \sigma^2_{\mathrm{tech}} \tag{3.2}$$

Note that the technical noise does not depend on the atom number. In this imaging configuration,[1] we obtain a $\sigma_{\mathrm{det}} = 86 \pm 15$ – and for a simpler comparison between different configurations – 2.5 atoms per pixel. The technical noise is below 10^{-3} (in $\sigma_{P_\uparrow}$) and not visible from these data.

In terms of contributions to the fractional frequency Allan deviation of the clock (our figure of merit), the detection noise and the QPN read, respectively

$$\sigma_{y,\mathrm{det}}(\tau) = \frac{\sigma_{\mathrm{det}}}{\sqrt{2}N\nu_{\mathrm{at}}}\left|\frac{\mathrm{d}P_\uparrow}{\mathrm{d}\nu}\right|^{-1}\sqrt{\frac{T_c}{\tau}} = \frac{\sigma_{\mathrm{det}}}{\sqrt{2}\pi\nu_{\mathrm{at}}NT_{\mathrm{R}}\mathcal{C}}\sqrt{\frac{T_c}{\tau}} \tag{3.3}$$

$$\sigma_{y,\mathrm{qpn}}(\tau) = \frac{1}{2\pi\nu_{\mathrm{at}}\sqrt{N}T_{\mathrm{R}}\mathcal{C}}\sqrt{\frac{T_c}{\tau}} \tag{3.4}$$

where ν_{at} is the clock frequency, and $|\mathrm{d}P_\uparrow/\mathrm{d}\nu|$ the sensitivity of the Ramsey fringes given by T_{R} and contrast $\mathcal{C}$ (Eq. 1.9). Note that here N is the detected final atom number in the presence of atom losses.

[1] This particular measurement is performed with imaging along $\vec{x}$, but only the magnification and number of pixels matter.

We can also quantify $\sigma_{y,\mathrm{det}}$ of a real clock measurement (Fig. 3.1(b)). Specifically, we run a Ramsey sequence with $T_\mathrm{R} = 3$ s, except that the second $\pi/2$ pulse is not applied. The contrast of the Ramsey fringes is 0.82 in the same condition. We can then separate the detection noise from the theoretical QPN, assuming an independent sum. Here we obtain $\sigma_\mathrm{det} = 48.2$ atoms, corresponding to 2.2 atoms per pixel.

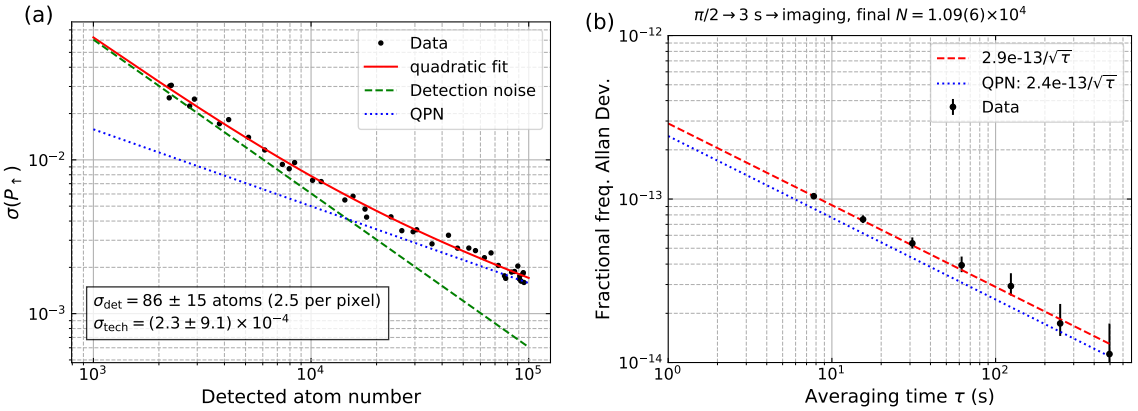

Figure 3.1 (a) Noise in $P_\uparrow$ as a function of atom number. Different scalings from detection noise and QPN can be identified and a fit gives a detection noise of 86 atoms and 2.5 atoms per pixel (b) Allan deviation of the total detection noise in the same condition as a typical clock evaluation. Knowing the atom number, we can extract the detection noise. From the ratio we deduce a detection noise of 48.2 atoms and 2.2 atoms per pixel.

Speaking about Ramsey fringe contrast and coherence, TACC-1 has demonstrated exceptionally long coherence time of almost 1 min thanks to atomic interactions [48]. Although the high density (10^{12} cm^{-3}) in that experiment is not always preferable for a clock, we do have in general very low dephasing rate close to the optimum field (see below). The contrast is normally between 0.8 to 0.9 at $T_\mathrm{R} = 3$ s. It is worth noting that for the densities ($\sim 10^{11}$ cm^{-3}) used in the clock measurements in this section, the contrast has a clear dependence on the density (trap frequencies, atom number and temperature). But more importantly, as we will see later, the deviation of the trap bottom field B_0 from the magic field B_m ($\Delta B \equiv B_0 - B_m$) determines the inhomogeneity of the Zeeman shift hence the decoherence. Fig. 3.2 shows two examples of the decoherence over time. As we will be working at shorter Ramsey times for reasons that will become clear, the contrast drop has little degradation on the clock sensitivity.

3.1.2 Dick effect

As I briefly explained in Sec. 1.1.3.3, the Dick effect is an aliasing effect of the periodic (non-continuous) sampling of the atomic frequency due to the dead time T_dead of the experimental cycle. As a result, the clock stability is also subject to the high-frequency phase noise of the LO close to multiples of the sampling frequency $1/T_c$, where $T_c = T_\mathrm{dead} + T_\mathrm{R}$ is the cycle time. The degradation of the stability can be calculated using the sensitivity function $g(t)$ (Eq. 1.21) in the Fourier space [76]:

$$\sigma^2_{y,\mathrm{Dick}}(\tau) = \frac{1}{\tau}\sum_{n=1}^{\infty}\left(\frac{g_n}{g_0}\right)^2 S_y^f\left(\frac{n}{T_c}\right) \tag{3.5}$$

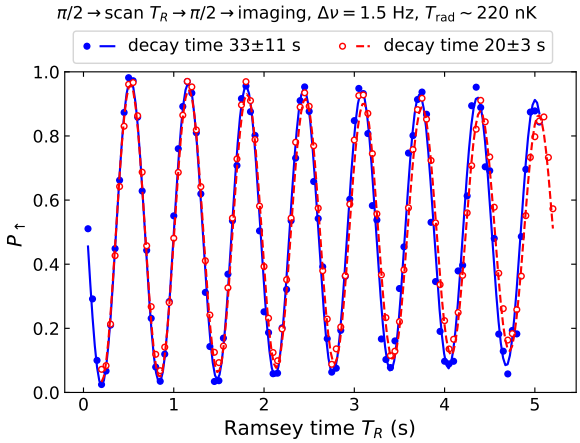

Figure 3.2 Ramsey fringes in time domain, showing the coherence of the system. The LO is strongly detuned (1.5 Hz) to see fringes as a function of T_{R}. Two sets of data are for two slightly different traps: $\{\omega_x, \omega_y, \omega_z\} \simeq 2\pi \cdot \{5, 97, 84\}$ Hz at $\Delta B = -40$ mG (solid blue) and $\sim \{3, 110, 99\}$ Hz , $\Delta B = -30$ mG (open red). The latter is used for clock measurements in this section. The difference in ΔB is the main cause of the different decay times.

where g_n is the Fourier component at nth sampling frequency:

$$g_n = \frac{1}{T_c} \int_{-T_c/2}^{T_c/2} g(t) \cos\left(\frac{2\pi n t}{T_c}\right) \mathrm{d}t \tag{3.6}$$

The PSD of the LO fractional frequency noise $S_y^f(f)$ is obtained from the phase noise of the MW source $S_\phi(f)$, as in [50]:

$$S_y^f(f) = f^2 S_\phi(f) / \nu_{\mathrm{mw}}^2 \tag{3.7}$$

where $\nu_{\mathrm{mw}} = 6.834$ GHz is the MW frequency. Fig. 3.3 shows the coefficients $(g_n/g_0)^2$ (circles) and S_y^f (black curves). Intuitively, the Dick coefficients are only non-negligible between $1/T_c \sim 0.1$ Hz and $1/\tau_p \sim 10$ Hz. Here we compare the operation conditions of TACC-2 and TACC-1. Thanks to the fast loading from a 2D-MOT, the dead time has been reduced from 11 s to 5 s. Despite the reduced Ramsey time due to limited atom lifetime (here we set $T_{\mathrm{R}} = 2$ s), the duty cycle has been improved in TACC-2, which pushes the Dick coefficients towards higher frequencies where the LO noise is smaller (0.1 Hz to 10 Hz). We obtain a $\sigma_{y,\mathrm{Dick}} = 2.1 \times 10^{-13} \tau^{-1/2}$ ($T_{\mathrm{R}} = 2$ s). This is still one of the major contributions to the clock instability.

3.1.3 Atom number fluctuation

Due to the relatively high density in a trapped-atom clock, the collisional shift compromises the clock stability through atom number fluctuation. However, as the total atom number is measured in each cycle, this collisional shift fluctuation can be corrected, based on the linear correlation k (μHz/atom) between the shift and detected atom number.

k can be understood from the ensemble average (Maxwell-Boltzmann) of the collisional

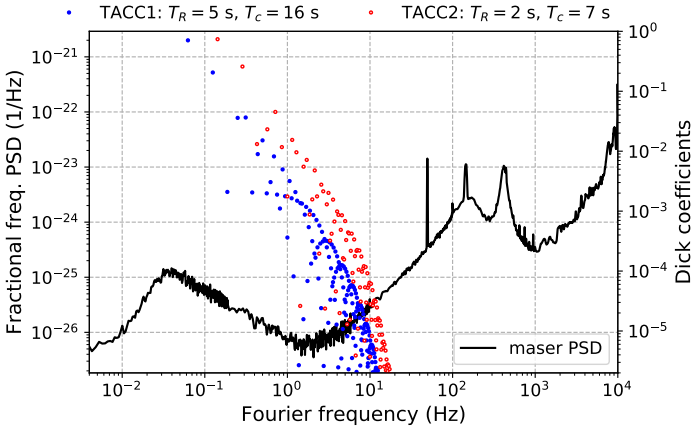

Figure 3.3 Calculated Dick coefficients and the noise power spectrum of the LO (maser), converted in fractional frequency. Maser data from [50].

shift (Eq. 1.13), assuming $N_\uparrow = N_\downarrow$:

$$\overline{\Delta\nu_{\mathrm{mf}}} = -\overline{N}\frac{\hbar\left(a_{\downarrow\downarrow} - a_{\uparrow\uparrow}\right)\sqrt{m}\omega_x\omega_y\omega_z}{4\left(\pi k_{\mathrm{B}}\right)^{3/2}\sqrt{T_x T_\perp^2}} \equiv \overline{k}\cdot\overline{N} \tag{3.8}$$

where we distinguish anisotropic temperatures T_x and $T_y = T_z = T_\perp$. We have used the temporal-average atom number during the Ramsey time in the presence of atom loss:

$$\overline{N} = \frac{1}{T_{\mathrm{R}}}\int_0^{T_{\mathrm{R}}} N_{\mathrm{i}} e^{-\gamma t} dt = N_{\mathrm{i}}\frac{1 - e^{-\gamma T_{\mathrm{R}}}}{\gamma T_{\mathrm{R}}} = N_{\mathrm{f}}\frac{e^{\gamma T_{\mathrm{R}}} - 1}{\gamma T_{\mathrm{R}}} \tag{3.9}$$

where N_{i} and N_{f} are the initial and final atom numbers respectively. For example, for $T_{\mathrm{R}} = 2$ s and the atom loss rate $\gamma = 2.7\ \mathrm{s}^{-1}$, $\overline{N} \approx 1.48 N_{\mathrm{f}}$. We then obtain an expression for k:

$$k = \frac{\overline{\Delta\nu_{\mathrm{mf}}}}{N_{\mathrm{f}}} = \overline{k}\cdot\frac{e^{\gamma T_{\mathrm{R}}} - 1}{\gamma T_{\mathrm{R}}} \tag{3.10}$$

This atom number correction is not perfect due to two reasons. Firstly, the measured atom number suffers from the detection noise. It contributes to the instability as

$$\sigma_y^k(\tau) = \frac{\sqrt{2}\sigma_{\mathrm{det}}\,|k|}{\nu_{\mathrm{at}}}\sqrt{\frac{T_c}{\tau}} \tag{3.11}$$

Note that it is not explicitly dependent on N_{i}. But it does depend on the atomic density therefore is affected by the atom number.

The second imperfection originates from the statistical nature of the atom loss, i.e., only knowing N_{f}, there is always uncertainty in the atom number that have contributed to the density shift during the Ramsey time. It can be shown that the average atom number uncertainty given N_{f} can be estimated as [50]:

$$\overline{\sigma_N} \simeq \frac{1}{T_{\mathrm{R}}}\int_0^{T_{\mathrm{R}}} \sqrt{N_{\mathrm{f}}(e^{\gamma(T_{\mathrm{R}}-t)} - 1)e^{\gamma(T_{\mathrm{R}}-t)}}\ \mathrm{d}t \tag{3.12}$$

The degradation to the stability then reads

$$\sigma_{y,\mathrm{loss}}(\tau) = \frac{\overline{\sigma_N}|\overline{k}|}{\nu_{\mathrm{at}}}\sqrt{\frac{T_c}{\tau}} \tag{3.13}$$

B-field independent instabilities and Ramsey time Up to now we have discussed a few noise sources that are weakly dependent on ΔB.[2] It is already helpful to see how they behave in the parameter space including Ramsey time, atom number, etc. Here we show calculations of these instabilities as a function of Ramsey time with two different initial atom numbers (Fig. 3.4). We use the experimental parameters: trap lifetime 2.7 s, 5 s dead time, trap frequencies $\{\omega_x, \omega_y, \omega_z\} \simeq 2\pi \cdot \{3, 110, 99\}$ Hz, and realistic temperatures (transversely $T_\perp = 220$ nK, and longitudinally much colder, $T_x = 20$ nK).

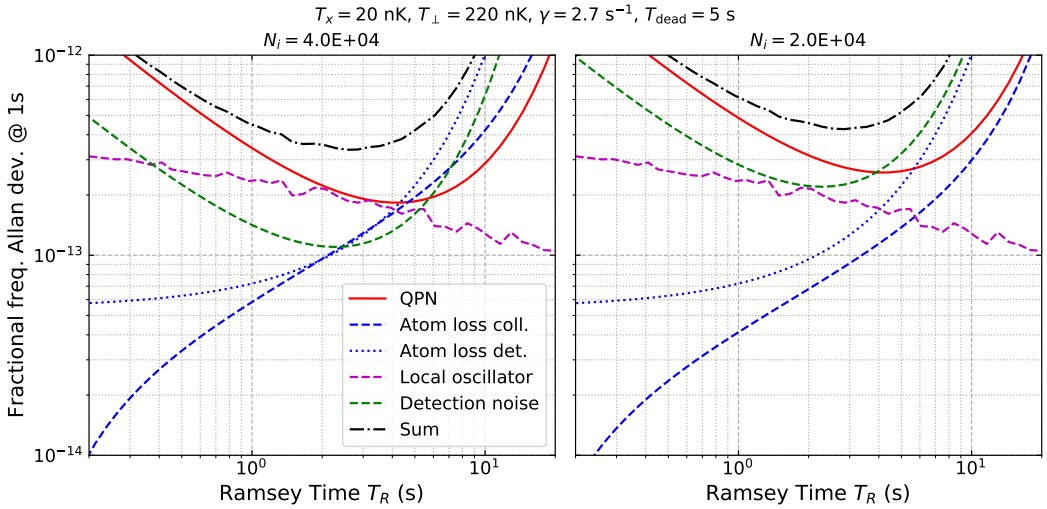

Figure 3.4 Estimations of noise sources that are weakly-dependent or independent of B-field as a function of Ramsey time. Here we show two initial atom numbers for comparison: 4×10^4 (left) and 2×10^4 (right). Trap frequencies are $\{3, 110, 99\}$ Hz. Here we assume a perfect contrast.

Let us have a closer look:

- The Dick effect (dashed magenta) is independent of N and reduces as T_{R} increases due to improved duty cycle.
- The detection noise (dashed green) and QPN (solid red) both grow at short T_{R} due to reduced sensitivity $|\mathrm{d}P_\uparrow/\mathrm{d}\nu| = \pi T_{\mathrm{R}}\mathcal{C}$. They also increase at long T_{R} simply because of the reduced detected atom number due to losses. Obviously, larger numbers of atoms are beneficial.
- The two sources related to atom number fluctuation (blue curves) both grow at longer T_{R}, while σ_y^k (dotted) is due to the increasing value of k from atom loss, and $\sigma_{y,\mathrm{loss}}$ is

[2] The contrast depends on ΔB, having a slight influence on $\sigma_{y,\mathrm{det}}$ and $\sigma_{y,\mathrm{qpn}}$. Due to atom-number-dependent temperature (Sec. 2.2.3), k can also depend on ΔB as we also have to account for the Zeeman shift which is temperature dependent.

due to the growing uncertainty in the atom number. As I pointed out, the former does not depend on N. But for the latter, larger numbers of atoms actually have higher fluctuations due to the stronger collisional shift.

The sum of these noise sources shows a clear optimum Ramsey time, close to the trap lifetime. Therefore, our trap lifetime of 2.7 s limits the Ramsey time below 3 s. However, if we can instead use spin squeezed state with cavity detection, we can in principle greatly suppress the contributions from the QPN, detection noise and even partly σ_y^k. We would then be able to increase T_R to reduce the Dick effect. Remarkably, lower atom number would appear preferable as the collisional shift is alleviated.

We will have later a quantitative estimation. Now we shall turn to the other major noise sources which are dependent on the B-field.

3.1.4 Magnetic and temperature fluctuations

As we have seen in Sec. 1.1.2.2, a pseudo-magic trap with Zeeman shift and density shift mutually compensated is possible if one shifts the bottom field slightly below the magic field $\Delta B \lesssim 0$. However, away from the magic field, the Zeeman shift is more sensitive to the technical fluctuations of the bottom field. On the other hand, temperature fluctuations affect the density distribution that influences both the Zeeman shift and the density shift. As we will see, the temperature dependence exhibits a minimum at certain field ΔB^T_opt such that the clock frequency is first-order insensitive to temperature fluctuation.

We again follow the treatment in [50], but extend to anisotropic temperatures. However, as we will consider the noise due to temperature fluctuations, it is more reasonable to suppose that these fluctuations are correlated among different axes. We will then distinguish the transverse temperature $T_y = T_z = T_\perp$ and a lower but correlated $T_x = \zeta T_\perp$.

Taking ensemble average (Maxwell-Boltzmann distribution) of the Zeeman shift (Eq. 1.11), we have

$$\overline{\Delta\nu_B} = \frac{b}{\mu_\mathrm{B}^2}\left(\frac{4g^2 m k_\mathrm{B} T_\perp}{\omega_z^2} + k_\mathrm{B}^2(8T_\perp^2 + 4T_\perp T_x + 3T_x^2) + 2\mu_\mathrm{B}\Delta B k_\mathrm{B}(2T_\perp + T_x) + \Delta B^2\mu_\mathrm{B}^2\right) \tag{3.14}$$

We will consider the total shift $\overline{\Delta\nu_B} + \overline{\Delta\nu_\mathrm{mf}}$. The optimal field as a function of ΔB is given by solving $\partial(\overline{\Delta\nu_B} + \overline{\Delta\nu_\mathrm{mf}})/\partial\Delta B = 0$:

$$\Delta B^B_\mathrm{opt} = -\frac{k_\mathrm{B} T_\perp(2+\zeta)}{\mu_\mathrm{B}} \tag{3.15}$$

which is generally very close to the magic field. For example, for $T_\perp = 200$ nK and $\zeta \sim 0.2$, $\Delta B^B_\mathrm{opt} \simeq 6.6$ mG. Supposing that the operating ΔB will not be far from this field, we can model the clock frequency fluctuation due to the technical magnetic field fluctuation σ_B as

$$\sigma_{y,B} = \frac{2b}{\nu_\mathrm{at}}\left|\Delta B - \Delta B^B_\mathrm{opt}\right|\sigma_B \tag{3.16}$$

For the temperature fluctuation, solving $\partial(\overline{\Delta\nu_B} + \overline{\Delta\nu_\mathrm{mf}})/\partial\, T_\perp = 0$ gives

$$\Delta B^T_\mathrm{opt} = -\frac{k_\mathrm{B} T_\perp(8 + 4\zeta + 3\zeta^2) + \frac{2g^2 m}{\omega_z^2}}{\mu_\mathrm{B}(2+\zeta)} - \frac{3\hbar\overline{N}\,(a_{\downarrow\downarrow} - a_{\uparrow\uparrow})\sqrt{m}\mu_\mathrm{B}\omega_x\omega_y\omega_z}{16b\pi^{3/2}\,(k_\mathrm{B}T_\perp)^{5/2}\,(2+\zeta)\sqrt{\zeta}} \tag{3.17}$$

Similarly, the frequency fluctuation due to temperature fluctuation σ_T can be modelled as

$$\sigma_{y,T} = \frac{2k_{\mathrm{B}}b(2+\zeta)}{\mu_{\mathrm{B}}\nu_{\mathrm{at}}} \left|\Delta B - \Delta B^T_{\mathrm{opt}}\right| \sigma_T \tag{3.18}$$

$\delta B^T_{\mathrm{opt}}$ deserves more attention. Firstly, $\delta B^T_{\mathrm{opt}} < \delta B^B_{\mathrm{opt}}$, so a compromise has to be found between the magnetic field fluctuation and temperature fluctuation. Obviously, given a technically limited σ_B and σ_T, one should try to bring $\delta B^T_{\mathrm{opt}}$ closer to $\delta B^B_{\mathrm{opt}}$, namely minimising $|\delta B^T_{\mathrm{opt}}|$.

3.1.4.1 Trap frequencies

Eq. 3.17 involves the temperatures and atom number from the density shift in the second term, but also involves ω_z due to the gravitational sag. if ω_z is low, the first term grows quickly (in absolute value). But if all trap frequencies are high, the second term will dominate due to high density. It hence justifies tight transverse confinement to counteract the gravitational sag, but shallow longitudinally to lower the density. Fig. 3.5 shows a few example calculations of $\delta B^T_{\mathrm{opt}}$ as a function of ω_z and of $T_\perp$. We fix $\omega_x/2\pi = 3$ Hz, which is the lowest for a stable trap, and set realistically $\omega_y = 1.1 \times \omega_z$. We also assume $\zeta = 0.2$. We see that at lower temperatures, a clear optimal trap frequency exists, but the minimum $|\delta B^T_{\mathrm{opt}}|$ is not globally optimum. At higher temperatures, $|\delta B^T_{\mathrm{opt}}|$ reduces at higher trap frequencies. In the experiment, $\omega_z/2\pi = 160$ Hz is achievable, but we have not yet explored those frequencies. We have seen again the limits imposed by the density in our clock.

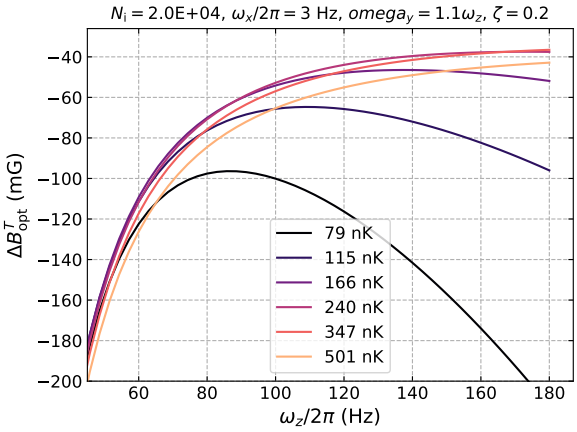

Figure 3.5 $\delta B^T_{\mathrm{opt}}$ as a function of ω_z for different temperatures. The assumption $\zeta = 0.2$ is probably not always realistic as the temperature varies.

3.1.4.2 Optimum magnetic field

With the two optimum fields against magnetic field fluctuation and temperature fluctuation respectively, an overall optimum field should be found in between, depending on σ_B and σ_T. Assuming that these noise sources are uncorrelated, we can then use the measured stability at different magnetic field to estimate σ_B and σ_T altogether.

Fig. 3.6 shows three datasets of clock stability ($T_R = 3$ s) as a function of ΔB at different temperatures. As we have seen that ΔB^T_{opt} depends on $T_\perp$ and T_x, the optimum field for the clock will be different at different temperatures. Indeed we observe such temperature dependence. We try to fit the data with all noise sources discussed above, leaving σ_B, σ_T and ζ as free parameters. The three datasets cannot fit with a single set of parameters but require very different ζ's. This reflects the limitation of the model assuming fully correlated $T_\perp$ and T_x. We plot instead the independent fit for data at each temperature. We see that at lower temperature (100 nK, solid black circles), the model requires a very small ζ to increase the density shift, since the overall noise is high. On the contrary, at higher temperature (290 nK, open red circles) the overall instability is very close to the "independent noise" (dotted curve, the dependence comes from the contrast). The model then requires an almost isotropic temperature to minimise the noise due to magnetic and temperature fluctuations. The contrast of the Ramsey fringes has a different dependence on ΔB, which we will discuss briefly in the following.

Obviously, a more refined model is needed to fully understand the temperature dependence. Nevertheless, the three fits actually give similar $\sigma_B \sim 30$ μG and $\sigma_T \sim 0.5\%$ $T_\perp$. The former is a bit higher than the one reported in TACC-1 (16 μG), analysed using a similar model [50]. It is also clear from these measurements that a cold cloud is not at all beneficial for the clock. In the end, a high density is detrimental, eventually also limiting the atom number.

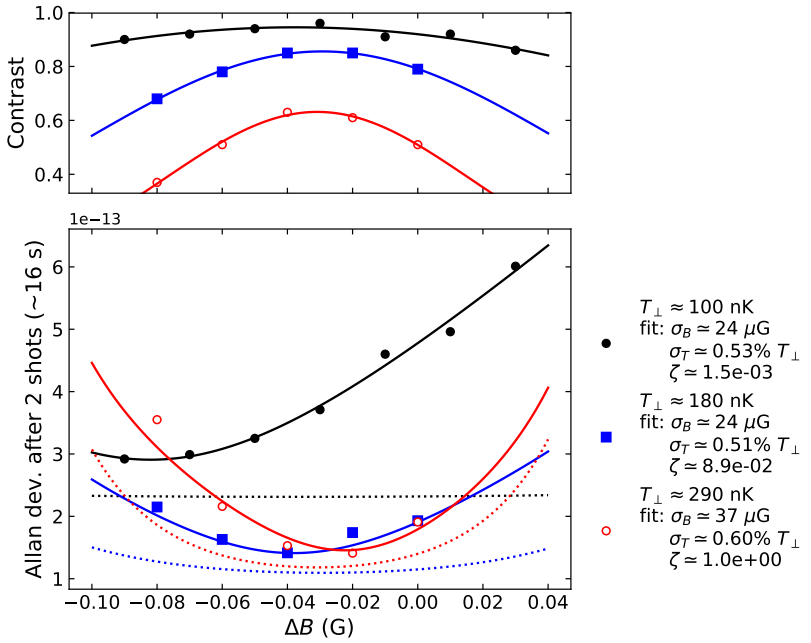

Figure 3.6 Clock stability at different magnetic fields. $T_R = 3$ s. The fringe contrast is shown on the top and the fractional frequency Allan deviations in the bottom at three different temperatures. The Allan deviations are not extrapolation to 1 s, but after 2 shots.[3] The solid curves in the top panel are fits to Eq. 3.22, while those in the bottom are fits to the full noise model with free parameters σ_B, σ_T and ζ. Dotted curves are noise contributions apart from the magnetic field and temperature fluctuation.

3.1.5 Ramsey Contrast

Let us have another look at the contrast, as a function of magnetic field. The above analyses consider the mean shift $\overline{\Delta\nu_B} + \overline{\Delta\nu_{\mathrm{mf}}}$, subject to shot-to-shot magnetic field and temperature fluctuations. However, the contrast concerns the inhomogeneity of the frequency shift during a Ramsey sequence.

A quantitatively understanding of the contrast is not easy. Firstly, the inhomogeneity is a result of both Zeeman shift and density shift upon motional averaging. Secondly, collisional spin exchange, namely the ISRE, will counteract the dephasing among atoms, extending the coherence.

For simplicity, here I only briefly discuss the inhomogeneity of the Zeeman shift, which dominantly determines the optimum ΔB (again $\Delta B \lesssim 0$). Density shift further lowers this optimum slightly, but the spin exchange effect counteracts both shifts. We will discuss the spin exchange effect a bit more in detail in Sec. 5.1.

We have been considering the position dependent $\Delta\nu_B(\boldsymbol{r})$ and $\Delta\nu_{\mathrm{mf}}(\boldsymbol{r})$ and their ensemble average. But as the atoms oscillate in the trap, the position dependence averages out. Since the lateral collision rate is low ($\sim 0.2\ \mathrm{s}^{-1}$), each atom preserves its energy over the oscillations. The average frequency shift of an atom then only depends on its energy. We can then express $\Delta\nu_B$ as a function of energy (a more detailed demonstration will be given in Sec. 5.1.4) and the inhomogeneity can be obtained from the ensemble average in the energy space:

$$\langle f \rangle \equiv \int_0^\infty \mathrm{d}E_x \int_0^\infty \mathrm{d}E_y \int_0^\infty \mathrm{d}E_z f e^{-E_x/k_\mathrm{B}T_x} e^{-E_y/k_\mathrm{B}T_y} e^{-E_z/k_\mathrm{B}T_z} \tag{3.19}$$

We quantify the dephasing using the standard deviation of the Zeeman shift:

$$\sigma(\overline{\Delta\nu_B}) = \sqrt{\left\langle \overline{\Delta\nu_B}^2 \right\rangle - \left\langle \overline{\Delta\nu_B} \right\rangle^2} \tag{3.20}$$

which takes the form

$$\sigma^2(\overline{\Delta\nu_B}) = \mathcal{A}(\Delta B - \Delta B_0^{\mathcal{C}})^2 + \mathcal{D} \tag{3.21}$$

For simplicity I will not show the analytic form of $\mathcal{A}$ and $\mathcal{D}$ as it is not a full model. But this asymptotic form remains valid in the presence of density shift and it agrees with the data (Fig. 3.7). The contrast can be estimated as (assuming a Gaussian distribution of phase shift with width $\sigma\left(\overline{\Delta\nu_B}\right)$)

$$\mathcal{C} = \exp\left[-\frac{\sigma^2(\overline{\Delta\nu_B})}{2}\right] = e^{-\mathcal{D}/2} \exp[-\frac{\mathcal{A}}{2}(\Delta B - \Delta B_0^{\mathcal{C}})] \tag{3.22}$$

The minimum inhomogeneity (maximum contrast) is reached at the field

$$\Delta B_0^{\mathcal{C}} = -\frac{k_\mathrm{B}T_\perp(8 + 2\zeta + 2\zeta^2 + 3\zeta^3) + \frac{2g^2 m}{\omega_z^2}}{\mu_\mathrm{B}(2 + \zeta^2)} \tag{3.23}$$

However, this theoretical optimum is lower than what we measured. For the data shown in Fig. 3.7, $T_\perp \simeq 220$ nK, Eq. 3.23 gives $\Delta B_0^{\mathcal{C}} \simeq -51$ mG, but the data show an optimum at

[3] The noise does not scale as $\tau^{-1/2}$ in some conditions. We then focus on the short term stability, but the shot-to-shot data is biased as we toggle the LO frequency every other shot to probe both sides of the half-fringe, to be insensitive to certain technical drifts.

$\Delta B = -35.7$ mG. The density shift can only further lowered this optimum. The discrepancy can be related to the spin exchange effect.

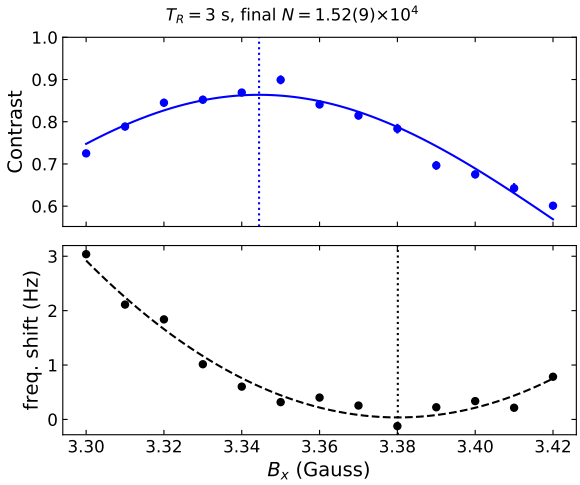

Figure 3.7 Ramsey fringe contrast as a function of bottom field (top). The clock frequencies (bottom) show the quadratic Zeeman shift (dashed black curve: quadratic fit). The solid blue curve is a fit to Eq. 3.22, showing the optimum field at $\Delta B = -35.7$ mG.

3.1.6 Preliminary stability results

Here I present two best examples from the preliminary clock stability measurements, exploring different Ramsey times. We achieve a fractional frequency stability of $5.2 \times 10^{-13}\tau^{-1/2}$ at $T_\mathrm{R} = 3$ s and $6.5 \times 10^{-13}\tau^{-1/2}$ at $T_\mathrm{R} = 1$ s, shown respectively in Fig. 3.8 and Fig. 3.9. As it is clear from Fig. 3.4, QPN and detection have bigger contributions at shorter Ramsey times.

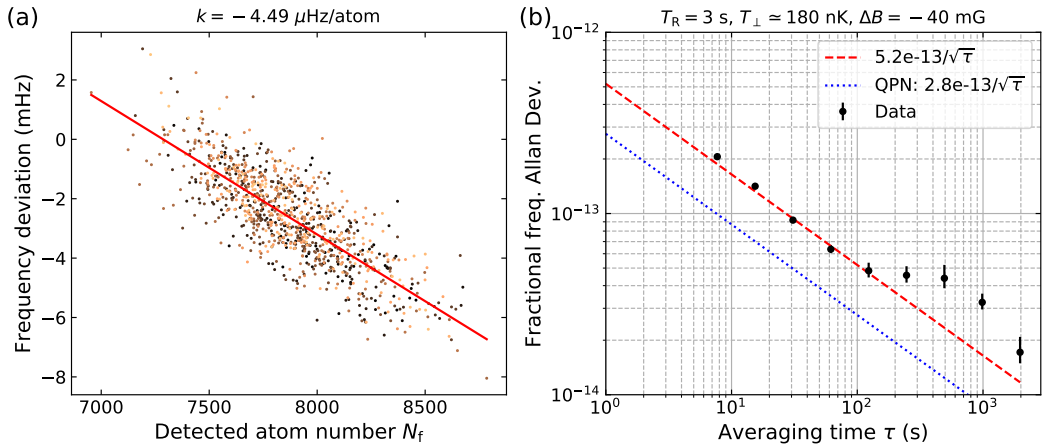

Figure 3.8 One of the best clock stability results at $T_\mathrm{R} = 3$ s (b). The atom number-clock shift correlation (k) is shown in (a), used for atom number correction. Initial atom number $N_\mathrm{i} \simeq 2.5 \times 10^4$. The density (atom number and temperature, reflected in k) and ΔB are all important to optimise the overall stability.

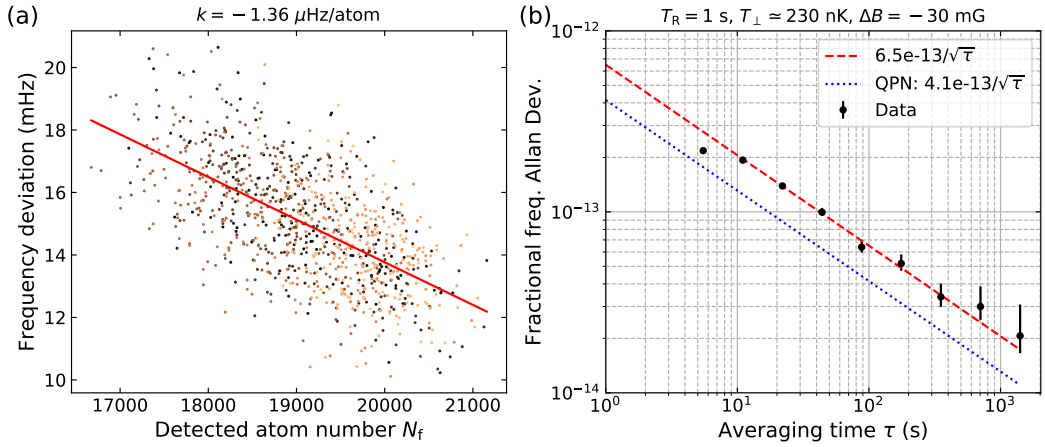

Figure 3.9 One of the best clock stability results at $T_R = 1$ s (b). The atom number-clock shift correlation (k) is shown in (a), used for atom number correction. Initial atom number $N_i \simeq 2.7 \times 10^4$. Here k is smaller due to less atom loss for the shorter T_R. The QPN alone contributes nearly half of the noise.

3.1.7 Prospects with spin-squeezed states

Finally, let us see how spin squeezing and cavity detection can help for the current setup. We again show all noise contributions from our model in Fig. 3.10 (left panel), using the parameters of the best measurement (Fig. 3.8). σ_B, σ_T and ζ are from the fit described previously.

In the right panel, we show the calculations using spin-squeezed states and cavity detection. In fact, for spin squeezing by cavity measurements that will be focused on in the rest of the thesis, the atoms are not projected and the noise in S_z ($P_\uparrow$) is limited by the cavity detection noise. Therefore we assume a cavity detection noise $\sigma_{\rm det} = 25$ atoms that corresponds to a squeezing about 12 dB for 2.5×10^4 atoms. We have also assumed that the total atom number can be measured by the cavity shift at the end of the clock cycle, reducing the error in atom number correction (k). Spin squeezing also allows us to increase the atom temperature that alleviates both the uncertainty due to collisional shift and the contributions from magnetic and temperature fluctuations. Slightly increasing the temperature to $T_\perp = 250$ nK, we can have an overall improvement of the clock stability from $5.7 \times 10^{-13}\tau^{-1/2}$ (from model) to $4.2 \times 10^{-13}\tau^{-1/2}$. Now the dominant noise sources are purely technical.

In fact, as I mentioned in the introduction, cavity QND measurements are more powerful than creating spin-squeezed states. In a more advanced sequence, one can envisage measuring the total atom number both at the beginning and at the end of the clock cycle. The uncertainty in the collisional shift can be further reduced. Moreover, one can perform a few short (complete) Ramsey sequences with the same atoms using QND measurements (already done in [104] and more advanced, phase coherent sequences in [56]). Without compromising the duty cycle, the Dick effect can be reduced.

Technical improvements The overall clock stability is largely determined by technical noise that limit the benefits from spin squeezing. However, as we have seen, using squeezed

states enlarges the parameter space which we can explore so that overall clock improvement is possible with the current setup. Nevertheless, improvements of the dominant technical noise sources are within reach:

- The LO noise can be reduced by further reduce the dead time, as increasing T_{R} is not an option facing atom losses.
- The magnetic field fluctuation can be improved by improving our current sources, especially the one for the weak confinement (as we discussed in Sec. 2.1.4).
- We also know that the temperature has an atom-number dependence (Fig. 2.11), therefore total atom number fluctuation directly contributes to temperature fluctuation. This dependence may be weaken by an improved evaporative cooling and trap decompression process. The atom number fluctuation can also be improved by e.g. introducing a well engineered loss channel.

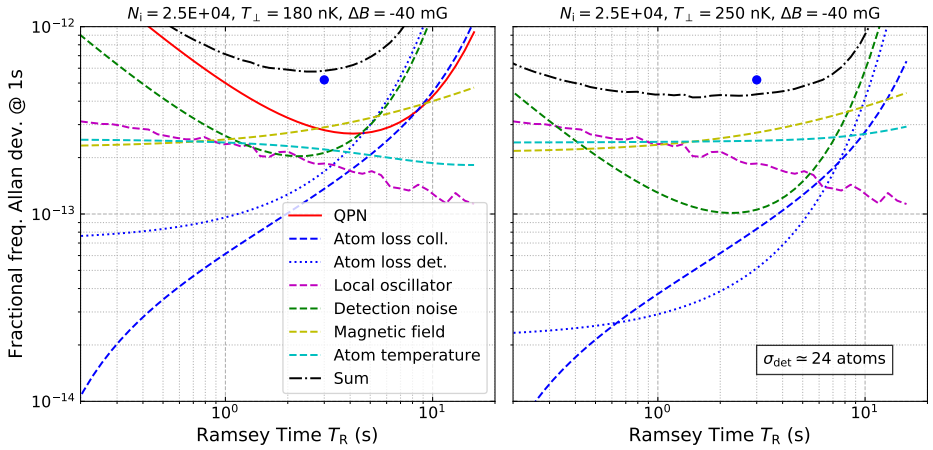

Figure 3.10 Prospective clock stability with spin-squeezed states and cavity detection. The left panel shows calculations with our noise model with the fitted σ_B and σ_T (Fig. 3.6) and other experimental parameters of the best data (blue circle, from Fig. 3.8). In the right panel we show prospective improvements using spin-squeezed state and cavity detection. We assume a detection noise $\sigma_{\mathrm{det}} \simeq 25$ atoms and no QPN in our model. This allows us to increase the temperature to alleviate the density related noise.

3.2 Characterisation of the atom-cavity coupling

3.2.1 Vacuum-Rabi splitting

Strong coupling between an atomic transition and a cavity mode gives rise to an avoided-crossing in the energy spectrum of the coupled system. At zero detuning between the two "oscillators", the eigenenergies split into a doublet with the so-called vacuum Rabi splitting (VRS), described by the Jaynes-Cummings (J-C) Hamiltonian (Eq. 1.39). The eigenenergies can be probed by probing the cavity spectrum, e.g. by the population probability (transmission) of the cavity with a scanning probe laser. This population probability also indicates how much a mode is photon-like.

The observation of VRS in the cavity spectrum has become the smoking gun of cavity-QED in the strong coupling regime. After tackling the cavity stabilisation, we also configured our setup to measure the VRS, in order to see smokes from the atom-cavity interaction.

3.2.1.1 Models and calculations

To understand the measured cavity spectrum in the experiment, we shall consider a model with real-world atoms, namely multiple levels and transitions between the ground state $5^2S_{1/2}$ ($|F=2\rangle$) and the excited state $5^2P_{3/2}$ for ^{87}Rb. Nevertheless, our system exhibits several advantages in terms of simplicity:

- Atoms are purely in $|2,1\rangle$ by transferring atoms prepared in $|1,-1\rangle$ with a MW π pulse.
- The atoms see a quantisation field along the cavity axis, so the π transitions cannot be exited by the cavity field (to a good extent).
- Since the atoms are magnetically trapped, there is almost no light shift on the atomic transition due to the optical lattice.
- Thanks to our imaging system, atom number in the cavity can be measured to high precision.

The only imperfection is the inhomogeneous coupling due to the finite temperature of the atoms. Luckily, it suffices to replace the collective coupling $\sqrt{N}g$ in the J-C model by an ensemble average $(\sum_i^N g_i^2)^{1/2}$ [103], without other effects on the cavity spectrum. It's worth mentioning that in the case of an intra-cavity lattice experiment, atomic transitions become inhomogeneous due to light shift from the 1560 nm trapping light. The linewidth of the eigenmodes can be strongly modified (see [124]).

Therefore we can work with a simple model with a single cavity mode and a single atom with multiple levels. The energy spectrum of the coupled system can be obtained by diagonalising the J-C Hamiltonian with the relevant transitions, namely all σ^+ and σ^- transitions starting from $|2,1\rangle$. In fact, if we consider σ^+ and σ^- excitations separately (as the cavity input polarisation can be controlled), we can further ignore the Zeeman sublevels. But to fully simulate the cavity transmission with arbitrary input polarisation (as in Fig. 3.13), one needs to include all involved Zeeman sublevels. More formally, the Hamiltonian of the coupled system is composed of

$$\hat{\mathcal{H}}_{\mathrm{JC}} = \hat{\mathcal{H}}_{\mathrm{ph}} + \hat{\mathcal{H}}_{\mathrm{at}} + \hat{\mathcal{H}}_{\mathrm{int}} \tag{3.24}$$

with the photonic energy

$$\hat{\mathcal{H}}_{\mathrm{ph}} = \sum_{q=\pm 1} \omega_c \hat{c}_q^\dagger \hat{c}_q \tag{3.25}$$

where q denotes the two modes with circular polarisations. The two modes are degenerate in frequency.

We consider a single ground state $|\mathrm{g}\rangle \equiv |2,1\rangle$ (zero energy), meaning we ignore the possible Raman transitions to the other trappable states $|2,2\rangle$, under the assumption of

weak photon occupation. The atomic energy reads

$$\hat{\mathcal{H}}_{\rm at} = \hbar \sum_{F'=1}^{3} \sum_{m'_F=-F'}^{F'} \omega_{\rm D2}(F') \left|F', m'_F\right\rangle \left\langle F', m'_F\right| + \mu_{\rm B} \left(g_{F=2} \left|{\rm g}\right\rangle \left\langle {\rm g}\right| + \sum_{F'=1}^{3} \sum_{m'_F=-F'}^{F'} g_{F'} m'_F |B| \right) \tag{3.26}$$

where the first line includes the hyperfine states of the excited state $5^2{\rm P}_{3/2}$ without Zeeman splitting, and the second line includes the Zeeman energy in weak magnetic field B. $g_{F'}$'s are the hyperfine Landé g-factors. Finally, the interaction energy reads:

$$\hat{\mathcal{H}}_{\rm int} = \hbar g_{23}^{+} \sum_{q=\pm 1} \left(\hat{c}_q^{\dagger} \hat{D}_q + \hat{D}_q^{\dagger} \hat{c}_q \right) \tag{3.27}$$

with the extended atomic lowering operator $\hat{D}_q$

$$\hat{D}_q = \sum_{F'=1}^{3} \left|{\rm g}\right\rangle \left\langle {\rm g}|\mu_q|F', m'_F = 1+q\right\rangle \left\langle F', m'_F = 1+q\right| \tag{3.28}$$

where $q = \pm 1$ again denotes the two circular polarisations, and μ_q is the corresponding dipole matrix elements [73]. g_{23}^{+} is defined such that $\langle \mu_{+1} \rangle = 1$ for the transition $\left|{\rm g}\right\rangle \rightarrow \left|F'=3, m_F=2\right\rangle$ (2-3).

The eigenenergies can be therefore obtained by diagonalising $\hat{\mathcal{H}}_{\rm JC}$. However, to calculate the cavity transmission spectrum which is measured experimentally, we shall include a cavity pump term,

$$\hat{\mathcal{H}}_{\rm pump} = -i\eta \left(\hat{c} e^{i\omega_p t} - \hat{c}^{\dagger} e^{-i\omega_p t} \right) \tag{3.29}$$

(or $-i\eta(\hat{c} - \hat{c}^{\dagger})$ in the rotating frame at ω_p) and consider the atomic and cavity decay in an open system. We employ the Lindblad master equation [133] of the system density matrix $\hat{\rho}$ (traced out the environment):

$$\dot{\hat{\rho}}(t) = -\frac{i}{\hbar}[\hat{\mathcal{H}}_{\rm sys}, \hat{\rho}(t)] + \sum_n \frac{1}{2}[2\hat{C}_n \hat{\rho}(t) \hat{C}_n^{\dagger} - \hat{\rho}(t) \hat{C}_n^{\dagger} \hat{C}_n - \hat{C}_n^{\dagger} \hat{C}_n \hat{\rho}(t)] \tag{3.30}$$

where $\hat{\mathcal{H}}_{\rm sys} = \hat{\mathcal{H}}_{\rm JC} + \hat{\mathcal{H}}_{\rm pump}$, and $\hat{C}_n$ are collapse operators. In our case, they include $\sqrt{\kappa}\hat{c}_q$ and $\sqrt{\Gamma}\hat{D}_q$ with $q = \pm 1$, where κ and Γ are as usual the cavity and atomic decay rates, respectively.

To obtain the cavity transmission spectrum, we look at the steady-state solution of the cavity population:

$$\langle \hat{c}^{\dagger} \hat{c} \rangle = {\rm Tr}(\hat{c}^{\dagger} \hat{c} \hat{\rho}_{\rm ss}) \tag{3.31}$$

where $\hat{\rho}_{\rm ss}$ satisfies $\dot{\hat{\rho}}_{\rm ss} = 0$.

Despite the simplification, this single-atom model agrees very well with the measured spectra. Numerical calculations[4] of the eigenenergies and cavity transmission spectra with essentially one free parameter g_0, are compared with data in the following.

[4] using python package QuTiP (quantum toolbox in Python)

3.2.1.2 Experimental methods and results

Our cavity stabilisation and probing scheme (Fig. 2.21) can be easily adapted to be operating in the resonant regime of the atomic transition $F = 2 \rightarrow F' = 3$, shown in Fig. 3.11. A spectrum is obtained by scanning the probe frequency and recording transmission with a single photon counting module (SPCM). The probe scan is achieved by an analog sweep of the EOM modulation frequency that generates the probe sideband. The carrier is sufficiently filtered by the cavity.

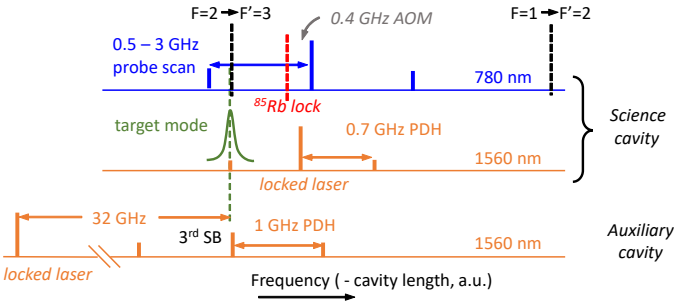

Figure 3.11 Frequency scheme for measuring the vacuum Rabi splitting in the resonant regime (cf. Fig. 2.21).

To completely avoid 1560 nm light in the science cavity, we can lock it with the auxiliary cavity. For the VRS measurement, we disabled the two-cavity interlock in order to have wide-range adjustments of the cavity detuning. As we have seen in Sec. 2.3.6, the relative drift between the two cavities is in the order of a few MHz, a negligible error in the cavity detuning in front of the VRS. It only introduces a small offset error (a fraction of the cavity linewidth) to the spectra.

In practice, changing the cavity detuning is very simple. We modify the offset frequency of ~ 32 GHz that bridges the two cavities. At a given cavity detuning, we take cavity spectra with different atom numbers, by changing the 2D-MOT flux (push beam power). Each scan takes about 100 ms, which is long enough that the cavity can be considered always in a steady state. The on-resonance transmission photon rate, generally below 1000 photons/ms, ensures very low average intra-cavity photon number (~ 0.02) that is assumed in the model.

Fig. 3.12 shows the classical avoided-crossing when the cavity detuning is varied across the atomic transitions (σ^+ input light). It resembles very much a simple two-level J-C model, but a third narrow peak appears, as there are two relevant atomic transitions (2-2 and 2-3 for σ^+). There is seemingly only one avoided-crossing, because the coupling ($\sqrt{N}g_{23}^+$) is larger than the hyperfine splitting between the two transitions. The "middle" state remains mostly atom-like, and is only slightly perturbed from the atomic transition.

For σ^- input, as there are three relevant atomic transitions, we shall expect four resonances. This is observed as we rotate a half-wave plate to change the probe polarisation from σ^+ to σ^- with the cavity resonant with the 2-3 transition (Fig. 3.13). In the mid-way with linear polarisation, we see all possible resonances.

The data agree well with the calculation using the simple model introduced above, not only in the eigen-frequencies, but also in the relative strength and width of the transmission peaks. The height of the peak is normalised to match the empty cavity spectrum. An ensemble average $g_{23}^+ = 2\pi \cdot 2.5$ MHz is obtained from fitting the data. After optimising the

atom cloud-cavity alignment (Sec. 3.2.3), g_{23}^{+} increases to $2\pi \cdot 4.7$ MHz, as shown in Fig. 3.14, where we vary the atom number and observe all resonances with linearly polarised probe at zero cavity detuning. The splitting scales nicely with $\sqrt{N}$, while the middle peaks are less visible (compared to Fig. 3.13) since they are less "photon-like" as the coupling increases.

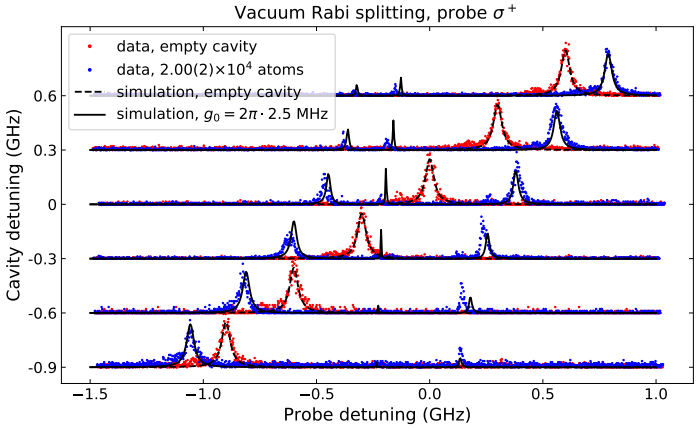

Figure 3.12 Cavity transmission spectra as a function of cavity detuning with σ^+ polarisation. The spectra are single-shot data with selection of measured atom number $2.00(2) \times 10^4$. The simulation assumes equal coupling for 2×10^4 atoms with single atom coupling $g_{23}^{+} = 2\pi \cdot 2.5$ MHz (g_0 in the figure). The cavity is locked via the auxiliary cavity without frequency interlock, so there is uncertainty in the absolute frequency.

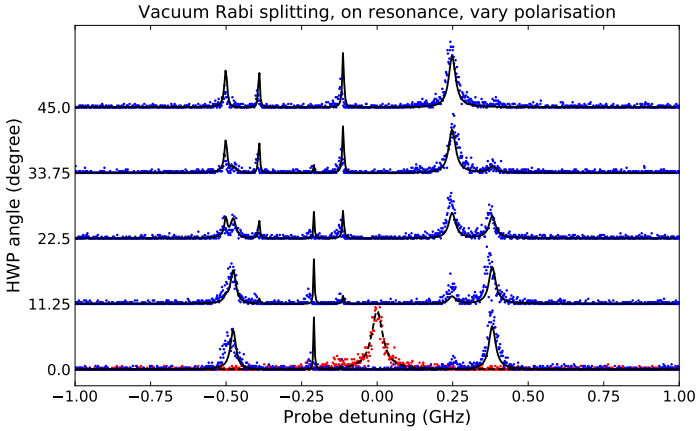

Figure 3.13 Cavity transmission spectra varying probe polarisation at zero cavity detuning. Same legend as in Fig. 3.12, except that the simulation uses $g_{23}^{+} = 2\pi \cdot 2.6$ MHz, and a frequency offset of -15 MHz is added to the simulation to better match the data. This is probably due to the uncertainty in the timing of the MW sweep (analog).

3.2.2 Cavity shift in the dispersive regime

We turn from now on to the dispersive coupling regime, where the cavity is tuned in the middle of the D2 transitions from $F = 1$ and $F = 2$ respectively (Fig. 1.4(b)). The laser

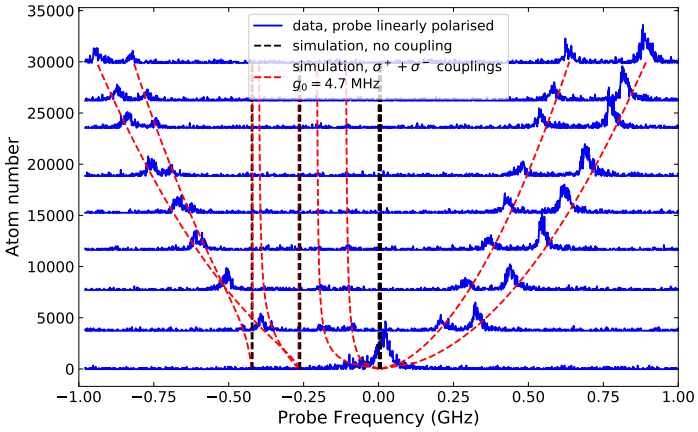

Figure 3.14 VRS spectra varying atom number. The spectra are shifted vertically according to the measured atom number. Bare cavity frequency and atomic transitions are shown in dashed black lines. Eigenenergies of the coupled system are shown in dashed red curves, which agree well with the data.

scheme is shown in Fig. 2.21. We continue to use the notation for the clock states: $|\downarrow\rangle = |1,-1\rangle$ and $|\uparrow\rangle = |2,1\rangle$.

3.2.2.1 Cavity detuning for equal coupling

In our theoretical model for spin squeezing (Sec. 1.3.2.3), we have considered a common excited states for $|\uparrow\rangle$ and $|\downarrow\rangle$ with equal coupling g. A cavity mode equally detuned from the clock states hence has equal dispersive coupling $2g^2/\omega_{\text{at}}$ to both states. For real Rb atoms, multiple transitions are involved to shift the cavity. They are polarisation dependent and have different strengths. But what matters is to find the cavity frequency such that an atom in either $|\downarrow\rangle$ or $|\uparrow\rangle$ shifts the cavity equally with opposite signs, as the model described.

Including both clock states in the Hamiltonian (Eq. 3.24), we can calculate the energy of the photonic eigenstate, whose difference from the bare cavity energy gives the cavity shift induced by either the atomic ground state ($F = 1$) or one atomic excitation ($F = 2$). For σ^+ and σ^- transitions, the sum of the cavity shifts from both atomic states is shown in Fig. 3.15(b). The zero-crossing indicates the detuning at which the cavity has equal coupling to the two clock states, slightly different for the two polarisations. For σ^+, it is 3.17 GHz with respect to $f_{23} \equiv F = 2 \rightarrow F' = 3$. We have again assumed equal coupling for the atoms with $g_{23}^+ = 2\pi \cdot 4.7$ MHz (Note that g_{23}^+ is the coupling for the 2-3 transition for σ^+ transition), as obtained from the VRS spectra (Fig. 3.14). We also plot the cavity shift per atom in either $|\uparrow\rangle$ or $|\downarrow\rangle$ for both polarisations in Fig. 3.15(c), as it is the figure of merit in the dispersive regime. The shift about 8 kHz per atom agrees with the data (see below), showing the consistency between the measurement of VRS and that in the dispersive regime.

Experimentally, finding this cavity detuning is straight-forward: if one starts with an equal population of $|\uparrow\rangle$ and $|\downarrow\rangle$, the cavity should have no frequency shift compared to an empty cavity at the correct detuning. Fig. 3.15(a) shows the cavity shift by atoms as a function of the cavity detuning, with the atoms prepared by a microwave $\pi/2$ pulse. The zero-crossing gives the optimum cavity detuning with respect to f_{23} at about 3.05 GHz.

The discrepancy turns out to be caused by the imperfect $\pi/2$ pulse. The measured atom

number indicates that the actual $P_\uparrow$ was about 48.5%. Calculation taking into account this population imbalance (blue dashed line in Fig. 3.15(b)) gives a zero-crossing that agrees with the data. The slope is however still different.

There are other sources that may affect the measurement. A nearby high-order cavity mode is coupled to the fundamental mode that may slightly shift the latter (see later in Fig. 3.16). Full understanding of these data turns out to be difficult.

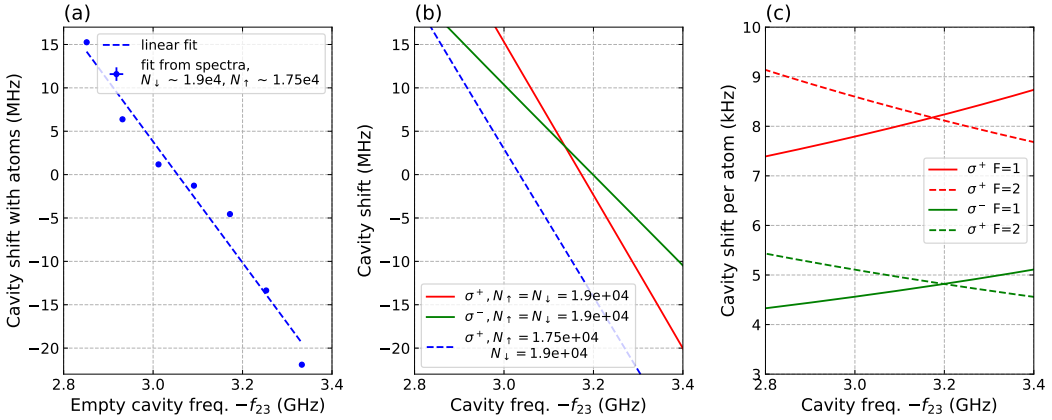

Figure 3.15 Cavity frequency for equal coupling. (a) cavity shift by atoms prepared by a $\pi/2$ pulse, as a function of the cavity detuning. The $\pi/2$ pulse turns out to have a 1.5% error. (b) Theoretical calculation of the cavity shift with $g_{23}^+ = 2\pi \cdot 4.7$ MHz, for σ^+ coupling (red) and σ^- coupling (blue). Calculation taking into account the population imbalance (dashed blue) agrees with the data. (c) Cavity shift per atom in either state from the same calculation.

3.2.2.2 Cavity shift per atom

Having the cavity properly detuned, the cavity shift now measures the atom number difference $N_\uparrow - N_\downarrow = 2S_z$:

$$\delta\omega_c = \tilde{\Omega}_c^{(q)} S_z \tag{3.32}$$

where $\tilde{\Omega}_c$ is the ensemble-average cavity shift per spin flip ($S_z = 1$), and (q) distinguishes σ^+ and σ^- transitions. Again we have adopted the homogeneous-coupling picture. The effect of inhomogeneous coupling will be discussed later (Sec. 4.1). Compared to Eq. 1.44, $\tilde{\Omega}_c^{(q)}$ includes the effect of all relevant transitions, and it is experimentally accessible since we have an accurate and independent measurement of the atom number through absorption imaging.

To find $\tilde{\Omega}_c^{(q)}$, we again measure the cavity spectrum by scanning the probe, but we prepare the atomic state with different S_z, namely a Rabi rotation with different angles. Selected spectra with different $N_\uparrow - N_\downarrow$ are shown in Fig. 3.16(a) (σ^+ probe). For $S_z < 0$, an unexpected avoided-crossing occurs. This is due to a known high-order cavity mode (from previous analysis [108], it is likely a 7th-order mode) that couples to the fundamental mode. This coupling is possible because the two modes are not perfectly orthogonal due to imperfect (non-spherical) mirror shape [134]. From a two-mode fit (Fig. 3.16(b)), we see that this mode also couples to the atoms (as it moves with S_z) but more weakly, as expected from its more extended spatial profile. The coupling between the cavity modes is also obtained.

For σ^- polarisation, the coupling is smaller than that of σ^+ as shown in the calculation (Fig. 3.15(c)). The cavity spectra would be similar but with a deeper slope. To see both couplings, we perform a similar measurement with linearly polarised probe (Fig. 3.17). The spectra can be understood by a calculation of eigenenergies of the system including a second cavity mode with properties from the fit in Fig. 3.16. The σ^+ and σ^- couplings are calculated separately as they don't couple, which is confirmed by the data.

It's worth noting that instead of preparing a coherent superposition of $|\uparrow\rangle$ and $|\downarrow\rangle$ by varying the MW pulse area, this measurement is taken with atoms purely in $|\downarrow\rangle$ or $|\uparrow\rangle$ with variable total atom number. Theoretically these two preparations should be identical for the cavity shift, while subtle differences can exist since the total atom number can influence the collective coupling through the thermal energy.

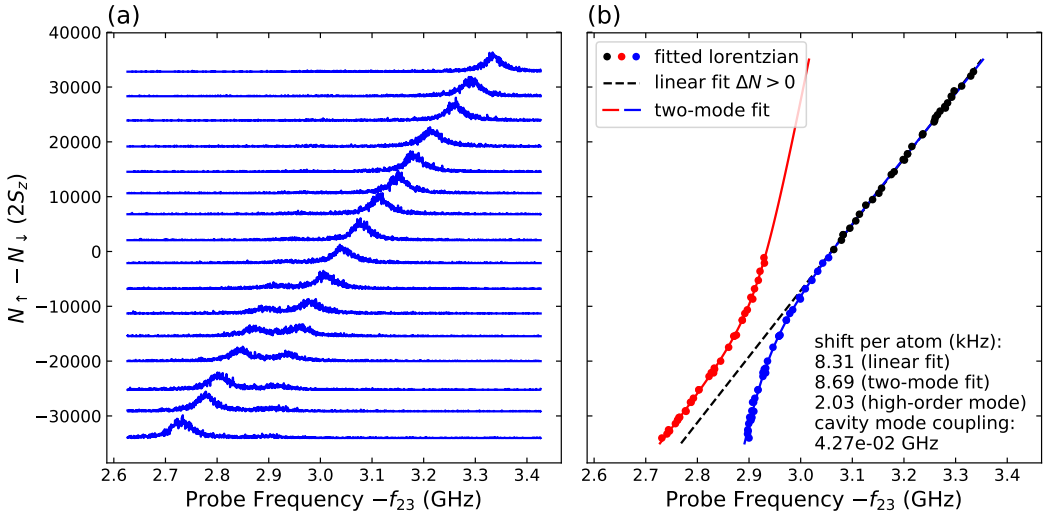

Figure 3.16 Cavity shift as a function of $N_\uparrow - N_\downarrow$ with σ^+ polarisation. (a) A few selected transmission spectra with different S_z. Atom numbers are measured from imaging. (b) A two-mode fit to the frequencies of the fundamental mode and of the coupled high-order mode. It obtains the dispersive coupling to the atoms of both modes, as well as the coupling between the two cavity modes.

3.2.3 Atom-cavity alignment

Trapped in the magnetic trap, the alignment between the atomic cloud and the cavity mode is not guaranteed. As mentioned in Sec. 2.2.4, the trap position can be tuned in $\vec{z}$ by the bias field B_y of the principal confinement. Displacing in $\vec{y}$ requires another bias field B_z which otherwise can be absent. The trap centre along $\vec{x}$, displaced from the cavity centre in a weak trap due to asymmetries in the bias fields, can be centred by employing another current parallel to the dimple.

3.2.3.1 Transverse direction

The thermal extent of the atomic cloud in the optimum condition for the clock would be only slightly smaller than the cavity mode in the transverse direction. The collective coupling

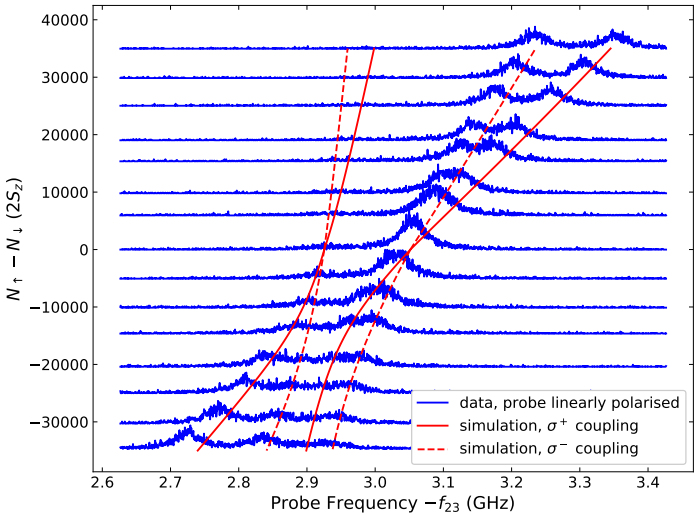

Figure 3.17 Cavity shift as a function of $N_\uparrow - N_\downarrow$, with probe linearly polarised. Here the spectra are taken with atoms prepared purely in either $|\uparrow\rangle$ or $|\downarrow\rangle$, $N_\uparrow - N_\downarrow$ is obtained by varying the total atom number. As a qualitative understanding, eigen-energies of the photonic modes are calculated including a second optical mode with properties from the two-mode fit in Fig. 3.16, with σ^+ or σ^- coupling separately as they don't couple. The calculations are shifted by -0.05 GHz to match the empty cavity spectrum.

is therefore sensitive to small displacements of the trap. We optimise the trap position by maximising the collective coupling.

Alignment via the VRS In the case of VRS, the splitting directly measures the coupling. However, the splitting also depends on the total atom number (hence its fluctuation), a stringent post-selection of atom number is necessary to compare the VRS precisely.

Experimentally, we scan the trap position iteratively along the two transverse direction ($\vec{y}$ and $\vec{z}$). At each position, we run a few experimental cycles to sample the atom number fluctuation for post-selection.

Alignment via the dispersive shift The cavity shift per $N_\uparrow - N_\downarrow$ in the dispersive regime also quantifies the coupling, and it is more robust as we only need the slope of the linear fit – relative shift versus measured $N_\uparrow - N_\downarrow$.

Concerned by the high-order mode on the red-side of the fundamental mode, we use only part of the spectrum with $N_\uparrow > N_\downarrow$. By scanning the preparation MW pulse area, a linear fit suffices to obtain the coupling. Fig. 3.18 shows the fitted coupling, while we vary the bias fields to displace the trap. To have an idea about the displacement from the numerical simulation of the magnetic field, the cloud moves in $\vec{z}$ by $\sim 10\,\mu$m for the scanned B_y (0.2 G variation) and it moves $\sim 8\,\mu$m in $\vec{y}$ for the scanned B_z (0.2 G variation).

3.2.3.2 Longitudinal direction

Along the cavity axis, the mode intensity varies weakly due to the long Rayleigh length ($\sim$ 750 μm), about 10% from the centre to the mirror. But we indeed observe an effect

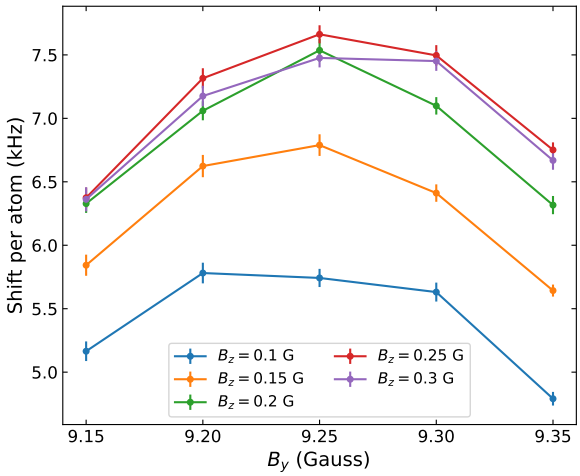

Figure 3.18 Shift per atom as a function of transverse cloud position, scanning both B_y and B_z to displace the cloud in $\vec{z}$ ($\sim 10\,\mu$m in total) and $\vec{y}$ ($\sim 8\,\mu$m in total) respectively.

of this intensity profile from the locking light, moving the cloud slightly towards the centre (seen from imaging). However, we did not observe a clear increase in the collective coupling after centring the trap (coarse alignment from imaging).

3.2.4 Intra-cavity optical lattice

Despite that trapping the atoms in the intra-cavity lattice is not intended in our goal to run a squeezed clock, performing a lattice experiment may help better understand our system. In fact, it is fairly straight-forward to switch to a lattice configuration with our setup. Here I report some preliminary characterisations of the intra-cavity lattice, and the atom-cavity coupling in the lattice.

3.2.4.1 Lattice loading

Setup advantages In conventional setups with intra-cavity lattice, the lattice light also serves as the locking light. One of the difficulties of this scheme is to load atoms into the lattice adiabatically, for which the lattice depth (power) is ramped up from very low level (e.g. three orders of magnitude lower than the final level). Keeping the cavity locked with a power variation of 30 dB can be difficult, especially when the optical power is low at the beginning of the ramp.

In our setup, instead of requiring a PDH signal with a limited output for large dynamic range, we could make use of the two-cavity interlock system (Sec. 2.3.6), i.e., the science cavity is locked via the auxiliary cavity, therefore the lattice power in the science cavity can be varied at will.

Another advantage of the experiment is that we start with very low temperature in the magnetic trap (typically 200 nK), hence loading the lattice can be very efficient.

Loading procedures The lattice power is controlled by the EOM modulation power (see Fig. 2.21). The RF source (Windfreak SynthHD) allows an external amplitude modulation

(AM) which determines the power ramp-up. We have briefly tried two types of ramp, exponential and linear, both multiplied by a turnOn function (Eq. 2.1). The Exponential ramp shows a better loading efficiency. Quantitative studies have not been carried out.

In an experimental sequence, the auxiliary cavity is always locked. After atoms are prepared in the clock trap, we turn on the two-cavity interlock, namely putting weak 1560 nm light in the science cavity for 10–20 ms for the lock to stabilise. We then hold the frequency lock and ramp up the lattice power in 10 ms. The residual drift between the two cavities has no visible effect on the lattice power, within about 100 ms.

Optimum trap depth Simply looking at the loaded number of atoms, we found a clear optimum lattice depth of about 50 μK (20 μW in-coupled power, 14 dBm EOM modulation power). The reason remains unclear. One possible explanation is parametric oscillations induced by the intensity noise of the lattice at the mechanical resonances of the cavity. For instance, above 50 μK lattice depth, the transverse trap frequency approaches half of the mechanical mode at 2.6 kHz (see Fig. 2.27). A solution to this would be a lattice intensity lock. In principle this intensity lock can be highly stable as we would not need to worry about it interfering with the cavity lock.

3.2.4.2 Atom lifetime and temperature in lattice

As usual, atoms are detected by absorption imaging after switching off the lattice. By varying the trapping time, we measure atom number decay, which agrees well with an exponential decay, giving a lifetime of about 0.2 s. In a particular measurement, state $|\uparrow\rangle$ and $|\downarrow\rangle$ have lifetime of 0.18(1) s and 0.19(1) s respectively, showing asymmetric losses. The lifetime is most likely limited by parametric oscillations caused by the intensity noise of the lattice.

By varying TOF after switching off the lattice, we can measure the expansion of the cloud (along $\vec{z}$) and fit the temperature. The data are noisy but we can fit $T_z \sim 2.4$ μK with loading ramp of 10 ms. In Fig. 3.20, we compare different ramping times of the lattice, showing more heating with shorter ramps. We have also tried an integrated Blackman ramp, which results in higher temperatures given the same duration (data not shown).

Theoretically, starting from a cloud with $T_z \sim 200$ nK in a trap with $\omega_z \sim 2\pi \cdot 110$ Hz, the optimal lattice loading acts as an adiabatic compression of the trap. The adiabaticity can be quantified by the conservation of phase-space density. We can estimate it for a thermal distribution in 1D as the product of the rms widths in position and momentum $N/x_T p_T$, where $x_T = v_T/\omega$ and $p_T = m v_T$ with trap frequency ω and thermal velocity $v_T = \sqrt{k_\mathrm{B} T/m}$. Therefore

$$x_T \cdot p_T = \sqrt{\frac{k_\mathrm{B} T}{m\omega^2}} \sqrt{m k_\mathrm{B} T} = \frac{k_\mathrm{B} T}{\omega} \tag{3.33}$$

meaning that for an adiabatic loading T/ω is conserved. Plugging in the transverse trap frequency ~ 1150 Hz, we will have $T_z \sim 2.1$ μK. This is very close to the measured temperature, suggesting that the lattice loading is close to adiabatic in the transverse direction.

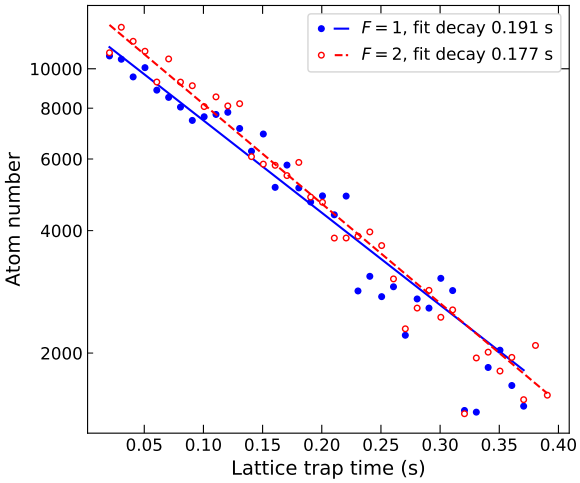

Figure 3.19 Atom lifetime in lattice

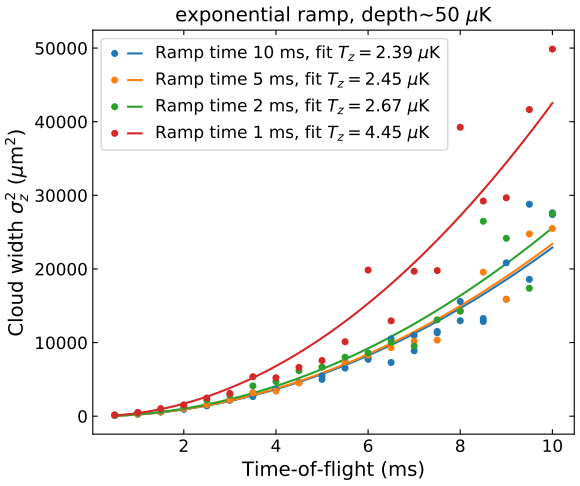

Figure 3.20 Cloud expansion after TOF to measure temperature in lattice

3.2.4.3 Coupling in lattice

Trapped in the 1560 nm intra-cavity lattice, we expect the collective coupling to increase. Firstly, the commensurate lattice wavelength guarantees maximum overlap[5] with the probe mode. The collective coupling can increase by a factor of two compared to averaging over the standing wave in a magnetic trap. Secondly, the thermal cloud size can also be greatly reduced in a deep lattice.

We measure the dispersive coupling again by the transmission spectrum varying S_z. We also vary the trap depth which results in different coupling, visualising the lattice trapping effect. One flaw is that the cavity detuning is kept the same while the excited state is subject to lattice induced light shift (up to tens of MHz). The cavity detuning differs from the one that couples equally to the clock state, depending on the trap depths. This renders the

[5]apart from the effect of the Gouy phase discussed in Sec. 2.3.1, not so significant for our cavity length.

dispersive shift to deviate from a straight line. The cavity frequency will also deviate from the empty cavity for $S_z = 0$. Nevertheless, the measurements only show a small shift at $S_z = 0$ even at the highest lattice power and no sign of deviation from the linear relation. we will then ignore the uncertainty in the measured coupling caused by lattice light shift.

The dispersive coupling at the optimal lattice depth (maximum loading) is shown in Fig. 3.21(a), where we see the coupling has increased by more than a factor of two. The coupling to the high order mode has increased similarly. In Fig. 3.21(b), the fitted coupling (linear fit for $S_z > 0$) is shown as a function of the lattice depth. Atoms are prepared in two different temperatures, showing a clear increase for a colder (smaller) cloud. These measurements have kept the magnetic trap on, to still keep the atoms while the lattice is not deep enough. But magnetic trap also reduces the effective coupling for deep lattices, as the atoms not captured by the lattice (5–10%) are still kept by the magnetic trap, contributing to the signal.

Note that for these measurements, only state $F = 2$ is detected at the end of the cycle after turning off the lattice. $N_\uparrow - N_\downarrow$ is inferred from the MW pulse length (rotation angle). The MW pulse error is generally below the QPN of the atoms.

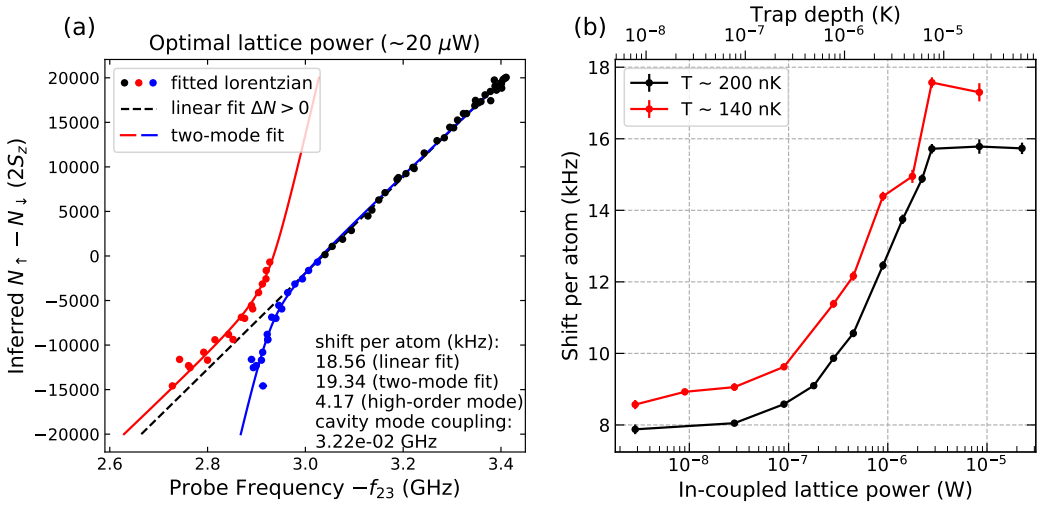

Figure 3.21 Dispersive coupling in lattice. (a) Cavity spectra varying S_z, with optimal lattice power (~ 20 μW in-coupled power) and magnetic trap turned off. We perform again a linear fit for $S_z > 0$ and a two-mode fit. (b) Cavity shift per atom (linear fit for $S_z > 0$) as a function of lattice depth, in two temperatures. Magnetic trap is always on to keep all the atoms, resulting in a smaller shift compared to (a).

Chapter 4

Spin squeezing by measurement

In the previous chapter, I have shown basic characterisations of our cavity measurement. As we know, if the measurement uncertainty of S_z is below the QPN of a CSS, the spin noise distribution will be squeezed after the measurement, conditioned on the measurement outcome. The metrological squeezing can be evaluated using the measurement uncertainty together with the coherence after the measurement.

In this chapter, we start with the characterisation of cavity-probe-induced decoherence. The inhomogeneity is particularly strong in our system so that spin echo is employed to preserve the coherence. I then detail the calibration of the spin-echo-based composite measurement, with which we achieve a conditional squeezing of 8(1) dB for 1.7×10^4 atoms. This preliminary result is believed to be limited by technical imperfections and future improvements are discussed. Preliminary results of squeezing by cavity feedback are also presented.

4.1 Inhomogeneous coupling and decoherence

We have assumed equal coupling for all atoms in the previous chapter, since we have been only considering the cavity resonance. As a single mode, the cavity sees the collective effect of the atoms, and an ensemble average of the coupling suffices.

For the atoms, inhomogeneous coupling leads to inhomogeneous AC-Stark shift (light shift), hence dephasing. The light shift of each atom depends on its position $\boldsymbol{r}_i$:

$$\delta\omega_{\mathrm{at}}^{(i)}(\boldsymbol{r}_i) = \Omega_c^+(\boldsymbol{r}_i)\langle\hat{c}^\dagger\hat{c}\rangle \tag{4.1}$$

where we only consider σ^+ transitions as shown in Sec. 3.2.2. We will write $\Omega_c(\boldsymbol{r}_i)$ from now on for simplicity. It is proportional to the intensity profile of the cavity mode (in the lab coordinates):

$$\Omega_c(x,y,z) = \Omega_{c0}\cos^2\left[\frac{2\pi}{\lambda_{\mathrm{L}}}x\right]\left(\frac{w_0}{w}\right)^2\exp\left[-2\cdot\frac{y^2+z^2}{w^2}\right] \tag{4.2}$$

where Ω_{c0} is the peak shift, λ_{L} the laser wavelength, w_0 the mode waist, and $w = w_0\sqrt{1+x^2/L_{\mathrm{R}}^2}$ with $L_{\mathrm{R}} = \pi w_0^2/\lambda$ the Rayleigh length.

4.1.1 Phase shift by cavity probe

As we have analysed in Sec. 1.3.3, the information gained by probing the cavity is quantified by the number of detected probe photons, which also determines the phase shift of the atoms and the dephasing among them. More precisely, the total phase shift $\phi_{\rm ac}^{(i)}$ of an atom i is an integral of $\delta\omega_{\rm at}^{(i)}(\boldsymbol{r}_i)$ during the probe duration τ_p, as in Eq. 1.56,

$$\phi_{\rm ac}^{(i)} = \int_0^{\tau_p} \mathrm{d}t\ \Omega_c(\boldsymbol{r}_i)\langle\hat{c}^\dagger\hat{c}\rangle = \frac{2n_d}{q_d\kappa_t\tau_p}\int_0^{\tau_p}\mathrm{d}t\ \Omega_c(\boldsymbol{r}_i) \tag{4.3}$$

where n_d is the detected photon number, with the detector efficiency q_d. The phase shift also depends on the trajectory of the atom, as $\boldsymbol{r}_i$ varies in time. $\kappa_t \approx \kappa = 2\pi \times 45.8(6)$ MHz for the 780 nm mode of the science cavity.

In the experiment, we shall distinguish a few timescales:

- The cavity lifetime ($\sim$ 22 ns) is much shorter than any atomic motion. So for each photon that passes through the cavity, the atoms are static.

- As the atoms are trapped magnetically instead of in the intra-cavity lattice, they move freely across the standing wave of the probe. For a typical temperature of 100 nK ($v_{T_x} = \sqrt{k_{\rm B}T_x/m} \approx 3$ mm/s) in the longitudinal direction, it would take ~ 130 μs to cross one period of the standing wave. For our typical probe duration of a few ms, the intensity variation due to the standing wave is well averaged out, i.e., the term $\cos^2(x)$ in Eq. 4.2 can be replaced by 1/2. The inhomogeneity in the transverse direction becomes dominant.

- The atoms undergo harmonic oscillations in the trap, partially averaging out the position-dependent inhomogeneity ($\exp[-2y^2/w^2]\exp[-2z^2/w^2]$). This reduces the dephasing among the atoms but far from perfectly, as atoms with different thermal energies have different oscillation amplitudes. Nevertheless, compared to static atoms, the coherence can be improved if the probe duration is long enough to allow averaging of the transverse motion. A minimum of half of the transverse trap period ($\sim$ 4.5 ms) or a multiple of it is required to benefit from a full average, but the timing cannot be perfect as the trap frequencies are slightly different, $\omega_y \neq \omega_z$. In practice, we use a probe duration of the full trap period ($2\pi/\omega_z$), taking into account the residual centre-of-mass oscillations (see Sec. 2.2.4.2).

- Along $\vec{x}$, the variation of the mode cross-section $(w_0/w)^2$ introduces another inhomogeneity, which is rather weak (<2% across the cloud width). The atoms can be seen as static since the trap period > 100 ms. Overall, this inhomogeneity is negligible compared to those along other directions.

- Another relevant timescale is for the lateral (energy-changing) collisions, which would unjustify the picture of classical oscillations in the trap. In our system with typical atom temperature $\sim$ 200 nK and 10^{11} cm^{-3} density, the collision rate is ~ 0.2 s^{-1}, and can be neglected.

In fact, as it will become more relevant in the next chapter, the phase shift of an atom only depends on its thermal energy after full motional average. The classical trajectory in a

harmonic trap – position $\boldsymbol{r} = (x, y, z)$ and momentum $\boldsymbol{p} = (p_x, p_y, p_z)$ – can be described by the energy and the oscillation phase angle in each direction, in $\vec{z}$ for example,

$$E_z = \frac{k_\mathrm{B} T_z}{2}\left[\left(\frac{z}{z_T}\right)^2 + \left(\frac{p_z}{m v_{T_z}}\right)^2\right], \quad \vartheta = \arctan(p_z/z) \tag{4.4}$$

where m is the atomic mass, T_z the cloud temperature along $\vec{z}$, $v_{T_z} = \sqrt{k_\mathrm{B} T_z/m}$ the thermal velocity, and $z_T = v_{T_z}/\omega_z$ with the trap frequency ω_z. Therefore, $z = \sqrt{2E_z/(m\omega_z^2)}\cos\vartheta$. Averaging over the phase angle ϑ gives an average light shift that only depends on energy:

$$\Omega_c(E_z) = \frac{1}{2\pi}\int_0^{2\pi} \Omega_c(z)\ \mathrm{d}\vartheta = \Omega_{c0}\exp\left[-\frac{2E_z}{m\omega_z^2 w_0^2}\right] I_0\left(\frac{2E_z}{m\omega_z^2 w_0^2}\right) \tag{4.5}$$

where $I_0(x)$ is the modified Bessel function of the first kind.

As we set the probe duration to be the trap period in the transverse direction, the motional average is not applicable in the longitudinal direction $\vec{x}$. The light shift is almost purely position dependent:

$$\Omega_c(x) = \Omega_{c0}\left(1 + \frac{x^2}{L_\mathrm{R}^2}\right)^{-1} \simeq \Omega_{c0}\left(1 - \frac{x^2}{L_\mathrm{R}^2}\right) \tag{4.6}$$

where $L_\mathrm{R} \approx 750\ \mu$m is much larger than the size of the cloud along $\vec{x}$. An expression of Ω_c as a function of E_x is still useful, as it gives the ensemble average of the phase shift for a cloud with average energy E_x. We denote the ensemble average with a tilde:

$$\tilde{\Omega}_c(E_x) = \frac{1}{2\pi}\int_0^{2\pi} \Omega_{c0}(x)\ \mathrm{d}\vartheta \simeq \Omega_{c0} - \frac{\Omega_{c0}}{m\omega_x L_\mathrm{R}} E_x \tag{4.7}$$

4.1.2 Monte-Carlo simulations

We perform Monte-Carlo simulations to quantitatively understand the inhomogeneous coupling and the motional average. An ensemble of atoms are sampled from thermal distribution in three independent dimensions and we ignore energy exchange between different axes. Kinetic equations of harmonic oscillation are solved numerically to obtain the trajectory of each atom for given time steps. At each time step, a phase is accumulated depending on the atoms' positions in the cavity mode (Eq. 4.2). The peak light shift Ω_{c0} in the cavity is calculated using the standard dipolar coupling formalism [73], taking into account all relevant σ^+ transitions.

Fig. 4.1 shows the simulation results that illustrate the features of the inhomogeneous light shift. (a)–(d) show the effect of motional averaging. After a full oscillation, the distribution is Gaussian-like (d). Its width will scale linearly with the probe power. (e) also shows the distribution as a function of the total thermal energy. The blurring from the 1D relation (Eq. 4.5) is simply due to the extension to higher dimensions. This gives an idea of the situation where energies in different axes do mix.

4.1.3 Contrast and phase measurements

To experimentally assess the dephasing induced by a cavity probe, we perform a standard Ramsey sequence scanning the phase of the second $\pi/2$ pulse. A cavity probe pulse is

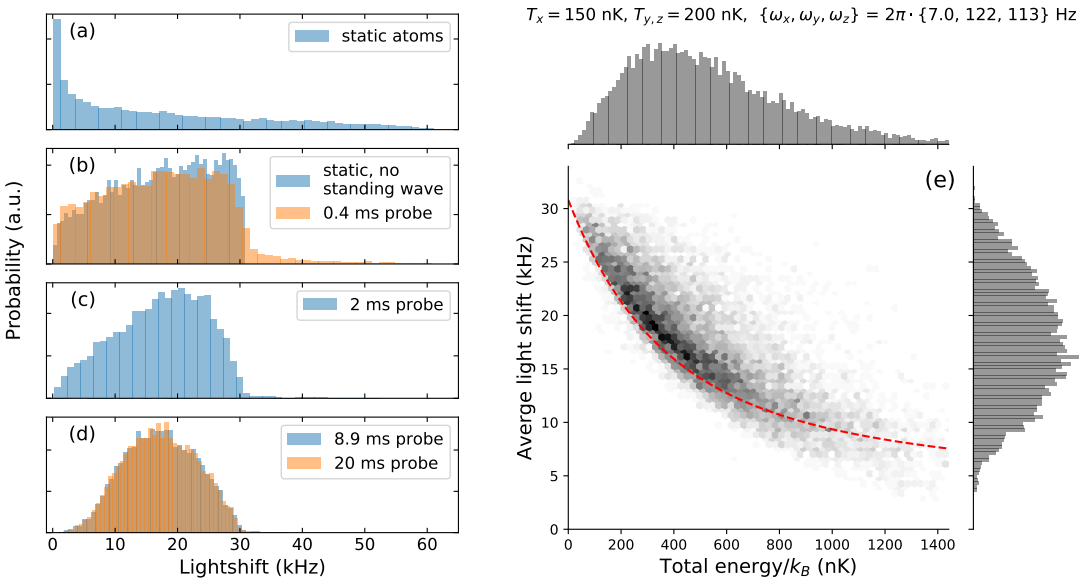

Figure 4.1 Light shift distribution from Monte-Carlo simulation. (a)–(d) Ensemble distribution of light shift after different averaging times (we show the time-averaged light shift with one intra-cavity photon, cf. Eq. 4.1): (a) Static atoms. This is the case seen by each photon. (b) Motional average over a 0.4 ms probe, already close to ignoring the standing wave. (c) Average over a 2 ms probe. (d) Averaging over a full period (8.9 ms) gives the minimum variance, a longer probe not exactly multiples of the trap period (20 ms) is almost the same. (e) Distribution of the average light shift (averaged over a full trap period 8.9 ms) as a function of the total thermal energy in the 3D harmonic trap (hence mean energy 550 nK). The distribution is a blurred version of the analytic integral over oscillations in 1D (dashed red curve, Eq. 4.5).

applied right after the first $\pi/2$ pulse, with the probe frequency fixed at the cavity resonance (sequence shown in Fig. 4.2). We obtain from the Ramsey fringes the phase (with respect to the fringes without probe) and the contrast at the same time. They measure the average phase shift and dephasing of the atoms respectively, induced by the cavity probe photons. We also vary the probe durations compared to the trap period. As in Eq. 4.3, the probe strength is measured in detected probe photon number n_d. Fig. 4.3 shows the fitted Ramsey contrast and the phase as a function of n_d. We indeed see that longer probe duration better preserves the contrast due to motional average in the trap. But in general the contrast decays very fast, losing 90% after merely ~ 3000 detected photons.

The phase of the Ramsey fringes well approximates the average phase shift of the ensemble, which can be calculated using the Monte-Carlo method mentioned above. Matching the slope (phase shift per photon) allows to determine the detection efficiency of the transmitted photons (including optical losses and quantum efficiency of the photon counter), which is otherwise difficult to calibrate. However, we observe an unexpected discrepancy in this slope from two datasets with different probe durations (Fig. 4.3). The reason is unclear but nonlinear effects of the photon counter can be excluded as the data remain on a straight line. Further investigation is underway. Nevertheless, we use the detection efficiency obtained from the slope to calculate the contrast from the same Monte-Carlo simulation, which agrees reasonably well with the data.

In summary, we have a reasonable understanding of the probe induced dephasing based on a model of classical trajectories in the trap. As this dephasing is particularly strong, simple cavity probes cannot be used as QND measurements for spin squeezing. Instead, spin-echo technique can be employed to compensate the dephasing, as in previous experiments [41, 92]. We discuss this compensation in the next section.

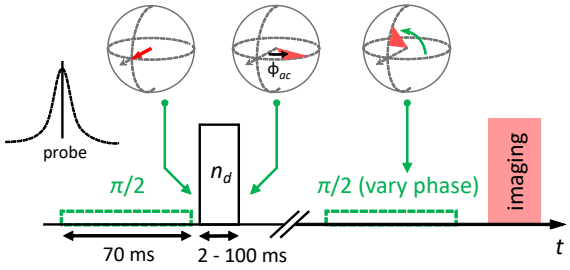

Figure 4.2 Sequence for contrast and phase measurements. Scanning the phase of the second $\pi/2$ pulse obtains Ramsey fringes with reduced contrast due to inhomogeneous light shift, and with average phase ϕ_{ac} of the light shift.

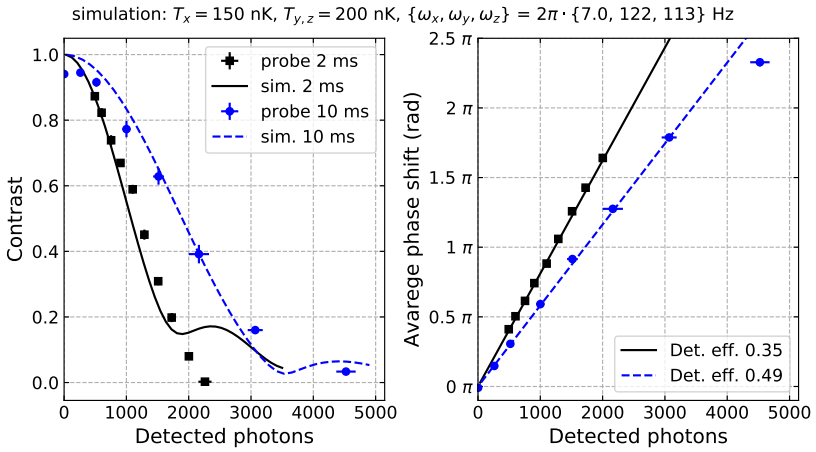

Figure 4.3 Contrast decay and phase shift induced by probe photons. We compare different probe durations (2 ms and 10 ms), showing the effect of motional average for the atomic coherence. Contrast (left) and phase (right) are extracted from a Ramsey sequence (Fig. 4.2). The solid and dashed curves are from Monte-Carlo simulations. The intracavity photon number is determined from the detection efficiency q_d, obtained by fitting the phase shift data (right). The difference between the two datasets (not taken together) is not clear and under investigation. We have not included other decoherence sources in the simulations, therefore giving perfect contrast at zero probe photon.

4.2 Composite measurements

4.2.1 Spin echo

Dephasing by the probe photons can be largely cancelled by a spin echo [135]. In our simplest implementation, the probe pulse is divided into two, and in between a MW π pulse is inserted

to flip the phase such that the phase shift from the first probe pulse cancels that from the second on average (see e.g. Fig. 4.8).

These spin-echo-based composite measurements have been successfully implemented in previous spin squeezing experiments (in the groups of Vuletić and Thompson, see e.g. [104, 101]), in which the inhomogeneous light shift mainly arises from incommensurate wavelengths of the probe laser and the intra-cavity lattice for trapping the atoms. In our experiment, however, the transverse inhomogeneity dominates. Consequently, There are several constraints related to the transverse thermal motion:

- The echo pulse should be error-free, otherwise it would alter S_z. It is particularly important for our cavity detection relying on the transmission with probe laser detuned at half-height ($\kappa/2$). An error in S_z due to the echo pulse will then modify the transmission of the second probe pulse, compromising the compensation between the two probes (more discussion in the following). To avoid decoherence (spread in S_z) due to the Rabi-frequency inhomogeneity of the echo pulse, we rely on the averaging of oscillations in $\vec{z}$ (as shown in Fig. 2.15), which constrains the pulse duration to be a multiple of $2\pi/\omega_z$ (~ 8.9 ms).

- The two probe pulses should give the same phase shift to any given atom to be well compensated. Therefore, either they can be very short compared to the transverse oscillation (instantaneous); or the probe pulses are as long as multiple oscillation periods (as discussed in the previous section). Due to the limited bandwidth of the photon counter, we have to apply probe pulses with duration $2\pi/\omega_z$.

Measurement construction We define, for the rest of the thesis, a cavity measurement M_i to be the detected transmission photon number. From the linearised cavity transmission $T = \frac{1}{2} + \frac{\delta\omega_c}{\kappa}$ with probe detuning $\delta_p = \kappa/2$ on the "blue slope", the cavity shift is inferred from the detected photon number as

$$\delta\omega_c \simeq \frac{\kappa}{2\langle M_i\rangle}(M_i - \langle M_i\rangle) \tag{4.8}$$

with some uncertainty from the PSN. $\langle M_i\rangle$ is the expectation value of detected photon number or the sample average. Subsequently, we define the collective spin measurement M_i^s that measures S_z through the cavity shift. Assuming homogeneous coupling with the ensemble-averaged $\tilde{\Omega}_c$ (or with effective coupling and atom number as shown in Sec. 1.3.2.4):

$$M_i^s (\simeq S_z = \frac{\delta\omega_c}{\tilde{\Omega}_c}) \equiv \frac{\kappa}{2\tilde{\Omega}_c\langle M_i\rangle}(M_i - \langle M_i\rangle) \tag{4.9}$$

I note $\simeq S_z$ to distinguish that the measurement outcome is not identical to S_z due to measurement noise. We will be mostly interested in the variance of the spin measurement

$$\mathrm{Var}(M_i^s) = \left(\frac{\kappa}{2\tilde{\Omega}_c\langle M_i\rangle}\right)^2 \mathrm{Var}(M_i) \tag{4.10}$$

For a composite measurement we define the constituent measurements $M_i^{(1)}$ and $M_i^{(2)}$ of the two probe pulses, with *a priori* $\langle M_i^{(1)}\rangle = \langle M_i^{(2)}\rangle$.

The cavity shifts probed by the two pulses are inverted since the echo pulse flips S_z. Therefore, the outcome of a composite measurement should be defined as

$$M_i \equiv \langle M_i \rangle + (M_i^{(1)} - M_i^{(2)}), \quad \text{with } \langle M_i \rangle = \langle M_i^{(1)} + M_i^{(2)} \rangle \tag{4.11}$$

the sign is chosen such that the measurement corresponds to the initially prepared S_z.

Correlation with S_z As the probe-induced dephasing is determined by the number of photons, the dephasing compensation by the spin echo relies on the two probes having the same photon number. While this is true on average, each shot $M_i^{(1)}$ ($M_i^{(2)}$) measures S_z ($-S_z$) which is subject to QPN, meaning that there is residual dephasing ($\sim |M_i^{(1)} - M_i^{(2)}|$), proportional to S_z. We will see that this correlation will lead to interesting phenomena in a timescale of hundreds of ms due to collisional interactions among the atoms. In this chapter, we will ignore the effect of this correlation with S_z.

I shall note that to circumvent the imperfect compensation correlated with S_z, one can simply toggle the probe laser detuning from $\delta_p = \kappa/2$ for the first probe pulse to $\delta_p = -\kappa/2$ for the second. The cavity shifts are then equal for the two probes, leading to the same transmitted photon number up to the PSN. The dephasing compensation should always be perfect except for the PSN.

The measurements presented in this chapter are performed with the probe laser fixed. Implementing the scheme with toggled probe frequencies should be straight-forward and is currently being carried out.

4.2.2 Composite π pulse

Our normal plain (square) MW pulses have a few imperfections:

- The pulse area suffers from errors due to power fluctuations of the MW and RF fields, which are generally temperature sensitive. Despite the excellent temperature stability of the lab ($\lesssim 0.2$℃), we have observed $\sim 1\%$ power fluctuation in the MW and RF power, mostly correlated with the temperature.
- Differential fluctuation of MW and RF also leads to frequency shift due to AC-Stark shift. But as we ensure two-photon light shift compensation (Sec. 2.2.6.3) which minimises the frequency sensitivity to the amplitude fluctuation of both fields, small power fluctuation is not critical in front of the the Fourier limited linewidth (~ 100 Hz) for a short pulse of ~ 9 ms.
- As we have discussed, field inhomogeneity in $\vec{z}$ constrains the pulse duration for averaging over the transverse oscillation. However, the MW field inhomogeneity in $\vec{x}$ cannot be averaged out and leads to position-dependent pulse errors along $\vec{x}$. Nevertheless, the cavity measurements are insensitive to this inhomogeneity (spread in S_z, as long as the sum stays constant) since the coupling in $\vec{x}$ is almost homogeneous (Sec. 4.1.1).

4.2.2.1 SCROFULOUS pulses

The slow power fluctuation and inhomogeneity in Rabi frequency can in principle be compensated using composite pulses, which have been widely applied in the field of nuclear

magnetic resonance (NMR) to cancel static errors [136]. Different types of composite pulses are designed to improve the pulse fidelity against either detuning errors, pulse-area errors, or both.

As in [104] and other experiments, it is most practical to employ the "SCROFULOUS pulse" which is the simplest composite pulse less sensitive to errors in pulse area. For a π pulse, it is composed of three plain π pulses with different phases: $\pi_{\phi-\pi/3}\pi_{\phi+\pi/3}\pi_{\phi-\pi/3}$, where the subscript denotes the phase of the π pulse, giving the global phase ϕ of the composite π pulse (later referred to as $\tilde{\pi}$).

However, note that composite pulses are designed to cancel static errors (errors common to all constituent pulses), and fail to work if e.g. the pulse amplitude (for each atom) varies during the constituent pulses. More specifically, we shall be aware of atomic motion during the composite pulse. This is not an issue if, as in an NMR experiment, the pulses are applied much faster than the atomic motion or the amplitude fluctuations. The atomic motion then appears as a static error.

In our experiment, however, we cannot achieve two-photon Rabi oscillation much shorter than a ms. So we have to adopt the other extreme: a constituent pulse lasts a full oscillation period in $\vec{z}$ to average over the inhomogeneity in $\vec{z}$. In this case, the three pulses are almost identical for each atom. Although now the composite pulse is quite long (3×8.9 ms), it is still short compared to the oscillation period in $\vec{x}$ (~ 250 ms). The field inhomogeneity in $\vec{x}$ can be largely cancelled by the composite pulse. Nonetheless, as mentioned in Sec. 2.2.6.2, the amplitude transient in the MW and RF fields makes the pulse errors of constituent pulses still different. This essentially limits the efficiency of the SCROFULOUS pulses.

4.2.2.2 Calibration sequence

Since the echo pulse is applied to atoms on the equator of the Bloch sphere, the resulting S_z can be maximally sensitive to the error in the pulse area depending on the rotation axis (phase). Assessing the pulse error by the transition probability from $|\downarrow\rangle$ to $|\uparrow\rangle$ is not sufficiently sensitive. So we perform a sequence similar to the real spin echo to assess the pulse error: after preparing the atoms with a long $\pi/2$ pulse (~ 70 ms), we perform the composite measurement with a variable phase ϕ of the echo pulse (plain or composite). The ϕ dependence of $P_\uparrow$ reveals the pulse error. If we assume only an error ϵ in the pulse area $\pi(1+\epsilon)$, $P_\uparrow$ after the π pulse reads

$$P_\uparrow = \frac{1}{2} - \frac{1}{2}\sin(\pi\epsilon)\cos\phi \tag{4.12}$$

In addition, MW inhomogeneity leads to position-dependent S_z, which can be revealed in the centre-of-mass positions of the two spin states. For example, if atoms on the left have $S_z > 0$ and atoms on the right have $S_z < 0$, the atoms projected in $|\uparrow\rangle$ have more contribution from atoms on the left, showing a centre-of-mass position to the left; the opposite for $|\downarrow\rangle$.

In Fig. 4.4, I plot the results – photon number in the two probes, $P_\uparrow$ measured by absorption imaging, and cloud positions for the two spin states[1], as a function of the echo pulse phase ϕ. We compare the plain π pulse and the SCROFULOUS $\tilde{\pi}$ pulse, with all π pulses tuned to one oscillation period in $\vec{z}$ and no time delay between the constituent pulses. For weak cavity probes, $P_\uparrow$ varies with the echo phase for the plain π, showing the pulse

[1] the cloud positions in $\vec{z}$ are featureless, hence not shown.

error in amplitude.[2] As it modifies S_z, the echo pulse error directly leads to an error in the photon number of the second probe pulse, On the contrary, these errors are not seen using $\tilde{\pi}$ pulses, as expected.

On the other hand, for stronger cavity measurements, the first probe can strongly dephase the atoms such that the π pulse phase is not any more well defined for the ensemble. This effectively averages out the phase-dependent error of the π pulse (blue circles in Fig. 4.4a). This reduced sensitivity to the phase-dependent pulse error has also been noted in [104] and studied as a technique for error cancellation in [137].

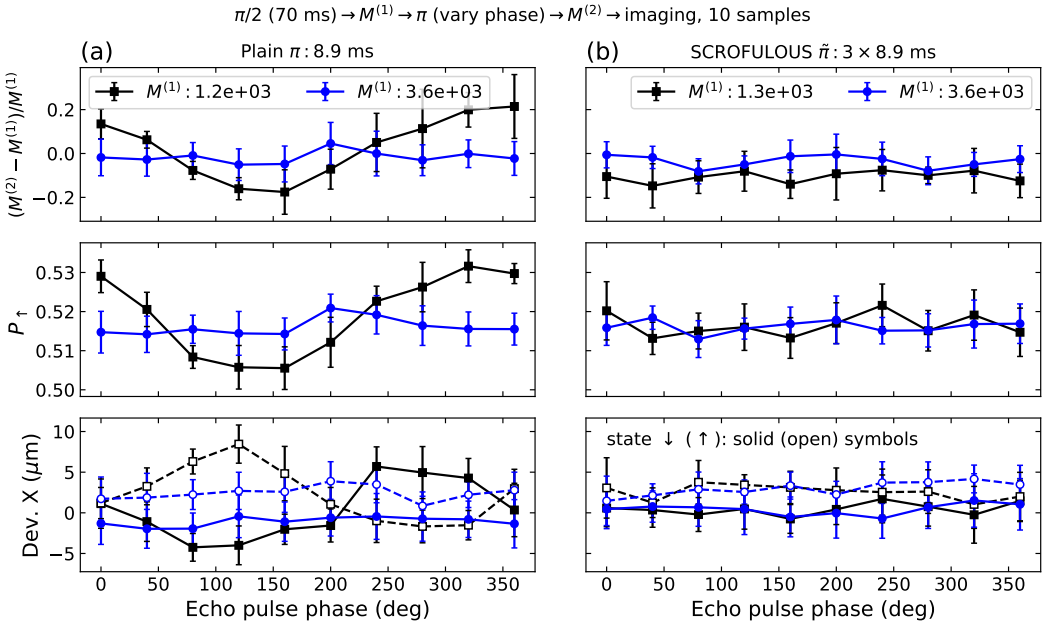

Figure 4.4 Here we scan the phase of the echo pulse between two cavity probes ($M^{(1)}$ and $M^{(2)}$), using a plain π pulse (a) or a SCROFULOUS $\tilde{\pi}$ pulse (b). Pulse errors show up as variation in $P_\uparrow$ (measured with absorption imaging) depending on the phase of the echo pulse (middle row), and subsequently modify the transmission of the second probe (top row). The average $P_\uparrow$ deviates from 0.5 because of an error in the preparation $\pi/2$ pulse. The phase-dependent cloud positions in $\vec{x}$ (bottom row) reflect inhomogeneity of the MW field in $\vec{x}$. We also compare two probe strengths (black squares and blue circles), showing that a strong probe ($M^{(1)}$) strongly dephases the atoms, washing out the phase dependence.

4.2.2.3 Limitations

However, it turned out that the insensitivity of the $\tilde{\pi}$ pulses to power drifts of MW and RF is compromised, because the power drift also leads to a detuning error, to which the SCROFULOUS pulse is more vulnerable. We have indeed observed reductions in pulse fidelity due to percent level drift of RF power, causing a shift in transition frequency by about 1 Hz. A regular (weekly) retuning of the pulse amplitude is still necessary.

[2] the phase dependence shown here cannot identify the error type since the probe photons introduce a phase offset. But we independently verified that it was pulse-area error.

In conclusion, the SCROFULOUS composite pulse indeed outperforms the plain pulse at the cost of a longer pulse duration. But the advantages diminish for stronger probe pulses, as we eventually do to achieve high levels of squeezing. Nevertheless, for the results presented in the following (and in Ch. 5), we use composite pulses to minimise the pulse error for all measurement strengths, and to reduce the frequency of pulse tuning routine.

The SCROFULOUS pulse is limited by the pulse amplitude transient and the power-drift-induced detuning error. The latter can in principle be overcome by using higher-order composite pulses that are insensitive to both pulse-area error and detuning error (such as the BB1 pulse [138]). But this requires a duration of at least 5 oscillation periods (~ 45 ms), and in reality worse off due to other technical imperfections. However, we later realised that some non-general (point-to-point) composite pulses can be less sensitive to both types of error with only 3 constituent pulses, such as the WALTZ pulse [139]. We are investigating the possible advantages of these types of pulses.

4.2.3 Coherence measurements

We proceed to evaluate the atomic coherence after a composite cavity measurement. Unlike the previous measurements (Fig. 4.3) using a Ramsey sequence, here we drive a Rabi rotation after the cavity measurement. The contrast of the Rabi oscillation quantifies the coherence. The reason is that the spin is anti-squeezed in the phase quadrature (with probe laser detuned at $\kappa/2$, there is additional anti-squeezing by cavity feedback). This leads to strong fluctuations of the Ramsey fringes, rendering it difficult to estimate the contrast with a small dataset. The axis of the Rabi rotation is tuned perpendicular to the Bloch vector to reveal the real coherence. At the same time, it is parallel to the anti-squeezing axis so the measured $P_\uparrow$ is not so sensitive to the anti-squeezing (Fig. 4.5).

The coherence as a function of detected photon number is shown in Fig. 4.6(a), where we compare the plain π pulse with the SCROFULOUS $\tilde{\pi}$ pulse. The $\tilde{\pi}$ indeed better preserves the coherence. We also compare the probe at zero detuning $\delta_p = 0$ or on the slope $\delta_p = \kappa/2$ (as in a real measurement). In principle, the only difference should be the correlation between the residual dephasing and fluctuation of S_z from QPN. As this fluctuation only reduces the contrast, it leads to an underestimation and a larger uncertainty of the contrast. Nevertheless, we use the measurement with $\delta_p = \kappa/2$ as a conservative estimation of the coherence for the assessment of squeezing in the next section.

PSN limit The measured contrast is still much lower than the PSN limit, predicted from two uncorrelated probe pulse, namely

$$\mathrm{Var}(M_i^{(1)} - M_i^{(2)}) = \langle M_i^{(1)} \rangle + \langle M_i^{(2)} \rangle \tag{4.13}$$

The measurement of contrast decay after a simple cavity probe (Fig. 4.6(b), open back diamonds, same as in Fig. 4.3) allows to estimate the contrast decay caused by certain amount of (uncompensated) detected probe photons. We fit the decay with

$$\mathcal{C} = \mathcal{C}_0 \exp[-(n_d/\gamma_1) - (n_d/\gamma_2)^2] \tag{4.14}$$

The second term in the exponent dominates, which is justified by the Gaussian-like distribution of the oscillation-averaged light shift (Fig. 4.1(d)). We can assume that the phase shift

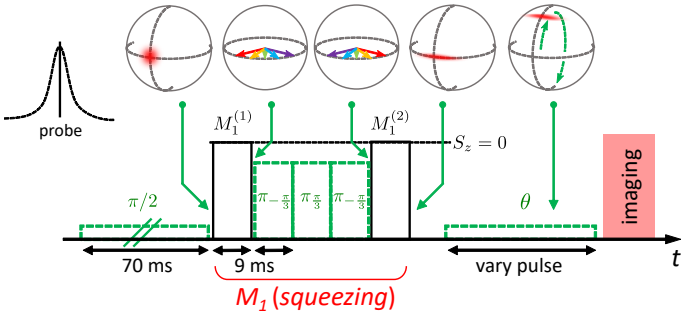

Figure 4.5 Sequence of coherence measurements using Rabi oscillations. The colour arrows on the Bloch sphere after the first probe $M_1^{(1)}$ represent the strong dephasing induced by the probe photons, which is subsequently rephased by the second probe $M_1^{(2)}$. Here the probe is on resonance so $M_1^{(2)} - M_1^{(1)} \approx 0$, not correlated with S_z. The decoherence is in principle only due to the transmitted probe photons, regardless of the probe detuning. Measurements with probe detuned at $\kappa/2$ are also compared in Fig. 4.6. After the composite measurement, we apply a MW pulse (same Rabi frequency as the first $\pi/2$ pulse) with variable lengths, along an axis perpendicular to the spin vector. The contrast of the Rabi oscillation measures the coherence.

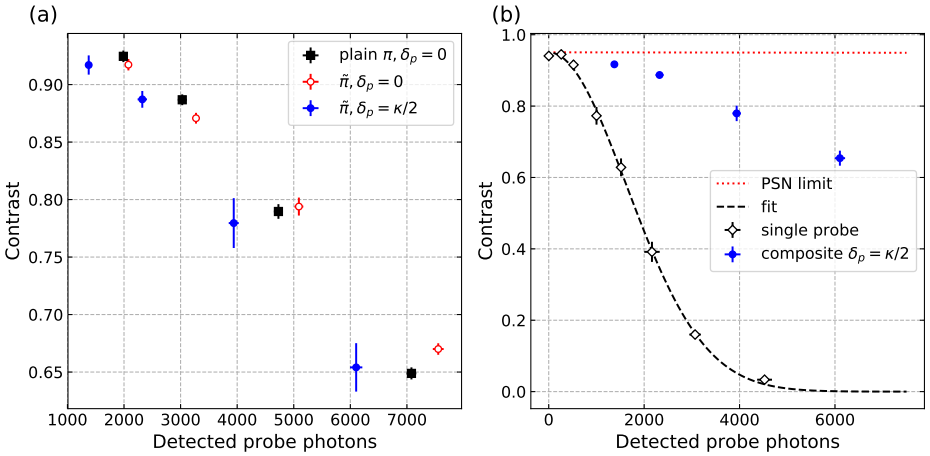

Figure 4.6 (a) Contrast of Rabi oscillations after a composite measurement, as a function of detected probe photons. We compare composite "measurements" (probe zero detuning $\delta_p = 0$) using either a plain π pulse (solid black squares) or a composite $\tilde{\pi}$ pulse (open red circles) for the spin echo. Measurements with probes detuned at $\kappa/2$ (solid blue circles) underestimate the contrast because of the increased phase fluctuation from the correlation with S_z. (b) Comparison of the contrast after a composite measurement ($\delta_p = \kappa/2$, solid blue circles) and after a single probe (open black circles, same data as in Fig. 4.3). The dotted red curve indicates the PSN limit of a composite pulse, using the fitted contrast decay due to probe photons (dashed black curve).

$\phi_{\rm ac}^{(i)}$ of an atom after a cavity probe follows a Gaussian distribution

$$p(\phi_{\rm ac}^{(i)}) = \frac{1}{\sqrt{2\pi\sigma^2}} \exp\left[-\frac{(\phi_{\rm ac}^{(i)} - \tilde{\phi}_{\rm ac})^2}{2\sigma^2}\right] \tag{4.15}$$

centred around the average phase shift $\tilde{\phi}_{\rm ac}$, with $\sigma = \sqrt{2}n_d/\gamma_2$ which scales linearly with the probe intensity. We can estimate the contrast by the projection along the average phase.

$$\mathcal{C} = \int_{-\infty}^{\infty} {\rm d}\phi' p(\phi') \cos\phi' = \exp\left[-\frac{\sigma^2}{2}\right] = \exp\left[-\frac{n_d^2}{\gamma_2^2}\right] \tag{4.16}$$

with $\phi' \equiv \phi_{\rm ac}^{(i)} - \tilde{\phi}_{\rm ac}$. We indeed recover the dominant term of our fitting function. γ_2 is determined essentially by the cloud size (trap frequency and temperature) compared to the cavity waist.

The fit gives $\gamma_1 \sim 10^{10}$ (negligible) and $\gamma_2 \simeq 2310(80)$. Applying the uncompensated PSN of the composite measurement to the fitted decay we obtain the dotted red curve, showing that the PSN limit is negligible.

Other limits As shown in Sec. 1.3.3.3, photon scattering into free space leads to contrast loss, $\mathcal{C} = \mathcal{C}_0 e^{-n_s}$. n_s is the scattered photon per atom (Eq. 1.55):

$$n_s = \tilde{\phi}_{\rm ac} \frac{\Gamma}{\omega_{\rm at}} \simeq 1.64 \times 10^{-6} \cdot n_d \tag{4.17}$$

where we have used the fit from Fig. 4.3. This yields a contrast of 0.987 for 8000 detected photons, clearly not the limiting factor of the experiment.

In summary, both the PSN and free-space scattering cannot explain the observed contrast decay. The contrast is probably limited by imperfections of the spin echo, relying on the motional average during each probe pulse. Further improvement is under investigation. Nevertheless, an alternative scheme to the spin echo can possibly improve the coherence preservation (see later in Sec. 4.5.2).

Coherence evolution We also check the coherence after the composite measurement at a longer timescale (Fig. 4.7). After the initial decay due to the probe pulses, the contrast decays much more slowly, by roughly 5% in 700 ms. This slow decay is most likely due to the magnetic filed inhomogeneity, since the bottom field is not optimised here (cf. Sec. 3.1.4.2) and the atomic density is not high enough to ensure spin-locking ([48] and Sec. 5.1).

In general, the coherence evolution in our system can be more complicated due to the interplay between collisional interactions and dephasing (either by magnetic field inhomogeneity or by probe photons). Nevertheless, here we observe that the evolution is not affected by the amount of probe photons nor by the atom number. For the squeezing measurement presented in this chapter, we can ignore the decoherence at this longer timescale.

4.3 Conditional spin squeezing

We now have all the ingredients to evaluate the metrological squeezing by a cavity measurement. The uncertainty of the collective spin state after a cavity measurement is constrained

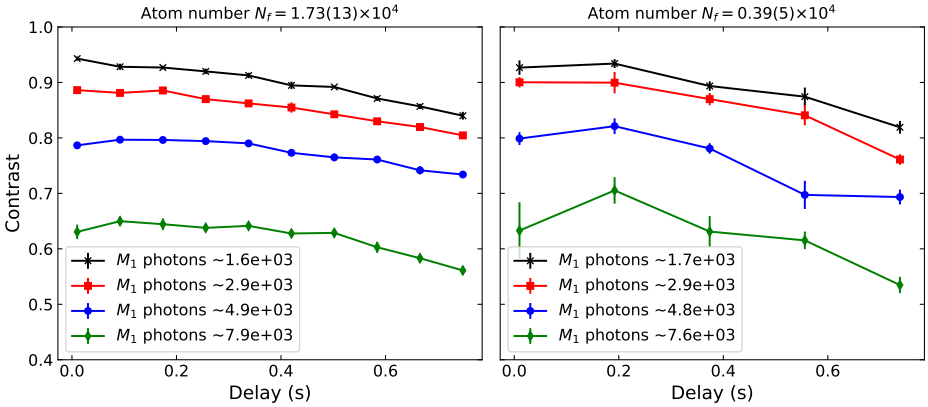

Figure 4.7 Coherence evolution after a composite measurement (M_1), measured by the contrast of Rabi oscillations. Different symbols correspond to different probe photon numbers, which do not influence the evolution. The decay is also independent of the atom number, 1.7×10^4 (left) and 3.9×10^4 (right). We shall note that the decoherence at this timescale does not compromise the squeezing assessment in this chapter.

by the information of both the initial state (CSS) and the measurement uncertainty. Recall Eq. 1.62, the uncertainty of S_z conditioned on measurement outcome M_1^s, written as $(\Delta S_z)^2|_{M_1^s}$, is determined by the measurement uncertainty. Here we use the spin measurement M_1^s that measures S_z with $\langle M_1^s \rangle = S_z$ (Eq. 4.9).

$$(\Delta S_z)^2|_{M_1^s} = \frac{\mathrm{Var}(S_z)(\Delta M_1^s)^2|_{S_z}}{\mathrm{Var}(S_z) + (\Delta M_1^s)^2|_{S_z}} \tag{4.18}$$

Note that only $(\Delta M_1^s)^2|_{S_z}$ for a given S_z represents the measurement uncertainty. $\mathrm{Var}(S_z)$ is unconditional, representing the noise in the prepared initial state (CSS + technical noise). Formally, the conditional spin noise is always lower than that of the initial state ($\mathrm{Var}(S_z)$) given the information from the measurement, even a weak one.

Theoretically, the measurement uncertainty is given by the PSN of the composite measurement, $\mathrm{Var}(M_1) = \langle M_1 \rangle$. In case of $(\Delta M_1^s)^2|_{S_z} \ll \mathrm{Var}(S_z)$, the conditional spin noise reduces linearly as the inverse probe photon number (Eq. 4.10):

$$(\Delta S_z)^2|_{M_1^s} \simeq (\Delta M_1^s)^2|_{S_z} = \left(\frac{\kappa}{2\tilde{\Omega}_c}\right)^2 \frac{1}{\langle M_1 \rangle} \tag{4.19}$$

The conditional metrological squeezing parameter ξ^2 further takes into account the contrast:

$$\xi^2 = \frac{(\Delta S_z)^2|_{M_1^s}}{\mathrm{Var}(S_z)} \cdot \frac{1}{\mathcal{C}^2} = \left(\frac{\kappa}{2\tilde{\Omega}_c}\right)^2 \frac{4}{\langle M_1 \rangle N \mathcal{C}^2} \tag{4.20}$$

We find that for a given measurement precision (given $\langle M_1 \rangle$), the squeezing also increases with the atom number. In this section, we verify the measurement uncertainty by varying $\langle M_1 \rangle$. We have used up to $N \simeq 1.7 \times 10^4$ to evaluate the squeezing parameter.

4.3.1 Measurement uncertainty

To verify the measurement uncertainty (that it is limited by PSN), one can measure the correlation between two consecutive cavity measurements. The measurement sequence is

shown in Fig. 4.8. After preparing a CSS on the equator, we perform two consecutive composite measurements M_1 and M_2, varying probe photon number as well as atom number. As usual, atom numbers in both states are detected through imaging at the end of the cycle. In each condition, we repeat the cycle 100 times to evaluate the fluctuation.

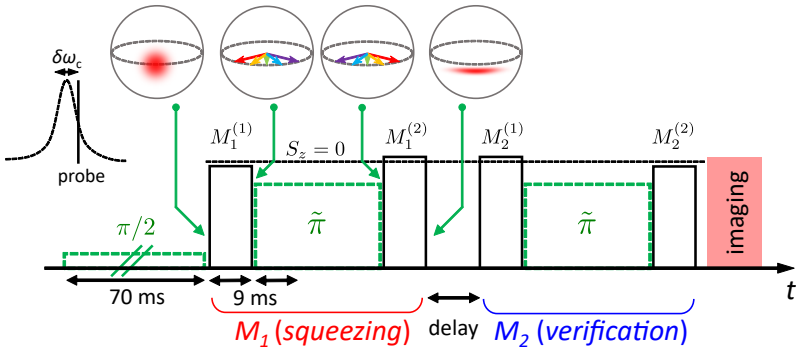

Figure 4.8 Sequence of squeezing measurements. The probe is detuned on the slope such that M_1 measures S_z, the uncompensated probe photons from $M_1^{(2)} - M_1^{(1)}$ is then correlated with S_z. The verification measurement M_2 is also a composite measurement for experimental simplicity. The delay between M_1 and M_2 is 10 ms for the main result (Fig.4.10).

We will first look at the fluctuations in M_1 and M_2 through the statistics of photon counts (Fig. 4.9). The standard deviation (Std.) of the photon counts of each dataset is shown as a function of the mean counts $\langle M_i \rangle$. The empty cavity measurements agree with the PSN limit $\sqrt{\langle M_i \rangle}$ (a), showing that the technical noise of the cavity measurements is not critical for these measurement strengths. Fluctuations of single measurements $\mathrm{Std}(M_1)$ and $\mathrm{Std}(M_2)$ clearly exceed the PSN, dominated instead by the QPN of the atoms. More formally, we can write a measurement as (cf. Eq. 4.8):

$$M_i = \langle M_i \rangle + \delta n_{d,i} + \frac{2\tilde{\Omega}_c \langle M_i \rangle}{\kappa} S_z \tag{4.21}$$

where we have added a fluctuation $\delta n_{d,i}$ to account for the PSN such that $\mathrm{Var}(\delta n_{d,i}) = \langle M_i \rangle$. We again consider homogeneous coupling with the ensemble average $\tilde{\Omega}_c$, and $\mathrm{Var}(S_z) = N/4$. The variance of a single measurement reads:

$$\mathrm{Var}(M_i) = \langle M_i \rangle + \left(\frac{2\tilde{\Omega}_c \langle M_i \rangle}{\kappa} \right)^2 \frac{N}{4} \tag{4.22}$$

The square root of the variance is plotted as the solid curves in Fig. 4.9. For two measurements with identical S_z,[3] the difference between M_1 and M_2 ideally has no S_z dependence,

$$M_1 - M_2 = \delta n_{d,1} + \delta n_{d,2} \tag{4.23}$$

Hence the variance of it reveals the PSN:

$$\mathrm{Var}(M_1 - M_2) = \langle M_1 \rangle + \langle M_2 \rangle \tag{4.24}$$

We plot $\sqrt{\mathrm{Var}(M_1 - M_2)/2}$ as a function of $\langle M_1 \rangle$. The data are in good agreement with $\sqrt{\langle M_1 \rangle}$, demonstrating the PSN-limited measurement uncertainty.

[3] In fact, as M_2 measures the state flipped by the echo pulse of M_1, we have to define $M_2 \equiv M_2^{(2)} - M_2^{(1)}$.

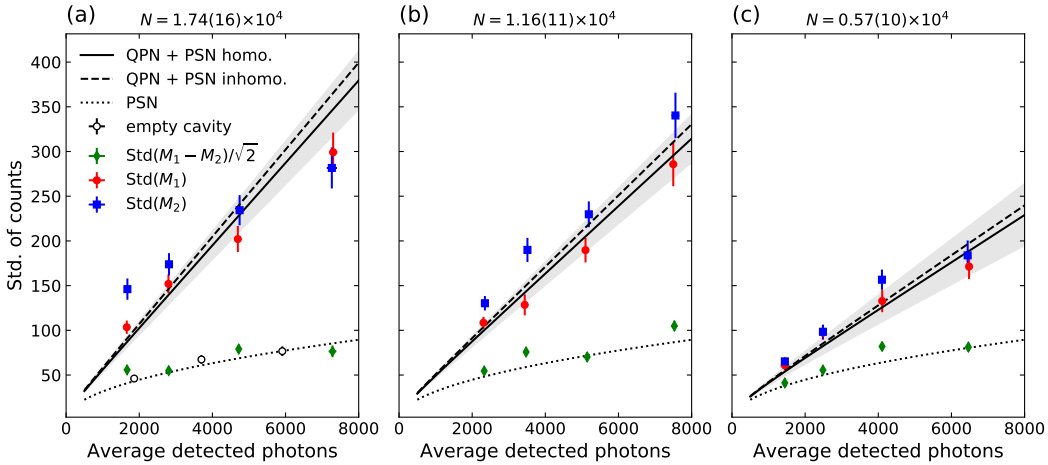

Figure 4.9 Standard deviation (Std.) of the photon counts from two consecutive composite measurements M_1 and M_2 with different atom numbers -1.7×10^4 (a), 1.2×10^4 (b) and 5.7×10^3 (c). The error bars of the Std. are estimated from a bootstrapping method, showing one standard deviation. Empty cavity measurements (open black circles) are shown in (a), lying on the PSN limit (dotted curve). The standard error of either measurement (red circles and blue squares) exceeds the PSN limit, but their correlation (green diamonds) approaches the PSN limit, confirming the measurement uncertainty to be only limited by the PSN for these measurement strengths. The solid lines indicate the expected fluctuations due to the atomic QPN plus PSN, assuming homogeneous coupling. The dashed lines include the effect of inhomogeneous coupling, which only deviate slightly from the homogeneous case, even within the uncertainty region of the latter (grey area). The uncertainties are obtained from the total atom number fluctuation in the dataset. The systematic deviation of the data from the QPN limit in (a) remains unclear. The delay between the measurements are different for these three datasets (10 ms, 50 ms, and 200 ms, respectively), which should not be relevant for this analysis.

Inhomogeneous coupling and effective atom number Now we discuss the effect of inhomogeneous coupling. In reality, we have N atoms with inhomogeneous coupling $\Omega_c^{(i)}$ for atom i, which is the time-averaged (motion-averaged) coupling for each atom during the probe pulse. As explained in Sec. 1.3.2.4, one can have an effective homogeneous system (including quantum fluctuations), using a properly defined effective atom number and effective coupling (Eq. 1.51,1.52, in terms of $\Omega_c^{(i)}$):

$$N_{\text{eff}} = \frac{\left(\sum_i^N \Omega_c^{(i)}\right)^2}{\sum_i^N (\Omega_c^{(i)})^2}, \quad \Omega_{\text{eff}} = \frac{\sum_i^N (\Omega_c^{(i)})^2}{\sum_i^N \Omega_c^{(i)}} \tag{4.25}$$

Surely, the two different treatments should give the same physical cavity shift $N\tilde{\Omega}_c = N_{\text{eff}}\Omega_{\text{eff}}$.

Using our Monte-Carlo simulation (Sec. 4.1.2), we can calculate the effective coupling in our system. Despite the strong decoherence due to the inhomogeneity, N_{eff} and Ω_{eff} are not that different from N and $\tilde{\Omega}_c$. We have $N_{\text{eff}}/N \simeq 0.90$ and $\Omega_{\text{eff}}/\tilde{\Omega}_c \simeq 1.11$. Using the effective atom number and coupling, the expected fluctuations of M_i are plotted as dashed curves in Fig. 4.9, even within the uncertainty region of the homogeneous case (Eq. 4.22). In view of the discrepancy of both the homogeneous and the inhomogeneous predictions with

the data, we will keep using the homogeneous assumption in the following, which gives a conservative estimation of spin squeezing.

4.3.2 Spin noise estimation

Using Eq. 4.18 and Eq. 4.10, we can translate the measurement uncertainty $(\mathrm{Var}(M_1-M_2)/2)$ into the conditional spin noise $(\Delta S_z)^2|_{M_1^s}$ normalised to that of the CSS. The data for 1.7×10^4 atoms (Fig. 4.9(a)) is shown in Fig. 4.10(a) (green diamonds), assuming homogeneous coupling. The metrological squeezing ξ^2 is obtained using Eq. 4.20 with the conservative estimation of the contrast (Fig. 4.6, $\delta_p=\kappa/2$). We achieve 8(1) dB squeezing, which can be considered as a lower bound. The squeezing is currently limited by the coherence loss, as the measurement uncertainty has not yet deviated from the PSN limit.

As the squeezing also scales with the atom number for a given measurement uncertainty, we show in Fig. 4.10(b) the conditional spin noise as a function of atom number. Three datasets are plotted for comparison. Even with the current measurement-induced decoherence, up to 11 dB squeezing can be expected for 5×10^4 atoms.

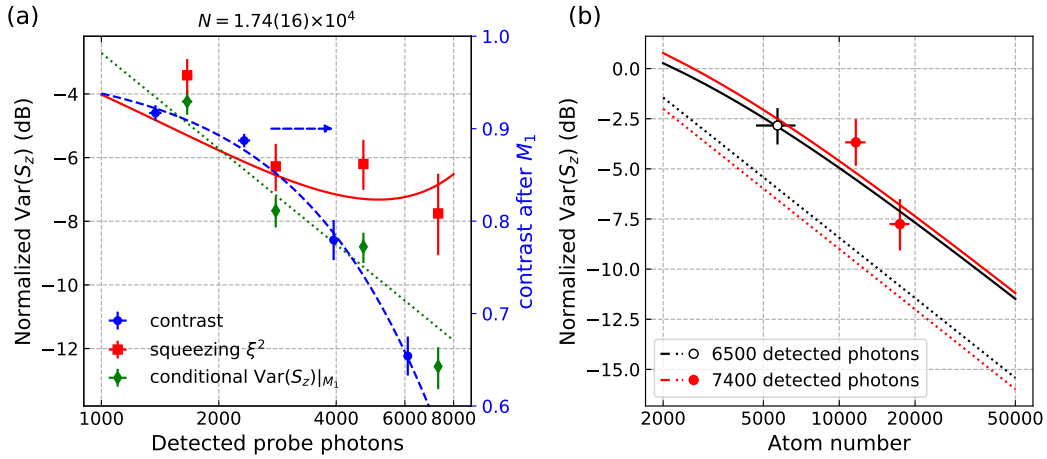

Figure 4.10 Conditional spin squeezing results. (a) same data as in Fig. 4.9(a), expressed in variance of S_z normalised to that of a CSS ($S/2$). Homogeneous coupling is assumed. We take the contrast data from the measurement with $\delta_p=\kappa/2$ and fit them with $\exp[-(M_1/\gamma_1)-(M_1/\gamma_2)^2]$ (dashed blue curve) to obtain the expected conditional squeezing (solid red curve) from the PSN limited measurement uncertainty (dotted green line), using Eq. 4.18. The last green diamond appears to be below PSN limit, probably due to the limited statistics (100 samples). (b) The squeezing scales with the atom number. Here we plot the normalised spin noise as a function of atom number, with two probe strengths in order to compare with three data points (at the highest photon numbers in Fig 4.9(a), (b) and (c)). The solid curves are the expected conditional squeezing using the same contrast decay fit, while the dotted lines are the PSN limits.

Open questions We have seen in Fig. 4.9(a) a systematic discrepancy between the $\mathrm{Std}(M_i)$ data and the expectations, i.e., higher than the prediction at low photon number, while lower at high photon number, which cannot be explained by inhomogeneous coupling. We have more data that show similar systematic deviation. One possible explanation is the spin

dynamics (detailed in the next chapter) taking place during the composite measurement. This spin dynamics is initiated by the cavity probe but also requires coherence (so stronger when the probe photon number is not too high), and alters the cavity resonance for the second probe, leading to a higher count variance. This hypothesis remains to be investigated.

4.4 Squeezing by cavity feedback

In fact, the correlation between the transmitted photon and S_z naturally realises the OAT Hamiltonian by cavity feedback (Sec. 1.3.4). However, S_z commutes with the OAT Hamiltonian and $\mathrm{Var}(S_z)$ stays as the CSS, if no further coherent operation on the spin state is performed. Hence we have ignored this effect in the previous analysis of squeezing by measurements.

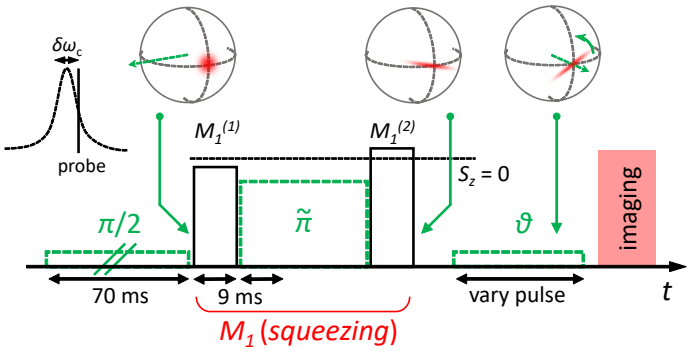

Figure 4.11 Sequence of noise tomography measurement

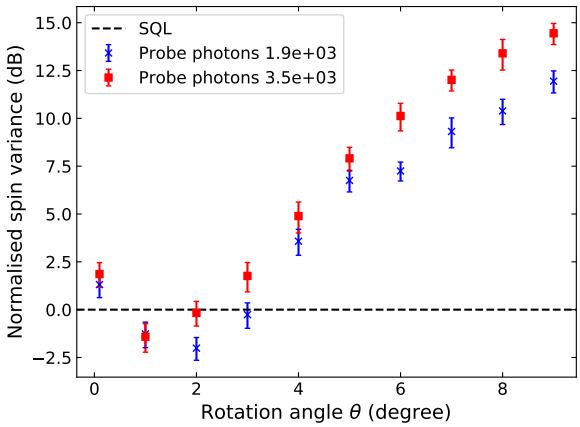

Figure 4.12 Preliminary spin noise tomography, measured by imaging. Detection noise is not subtracted. Error bars are obtained from bootstrapping. We observe the expected shift of the minimum uncertainty angle depending on the probe intensity.

Here I present preliminary results that reveal the squeezing by cavity feedback during a cavity measurement. We perform a spin noise tomography (see e.g. [44, 34, 33]) by measuring the variance of S_z after a rotation around the spin vector itself (Fig. 4.11). In the first

attempt, we use absorption imaging to obtain S_z, which is strongly limited by the detection noise, and we limit ourselves to small rotation angles. The normalised spin variance is shown as a function of the rotation angle (Fig. 4.12) and squeezing is clearly observed around $1 \sim 2$ degree rotation. We show here two probe intensities. Qualitatively, the minimum-noise angle is indeed shifted to lower value at higher probe intensity as expected [43]. In the next step, we will perform this noise tomography more thoroughly and with cavity measurements to improve the measurement precision.

4.5 Outlook

4.5.1 Squeezing lifetime

How the prepared spin squeezed state is preserved over time is an important open question. In previous studies, a lifetime of squeezing over 10 ms in a BEC [35] has been measured. In cavity-QED based spin squeezing experiments, lifetime of 5 ms has been observed [46]. The entire squeezing evaluation sequences in similar experiments are generally below a millisecond [44, 89, 42].

In our experiments, the above results already show conditional squeezing at a timescale of tens of milliseconds. However, a longer delay between the measurements will show an effect due to the cold collisions that alters the second measurement in a way that resembles an amplification. This effect is linked to the way we perform the composite measurement (residual dephasing correlated with S_z) and is studied in the next chapter. I shall summarise here that despite the second measurement being amplified, there is almost full correlation between the two measurements up to 800 ms, meaning that the squeezed state is still preserved.

The next experiments are to use composite measurement with toggled probe frequencies to eliminate the amplification effect such that the squeezing can be properly evaluated after long delays.

4.5.2 Alternative inhomogeneous-light-shift compensation

An alternative solution, to compensate the inhomogeneous light shift by the probe without employing the spin echo, is by a well-engineered light shift from another longitudinal mode of the cavity. The closest possible compensation mode (a FSR away) is 123 GHz detuned from both clock states and generates a negative differential light shift on the clock transition. In principle, this mode has the same intensity profile as the probe, so the compensation will be automatic for all atoms in any timescale. But for practical simplicity, the probe and the compensation light can even be separated in time. In this case the transverse oscillation period of the atoms has to be respected again, limiting the minimum probe and compensation pulse to be half of the trap period (4.5 ms).

I shall note that as the compensation light has to be $(2\nu_{\mathrm{fsr}}/\nu_{\mathrm{at}})^2 \sim 1300$ times stronger than the probe, the fluctuation of the compensation light shift due to the PSN is negligible compared to that of the probe. On the other hand, the probe photon number still correlates with S_z, which is not the case for the compensation mode (due to the large detuning). The compensation then again works only on average. Toggling probe frequency is still needed to avoid this correlation with S_z.

Another limitation comes from the sensitivity of the compensation mode frequency to the total atom number which is subject to technical fluctuations. An analysis of the noise sensitivity of this scheme is given in Appendix B.

Chapter 5

Quantum amplification by ISRE

In this chapter we study the interplay between squeezing measurements and the identical spin rotation effect (ISRE). As an interesting topic on its own right, the ISRE is a general phenomenon in spin polarized systems, and has manifested itself in cold atom systems in recent years, particularly relevant to the understanding and improvement of atomic coherence. Here I will start with an overview of ISRE and later explain its relevance in our experiment, especially to the cavity measurements. Consecutive measurements in a longer timescale (in contrast to the squeezing assessment in the previous chapter) clearly show the influence of the ISRE, which interestingly resembles an *amplification* of the cavity signal. Surprisingly, quantum correlations set up by the squeezing measurements have been almost perfectly preserved. This phenomenon provides another scheme of the "quantum phase magnification" [54, 55] that could facilitate quantum measurements. It may open another way to study the interaction between quantum correlations in the spin degree of freedom (spin-squeezed states) and correlations with motional degrees of freedom (spin dynamics), besides e.g. in BECs [140, 141, 142] and in fermionic optical lattice clocks [53].

5.1 Identical spin rotation effect (ISRE)

5.1.1 Basic principles

The ISRE was first studied as a microscopic phenomenon taking place in a binary collision between two identical atoms with internal degrees of freedom (e.g. nuclear spins), and finds applications in the transport properties and spin waves in liquid helium as well as in polarised hydrogen [143, 144]. The effect originates from quantum indistinguishability in cold collisions: two colliding particles having parallel spins (indistinguishable) or having opposite spins (distinguishable) will have different effective interaction energies. In general, this asymmetry leads to spin exchange effects. For spin 1/2-like particles, the exchange effects manifest as a rotation of individual spins around their sum [144], hence the name "identical spin rotation". It bears similarities to the polarisation rotation of photons in the Faraday effect. For instance, when a single atom with a given spin polarisation passes through a gas of identical atoms in another polarisation, the spin of the transmitted atom will undergo a rotation. More profoundly, the sense of the rotation is linked to the scattering lengths, irrespective of the trajectory of the atoms. When the same atom is sent back through the

gas in the opposite direction (e.g. by a trapping potential), the spin rotation is accumulative as in the Faraday effect.

We shall distinguish the coherent forward scattering from the lateral scattering in the following. While both are results of the s-wave scattering, the former gives rise to the ISRE but the latter involves an energy exchange. However, the forward scattering rate (spin exchange rate ω_{ex}) scales as $\omega_{\text{ex}} \sim na$, where n is the density and a the scattering length, while the lateral scattering rate $\gamma_c \sim na^2 v_T$, where v_T is the thermal velocity. At low temperatures v_T goes to zero, so does γ_c, therefore the forward collision dominates.

A heuristic derivation for fermions The ISRE can be understood in a heuristic way considering s-wave scattering of spin-1/2 fermions. We can model two-body collisions as contact interactions: $\hat{\mathcal{H}}' = g_{\text{col}}\delta(\boldsymbol{r}_1 - \boldsymbol{r}_2)\hat{P}_0$, where $\hat{P}_0$ is the projection operator for the singlet state $(|\uparrow\downarrow\rangle - |\downarrow\uparrow\rangle)/\sqrt{2}$ – the only state allowing s-wave collisions for fermions. g_{col} is determined by the scattering lengths. For spin-1/2 particles, one can verify that $\hat{P}_0$ takes the form $\hat{P}_0 = 1 - \hat{\boldsymbol{S}}^2/2$, where $\hat{\boldsymbol{S}} = \hat{\boldsymbol{s}}_1 + \hat{\boldsymbol{s}}_2$ is the total spin, and $\hat{\boldsymbol{S}}^2 = S(S+1) = 0$ or 2 for the singlets or triplets respectively. We have $\hat{\boldsymbol{S}}^2 = 3/2 + 2\hat{\boldsymbol{s}}_1 \cdot \hat{\boldsymbol{s}}_2$, and

$$H' = g_{\text{col}} \left(\frac{1}{4} - \hat{\boldsymbol{s}}_1 \cdot \hat{\boldsymbol{s}}_2 \right) \delta(\boldsymbol{r}_1 - \boldsymbol{r}_2) \tag{5.1}$$

The equation of motion for the spins reads

$$\dot{\hat{\boldsymbol{s}}}_1 = \frac{i}{\hbar} \left[\hat{\mathcal{H}}', \hat{\boldsymbol{s}}_1 \right] \propto g_{\text{col}} \hat{\boldsymbol{s}}_2 \times \hat{\boldsymbol{s}}_1 = -\dot{\hat{\boldsymbol{s}}}_2 \tag{5.2}$$

following the commutation relations of the spin operators. It resembles a Bloch equation of $\hat{\boldsymbol{s}}_1$ in a magnetic field given by $g_{\text{col}}\hat{\boldsymbol{s}}_2$, and we see the emergence of the spin rotation.

In fact, despite being a boson, ^{87}Rb has a similar two-particle energy spectrum as fermions. This is because the three relevant scattering lengths, $a_{\uparrow\uparrow}$, $a_{\uparrow\downarrow}$, and $a_{\downarrow\downarrow}$ are almost identical, which shift all spin-symmetric triplet states by the same energy but not the singlet state. This is why we are able to study ISRE in our system [145].

Theoretical frameworks ISRE has been studied based on a transport equation of the density matrix describing two spin components [144, 51]. The spin exchange effect arises from a commutator with the mean-field energy which depends on the spin (as in Eq. 5.2). The external degrees of freedom are treated classically as position- and momentum-dependent spins. Quantum correlations are lost in the mean field. We will use this kinetic equation for the simulations presented in this chapter (Sec. 5.1.4).

I shall point out that in recent years a theoretical framework beyond mean-field approximation has been developed in the context of fermionic optical lattice clocks [146, 52, 147]. It is based on a many-body Hamiltonian (second quantisation), where finite temperatures and collisional interactions are described in the basis of harmonic oscillator modes of the trap. An effective spin model can be derived considering that the motional energies are frozen during the collision events. Terms proportional to $\hat{\boldsymbol{S}}^{(\boldsymbol{n}_i)} \cdot \hat{\boldsymbol{S}}^{(\boldsymbol{n}_j)}$ and $\hat{S}_z^{(\boldsymbol{n}_i)} \hat{S}_z^{(\boldsymbol{n}_j)}$ arise for each mode $\boldsymbol{n}_i$ [147]. The first term can be understood as an energy gap between the symmetric Dicke manifold $S = N/2$ (Eq. 1.4) and other Dicke states. The mixing between the manifolds, hence decoherence, is caused by dephasing between the modes $\boldsymbol{n}_i$. The energy gap

then suppresses dephasing and locks individual spin orientations (see an intuitive picture below). This further allows to simplify the Hamiltonian by projection into the $S = N/2$ Dicke manifold, in terms of collective spins: $\hat{\boldsymbol{S}} \cdot \hat{\boldsymbol{S}}$ and $\hat{S}_z^2$. The latter gives rise to one-axis twisting dynamics that can generate spin squeezing [52, 148]. Numerical methods including losses and non-negligible inhomogeneities are also developed that achieved good agreement with experiments [52, 53].

5.1.2 An intuitive picture with atoms in two energy classes

To understand the effects of ISRE in trapped cold-atom experiments, we start with a simplistic model with two classes of atoms having fast and slow spin precession rates in a trap. Different spin precession rates originate from the inhomogeneous shift of the transition frequency $\Delta_D(\boldsymbol{r})$ which is generally position dependent (e.g. due to the trapping potential).

Which class an atom belongs to depends on the average $\Delta_D(\boldsymbol{r})$ it experiences. In the so-called Knudsen (collisionless) regime, where we assume low ISRE (forward collision) rate ω_{ex} compared to the trap frequency (or mean-free-path longer than the trap size), the precession rate only depends on the motional energy, as a result of integrating $\Delta_D(\boldsymbol{r})$ over oscillations in the trap. Therefore, the two classes in our model, can be understood as two energy classes – the hotter atoms and colder atoms (depicted in red and blue respectively in Fig. 5.1). We shall see that this picture is more helpful. Furthermore, we assume that the energy-changing collisions (lateral collision rate γ_c) are rare ($\gamma_c < \omega_{\text{ex}}$), then an atom remains in its class for a long time.

As illustrated in Fig. 5.1, we consider that all spins are aligned initially on the equator of the Bloch sphere. The two classes start to dephase due to their different precession rates (a), depicted as opposite dephasing vectors $\boldsymbol{D}$ (in the reference frame of the total spin). The ISRE then rotates each spin around their sum, along the vector $\omega_{\text{ex}}\boldsymbol{S}$, where $\boldsymbol{S}$ is the total spin. In the presence of dephasing, each spin actually rotates around $\boldsymbol{D} + \omega_{\text{ex}}\boldsymbol{S}$ (b). While the total spin is always on the equator due to energy conservation, individual spins can leave the equator, showing a non-zero S_z for each class.

From an experimental point of view, this means that the probability for each class to be measured in $|\uparrow\rangle$ or $|\downarrow\rangle$ would be different from $\frac{1}{2}$ ($\frac{1}{2} \pm s_z^{(i)}$ for atom i). As a result, for example, the projected $|\uparrow\rangle$ has more contribution from the hotter atoms and $|\downarrow\rangle$ more from the colder ones. Therefore, $|\uparrow\rangle$ and $|\downarrow\rangle$ have different average energies, which can be readily captured in a state-resolved TOF measurement.

Moreover, the clouds in states $|\uparrow\rangle$ and $|\downarrow\rangle$ will also have different spatial distributions, since the two energy classes have different spatial distributions in the trap. This is more generally known as position-dependent spin polarisation or spin waves. We can imagine an extreme case where the colder atoms have zero motional energy so they stay in the centre of the trap, and the hotter ones have finite energy so they spend more time away from the centre. As $|\downarrow\rangle$ has more contribution from the cold atoms and oppositely for $|\uparrow\rangle$, the spatial profile of $|\downarrow\rangle$ will resemble more that of the colder atoms – concentrated at the trap centre, while state $|\uparrow\rangle$ closer to the hotter atoms. This can also be measured by a state-resolved imaging.

If the spin rotation happens at a rate faster than the dephasing $\omega_{\text{ex}} > \Delta_D$, as sketched in Fig. 5.1(c), the dephasing can be "refocused" after a π rotation, similar to an echo sequence. In fact, if the rotation is fast enough, the spins never dephase significantly. This effect, known

as spin self-rephasing or spin locking, can be revealed in the atomic coherence measured e.g. by a Ramsey sequence.

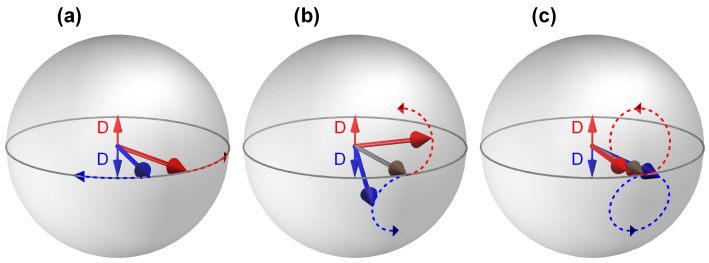

Figure 5.1 Schematics of ISRE for two classes of spins. The Bloch sphere is shown in the rotating frame of the total spin. (a) Without ISRE, the two classes dephase in opposite directions, under the inhomogeneous shift $\boldsymbol{D}$. (b) and (c) With ISRE, proportional to the total spin $\omega_{\mathrm{ex}}\boldsymbol{S}$ (grey arrow), the two spins start to rotate. In this reference frame, they rotate around the sum of $\boldsymbol{D}$ and $\omega_{\mathrm{ex}}\boldsymbol{S}$, tracing a circle above (red) or below (blue) the equator. After a full rotation (c), the two spins can be fully rephased.

5.1.3 Experimental signatures

Before proceeding to a more quantitative description, let us have a look at the experiments. There have been several cold atom experiments capturing different manifestations of the ISRE, which we have already sketched in the simplistic two-class picture. Certainly, in a real experiment, the atoms are in a thermal distribution. But it can be regarded as many classes of motional energy. The essential role of the ISRE remains the same: it introduces a correlation between the local spin distribution and the motional energy.

Spin wave and segregation The first manifestation of the ISRE observed in a cold atomic gas was a spin wave in a trapped ^{87}Rb cloud [149, 150], subsequently explained by the ISRE model [51] (cf. [151]). It was in fact not in the collisionless regime we assumed above, but closer to a 1D hydrodynamic regime where equilibrium is reached locally. This means that the precession rate is not a function of motional energy any more, but rather a function of position. The result is nevertheless similar: a position-dependent longitudinal polarisation (spin segregation or spin waves) builds up due to the ISRE, but dies out as the atoms move around.

The evidence has been clearer in a later experiment with a Fermi gas (^{6}Li) having tunable interaction strength through a Feshbach resonance [152]. This experiment also measured the spatial distribution of the two spin states. In contrast to the Rb experiment, the system was deeply in the collisionless regime such that the results were not successfully explained initially by a model in the hydrodynamic regime, but the mystery was quickly resolved [153]. The difference is that now the spin segregation is preserved for much longer time since the lateral collision rate is extremely low.

An additional advantage of the lithium experiment is the tunable scattering length such that it can change sign. The spin segregation is subsequently reversed, which indubitably verifies the role of ISRE. The more recent in-depth experiment has also extended to degenerate gasses [154].

Spin self-rephasing As explained in the two-class model, we expect the ISRE rotation to induce a rephasing or locking effect if the rotation rate is comparable to the dephasing rate. The previous experiments were however not in this regime. The TACC experiment can reach very cold temperature as well as having very low dephasing due to the trapping potential. Indeed, spin self-rephasing has been noticed from an exceptionally long coherence time [48]. The spin dynamics is further verified at an intentionally augmented dephasing by the trap, where the coherence shows a revival and a clear dependence on the atomic density.

The same effect has also been observed recently in a ^{87}Rb gas in an optical dipole trap [155], and in a ^{87}Sr optical lattice clock [53] (called as "spin locking").

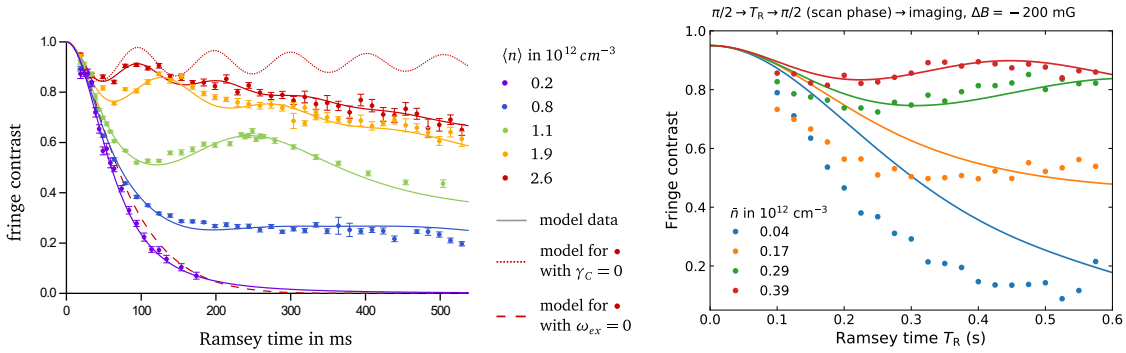

Figure 5.2 Ramsey fringe contrast showing the spin self-rephasing as a function of atomic density. Left: Data from TACC-1, +527 mG from the magic field, extracted from [72]. Right: preliminary data in TACC-2, −200 mG from the magic field. Simulations (see below) are shown in solid curves. The discrepancies at lower densities are most likely due to the atom-number dependence of temperature (see Fig. 2.11), i.e., the atom temperature for low atom numbers can be higher than what is used in the simulation. Independent temperature measurements were unfortunately not available for these data. Densities are much lower than the TACC-1 data because of the shallower trap.

5.1.4 Mean-field kinetic equation

Now we try to have a quantitatively understanding of the spin dynamics in a mean field approach, following [153, 48]. As previewed earlier, the evolution of the spins has the form of a Bloch equation with a magnetic field contributed from all atoms:

$$\dot{\boldsymbol{S}} \propto [\Delta_D \mathbf{e}_z + \omega_{\mathrm{ex}} \bar{\boldsymbol{S}}] \times \boldsymbol{S} \tag{5.3}$$

where the average spin $\bar{\boldsymbol{S}}$ represents the spin mean field. For initially polarised spins, the dephasing Δ_D (along $\mathbf{e}_z$, i.e. $\vec{z}$ axis on the Bloch sphere) is important to have a non-trivial dynamics.

With a semi-classical treatment of the thermal motion in the trap, $\boldsymbol{S}$ depends on the position $\boldsymbol{r}$ and momentum $\boldsymbol{p}$. For harmonic oscillations, we again move to the energy-phase variables (Eq. 4.4), in $\vec{z}$ for example: $z/z_T = \sqrt{2\beta E_z}\cos\vartheta$ and $p_z/(mv_T) = \sqrt{2\beta E_x}\sin\vartheta$, where $\beta = (k_{\mathrm{B}}T)^{-1}$ and we assume an isotropic temperature T for simplicity. Again $v_T = \sqrt{k_{\mathrm{B}}T/m}$, and $z_T = v_T/\omega_z$.

The advantage is that in the Knudsen regime, we can perform an averaging over the phase angle, such that the spin only depends on the three energies $\boldsymbol{S}(E_x, E_y, E_z, t)$. The dependence on each energy only comes via the dephasing $\Delta_D(\boldsymbol{r})$.

Let us have a closer look at $\Delta_D(\boldsymbol{r})$. It contains the mean-field shift $\Delta_{\mathrm{mf}}(\boldsymbol{r})$ (Eq. 1.13) and the Zeeman shift from the trap $\Delta_B(B) = b(B - B_m)^2$, close to the magic field B_m of the clock transition. In fact, at the optimal field which is slightly below B_m (Sec. 3.1.4.2), the total dephasing is much smaller than the ISRE rate in our system (see below). To study the spin dynamics in general, we will consider a B-field away from the optimal field, such that $\Delta_{\mathrm{mf}}(\boldsymbol{r})$ is negligible compared to Δ_B, and we can have a linear expansion around the trap bottom field B_0:

$$\Delta_B(\delta B) = b\Delta B^2 + 2b\Delta B \cdot \delta B, \tag{5.4}$$

where $\Delta B \equiv B_0 - B_m$, and δB is the local field in the harmonic trap with respect to B_0. The harmonic trap potential gives: $\delta B(\boldsymbol{r}) = \frac{k_{\mathrm{B}}T}{\mu_{\mathrm{B}}}[(x/x_T)^2 + (y/y_T)^2 + (z/z_T)^2]$ where we have assumed a Landé factor of 0.5 for our clock states, and μ_{B} is the Bohr magneton. Therefore we have

$$\Delta_D(\boldsymbol{r}) \approx \Delta_{D0}\left[\left(\frac{x}{x_T}\right)^2 + \left(\frac{y}{y_T}\right)^2 + \left(\frac{z}{z_T}\right)^2\right] \tag{5.5}$$

with $\Delta_{D0} = 2b\Delta B/(\beta\mu_{\mathrm{B}})$. The constant shift $b\Delta B^2$ does not induce dephasing.

In this case, the energy dependence of Δ_D is rather simple. The phase angle average gives, in $\vec{z}$ for example (no gravitational sag),

$$\Delta_D(E_z) = \frac{1}{2\pi}\int_0^{2\pi} \Delta_{D0}\left(\sqrt{2\beta E_z}\cos\vartheta\right)^2 \mathrm{d}\vartheta = \frac{2b\Delta B}{\mu_{\mathrm{B}}}E_z \tag{5.6}$$

Δ_D then only depends on the total energy $E = E_x + E_y + E_z$. In this simple case, the spin dynamics is independent of the geometry – whether it is anisotropic ($\omega_x \neq \omega_y \neq \omega_z$), or whether temperatures in different axes are different. Therefore we can have a kinetic equation for the spin density $\boldsymbol{S}(E,t)$ that only depends on the total energy [48, 72, 156]:

$$\begin{aligned}&\partial_t \boldsymbol{S}(E,t) + \gamma_c[\boldsymbol{S}(E,t) - \bar{\boldsymbol{S}}]\\ &\simeq \left[\Delta_D(E)\mathbf{e}_z + \omega_{\mathrm{ex}}\int_0^\infty \mathrm{d}E'\frac{\beta^3 E'^2}{2}e^{-\beta E'}K(E,E')\boldsymbol{S}(E',t)\right]\times \boldsymbol{S}(E,t)\end{aligned} \tag{5.7}$$

where $\bar{\boldsymbol{S}} \equiv \int_0^\infty \mathrm{d}E\frac{\beta^3E^2}{2}e^{-\beta E}\boldsymbol{S}(E)$ is the average spin in a 3D harmonic trap. The spin mean field is long-ranged in energy space after angle averaging. This is described by the kernel $K(E,E')$, which we will approximate by an infinite-ranged $K(E,E') \approx 1$ [48, 156].

The exchange rate, responsible for the ISRE, is given by $\omega_{\mathrm{ex}}/2\pi = 2\hbar|a_{\uparrow\downarrow}|\bar{n}/m$, where $\bar{n}$ is the average density, and $a_{\uparrow\downarrow}$ is the relevant scattering length. We have included a decay of the spin polarisation towards the mean field due to the lateral collision rate $\gamma_c = (32\sqrt{\pi}/3)a_{\uparrow\downarrow}^2\bar{n}v_T$.

However, it is harder to treat a case where Δ_D depends separately on E_x, E_y and E_z, e.g. a dephasing by the cavity field (see below) or by the Zeeman shift in the presence of gravitational sag. Eq. 5.7 then has to be rewritten for $\boldsymbol{S}(E_x,E_y,E_z,t)$. Nevertheless, one only has to modify $\Delta_D(E_x,E_y,E_z)$ as detailed in the simulation paragraph below.

Orders of magnitude Let us have an impression on the hierarchy of different timescales. We have our trapping frequencies $\{\omega_x,\omega_y,\omega_z\} \simeq 2\pi \times \{7,120,110\}$ Hz, where the transverse trap period of 8.9 ms sets the shortest timescale.

In our experiment, for a typical transverse temperature $T_y = T_z \simeq 200$ nK and $T_x \simeq 150$ nK (for the experiments in this section). We reach an average density (Eq. 1.12) of $\bar{n} \simeq 1.5 \times 10^{11}$ cm^{-3} for 2×10^4 atoms. As an example, for $\bar{n} = 10^{11}$ cm^{-3}, the exchange rate $\omega_{\rm ex}/2\pi \simeq \times 0.76$ Hz is indeed much slower than the longitudinal trap frequency. The lateral collision $\gamma_c \simeq 0.22$ s^{-1} is the slowest process. We are indeed in the collisionless regime.

The dephasing rate is also important. The dephasing due to collisional shift $\Delta_{\rm mf} \sim -0.07 \times \bar{n}\beta E$ Hz with $\bar{n}$ in 10^{11} cm^{-3}, is small compared to other dephasing processes. While the dephasing due to the Zeeman shift can be tuned by ΔB, however, close to the magic field, the gravitational sag can lead to very different energy-dependent dephasing along $\vec{z}$ from those in $\vec{y}$ and $\vec{x}$. The dephasing can no longer be approximated by Eq. 5.5. To give an idea, the numerical simulation gives a minimum ~ 0.14 Hz (standard deviation of the ensemble shift) including both the collisional shift and the Zeeman shift.

Numerical simulations We implement numerically Eq. 5.7 with three independent energies E_x, E_y and E_z.[1] Accordingly, the integral over energy is now three integrals over E_x, E_y and E_z with 1D density of states, namely $\int_0^\infty {\rm d}E'_x \beta e^{-\beta E'_x} K'(E_x, E'_x) \cdot \int_0^\infty {\rm d}E'_y \beta e^{-\beta E'_y} K'(E_y, E'_y) \cdot \int_0^\infty {\rm d}E'_z \beta e^{-\beta E'_z} K'(E_z, E'_z)$, where $K'(E_i, E'_i) \approx 1$ are the 1D kernels. The energies of each spin are drawn from a Boltzmann distribution ($\sim 10^4$ samples) and the differential (difference) equation is calculated for each spin with a time step of normally 5 ms.

To model the inhomogeneity Δ_D more accurately, we include the density shift and the effect of gravitational sag. Integrating Eq. 1.11 over the phase angle yields:

$$\begin{aligned}\Delta_B(E_x, E_y, E_z) =& b\Delta B^2 + 2\frac{b\Delta B}{\mu_{\rm B}}(E_x + E_y + E_z) \\ &+ \frac{2b}{\mu_{\rm B}^2}\left(E_x E_y + E_x E_z + E_y E_z + 2E_z \frac{mg^2}{\omega_z}\right) \\ &+ \frac{3b}{2\mu_{\rm B}^2}(E_x^2 + E_y^2 + E_z^2)\end{aligned} \tag{5.8}$$

The first term on the right-hand-side is the linear relation without the gravitational sag as we have seen earlier. The energy-dependent density shift is given by the integral of the Gaussian spatial distributions over phase angles (Eq. 1.12):

$$\Delta_{\rm mf}(E_x, E_y, E_z) = \Delta_{\rm mf0} \cdot e^{-\frac{E_x}{2k_{\rm B}T_x} - \frac{E_y}{2k_{\rm B}T_y} - \frac{E_z}{2k_{\rm B}T_z}} {\rm I}_0\left(\frac{E_x}{2k_{\rm B}T_x}\right) {\rm I}_0\left(\frac{E_y}{2k_{\rm B}T_y}\right) {\rm I}_0\left(\frac{E_z}{2k_{\rm B}T_z}\right) \tag{5.9}$$

where the peak shift is (Eq. 1.13):

$$\Delta_{\rm mf0} = \frac{2\hbar}{m}(a_{\uparrow\uparrow} - a_{\downarrow\downarrow}) \frac{N\omega_x\omega_y\omega_z}{\sqrt{T_x T_y T_z}} \left(\frac{m}{2\pi k_{\rm B}}\right)^{\frac{3}{2}} \tag{5.10}$$

In fact, one can also use the position dependence of Δ_D expressed in $E_{x,y,z}$ with a random initial phase angle for each atom. The phase angles evolve subsequently according to the harmonic oscillations. Specifically, we solve for $\boldsymbol{S}(E_x, \vartheta_x(t), E_y, \vartheta_y(t), E_z, \vartheta_z(t), t)$ through

[1] Based on the code of Jean-Noël Fuchs

$\Delta_D(E_x, \vartheta_x(t), E_y, \vartheta_y(t), E_z, \vartheta_z(t))$ This requires finer time steps (e.g. 0.5 ms) but allows to model imperfect motional averaging.

We also take into account the atom loss phenomenologically through an exponentially decaying (lifetime ~ 2.7 s) average density.

5.1.5 Observation of ISRE via motional energy

During my thesis, we realised that we could have another demonstration of ISRE in our system, based on the direct observation of the spin-energy correlation.[2] As explained in the two-class model, the key is that individual spins leave the equator in correlation with their motional energies, modifying the probability to be projected into state $|\uparrow\rangle$ or $|\downarrow\rangle$. As a result, the two eigenstates will have different average motional energies (or temperatures), measurable by imaging the expansion of the cloud.

In the picture of Fig. 5.1(b), which state gets an increase in its motional energy (more contributions from the hotter atoms) is determined by the direction of the spin rotation as well as the sense of dephasing (in the rotating frame of the total spin). Although the direction of the spin rotation is determined by the sign of the scattering length $a_{\uparrow\downarrow}$, not tunable in our experiment, the sign of dephasing can be reversed through ΔB (Eq. 5.5). In other words, by varying the sign of ΔB, one can determine if the hotter atoms rotate above or below the equator (opposite for the colder atoms), hence the sign of the energy evolution of the detected spin states.

In the experiment, we prepare a CSS on the equator with a $\pi/2$ pulse and then image the two spin states after a variable free evolution in the trap. The two states are spatially separated using the ARP method (Sec. 2.2.7.1) before imaging. After a sufficient TOF, the size of each cloud reflects the average thermal energy of the state. More rigorously, we can fit the expansion of the clouds using images at different TOFs.

As the cloud is imaged along $\vec{y}$, we have access to the thermal energies in both the longitudinal ($\vec{x}$) and transverse ($\vec{z}$) directions. In fact, they are different because the trap decompression into the extreme aspect ratio after the evaporative cooling is not sufficiently slow to allow thermalisation among different axes.

As shown in Fig. 5.3, far below or above the magic field (left and right columns) such that the dephasing due to Zeeman shift is strong enough, we indeed observe the departure of the two spin states in their thermal energies, both in $\vec{z}$ and $\vec{x}$. The signs of the evolution are opposite at opposite sides of the magic field.

The middle column deserves more attention. While it is not at the magic field ($B_x = 3.6$ G), the energy evolution in $\vec{z}$ (first row) is suppressed, different from that in $\vec{x}$ (second row). This is because the gravitational sag in $\vec{z}$ modified $\Delta_D(E_z)$ such that the minimum (absolute value) is shifted away from the magic field $\Delta B = 0$ (see Eq. 5.8). Here we are close to this field and hence almost no (dephasing induced) energy evolution in $\vec{z}$ is observed. But we do observe energy evolutions in $\vec{x}$, because the optimum field in $\vec{x}$ is close to the magic field. This is confirmed in a similar measurement where we fine-tune the bottom field around the magic field (Fig. 5.4).

Unfortunately, the fit to the cloud expansion is not perfect and results in systematic errors of the inferred temperature, most likely due to our detection scheme. As mentioned in Sec. 2.2.7.1, the ARP perturbs the trap and gives a momentum kick to the atoms (different

[2] It should have been measurable in the previous setup as well.

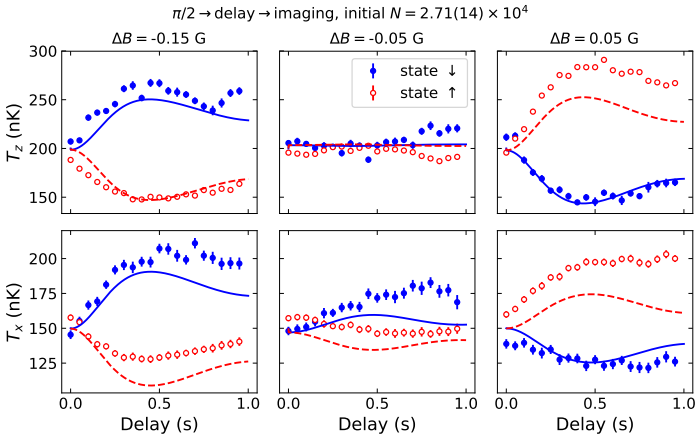

Figure 5.3 Cloud temperatures as a function of evolution time in the trap, at different bottom fields. Temperatures are obtained from a fit of the cloud expansion at six different TOFs, both in $\vec{z}$ (first row) and in $\vec{x}$ (second row). The fit is not perfect and may have systematic errors, e.g. the temperature difference of the two states at zero delay (different in $\vec{z}$ and $\vec{x}$) is most likely a bias of the temperature estimation. The middle column corresponds to the optimum field in the transverse direction, showing a suppressed evolution. But it is not the optimum field in $\vec{x}$. Further below (left column) or above (right column) the magic field, strong departures in temperature appear and have opposite signs. All these features are reproduced by the simulation (solid and dashed curves). We assumed $T_z = 200$ nK and $T_x = 150$ nK, so the two states have the same temperature at zero delay. Quantitative comparison is limited by the accuracy of the temperature measurements.

for the two states). This is maybe responsible for, e.g. the initial temperature difference of the two states. Nevertheless, the evolution can be clearly identified, allowing qualitative comparison with the theory.

Numerical simulations using Eq. 5.7[3] well reproduce the evolutions, including the different optimal (minimum-dephasing) fields in $\vec{x}$ and $\vec{z}$. There is no free parameters in the model apart from a factor of 0.8 in ω_{ex} to better fit the data.[4] The average transverse energy $(E_y + E_z)/2$ instead of E_z better matches the data in $\vec{z}$, meaning that there is probably energy mixing between the transverse directions, due to e.g. anharmonicity of the trap and collisions. There is probably energy mixing between $\vec{x}$ and the transverse directions as well, shown as the slow rising of temperature in $\vec{x}$ at the magic field (Fig. 5.4, right-most panel).

In the following, this evolution of thermal energies of the spin states will serve as a signature of ISRE in our system.

5.2 Interplay between ISRE and cavity measurements

In the previous context, the ISRE is initiated by the dephasing between atoms in different energy classes, due to inhomogeneous Zeeman shift in the magnetic trap. Nevertheless, close to the magic field, the motional-energy evolution caused by ISRE is suppressed. In

[3] More precisely, with three independent energies $\boldsymbol{S}(E_x, E_y, E_z, t)$.

[4] Similar discrepancy is found in [48]. This is because the infinite-range assumption ($K(E, E') = 1$) artificially enhances the effect of the ISRE, which is compensated by reducing the numerical value of ω_{ex}.

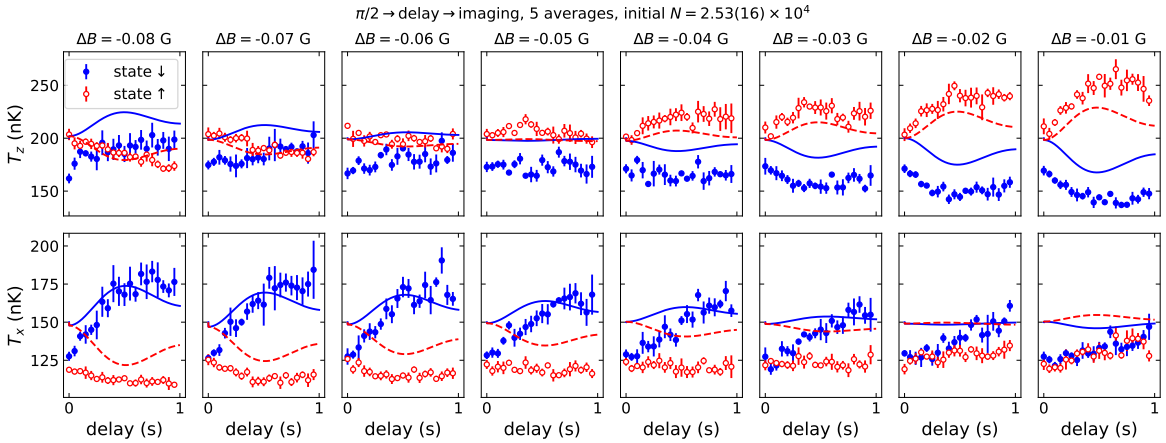

Figure 5.4 Evolution of cloud temperature varying ΔB in smaller steps. Here the temperature is inferred from the cloud size after a fixed TOF (10 ms for $|\uparrow\rangle$ and 12.5 ms for $|\downarrow\rangle$), possibly containing even larger systematic error (no correction here). Nevertheless, the different evolutions of the two states can be seen qualitatively. The bottom fields at which ISRE is minimum differ in $\vec{z}$ (first row) and in $\vec{x}$ (second row). We also plot the simulation for comparison, again assuming $T_z = 200$ nK and $T_x = 150$ nK.

the following, we consider the dephasing induced by the inhomogeneous light shift from the cavity field, which will also trigger the ISRE. A key difference is that the inhomogeneity is only present during a probe pulse (e.g. at the beginning of a sequence) but is almost vanishing thereafter, setting a kind of initial condition for the spin evolution. We shall see that the cavity measurement is in turn affected by the ISRE.

5.2.1 Origin: inhomogeneous coupling

Correlation between energy and light shift As discussed in Sec. 4.1, the atom-cavity coupling is inhomogeneous due to the comparable sizes of the atomic cloud and the cavity mode in the transverse direction. It leads to inhomogeneous light shift and hence dephasing. We have also considered motional averaging if the probe is sufficiently long, leading to the energy-dependent dephasing rate, e.g. in $\vec{z}$ (Eq. 4.5):

$$\Delta_D^{\mathrm{ls}}(E_z) = \Omega_c(E_z) = \Omega_{c0} \exp\left[-\frac{2E_z}{m\omega_z^2 w_0^2}\right] \mathrm{I}_0\left(\frac{2E_z}{m\omega_z^2 w_0^2}\right) \tag{5.11}$$

As we know from the previous section, this correlation between motional energy and dephasing rate leads to ISRE. The spins rotate out of the equator (for a given energy class) and the energies of the two spin states subsequently evolve (as in Fig. 5.3).

Cavity frequency affected by the motional energy On the other hand, the cavity frequency is determined by the spin $s_z^{(i)}$ of each atom i and by the couplings $\Omega_c^{(i)}$. Again in a simplistic picture, we consider atoms in two energy classes (hot (h) and cold (c)),

$$\delta\omega_c = \Omega_c^{(h)} S_z^{(h)} + \Omega_c^{(c)} S_z^{(c)} \tag{5.12}$$

Obviously, colder atoms stay closer to the cavity centre, having a stronger coupling to the cavity, $\Omega_c^{(c)} > \Omega_c^{(h)}$. The important role of the ISRE is to rotate each class out of the equator

(Fig. 5.1 and 5.5) $S_z^{(h)} = -S_z^{(c)} \neq 0$. The cavity frequency will shift even if the total spin $S_z = S_z^{(h)} + S_z^{(c)} = 0$ stays on the equator.

An alternative picture can be drawn considering only the average motional energies of the two spin states. As we know, the deviation of the energies for the two spins is a measurable signature of ISRE. The cavity shift can also be written as

$$\delta\omega_c = \tilde{\Omega}_c S_z = \frac{1}{2}\tilde{\Omega}_c(E_\uparrow)N_\uparrow - \frac{1}{2}\tilde{\Omega}_c(E_\downarrow)N_\downarrow \tag{5.13}$$

where $\tilde{\Omega}_c(E_\uparrow)$ is the average coupling of $|\uparrow\rangle$ with its average energy $E_\uparrow$. Even though $N_\uparrow = N_\downarrow$, we can have $\delta\omega_c \neq 0$ if $E_\uparrow \neq E_\downarrow$, which is a result of ISRE.

In summary, cavity probing introduces energy-dependent light shift on the atoms that will trigger ISRE. But the spin dynamics – correlation between motional energy and $s_z^{(i)}$ – again shifts the cavity. This is the essential picture that is demonstrated in the following experiments.

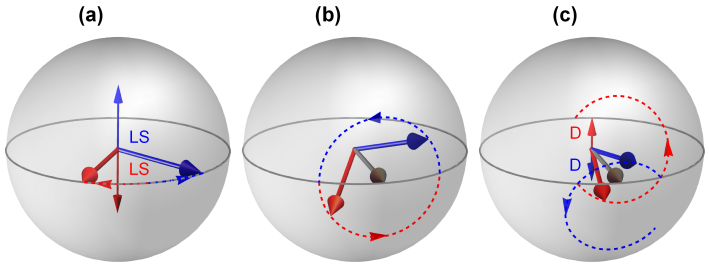

Figure 5.5 Schematics of ISRE for two classes of spins, triggered by cavity light shift. The Bloch sphere is again in the rotating frame of the total spin. Here the dominant dephasing is the light shift (LS) from the cavity field. A cavity probe dephases the two spins instantly (a). Afterwards, the two spins are left evolving under ISRE without dephasing (b). Note that the two spins rotate around their sum but don't rephase. In case of some residual dephasing (c), e.g. due to the trap, the trajectories of the two spins are shifted, therefore an "irregular" oscillation of the motional energy can be observed.

5.2.2 Cavity shift in a continuous probing

Here I describe the first measurement that pointed us towards the interaction between cavity measurements and spin dynamics. Simply sending probe light into the cavity continuously and monitoring the cavity resonance,[5] we observe a "drift" of the cavity frequency. Change in the total S_z is excluded by the final detection through imaging. As I explained above, if the atom-cavity coupling evolves differently for the two spin states, a cavity shift would appear. But before knowing this, we have been looking for dependences of this cavity shift, finding that the cavity shift is generally related to the probe power as well as the number of atoms (Fig. 5.6). In particular, the evolution of cavity resonance stops earlier with a stronger probe, and the cavity shift is larger with more atoms. Once linking the cavity shift to the ISRE, it is easy to understand these features: the stop of the cavity shift is due to the loss of coherence, without which the ISRE no longer happens; and the strength of the ISRE (ω_{ex}) is determined by the atomic density, or the atom number in practice.

[5] We monitor the cavity transmission with different probe detunings, and reconstruct the cavity resonance.

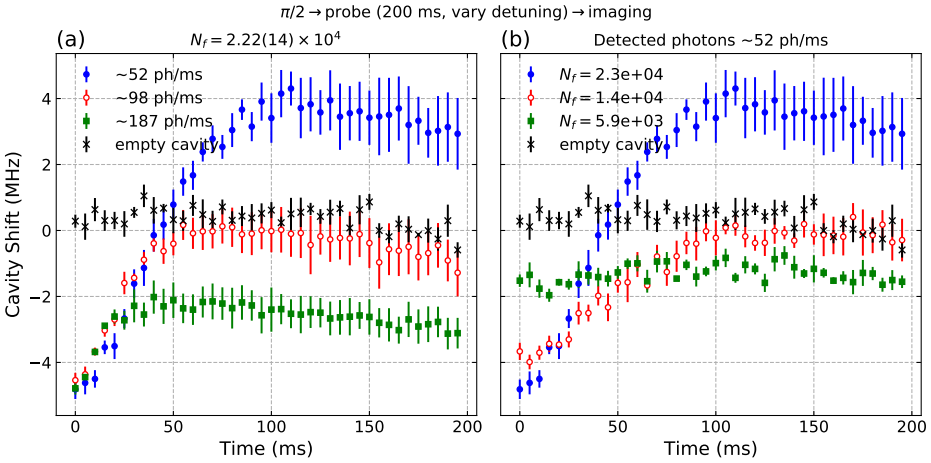

Figure 5.6 The evolution of cavity resonance with different probe powers (a) and different atom numbers (b). The cavity resonance frequency is reconstructed from the transmission signals in time at six different probe detunings. As the cavity shift does depend on the transmission, this method leads to large errors in determining the cavity shift (large error bars in case of strong evolution).

5.2.3 ISRE triggered by a probe pulse

To confirm that a cavity measurement indeed triggers the ISRE, we should be able to see its signature: the evolution of thermal energies of the two eigenstates. So we perform a similar experiment as in Sec. 5.1.5. After initial preparation with a $\pi/2$ pulse, we send a short cavity probe (10 ms) and then image the clouds of the two states after different delays in the trap. The experiment is performed at the magic field, such that the dephasing in the system is easily dominated by the dephasing from a cavity probe.

Unlike the dephasing from the trap which is always present (recall Fig. 5.1), the cavity-induced dephasing can be turned off. In fact, the cavity probe is short compared to the timescale of spin dynamics such that the dephasing is almost instantaneous. But it is long enough to establish the energy dependence[6] (transversely as in Eq. 5.11). Therefore, as sketched in Fig. 5.5 for the two-energy-class model, the cavity probe introduces some initial dephasing which triggers the ISRE (a). In the absence of dephasing from the trap, the spins rotate purely around their sum under ISRE (b). It is qualitatively different from Fig. 5.1 as the contrast does not evolve after the cavity probe, and rephasing never occurs. However, in the presence of residual dephasing from the trap (c), the pure ISRE rotation will be shifted, resulting in a modulation in the coherence. As for the energies of the spin states upon projection, we expect that they evolve in an oscillatory manner – a pure oscillation with a period $\sim 2\pi/\omega_{\mathrm{ex}}$ in the absence of residual dephasing.

Experimentally, the probe light is at cavity resonance – in contrast to a real cavity measurement – to minimise fluctuations in the transmitted photons (due to frequency shift by atomic QPN). We vary the probe power hence the initial dephasing, measured in detected photons n_d (Fig. 5.7). We indeed observe an oscillatory evolution of the temperatures of the two states, most visible along $\vec{z}$ (the temperatures are inferred from the size of the cloud

[6] Even for a really instantaneous probe, there is always some energy dependence.

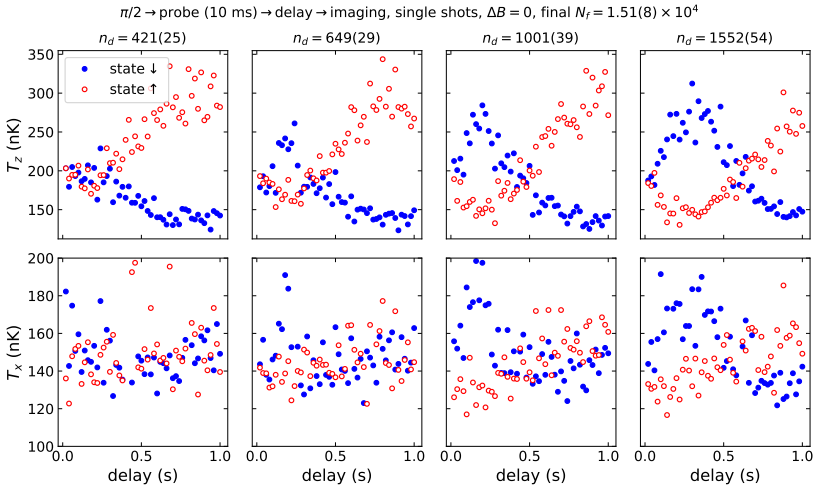

Figure 5.7 Evolution of thermal energies of the two spin states after a cavity probe of various power. From left to right, increasing probe power (measured in detected photons n_d). Data are single shots. Measured at a fixed TOF (10 ms for $|\uparrow\rangle$ and 12.5 ms for $|\downarrow\rangle$), the inferred temperatures along $\vec{z}$ are shown in the first row, and those along $\vec{x}$ are shown in the second row.

after TOF). The amplitude of the oscillation increases as the probe power increases. But the oscillation is not regular, making it hard to estimate the oscillation period. As I pointed out, this is the effect of residual dephasing from the trap (Fig. 5.5(c)). Numerical simulations well reproduce the combined effect of both types of dephasing, for the following experiment shown in Fig. 5.8.

5.2.4 Dynamics in motional energy sensed by cavity shift

One step further, we should also be able to see that the cavity frequency is in turn affected by the spin dynamics. In a slightly more sophisticated measurement, we again measure the thermal energies with a delay after a cavity probe. But now this cavity probe (10 ms) has a small sweep in frequency, capable of determining the cavity resonance in a single shot (similar to the cavity spectra in Sec. 3.2.2, but with a small range covering $\sim 2\kappa/2\pi$). In terms of induced dephasing, only the number of transmitted photons is relevant (as we have characterised the probe induced dephasing in Sec. 4.1.3). Immediately before the imaging, we perform another cavity probe, measuring the cavity frequency at the end of the evolution. The dephasing introduced by the second probe should not immediately affect the motional energies, since the 10 ms probe is much shorter than the ISRE timescale. Therefore we obtain not only the information of the thermal energies as in the previous experiment, but also the cavity shift (with respect to the first cavity probe) at the end of the evolution.

As shown in Fig. 5.8, we observe again the oscillatory evolution of the thermal energies of the two states (most clearly in $\vec{z}$). We also observe a similar evolution of the cavity resonance: $\delta\omega_c$ is almost proportional to the energy E_z of $|\downarrow\rangle$. It is not surprising if we consider the simple model (Eq. 5.13) with coupling $\tilde{\Omega}_c(E)$ a linear function of energy. This is a direct evidence of the interaction between the ISRE and the cavity measurement.

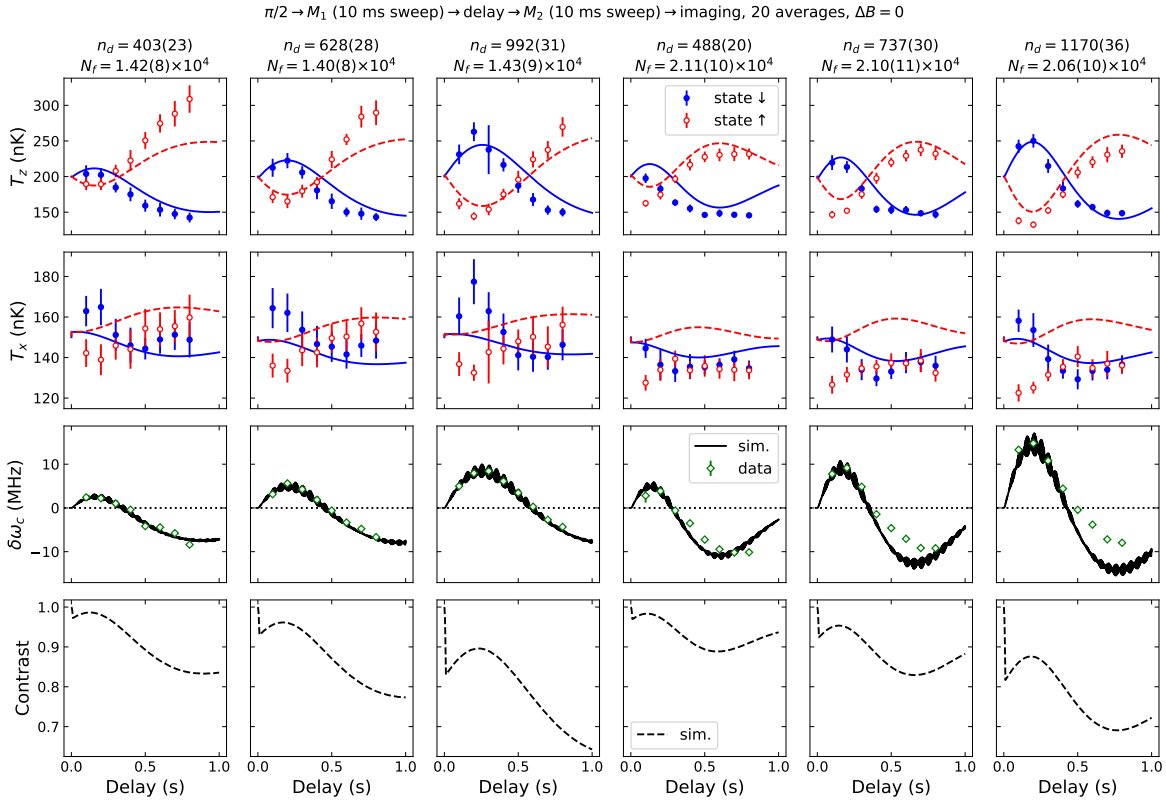

Figure 5.8 Evolution of thermal energies of the two spin states and of the cavity frequency shift $\delta\omega_c$ as a function of the delay after a cavity probe. The columns correspond to different experimental conditions: the first three have the same number of atoms (final atom number N_f) but increasing probe power (n_d); same for the last three but with a larger atom number. The inferred temperatures along $\vec{z}$ ($\vec{x}$) are shown in the first (second) row, with numerical simulations shown in solid and dashed curves for $|\downarrow\rangle$ and $|\uparrow\rangle$ respectively. Again the temperature estimations are not accurate, especially in $\vec{x}$, while the simulation assumes $T_z = 200$ nK and $T_x = 150$ nK. The third row shows the cavity shift (open green diamonds) as well as the simulation. The fast oscillation in the simulation is a result of imperfect motional averaging. The simulated contrast (no data) is also shown in the forth row. The contrast evolution is due to the residual dephasing from the trap.

Numerical simulation Same as the methods in Sec. 5.1.4, the numerical simulation has no free parameters apart from using $0.8 \times \omega_{\text{ex}}$ instead of the theoretical value. The cavity light shift Ω_{c0} (as a function of n_d) is calculated based on cavity parameters (cf. Sec.2.3.1), with a detection efficiency $q_d = 0.5$ (Fig. 4.3). The cavity shift is obtained from the position dependent coupling (Eq. 4.2), using the position of each atom at each time step (keeping track of the trajectories). In fact, the dephasing is also numerically introduced in this way. The fast modulation (frequency ~ 220 Hz) in the cavity shift is a result of imperfect motional averaging (as it is in reality). Indeed, the fast oscillation has been observed in other measurements (not shown).

The motional-energy simulations in $\vec{x}$ do not agree with the data, despite possible bias in the temperature estimation. In the simulation, the evolution in $\vec{x}$ is essentially given by the dephasing from the trap, since the dephasing due to the probe is weak and the optimal field is not at $\Delta B = 0$ due to density shift. However, the data show an optimum field in $\vec{x}$ very close to $\Delta B = 0$ (see also the discrepancy in Fig. 5.4) and there seems to be an impact from the probe. The reason is still unclear, possibly related to the energy mixing among different axes.

5.3 Amplification of quantum fluctuations

In the previous chapter, the squeezing measurements (Fig. 4.9) show a near-perfect correlation between two consecutive (composite) cavity measurements. However, we shall see in this section that when the second measurement is further delayed, it gives an amplified signal compared to the first one, depending on the delay and other parameters. I will show that this amplification effect is a result of ISRE induced by our particular composite-measurement scheme, namely a measurement M_1 is in fact $M_1^{(1)} \to \pi \to M_1^{(2)}$. While the effect can be understood semi-classically, there are still open questions concerning how the quantum correlation of the spin-squeezed states is affected by the spin-energy correlation due to the ISRE.

5.3.1 Experimental observations

Let us start with the experimental observations. As in the squeezing measurements (Fig. 4.8), we prepare a CSS with a $\pi/2$ pulse and perform two composite measurements M_1 and M_2 (recall Sec. 4.2.1), now with a variable delay in between that extends to almost a second.[7] The probe power is also varied, and the experiment is repeated 100 times in each condition for statistics.

We keep the same definition used in Ch. 4: a cavity measurement M_i is the detected transmission photons (Eq. 4.11). The fluctuations in M_1 and M_2 are evaluated through the statistics of the photon counts, shown in Fig. 5.9 (cf. Fig. 4.9). If we recall how QND measurements look: the fluctuation of M_1 or M_2 alone is limited by the QPN of the atoms (solid black lines) while their correlation $\text{Std}(M_1 - M_2)$ is determined by the measurement uncertainty, limited by the PSN: $\text{Std}(M_i) = \sqrt{\langle M_i \rangle}$ (dotted curves).

However, the fluctuation of M_2 appears to be much larger than expected, also dependent on the delay between the measurements. But looking at the raw data (Fig. 5.10), M_2 is

[7] In fact, we also added a third measurement right after the second, but it agrees with the second and is not relevant in this discussion.

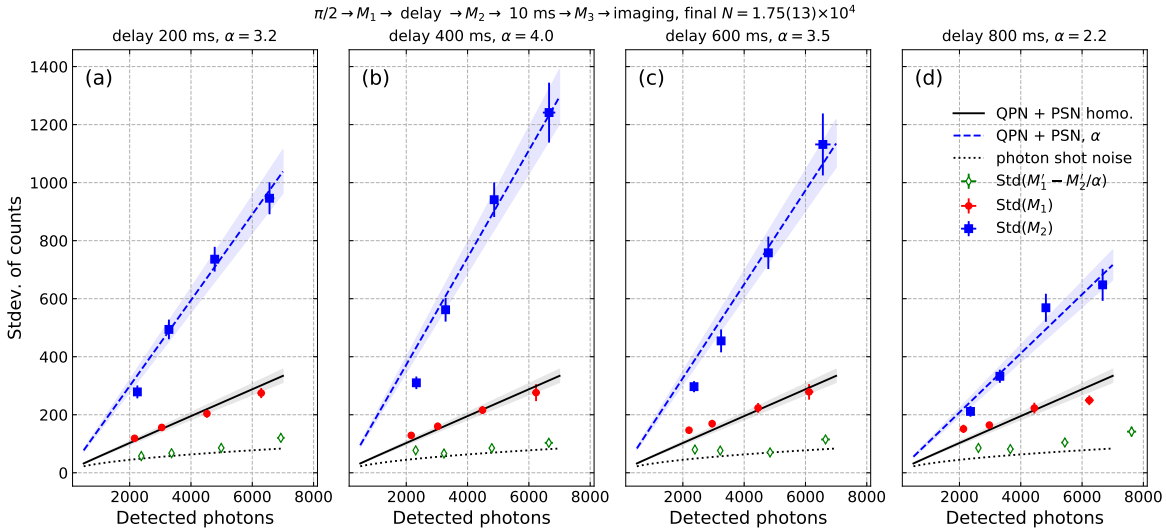

Figure 5.9 Statistics of cavity measurements showing the amplification effect. Each panel shows the standard deviation of 100 repeated measurements (M_1, red circles and M_2, blue squares) at four different probe powers. (a)-(d) show four different delays between the two measurements. Error bars are obtained from bootstrapping. M_2 has larger fluctuations while the dashed blue lines are simply estimations with a constant amplification factor. $\mathrm{Std}(M_1' - M_2'/\alpha)$ (open green diamonds) shows a strong correlation between the two measurements.

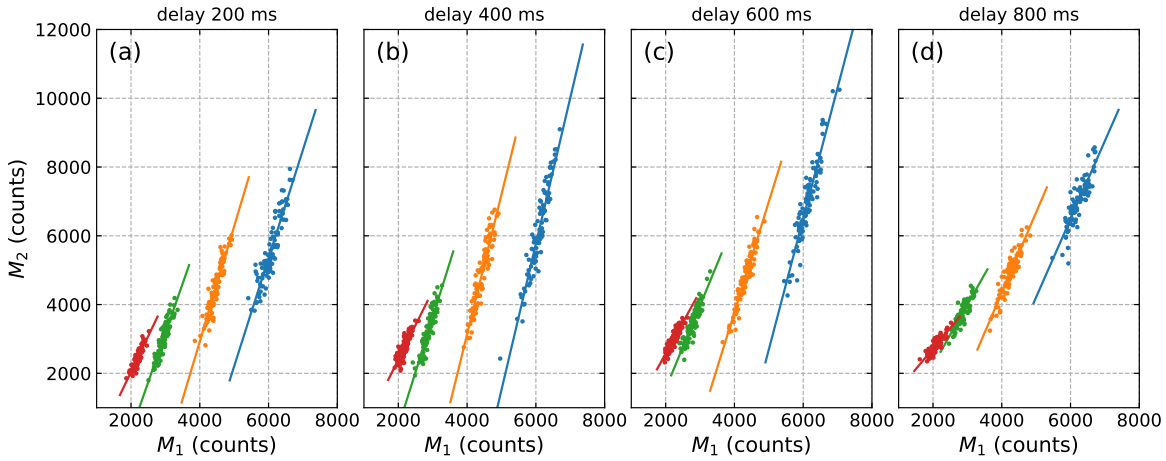

Figure 5.10 Raw data showing M_1 versus M_2. Correlations are clearly visible, though the scaling factors vary over datasets with different measurement strengths (different colours). Solid lines are linear fits to guide the eye.

clearly correlated with M_1. For convenience, we define the measurement deviation from the expectation value

$$M_i' \equiv M_i - \langle M_i \rangle \tag{5.14}$$

Note that $\mathrm{Var}(M_i') = \mathrm{Var}(M_i)$. While the two measurements have the same average signal $\langle M_1 \rangle = \langle M_2 \rangle$, we observe that M_2' has been "amplified" with respect to M_1', rather than being noisier. The linear fits reveal the "amplification factors", which vary with the delay and with the measurement strengths.

To quantify the correlations, we can evaluate the variance $\mathrm{Var}(M_1' - M_2'/\alpha)$ with the amplification factor α. In fact, in Fig. 5.9, we start with a simpler approach: finding a constant amplification α at each delay that roughly produces the M_2 fluctuations (dashed blue lines). This α is already close: the corresponding $\mathrm{Var}(M_1' - M_2'/\alpha)$ approaches the PSN limit (dotted curve).

Let me clarify the PSN limit with amplified signals. Recall Eq. 4.21, we can write the measurement deviation as (probe detuning $\kappa/2$)

$$M_i' = \delta n_{d,i} + \frac{2\tilde{\Omega}_c}{\kappa} \langle M_i \rangle S_z \tag{5.15}$$

where $\mathrm{Var}(\delta n_{d,i}) = \langle M_i \rangle$ accounts for the PSN. With $\langle M_1 \rangle = \langle M_2 \rangle$, the correlation between M_1' and the rescaled M_2' can be quantified as:

$$\mathrm{Var}\left(M_1' - \frac{M_2'}{\alpha}\right) = \mathrm{Var}\left[\delta n_{d,1} - \frac{\delta n_{d,2}}{\alpha} + \frac{2\langle M_1 \rangle}{\kappa}\left(\tilde{\Omega}_c S_z\big|_{M_1} - \frac{\tilde{\Omega}_c S_z}{\alpha}\bigg|_{M_2}\right)\right] \tag{5.16}$$

In the last (round) brackets we use $|_{M_i}$ to distinguish the two measurements. For QND measurements, S_z is conserved, and we will see that it is the coupling that gets "amplified" between the measurements. Nevertheless, without knowing the detail, the variance is minimised if the term in these brackets vanishes, reaching the PSN limit

$$\mathrm{Var}\left(M_1' - \frac{M_2'}{\alpha}\right)\bigg|_{\mathrm{psn}} = \langle M_1 \rangle + \frac{\langle M_2 \rangle}{\alpha^2} \tag{5.17}$$

same as a measurement with $\langle M_1 \rangle + \langle M_2 \rangle/\alpha^2$ photons. In Fig. 5.9, we plot $\mathrm{Std}(M_1' - M_2'/\alpha)$ versus $\langle M_1 \rangle + \langle M_2 \rangle/\alpha^2$ to compare with the normal PSN scaling (dotted curves). On the other hand, approaching this scaling means that there is indeed near-perfect correlation between M_1 and M_2.

Amplification factors More rigorously, we can estimate the amplification factor α in two different ways. Firstly, we have the fluctuation of each measurement from Eq. 5.15:

$$\mathrm{Var}(M_i) = \langle M_i \rangle + \left(\frac{2\tilde{\Omega}_c \langle M_i \rangle}{\kappa}\right)^2 \mathrm{Var}(S_z) \tag{5.18}$$

with $\mathrm{Var}(S_z) = N/4$.[8] For α such that Eq. 5.16 is minimised, i.e., $\tilde{\Omega}_c|_{M_2} = \alpha \tilde{\Omega}_c|_{M_1}$, we can obtain α simply from the statistics of individual measurements

$$\alpha = \sqrt{\frac{\mathrm{Var}(M_2) - \langle M_2 \rangle}{\mathrm{Var}(M_1) - \langle M_1 \rangle}} \tag{5.19}$$

[8] We will assume homogeneous coupling in this chapter, which does not affect our discussions.

The second way is to minimise $\mathrm{Var}(M_1' - M_2'/\alpha)$ with respect to α, equivalent to $\alpha = \mathrm{Var}(M_2')/\mathrm{Cov}(M_1', M_2')$, where Cov( ) denotes covariance. Interestingly, this is not the same as minimising $\mathrm{Var}(\alpha M_1' - M_2')$ (equivalently $\alpha = \mathrm{Cov}(M_1', M_2')/\mathrm{Var}(M_1')$) due to the uncorrelated PSN in M_1 and M_2. The former expression gives a larger and less biased α than the latter. More accurately, one can minimise the variance normalised to the PSN, namely $\mathrm{Var}(M_1' - M_2'/\alpha)/(\langle M_1\rangle + \langle M_2\rangle/\alpha^2)$ (or equivalently $\mathrm{Var}(\alpha M_1' - M_2')/(\alpha^2\langle M_1\rangle + \langle M_2\rangle)$, which now gives the same result). We perform this minimisation numerically.

We obtain the amplification factors from each dataset using the two methods and the results are shown in Fig. 5.11. In the second row we plot again the correlation ($\mathrm{Std}(M_1' - M_2'/\alpha)$ versus $\langle M_1\rangle + \langle M_2\rangle/\alpha^2$) with the corresponding α to compare with the PSN limit. In general, the two methods agree well. The α's obtained from the statistics of individual measurements (the first method) indeed provide the minimum $\mathrm{Std}(M_1' - M_2'/\alpha)$.

We observe that for a given delay, the amplification factor is not a constant, but generally increases as the measurement strength increases. It also varies with atomic density (data not shown).

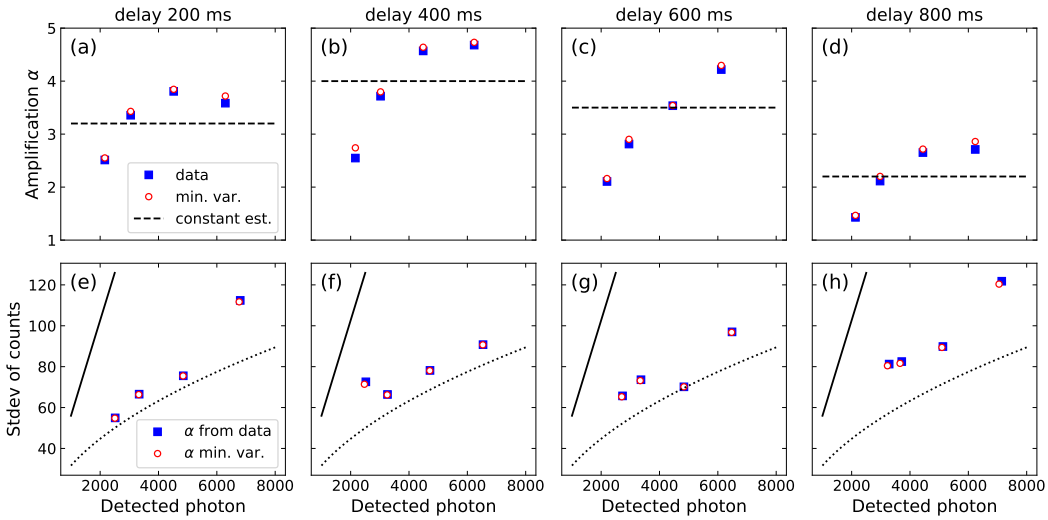

Figure 5.11 The amplification factors (first row) calculated using Eq. 5.19 (blue squares) and those minimise $\mathrm{Var}(M_1' - M_2'/\alpha)$ (open red circles). The dashed lines indicate the constant amplifications used for illustration purpose in Fig. 5.9. Shown in the second row, the α's from Eq. 5.19 almost minimise $\mathrm{Std}(M_1' - M_2'/\alpha)$ (blue squares), compared to the true minima (open red circles). The dotted and solid curves are the PSN limit and the QPN+PSN as in Fig. 5.9 for comparison.

A heuristic picture We can have a heuristic understanding of the amplification mechanism before going to a microscopic model. Here we only consider average motional energies of the two spin eigenstates. Following the idea of Eq. 5.13, we can write the measurement deviation as (Eq. 5.15, ignoring PSN):

$$M_i' = \frac{2\tilde{\Omega}_c}{\kappa}\langle M_i\rangle S_z = \frac{\langle M_i\rangle}{\kappa}\left[\tilde{\Omega}_c(E_\uparrow)N_\uparrow - \tilde{\Omega}_c(E_\downarrow)N_\downarrow\right] \tag{5.20}$$

such that the average coupling $\tilde{\Omega}_c(E_{\uparrow(\downarrow)})$ is a function of the energy $E_{\uparrow(\downarrow)}$ of the two spin eigenstates, and they can deviate from each other due to ISRE. For the first measurement, we shall assume that $E_\uparrow = E_\downarrow$, and the initial coupling $\tilde{\Omega}_c^{(0)}$ is common to both states,

$$M_1' = \frac{\langle M_1 \rangle}{\kappa} \tilde{\Omega}_c^{(0)} \left(N_\uparrow - N_\downarrow\right) \tag{5.21}$$

While for the second measurement, $E_{\uparrow(\downarrow)}$ can evolve. Let us assume a first-order perturbation $\delta E_{\uparrow(\downarrow)}$ with $k_e \equiv \partial\tilde{\Omega}_c/\partial E$. We have

$$M_2' = \frac{\langle M_2 \rangle}{\kappa} \tilde{\Omega}_c^{(0)} \left[\left(1 + k_e \delta E_\uparrow\right) N_\uparrow - \left(1 + k_e \delta E_\downarrow\right) N_\downarrow\right] \tag{5.22}$$

The ISRE and the subsequent energy evolution are triggered by an energy-dependent dephasing (Sec. 5.2.3). This missing piece is provided by the way we perform the composite measurements (Sec. 4.2.1). M_1 introduces a correlation between the residual dephasing and S_z (different in each realisation). We can write, in a heuristic manner, that $\delta E_\uparrow = -\delta E_\downarrow = k_s S_z$. We find

$$\begin{aligned} M_2' &= \frac{\langle M_2 \rangle}{\kappa} \tilde{\Omega}_c^{(0)} \left[\left(1 + k_e k_s S_z\right) N_\uparrow - \left(1 - k_e k_s S_z\right) N_\downarrow\right] \\ &= \frac{\langle M_2 \rangle}{\kappa} \tilde{\Omega}_c^{(0)} \left(1 + \frac{1}{2} k_e k_s N\right) \left(N_\uparrow - N_\downarrow\right) \end{aligned} \tag{5.23}$$

where $N = N_\uparrow + N_\downarrow$. Indeed, M_2' appears to be amplified compared to M_1' with $\alpha = 1 + k_e k_s N/2$.

This picture, in terms of the motional energies of the spin eigenstates, is based on our knowledge of ISRE developed in the previous section. In the following I will provide a more microscopic picture, again in the two-energy-class model, as we have used earlier.

5.3.2 Simple model with two energy classes

Here I will demonstrate the advent of the amplification effect in the simple two-class model introduced at the beginning of this chapter. We start again with Eq. 5.15, now distinguishing two energy classes (hot (h) and cold (c), cf. Eq. 5.12)

$$M_i' = \frac{\langle M_i \rangle}{\kappa} \left[\Omega_c^{(h)} S_z^{(h)} + \Omega_c^{(c)} S_z^{(c)}\right] \tag{5.24}$$

Remember that we have $\Omega_c^{(h)} < \Omega_c^{(c)}$. Now we introduce

$$c_0 = \frac{1}{2\kappa}\left(\Omega_c^{(h)} + \Omega_c^{(c)}\right) \;; \quad \gamma = \frac{1}{2\kappa}\left(\Omega_c^{(h)} - \Omega_c^{(c)}\right) \tag{5.25}$$

$$S_z = S_z^{(h)} + S_z^{(c)} \;; \quad \delta S_z = S_z^{(h)} - S_z^{(c)} \tag{5.26}$$

Therefore

$$\begin{aligned} M_i' &= \langle M_i \rangle (c_0 + \gamma) \left(\frac{S_z + \delta S_z}{2}\right) + \langle M_i \rangle (c_0 - \gamma) \left(\frac{S_z - \delta S_z}{2}\right) \\ &= \langle M_i \rangle (c_0 S_z + \gamma \delta S_z) \end{aligned} \tag{5.27}$$

Note that $\gamma < 0$. Initially, after the $\pi/2$ pulse that prepares the CSS, $S_z^{(h)} = S_z^{(c)}$ hence $\delta S_z = 0$. So for the first measurement we recover $M_1' = \langle M_1 \rangle c_0 S_z$.

Residual dephasing by the composite measurement Consider first a single class of atoms, the phase shift induced by a cavity probe is related to transmitted photons, recall Eq. 1.56,

$$\tilde{\phi}_{\rm ac} = \frac{2\tilde{\Omega}_c}{q_d\kappa} n_d \tag{5.28}$$

For a composite measurement, where a π pulse separates two probe pulses, the phase shifts from two probes largely cancel each other. Now we consider the first composite measurement M_1 after preparing the CSS, consisting of two probes with photons $M_1^{(1)}$ and $M_1^{(2)}$ (see Eq. 4.21). Ignoring the PSN, the total phase shift reads:

$$\begin{aligned}
\Delta\phi_{\rm ac} = \tilde{\phi}_{\rm ac}^{(1)} - \tilde{\phi}_{\rm ac}^{(2)} &= \frac{2\tilde{\Omega}_c}{q_d\kappa} M_1^{(1)}(S_z) - \frac{2\tilde{\Omega}_c}{q_d\kappa} M_1^{(2)}(-S_z) \\
&= \frac{2\tilde{\Omega}_c}{q_d\kappa}\left[\left(\langle M_1^{(1)}\rangle + \langle M_1^{(1)}\rangle c_0 S_z\right) - \left(\langle M_1^{(2)}\rangle - \langle M_1^{(2)}\rangle c_0 S_z\right)\right] \\
&= \frac{2\tilde{\Omega}_c}{q_d\kappa}\langle M_1\rangle c_0 S_z
\end{aligned} \tag{5.29}$$

where we explicitly write $M_1^{(1,2)}$ as a function of S_z to remark that S_z is flipped by the π pulse. We used our definition $M_i = \langle M_i\rangle + M_i'$ and Eq. 5.27 in the second line. We assume $\delta S_z = 0$ for the first measurement.

Therefore, M_1 induces a residual phase shift that depends on S_z. Now we return to the two classes of atoms. This phase shift is larger for the colder atoms than for the hotter atoms $\Delta\phi_{\rm ac}^{(h)} < \Delta\phi_{\rm ac}^{(c)}$, since $\Omega_c^{(h)} < \Omega_c^{(c)}$. There is a dephasing $\delta\phi_{\rm ac}$ between the two classes of atoms:

$$\delta\phi_{\rm ac} \equiv \Delta\phi_{\rm ac}^{(h)} - \Delta\phi_{\rm ac}^{(c)} = \frac{2}{q_d}\langle M_1\rangle c_0 S_z\left(\frac{\tilde{\Omega}_c^{(h)}}{\kappa} - \frac{\tilde{\Omega}_c^{(c)}}{\kappa}\right) = \frac{4}{q_d}\langle M_1\rangle c_0\gamma S_z \tag{5.30}$$

A $\delta S_z \neq 0$ generated by ISRE As we know, M_1 generates a residual dephasing between the two classes if $S_z \neq 0$. The ISRE transforms this $\delta\phi_{\rm ac} \neq 0$ into $\delta S_z \neq 0$ as it rotates the two dephased spins around their sum (with spin length $N/4$ for each class). Here we ignore the residual dephasing from the trap:

$$\delta S_z \simeq 2\cdot\frac{N}{4}\frac{\delta\phi_{\rm ac}}{2}\sin(\omega_{\rm ex}t) \tag{5.31}$$

where t is the evolution time. The sign is determined by the ISRE rotation and our definitions: for $\delta\phi_{\rm ac} < 0$, the colder atoms rotate above the equator. With the expression for $\delta\phi_{\rm ac}$, we finally have

$$\delta S_z \simeq \frac{N}{q_d}\langle M_1\rangle c_0\gamma S_z\sin(\omega_{\rm ex}t) \tag{5.32}$$

And the second measurement M_2 is modified according to Eq. 5.27:

$$M_2' = \langle M_2\rangle c_0 S_z\underbrace{\left(1+\gamma^2\frac{\langle M_1\rangle}{q_d}N\sin(\omega_{\rm ex}t)\right)}_{\alpha} \tag{5.33}$$

where we see the advent of the amplification α. At a given evolution time, it depends on the measurement strength $\langle M_1 \rangle$ as well as the atom number. The ISRE rate ω_{ex} depends on the atomic density hence on the atom number. The dynamics is quite complex even for two classes of atoms. Nevertheless, for a continuum of energy classes in reality, the complexity is contained in γ. The essential dependences of the amplification remain the same.

5.3.3 Simulation using classical spins

A quantitative understanding is only possible via numerical simulation. The kinetic equation Eq. 5.7 does not include quantum correlations. Nevertheless, we can estimate the amplification factor classically by calculating the cavity shift induced by the spin dynamics. More precisely, we start with a spin vector slightly away from the equator, to mimic a S_z due to QPN (e.g. half the QPN). We also manually introduce a residual dephasing (in terms of uncompensated probe photons) corresponding to this S_z. We will have an initial cavity shift, corresponding to M_1, while the cavity shift after the evolution gives the amplification.

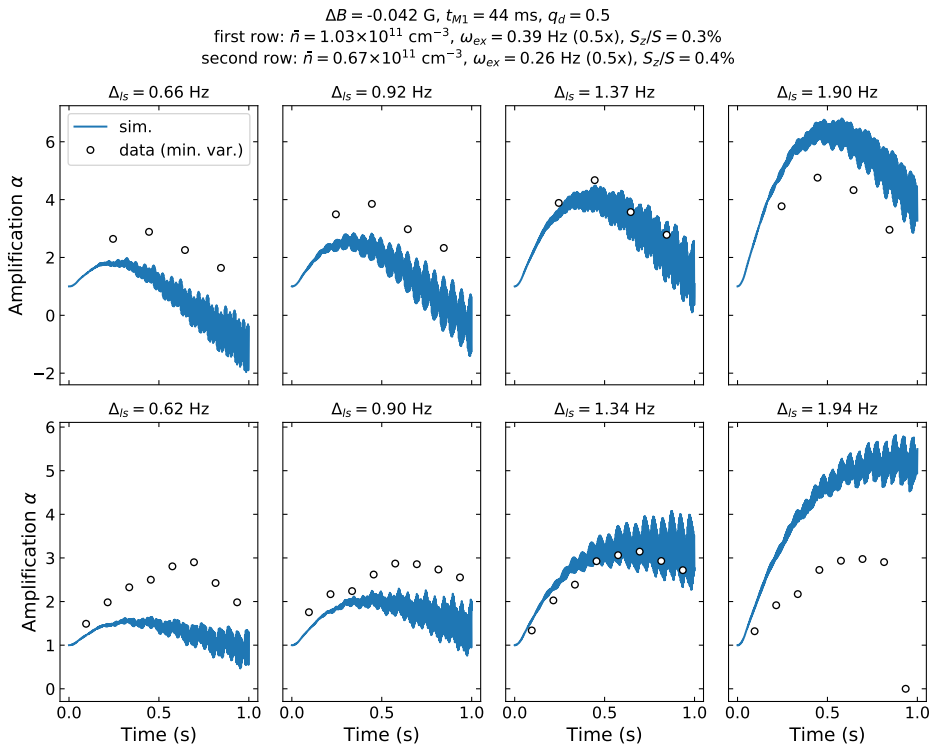

Figure 5.12 Preliminary results of simulations of the amplification factor, shown as a function of evolution time at different M_1 strengths (columns). The same data in Fig. 5.11 (minimum variance) are shown in the first row. Another dataset with a lower atom number (1.1×10^4) is shown in the second row. The simulations use a ΔB that is 2 mG lower than the measured value, and an ω_{ex} that is 0.5 times the theoretical value, to approach the data globally. Yet, the simulations fail to reproduce the data quantitatively, especially for the difference between different M_1 strengths. Surprisingly, the data show very little increase in α as M_1 increases. Again the fast oscillation in the simulations comes from the residual position dependence of the light shift.

Preliminary results are shown in Fig. 5.12, in comparison with the data (those in Fig. 5.11 and another dataset with a lower atom number). Here we plot the amplification α at different strengths of the first measurement (M_1) as a function of delay to observe the evolution of α. However, even allowing some margins in the parameters (e.g. ΔB and ω_{ex}), the simulations fail to reproduce the data, especially the difference as M_1 varies. One drawback of the simulation is the assumption of constant dephasing due to the uncompensated photons, not taking into account the two pulses in reality that dephase and rephase the atoms. In reality, if M_1 is strong enough, the first probe pulse ($M_1^{(1)}$) almost completely dephases the atoms, and the ISRE does not occur before the rephasing by the second probe pulse. However, for relatively weak M_1, the coherence after $M_1^{(1)}$ allows a considerable spin rotation to happen between the two probe pulses (during the π pulse). This is one possible explanation for the similar amplification factors observed for different measurement strengths. Refinements of the simulation to account for the real composite measurements are being carried out.

5.3.4 Circumventing the amplification

The amplification effect renders the cavity signal sensitive to all factors that affect the ISRE. From a metrological point of view, it might not be favourable for a clock. In general, we would like to be able to run a clock with squeezed states but without the amplification.

The key element for the amplification to take place is the S_z-correlated residual dephasing in a composite measurement. But as I pointed out in Sec. 4.2.1, this correlation can be avoided by toggling the probe frequency on opposite slopes of the resonance for the two probes. In this case, measurement deviations $M_1^{(1)\prime}$ and $M_1^{(2)\prime}$ are the same for the two probes and no residual dephasing will occur to the PSN limit.

In the preliminary results with this probing scheme, the amplification does not occur (Fig. 5.13). However, the correlation between two measurements is reduced at longer delay between them. The reason remains to be understood. One possible explanation is the frequency and amplitude noise of the probe as we toggle the probe frequency with an AOM driven by a VCO. Further investigation will be carried out in the near future.

5.3.5 Future work

Clock measurements Once we achieve circumventing the amplification effect with a modified measurement scheme, we will be able to perform clock measurements with spin squeezed states and also to study the squeezed state lifetime in a clean setting. Nevertheless, it is also exciting to explore clock measurements in the presence of the amplification, which require a quantitative understanding and a careful calibration of the spin dynamics. On the other hand, as the amplification depends on atomic density, it is possible that the former may serve to cancel the density dependence of the clock frequency measured by the cavity. To this end, a more accurate theoretical model is also needed.

Squeezing and quantum correlations The fact that the correlation between the two measurements is preserved is quite remarkable. The spin state is essentially squeezed after the first measurement, witnessing entanglement in the spin degree of freedom. The advent of the ISRE further modifies the spin of each atom in correlation with its motional state. The second measurement, in full correlation with the first one, shows that the collective spin is

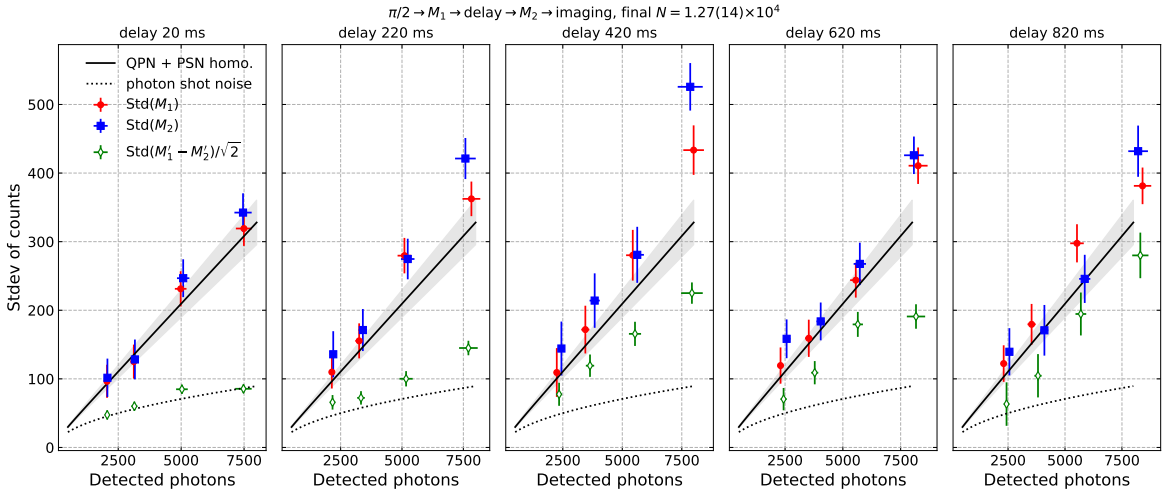

Figure 5.13 Preliminary results with the modified measurement scheme that prevents the correlation between S_z and residual dephasing. Two probes of the composite measurements are at $\pm\kappa/2$ detuning respectively. M_2 has the same fluctuations as M_1 even at long delay. However, correlations between M_1 and M_2 disappear at longer delay, suggesting either technical noise or unknown mechanism.

still squeezed. But how is the entangled state modified? Though spin squeezing (collective state) seems to be preserved, entanglement might be extended in the motional degrees of freedom. Theoretically, it is interesting (but challenging) to describe the spin dynamics starting with a squeezed state and to study the entanglement in the motional degrees of freedom.

Experimentally, we will be able to characterise the spin-squeezed state (e.g. by spin tomography) in the presence of spin dynamics. Assessing entanglement in the motional degrees of freedom may also be accessible through imaging (see e.g. [141]).

Conclusion and outlook

In this thesis, we have set up and characterised a new apparatus (TACC-2) to study spin squeezing in a metrological context. As a trapped-atom clock, TACC-2 reaches a fractional frequency instability of $\sim 6 \times 10^{-13}\tau^{-1/2}$ using standard Ramsey interferometry, to which the QPN has the biggest contribution. I have presented in Ch. 3 a detailed analysis of the major instability sources, showing that despite other prominent technical noise, using spin-squeezed states and QND measurements can improve the overall clock performance. On the other hand, we have demonstrated clean cavity-QED signatures thanks to the efforts in cavity stabilisation. In particular, cavity frequency measurement (via transmission) is limited by photon shot noise up to 10^4 detected photons.

With this highly stable cavity-QED platform, and a spin-echo technique to mitigate the probe-induced dephasing due to inhomogeneous coupling, we achieved 8(1) dB conditional spin squeezing by cavity measurement for 1.7×10^4 atoms (Ch. 4). It is believed to be limited by the decoherence due to technical noise, allowing further improvements. I have also presented preliminary results of cavity-feedback squeezing, showing 2 dB squeezing which is limited by detection noise (absorption imaging).

The long coherence time of the system (~ 20 s) allows us to study spin-squeezed states at an unprecedented timescale. We have seen, though indirectly, that atoms remain squeezed after 800 ms in the trap. Moreover, spin dynamics due to cold collisions, the ISRE, comes into play, and we observed the interplay between the ISRE and cavity measurements through inhomogeneous atom-light coupling (Ch. 5). Remarkably, with our composite measurement scheme using spin echo, the ISRE dynamics is rendered correlated with the measurement result (S_z), and manifests itself as an amplification effect of the cavity measurement. I have shown an intuitive explanation using a toy model with atoms in two energy classes. Preliminary results of a numerical simulation using a semi-classical model also show qualitative agreement with the observation.

Starting from the work in this thesis, the major objectives of TACC-2 are readily within reach. We will apply the spin-squeezed states, either conditionally by QND measurement or deterministically by cavity feedback, in a clock sequence at mid-$10^{-13}\tau^{-1/2}$ instability level.

It should be possible to use the QND measurement to determine more precisely the total atom number at the beginning and the end of the Ramsey sequence, reducing the uncertainty in the collisional shift due to atom loss. Furthermore, QND measurements will allow us to reuse our atoms in a few shorter Ramsey sequences, possibly reducing the Dick effect. For example, after a Ramsey sequence ended up by a QND measurement, atoms can be rotated back and repumped into the initial state ($|\downarrow\rangle$) to start a new clock measurement, or they can be put back to the equator coherently while gaining phase information [56].

Beyond a clock, our cavity-QED platform allows to explore the rich spin dynamics due to cold collisions in the quantum regime, closely related to the state-of-the-art optical lattice clocks [53]. For example, the interplay between the light-mediated entanglement (squeezed states) and the collision-mediated entanglement (correlations between the internal and external degrees of freedom) may shed light on new non-classical states or many-body physics in general. A first study can be investigating the quantum correlations through spin-noise tomography, with a combination of cavity measurement and high resolution imaging.

Appendix A
PDH error signal

A.1 Frequency noise from PSN

Here I give a brief analysis following the treatment in [130]. Let us recall the general reflection coefficient (the ratio between incident and reflected electric field E_r and E_i) of a F-P cavity (ignoring losses):

$$F(\omega) = \frac{E_r}{E_i} = \frac{r\left(\exp\left(i\frac{\omega}{\nu_{\rm fsr}}\right) - 1\right)}{1 - r^2\exp\left(i\frac{\omega}{\nu_{\rm fsr}}\right)} \tag{A.1}$$

where r is the reflection coefficient of each mirror. The incident field is phase modulated. We shall consider only the first order for weak modulation:

$$\begin{aligned} E_i &= E_0 e^{i(\omega t + \beta\sin\Omega t)} \\ &\approx E_0[J_0(\beta)e^{i\omega t} + J_1(\beta)e^{i(\omega+\Omega)t} - J_1(\beta)e^{i(\omega-\Omega)t}] \end{aligned} \tag{A.2}$$

where β is the modulation depth and $J_n(\beta)$ is the Bessel function of the first kind. The reflected power from FP cavity then reads

$$\begin{aligned} P_r = {} & P_c|F(\omega)|^2 + P_s\left(|F(\omega+\Omega)|^2 + |F(\omega-\Omega)|^2\right) \\ & + 2\sqrt{P_c P_s}\Big(\mathrm{Re}\left[F(\omega)F^*(\omega+\Omega) - F^*(\omega)F(\omega-\Omega)\right]\cos\Omega t \\ & + \mathrm{Im}\left[F(\omega)F^*(\omega+\Omega) - F^*(\omega)F(\omega-\Omega)\right]\sin\Omega t\Big) + (2\Omega \text{ terms}) \end{aligned} \tag{A.3}$$

with power in the carrier $P_c = J_0^2(\beta)P_0$ and in the sidebands $P_s = J_1^2(\beta)P_0$.

In our case, only the blue sideband enters the cavity. At high modulation frequency, $F(\omega-\Omega) \approx F(\omega) \approx -1$ and $F(\omega)F^*(\omega+\Omega) - F^*(\omega)F(\omega-\Omega) \approx -F^*(\omega+\Omega) - 1$. Near resonance of a high finesse cavity, $F \approx \frac{2i\delta\omega}{\kappa}$, where $\kappa/2\pi = \nu_{\rm fsr}/\mathcal{F}$ (FWHM). Therefore,

$$P_r \approx P_s + P_c - 2\sqrt{P_c P_s}(\cos\Omega t - \frac{2i\delta\omega}{\kappa}\sin\Omega t) + (2\Omega \text{ terms}) \tag{A.4}$$

Demodulation at quadrature phase gives the error signal ($\sin\Omega t$ term): $\epsilon \approx 4\sqrt{P_c P_s}\frac{\delta\omega}{\kappa}$, from which we can define a frequency discriminant

$$D = \frac{\epsilon}{\delta\omega/2\pi} = -\frac{4\sqrt{P_c P_s}}{\kappa/2\pi} \quad (\mathrm{W/Hz}) \tag{A.5}$$

The detected power is associated with PSN. As it is dominated by the reflected carrier, we can approximate it by a white spectrum. The spectral density in the error signal reads

$$S_e = \sqrt{2\frac{hc}{\lambda}P_r} \approx \sqrt{2\frac{hc}{\lambda}P_c} \quad (\mathrm{W/Hz^{1/2}}) \tag{A.6}$$

where λ is the laser wavelength, h the Planck constant, and c the speed of light. This shall be compared with the noise equivalent power (NEP) of the photodetector. Would the detection be PSN limited, we could estimate the noise in frequency. Dividing the signal by D, we have

$$S_f = \sqrt{\frac{hc}{8\lambda}}\frac{(\kappa/2\pi)}{\sqrt{P_s}} \quad (\mathrm{Hz/Hz^{1/2}}) \tag{A.7}$$

We see that it only explicitly depends on the power in the sideband – the PSN of the photons that carry phase information of the cavity.

A.2 Comparison of two photodetectors

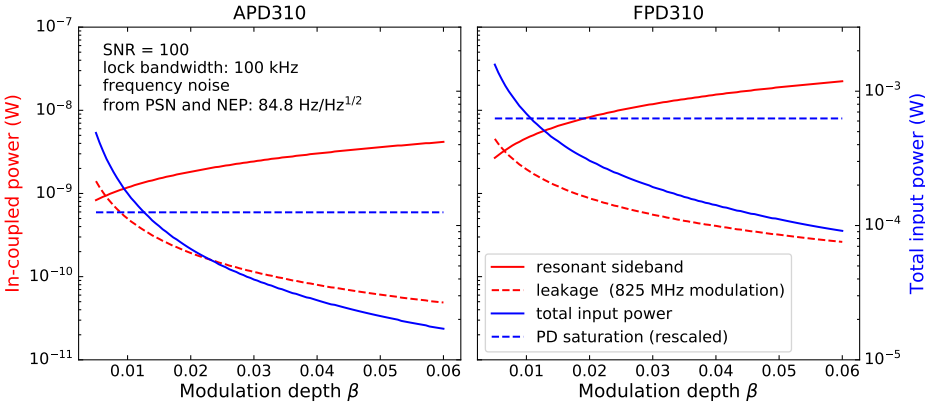

Figure A.1 Noise estimation for two photodiodes – APD310 and FPD310 from MenloSystems. We plot as a function of modulation depth the in-coupled sideband power, as well as the total detected power. Curves are in the same colour as their corresponding axes. The detection efficiencies have been taken into account. We assume a fixed SNR of 100 and a bandwidth of 100 kHz for this analysis. Mode-matching and optical losses are taken into account.

Here I examine two good photodetectors available in the experiment, APD310 and FPD310, both from MenloSystems. The detection is PSN limited when the PSN exceeds the NEP of the detector, or $S_e > S_{\mathrm{NEP}}$ in spectral density. However, from the specifications,[1] the FPD310 simply cannot be PSN-limited before saturation. Therefore we rather evaluate the required sideband power at a given SNR. In Fig. A.1, we plot as a function of β the sideband power (solid red), the total power (solid blue) at SNR of 100 with a bandwidth of 100 kHz. The noise is a sum of the PSN and NEP. APD310 can in principle achieve a

[1] APD310: gain 2.5×10^4 V/W, NEP (calculated) 2 pW/$\sqrt{\mathrm{Hz}}$;
FPD310: gain 5×10^3 V/W, NEP (calculated) 15.7 pW/$\sqrt{\mathrm{Hz}}$

PSN-limited detection. It requires less in-coupled power to achieve the same SNR, due to the lower specified NEP. Yet, this is a highly idealised analysis, only to give an idea of the order of magnitude.

Appendix B

Alternative light shift compensation

B.1 Background

The cavity probe introduces inhomogeneous light shift on the atoms, causing dephasing. We now perform composite measurements in which two probes are separated by a π pulse, forming an echo sequence. Probing at a fixed detuning $\kappa/2$, the transmitted photon numbers in the two probes differ if $\Delta N \equiv N_\uparrow - N_\downarrow \neq 0$. This causes a residual dephasing correlated to ΔN (S_z), initiating the amplification effect. Nevertheless, this correlation can be removed by toggling the probe at $\pm\kappa/2$ respectively for the two probes.

To achieve a good π pulse, we apply composite pulses, whose constituent pulses have to respect the thermal oscillations in $\vec{z}$, each having a minimum duration of the trap period $\sim$ 9 ms. The entire $\tilde{\pi}$ pulse takes 27 ms, and each composite measurement takes about 45 ms. This is clearly a disadvantage. Note that the long $\tilde{\pi}$ is not necessarily affected by the ISRE. Because at high probe power, the spins are completely dephased after the first probe, ISRE then would not happen. It is only after the rephasing by the second pulse that ISRE starts to play a role.

An alternative solution is to use another cavity field (another longitudinal mode of the cavity, e.g. 1 FSR away) to compensate the probe. this field should produce the same but negative light shift on the clock transition. Having the same intensity profile as the probe (a reasonable assumption), it compensates the probe light shift exactly for all atoms. The experiment can be further simplified if we separate the two cavity fields in time, namely a normal probe pulse followed by a compensation pulse. However, if they are separated in time, they do have to respect the oscillation period such that the transverse oscillations are averaged. The minimum total duration will be 9 ms.

In the following, we first show that the compensation field cannot compensate the light shift exactly in the presence of QPN (in S_z), namely the correlation between dephasing and S_z persists. Possible resolution is discussed. We also evaluate the compensation in the presence of atom number fluctuation and show that this scheme would work in realistic situations.

Compensation setting

Recall that for the cavity shift by the atoms

$$\delta\omega_c = \frac{g^2}{\omega_{\rm at}/2}N_\uparrow + \frac{g^2}{-\omega_{\rm at}/2}N_\downarrow = \frac{2g^2}{\omega_{\rm at}}\Delta N \tag{B.1}$$

where we assume equal coupling g of the two clock states, and an effective equal detuning $\sim \omega_{\rm at}/2$. For the second cavity field, one FSR away ($\omega_{\rm fsr} = 2\pi\nu_{\rm fsr}$):

$$\delta\omega_c' = \frac{g^2 N_\uparrow}{\omega_{\rm fsr}+\omega_{\rm at}/2} + \frac{g^2 N_\downarrow}{\omega_{\rm fsr}-\omega_{\rm at}/2} = \frac{g^2}{\omega_{\rm fsr}^2-\omega_{\rm at}^2/4}\left(\omega_{\rm fsr}N - \frac{\omega_{\rm at}}{2}\Delta N\right) \tag{B.2}$$

with N the total atom number. Note that g is geometrical, which we assume the same for the two cavity modes.

Simultaneously, the light shifts on the clock transition for both fields read:

$$\delta\omega_{\rm at} = \frac{4g^2}{\omega_{\rm at}}n_c \quad \delta\omega_{\rm at}' = \left(\frac{g^2}{\omega_{\rm fsr}+\omega_{\rm at}/2} - \frac{g^2}{\omega_{\rm fsr}-\omega_{\rm at}/2}\right)n_c' = -\frac{g^2\omega_{\rm at}n_c'}{\omega_{\rm fsr}^2-\omega_{\rm at}^2/4} \tag{B.3}$$

where n_c and n_c' are the average intra-cavity photon numbers for the two fields, respectively. The light shift compensation requires $\delta\omega_{\rm at}' = -\delta\omega_{\rm at}$, giving

$$n_c' = \frac{4}{\omega_{\rm at}^2}\left(\omega_{\rm fsr}^2 - \frac{\omega_{\rm at}^2}{4}\right)n_c = \left(\frac{4\omega_{\rm fsr}^2}{\omega_{\rm at}^2} - 1\right)n_c \equiv G n_c \tag{B.4}$$

$G \approx 4\omega_{\rm fsr}^2/\omega_{\rm at}^2 \approx 1300$ is the "gain" needed for the compensation condition. We find that the frequency shift of the compensation mode has been attenuated by the same factor compared to the probe:

$$\begin{aligned}\delta\omega_c' &= \frac{g^2}{4\omega_{\rm fsr}^2/\omega_{\rm at}^2 - 1}\left(\frac{4\omega_{\rm fsr}}{\omega_{\rm at}^2}N - \frac{2}{\omega_{\rm at}}\Delta N\right) = \frac{g^2}{G-1}\left(\frac{G}{\omega_{\rm fsr}}N - \frac{\delta\omega_c}{g^2}\right)\\ &\approx \frac{g^2 N}{\omega_{\rm fsr}} - \frac{\delta\omega_c}{G}\end{aligned} \tag{B.5}$$

We notice that $\delta\omega_c'$ also depends on N, susceptible to technical fluctuations.

B.2 Residual dephasing

More importantly, we shall look at the correlation between the light shift and ΔN. It is better to note the phase shift induced on an atom by n_c transmitted photons, namely the light shift integrated over the cavity lifetime $1/\kappa$:

$$\phi_{\rm ac} = \frac{\delta\omega_{\rm at}}{\kappa} \approx \frac{4g^2}{\omega_{\rm at}}\frac{n_c}{\kappa} \tag{B.6}$$

n_c is a function of the probe input photon number n_p (a constant) and the cavity shift. With the probe detuned at $\kappa/2$ from resonance, we have

$$n_c = T n_p \approx \left(\frac{1}{2} + \frac{\delta\omega_c}{\kappa}\right)n_p \approx \left(\frac{1}{2} - \frac{2g^2}{\kappa\omega_{\rm at}}\Delta N\right)n_p \tag{B.7}$$

We shall assume that the compensation condition is satisfied in the average case, $\Delta N = 0$ hence $\delta\omega_c = 0$, and focus on the deviation from $\Delta N = 0$:

$$\delta\phi_{\mathrm{ac}} = \frac{\partial(\delta\omega_{\mathrm{at}})}{\partial n_c}\frac{\delta n_c}{\kappa} \approx \frac{\partial(\delta\omega_{\mathrm{at}})}{\partial n_c}\frac{\delta\omega_c}{\kappa^2}n_p \approx \frac{8g^4 n_p}{\omega_{\mathrm{at}}^2\kappa^2}\Delta N \tag{B.8}$$

For the second mode, we have similarly:

$$\delta\phi'_{\mathrm{ac}} = \frac{\partial(\delta\omega'_{\mathrm{at}})}{\partial n'_c}\frac{\delta n'_c}{\kappa} \approx -\frac{1}{G}\frac{\partial(\delta\omega_{\mathrm{at}})}{\partial n_c}\frac{\delta n'_c}{\kappa} \tag{B.9}$$

where we have used the result that $\delta\omega'_{\mathrm{at}} = -\delta\omega_{\mathrm{at}}$ is ensured by $n'_c = Gn_c$. If we hope to get $\delta\phi'_{\mathrm{ac}} \sim -\delta\phi_{\mathrm{ac}}$, we should fix the compensation field on the slope with the opposite detuning $-\kappa/2$, because according to Eq. B.5, $\delta\omega'_c = -\delta\omega_c/G$ (we assume the other term a static shift from a constant N). Therefore,

$$\delta n'_c = -\frac{\delta\omega'_c}{\kappa}n'_p \approx \frac{\delta\omega_c}{G\kappa}(Gn_p) \approx \delta n_c \tag{B.10}$$

where we used the fact that the compensation condition $n'_c = Gn_c$ leads to $n'_p = Gn_p$ for detuning $\pm\kappa/2$. Finally, we have

$$\delta\phi'_{\mathrm{ac}} = -\frac{1}{G}\delta\phi_{\mathrm{ac}} \tag{B.11}$$

The residual dephasing due to $\Delta N \neq 0$ cannot be compensated by the compensation field.

B.3 Noise from fluctuations of total atom number

In practice, we might be more concerned about the fluctuation in $\delta\phi'_{\mathrm{ac}}$ due to fluctuations in N (Eq. B.5). As the compensation field can not compensate the fluctuations in ϕ_{ac}, we should instead choose zero detuning to be less sensitive to N fluctuation.

The benchmark would be the fluctuation in ϕ_{ac} (standard deviation Δ) due to the PSN of the probe:

$$\Delta\phi_{\mathrm{ac,psn}} = \left|\frac{\partial(\delta\omega_{\mathrm{at}})}{\partial n_c}\right|\frac{\sqrt{\langle n_c\rangle}}{\kappa} \tag{B.12}$$

where $\langle n_c\rangle = n_p/2$. For the compensation field, at zero detuning, $\delta\omega'_c$ is first-order insensitive to δN, so we consider the second order:

$$\delta n'_c \approx -n'_p\left(\frac{\delta\omega'_c}{\kappa/2}\right)^2 \approx -\left(\frac{2g^2\delta N}{\omega_{\mathrm{fsr}}\kappa}\right)^2\frac{Gn_p}{2} \tag{B.13}$$

Note that now as the compensation field is on resonance, the compensation condition is modified to $n'_p = Gn_p/2$. Recall Eq. B.9, we have

$$\delta\phi'_{\mathrm{ac}} = \frac{1}{G}\frac{\partial(\delta\omega_{\mathrm{at}})}{\partial n_c}\left(\frac{2g^2\delta N}{\omega_{\mathrm{fsr}}\kappa}\right)^2\frac{Gn_p}{2\kappa} \tag{B.14}$$

Now we compare it with PSN of the probe:

$$\left|\frac{\delta\phi'_{\rm ac}}{\Delta\phi_{\rm ac,psn}}\right| \approx \frac{1}{G}\left(\frac{2g^2\delta N}{\omega_{\rm fsr}\kappa}\right)^2 \frac{Gn_p/2}{\sqrt{n_p/2}} = \left(\frac{g^2}{\omega_{\rm fsr}\kappa}\right)^2 \sqrt{8n_p}(\delta N)^2 \tag{B.15}$$

$$\approx 7\times 10^{-11}\sqrt{n_p}(\delta N)^2 \tag{B.16}$$

In a realistic situation, $n_p \approx 10^4$ and $\delta N \approx 10^3$, $|\delta\phi'_{\rm ac}| \sim 7\times 10^{-3}\Delta\phi_{\rm ac,psn}$, which seems sufficiently good.

Trapping and scattering rate

We briefly discuss the trapping effect and spontaneous scattering of the compensation field. Recall the trapping potential

$$U \propto \frac{I_c}{\Delta_c} \propto \frac{n_c}{\omega_{\rm at}/2} \tag{B.17}$$

where I_c is the intra-cavity intensity. And the scattering rate

$$\Gamma_{\rm sc} \propto \frac{I_c}{\Delta^2} \propto \frac{n_c}{\omega_{\rm at}^2/4} \tag{B.18}$$

For the compensation field at $n'_c = Gn_c$:

$$U' \propto \frac{n'_c}{\omega_{\rm fsr}} \approx \frac{Gn_c}{\omega_{\rm at}/2}\left(\frac{\omega_{\rm at}}{2\omega_{\rm fsr}}\right) = \sqrt{G}U \tag{B.19}$$

$$\Gamma'_{\rm sc} \propto \frac{n'_c}{\omega_{\rm fsr}^2} \approx \frac{Gn_c}{\omega_{\rm at}^2/4}\left(\frac{\omega_{\rm at}^2}{4\omega_{\rm fsr}^2}\right) = \Gamma_{\rm sc} \tag{B.20}$$

The concern is more the trapping effect. Our calculation shows that for a realistic probe power, the trapping potential of the compensation field can reach 0.2 recoil energy which is more than 10% of the thermal energy. The real effect on the atoms needs to be verified experimentally.

B.4 Possible scheme

Although I showed that the compensation field cannot compensate the residual light shift from ΔN, a modified scheme can work. Similar to the original composite measurement, we can have two probes with toggled detuning at $\pm\kappa/2$ respectively. It is the two probes that ensures the total probe photon number always average to $n_p/2$, independent of ΔN. The compensate field is at zero detuning to compensate the total light shift. If they are separated in time, the minimum duration would be 3/2 trapping period $\sim$ 13.5 ms. There are still advantages compared to a composite measurement with a MW π pulse.

Appendix C

Résumé en français

Chapitre 1 : Compression de spin pour la métrologie

Ce chapitre donne une brève introduction aux deux aspects de la thèse: d'une part, les horloges atomiques et leurs stabilités, et d'autre part, la compression de spin des atomes neutres dans les systèmes en électrodynamique quantique en cavité (cQED).

Tout d'abord, à partir de la notion d'état de spin collectif d'un ensemble de particules de spin 1/2 dans la représentation de la sphère de Bloch, nous formulons la rotation de spin (rotation de Rabi) dans un champ électromagnétique résonant. Nous expliquons la spectroscopie de Ramsey, qui est un interféromètre d'états internes ($|\uparrow\rangle$ et $|\downarrow\rangle$) à deux impulsions. La mesure de la fréquence d'horloge est effectuée sur la probabilité de transition $P_\uparrow$ (équation 1.8). La sensibilité de cette mesure de fréquence augmente avec le temps de Ramsey, favorisant les temps d'interrogation longs, ce qui est obtenu par exemple dans des horloges à atomes piégés. Nous nous concentrons ensuite sur notre expérience TACC, une horloge à micro-ondes utilisant des atomes ultra-froids de ^{87}Rb, piégés magnétiquement sur une puce à atomes. La transition d'horloge entre $|F = 1, m_F = -1\rangle$ et $|F = 2, m_F = 1\rangle$ (états d'horloge) utilisée dans TACC repose sur un piège pseudo-magique dans lequel la fréquence de transition est homogène pour tous les atomes et suffisamment insensible a un champ magnétique externe. L'homogénéité est le résultat de l'annulation entre le déplacement de Zeeman du piège et le déplacement collisionnel dû à la densité atomique et assure une longue cohérence pour une mesure de précision.

Nous introduisons la variance d'Allan en tant que facteur de mérite pour la caractérisation de la stabilité de l'horloge. Les sources de bruit principales dans TACC sont brièvement expliquées, y compris le bruit de détection, le bruit de projection quantique, le bruit de l'oscillateur local (l'effet de Dick), le déplacement collisionnel et les fluctuations du champ magnétique et de la température des atomes.

Dans la deuxième partie du chapitre, nous revenons sur la nature collective et les relations d'incertitude des opérateurs de spin qui mènent au bruit de projection quantique (QPN) et à la limite quantique standard (SQL) d'une horloge à état classique (non corrélé). La métrique de compression de spin (paramètre de compression de Wineland) est introduite et les méthodes les plus étudiées pour créer des états comprimés de spin dans les atomes neutres sont passées en revue. Nous nous concentrons alors sur le cadre de cQED, où, en raison du fort couplage entre photon de la cavité et transition atomique, l'état interne d'un atome peut

modifier la résonance de la cavité. En particulier, dans le régime dispersif où la résonance de la cavité est désaccordée de manière égale et opposée par rapport aux transitions des deux états fondamentaux hyperfins (états d'horloge, figure 1.4), la fréquence de la cavité mesure effectivement la polarisation collective du spin (S_z, équation 1.44). En faisant une mesure de la résonance de la cavité, l'état de spin collectif est également partiellement projeté, sans distinction d'atomes individuels (en cas de couplage homogène, section 1.3.2.4), suffisant pour générer des corrélations entre atomes et créer des états comprimés de spin. Intuitivement, l'incertitude du spin est donc déterminée par l'incertitude de la mesure de la cavité (équation 1.60). La limite théorique de la compression est due à l'émission spontanée en dehors du mode de la cavité, ce qui mène éventuellement à une décohérence ou modifie l'état atomique. Nous estimons que cette limite pour TACC-2 atteint 20 dB pour 4×10^4 atomes (Fig. 1.5). Une autre méthode possible est d'introduire une corrélation entre S_z (fréquence de la cavité) et le nombre de photons dans la cavité (qui génèrent un déphasage des atomes, équation 1.45), en désaccordant le laser sonde à la moitié de la largeur de raie de la cavité, on peut réaliser le hamiltonien dit « one-axis-twisting » (OAT) qui crée aussi l'état comprimé (section 1.3.4).

Chapitre 2 : Méthodes expérimentales

Ce chapitre est divisé en trois parties. La première décrit le dispositif expérimental, c'est-à-dire l'assemblage de la puce à atomes (le schéma et les photographies sont illustrées aux figure 2.1 et 2.2), le système à vide (et le problème rencontré après l'étuvage qui limite finalement la durée de vie des atomes à 2–3 s, figure 2.4), le système optique (génération de fréquence laser, figure 2.6 et configuration des optiques, figure 2.7 et 2.8) et le contrôle des champs magnétiques. La géométrie des champs optiques et magnétiques est illustrée sur la figure 2.5.

La deuxième partie détaille les procédures pour un cycle expérimental typique, allant du refroidissement au laser, au pompage optique, au transport sur puce, au refroidissement évaporatif jusqu'au piège d'horloge. Le transport des atomes consiste en une rotation dans un piège quadripolaire, dont le lien avec les pièges harmoniques (« dimple ») se déroulant avant et après la rotation a mérité une attention particulière. Nous expliquons également le passage au piège d'horloge extrêmement peu profond (fréquences de piège $\{\omega_x, \omega_y, \omega_z\}/2\pi \simeq \{4, 120, 110\}$ Hz), en essayant d'éviter les oscillations résiduelles du centre de masse.

L'oscillateur local pour l'interrogation de l'horloge (une transition à deux photons) est composé d'une chaîne de fréquence (micro-onde) fait maison et d'un synthétiseur numérique direct (DDS), respectivement. L'architecture est illustrée sur la figure 2.13. Puisque les champs micro-onde et radiofréquence sont délivrés par le guide d'onde et les fils sur la puce, ils présentent une inhomogénéité dont nous présentons une estimation simple et des preuves expérimentales (figure 2.15). Par conséquent, la durée des impulsions d'interrogation doit être multiple de la période de piégeage dans la direction verticale ($\sim$ 9 ms) ou être suffisamment longue.

Nous montrons également la procédure de réglage des impulsions, y compris le réglage de l'amplitude des deux champs pour la compensation du déplacement lumineux (figure 2.17), l'étalonnage du champ magique par spectroscopie de Rabi (figure 2.16) et le réglage précis de la durée de l'impulsion par les oscillations de Rabi. Nous terminons cette section par une

brève discussion sur l'imagerie d'absorption et sur le bruit de détection.

La troisième partie du chapitre est consacrée à la détection et à la stabilisation des cavités fibrées, dont les différents paramètres sont résumés dans la table 2.3. Dans cette thèse, nous utilisons la cavité de faible finesse ($\mathcal{F} = 2700$ pour 780 nm) comme cavité scientifique et celle de haute finesse ($\mathcal{F} = 38000$ pour 780 nm) comme auxiliaire. Ils sont fixés sur les mêmes câles piézoélectriques et permettent en principe de stabiliser la cavité scientifique avec l'auxiliaire. Le schéma général de la stabilisation et la détection des cavités est illustré sur la figure 2.20.

Nous appliquons la technique Pound-Drever-Hall (PDH) pour la stabilisation des deux cavités. Les bandes latérales optiques générées par les modulateur électro-optiques sont utilisées pour asservir la cavité à une fréquence réglable et pour sonder la cavité avec un désaccord variable (figure 2.21). La configuration complète est illustrée sur la figure 2.22. L'asservissement direct de la cavité scientifique nécessite une très faible puissance optique intra-cavité afin d'éviter de piéger les atomes par le réseau optique (car ils devraient être piégés magnétiquement) et de minimiser le déplacement lumineux induit par le laser d'asservissement. Le calcul montre que nous sommes limités à dizaine de nW de puissance d'entrée pour l'asservissement (figure 2.23). nous sommes parvenus à asservir la cavité avec une puissance d'entrée de 9 nW et mesurons un déplacement lumineux négligeable dû au laser d'asservissement en utilisant la spectroscopie de Ramsey (figure 2.25).

Nous détaillons deux autre techniques qui permettent un bon asservissement de la cavité pendant une séquence expérimentale. Le premier est un filtre numérique (à réponse impulsionnelle infinie, IIR) implémenté par une carte Red Pitaya dans la boucle d'asservissement pour supprimer les résonances mécaniques de la cavité à des fréquences assez basses, ce qui limite initialement la bande passante d'asservissement bien en dessous de la première résonance (2,6 kHz, figure 2.28). La détermination précise du filtre est obtenue par une mesure de la réponse du système (figure 2.27). Ce filtre permet une bande passante jusqu'à 20 kHz (figure 2.29). La deuxième technique indispensable est une compensation de la forte dérive thermique de la cavité due au chauffage par les courants électriques sur puce pendant la séquence expérimentale (figure 2.30).

Enfin, nous mettons en œuvre l'idée d'asservir la cavité scientifique avec la cavité auxiliaire. Le défi est la dérive relative entre les deux cavités (dérive thermique des longueurs des cavités), si on n'asservit que la cavité auxiliaire. Nous avons conçu un « interlock » à deux cavités tel que le signal PDH de la cavité auxiliaire soit appliqué en permanence au piézo tandis que la fréquence de la cavité auxiliaire est contrôlée par le signal PDH de la cavité scientifique, de sorte que la cavité scientifique soit asservie à une fréquence prédéfinie. (figure 2.31). Lorsque la lumière d'asservissement dans la cavité scientifique n'est pas désirée (par exemple pendant l'interrogation), cet asservissement de fréquence peut être suspendu et la cavité scientifique n'est asservie que via l'auxiliaire.

Chapitre 3 : Une plate-forme cQED stable

Ce chapitre présente les caractérisations de TACC-2 sous deux aspects essentiels : la stabilité de l'horloge dans une configuration standard et les interactions cQED pour une mesure du spin atomique par cavité. Dans la première partie, nous évaluons différentes contributions de bruit en évaluant la variance d'Allan en fréquence relative. Le bruit de détection est

séparé du QPN par leurs différentes dépendances en fonction du nombre d'atomes dans la mesure du bruit de $P_\uparrow$ (figure 3.1(a)). Nous obtenons un bruit de détection (écart type de chaque état) d'environ 50 atomes ou 2–3 atomes par pixel. La contribution de l'effet Dick est calculée à l'aide du bruit de phase de la chaîne micro-onde (équation 3.5, figure 3.3). Pour TACC-2, la contribution est d'environ 2×10^{-13} $s^{-1/2}$, ce qui contribue de manière notable au bilan de bruit. Le déplacement collisionnel, qui dépend de la densité, contribue à l'instabilité de l'horloge par l'incertitude liée à la mesure du nombre total d'atomes, ce qui permet de corriger le déplacement collisionnel à chaque cycle. Cette correction reste toutefois limitée par la nature stochastique de la perte d'atomes pendant le temps de Ramsey (équation 3.13), ce qui limite finalement le temps de Ramsey à une durée de l'ordre de la durée de vie d'atomes. L'examen des sources de bruit susmentionnées qui ne dépendent pas explicitement du champ magnétique donne déjà une idée de l'amélioration potentielle avec les états comprimés de spin. En fait, le déplacement collisionnel favorise un nombre d'atomes plus faible, ce qui dégrade la stabilité de l'horloge due au QPN. Cependant, si ce dernier peut être diminué en utilisant l'état comprimé, nous pouvons explorer un plus grand espace de paramètres pour l'amélioration de l'horloge, au-delà d'une simple réduction de la contribution de QPN.

Nous analysons ensuite les contributions de la fluctuation magnétique et de la température atomique qui dépendent du champ de biais de manière convoluée. Avec un modèle simple, nous pouvons comprendre qualitativement les données (en fonction du champ de biais, figure 3.6). Nous présentons enfin deux exemples de mesure d'horloge standard montrant une stabilité de 5.2×10^{-13} $s^{-1/2}$ pour un temps de Ramsey de 2 s (figure 3.8) et de 6.5×10^{-13} $s^{-1/2}$ pour un temps de Ramsey de 1 s (figure 3.9). Nous donnons également une estimation utilisant des états comprimés réalistes, montrant qu'une amélioration globale de la stabilité de l'horloge est possible (figure 3.10). Dans la deuxième partie du chapitre 3, nous commençons par une expérience de « vacuum Rabi splitting » (VRS) dans le régime « résonant » (la cavité en résonance avec $F=2\rightarrow F=3$, schéma des lasers illustré sur la figure 3.11) et une brève revue du modèle théorique pour les calculs numériques. Un calcul simple avec l'hamiltonien de Jaynes-Cummings (JC) d'un seul atome est bien d'accord avec les données expérimentales, comparant les spectres VRS typiques en fonction du désaccord de la cavité (figure 3.12). Nous varions également la polarisation de la sonde et le nombre d'atomes pour démontrer que le système est bien décrit par le modèle simple de JC.

Nous passons ensuite au régime dispersif où la compression de spin aura lieu. Le désaccord de la cavité, effectivement égal pour les deux états de l'horloge, est déterminé expérimentalement, de sorte qu'un atome dans l'état de superposition $((|\uparrow\rangle+|\downarrow\rangle)/\sqrt{2})$ ne déplace pas la cavité (figure 3.15). Ensuite, nous mesurons le couplage moyenné sur l'ensemble, c'est-à-dire décalage de la cavité par atome, en mesurant les spectres de cavité en préparant différents états de superposition (rotation de Rabi à partir de $|\downarrow\rangle$, figure 3.16). En utilisant ce couplage atome-cavité, nous pouvons facilement aligner le piège d'horloge par rapport au mode de la cavité.

Enfin, nous présentons les résultats préliminaires d'un détour pour piéger les atomes dans le réseau optique intra-cavité. Le chargement des atomes dans le réseau est en fait facilité par le « interlock » entre les deux cavités, de sorte que la cavité scientifique soit asservie par la cavité auxiliaire et que la puissance du réseau dans la cavité scientifique puisse être modifiée à volonté sans interférer l'asservissement. Nous montrons les données de durée de vie des atomes (figure 3.19) et de température (figure 3.20) dans le réseau, ainsi que la mesure du décalage de la cavité par atome (figure 3.21)

Chapitre 4 : Compression de spin par mesure

Ce chapitre présente le résultat principal de la compression de spin par mesure. Pour quantifier la compression métrologique, nous commençons par la caractérisation de la décohérence induite par une sonde de cavité. La décohérence est due au couplage inhomogène puisque la taille du nuage atomique est comparable à la taille du mode de la cavité. Il est quantifié par le contraste des franges de Ramsey (figure 4.2), avec laquelle nous obtenons également le déphasage moyen par la sonde. La décroissance du contraste en fonction du nombre de photons détectés peut être comparée à la simulation de Monte Carlo pour estimer l'efficacité de la détection (figure 4.3). Il ressort clairement de cette mesure que de simples impulsions de sonde déphasent les atomes trop rapidement, détruisant 90% du contraste après 3000 photons détectés. Un écho de spin est nécessaire pour conserver la cohérence (figure 4.5). Nous construisons donc la mesure de la cavité composite utilisée pour la suite de la thèse et ignorons dans ce chapitre la corrélation entre S_z et le déphasage résiduel.

Pour obtenir une bonne impulsion d'écho, nous implémentons une impulsion composite SCROFULOUS qui est moins sensible aux erreurs dans l'aire des impulsions (l'amplitude et la durée), tandis que chaque impulsion constitutive doit toujours respecter la durée d'une période de piégeage le long de $\vec{z}$. Nous caractérisons ensuite la cohérence après une mesure composite en utilisant maintenant les oscillations de Rabi. La mesure composite préserve en effet beaucoup mieux la cohérence qu'une simple impulsion de sonde (figure 4.6) en conservant au moins 65% de contraste après 6000 photons détectés. Nous effectuons ensuite une mesure de compression de spin dans laquelle deux mesures composites consécutives sont appliquées, la première mesure comprimant l'état et la seconde vérifiant la compression. Idéalement, la deuxième mesure devrait correspondre à la première jusqu'au bruit de photon. Ceci est en effet vérifié dans les statistiques des mesures, en faisant varier le nombre de photons de sonde et le nombre d'atomes (figure 4.9). Cette mesure peut être traduite, sous une forme plus courante, en variance de spin normalisée et en paramètre de compression (Wineland). Nous obtenons une compression de 8 (1) dB pour 1.7×10^4 atomes (figure 4.10).

Enfin, nous présentons les résultats préliminaires de compression par rétroaction de la cavité. La compression est vérifiée par une « tomographie de spin » (figure 4.11) mesurée par imagerie d'absorption, qui est fortement limitée par le bruit de détection. Nous observons une compression de 2 dB à un petit angle de tomographie (sans correction du bruit de détection, figure 4.12).

Chapitre 5 : Amplification quantique par ISRE

Dans ce dernier chapitre, nous présentons l'observation d'un effet d'amplification du signal de décalage en fréquence de la cavité, qui se révèle être une interaction entre la mesure de la cavité (avec inhomogénéité) et la dynamique de spin due aux collisions à basse température. Ce dernier, appelé effet de rotation de spin identique (ISRE), est connu dans notre système et est responsable du rephasage automatique du spin (figure 5.2). Nous donnons une brève introduction à l'ISRE et une image intuitive avec deux classes d'atomes (figure 5.1), c'est-à-dire avec des énergies thermiques élevées et basses (chaud et froid). Il est important de comprendre que l'ISRE est initié par un déphasage entre les classes d'énergie qui, après échange de spin (rotation), corrèle davantage l'énergie avec le spin (S_z). Nous expliquons les

équations cinétiques qui ont été utilisées précédemment pour comprendre quantitativement l'ISRE. Expérimentalement, nous démontrons d'abord une observation directe de l'ISRE à travers les énergies thermiques des deux états de spin par mesure du temps de vol. Une des caractéristiques de l'ISRE est l'évolution de l'énergie thermique (température du nuage), distincte pour les deux États. L'évolution dépend du déphasage dû au piège et donc du champ de biais (figure 5.3). La simulation numérique utilisant l'équation cinétique montre un accord qualitatif.

Nous ajoutons ensuite le rôle joué par la mesure de cavité. Une simple impulsion de sonde, qui introduit un fort déphasage (entre les classes d'énergie), déclenchera également l'ISRE (figure 5.5). En redistribuant le spin entre les classes d'énergie ayant des couplages différents avec la cavité, l'ISRE modifie ensuite la fréquence de la cavité (équation 5.12 et 5.13). Cette interaction entre la mesure de cavité et l'ISRE est bien observée (figure 5.8), en accord qualitatif avec la simulation.

Cependant, avec une mesure composite comme dans les mesures de compression, le déphasage est annulé en moyenne par l'écho de spin. Mais maintenant, la corrélation entre S_z et le déphasage résiduel (car nous mesurons la résonance de la cavité par la transmission) est l'élément clé qui mène à l'effet d'amplification : l'ISRE est déclenché par le déphasage résiduel, mais en corrélation avec S_z. Précisément, après la première mesure (donnant une certaine valeur de S_z et un décalage de la cavité), l'ISRE déplace la cavité en corrélation avec S_z (d'une manière qui augmente le décalage initial). La deuxième mesure de S_z (mesurant le décalage de la cavité) est donc effectivement amplifiée. C'est une amplification puisque les deux mesures sont idéalement corrélées, jusqu'au bruit de photon. Les données vérifient en effet la corrélation (figure 5.9 et 5.11). Le facteur d'amplification obtenu est une fonction complexe du nombre de photons de la sonde, du nombre d'atomes et du temps d'évolution.

Nous illustrons un modèle simple avec deux classes d'atomes pour expliquer l'effet d'amplification, mais la comparaison quantitative n'est possible qu'avec la simulation numérique. La simulation préliminaire montre des caractéristiques prometteuses (figure 5.12), mais celle-ci nécessite encore d'être affinée pour mieux comprendre les données.

List of Figures

1.1 Two-mode Mach-Zehnder interferometer and Ramsey interferometer 2
1.2 The clock transition and pseudo-magic trap in TACC 8
1.3 Concepts of squeezing by QND measurement and by OAT dynamics 15
1.4 Schematics of the cavity-QED system in TACC-2 21
1.5 Achievable squeezing in TACC-2 26

2.1 Layout of the atom chip 30
2.2 Photograph of chip assembly and vacuum cell 30
2.3 Schematics of the vacuum system. 32
2.4 Vacuum after bake-out and cold atom lifetime in the clock trap 33
2.5 Geometry of fields 34
2.6 Diagram of laser frequencies 35
2.7 Layout of the optical table 36
2.8 Schematics of the optical hat 37
2.9 Residual magnetic field 39
2.10 Images taken in various steps during the transport 41
2.11 Atom number dependence of the atom temperature after evaporation 46
2.12 Residual oscillations in the clock trap 47
2.13 Schematics of the generation of MW and RF photons 49
2.14 Amplitude dependence of the MW phase 50
2.15 Evidence of field inhomogeneity 53
2.16 RF pulse tuning 54
2.17 Two-photon light shift compensation 55
2.18 Cloud compression 59
2.19 Transmission and reflection spectra of the science cavity 63
2.20 Schematics of lasers and cavity stabilisation for cavity-QED experiments . . . 64
2.21 Cavity probing frequencies of the two cavities 65
2.22 Complete laser setup for cavity probing and stabilisation 66
2.23 Calculated trapping potential and light shift induced by 1560 nm locking light 67
2.24 Calibration of the locking light power 69
2.25 Clock shift at different locking light power 69
2.26 Feedback control model 70
2.27 Bode plot of cavity response 72
2.28 Finite elements simulation of the bridge 72
2.29 Lock improvement with IIR filter 74

2.30 Thermal drift of the cavity frequency . . . 75
2.31 Two-cavity interlock setup . . . 77
2.32 Additional frequency feedback . . . 78

3.1 Calibration of the detection noise . . . 81
3.2 Coherence time . . . 82
3.3 Calculated Dick coefficients and the noise spectrum of the LO . . . 83
3.4 Calculations of noise sources independent of B-field as a function of Ramsey time . . . 84
3.5 Optimum B-field against temperature variation as a function of trap frequency 86
3.6 Clock stability at different magnetic fields . . . 87
3.7 Ramsey fringe contrast as a function of bottom field . . . 89
3.8 Best clock stability at 3 s Ramsey time . . . 89
3.9 Best clock stability at 1 s Ramsey time . . . 90
3.10 Prospective clock stability with spin-squeezed states and cavity detection . . . 91
3.11 Frequency scheme for vacuum Rabi splitting measurement . . . 94
3.12 VRS spectra as a function of cavity detuning . . . 95
3.13 VRS spectra varying probe polarisation . . . 95
3.14 VRS spectra varying atom number . . . 96
3.15 Cavity frequency for equal coupling . . . 97
3.16 Cavity shift as a function of $N_\uparrow - N_\downarrow$ with σ^+ polarisation . . . 98
3.17 Cavity shift as a function of $N_\uparrow - N_\downarrow$ with linear polarisation . . . 99
3.18 Coupling scanning transverse cloud position . . . 100
3.19 Atom lifetime in lattice . . . 102
3.20 Cloud expansion after TOF to measure temperature in lattice . . . 102
3.21 Dispersive coupling in lattice . . . 103

4.1 Light shift distribution from Monte-Carlo simulation . . . 108
4.2 Sequence for contrast and phase measurements . . . 109
4.3 Contrast decay and phase shift induced by probe photons . . . 109
4.4 Spin echo pulse errors . . . 113
4.5 Sequence of coherence measurements using Rabi oscillations . . . 115
4.6 Coherence after a composite measurement . . . 115
4.7 Coherence evolution after measurement . . . 117
4.8 Sequence of squeezing measurements . . . 118
4.9 Statistics of squeezing measurements . . . 119
4.10 Conditional spin squeezing results . . . 120
4.11 Sequence of noise tomography measurement . . . 121
4.12 Preliminary spin noise tomography . . . 121

5.1 Schematics of ISRE for two classes of spins . . . 128
5.2 Spin self-rephasing seen in Ramsey-fringe contrast . . . 129
5.3 Energy evolution of spin states at different bottom fields . . . 133
5.4 Energy evolution of spin states, varying bottom field in finer steps . . . 134
5.5 Schematics of ISRE for two classes of spins triggered by cavity light shift . . . 135
5.6 Evolution of cavity resonance with different probe powers and different atom numbers . . . 136

5.7 Evolution of cloud temperatures, varying cavity probe power 137
5.8 Evolution of thermal energies and cavity frequency 138
5.9 Statistics of cavity measurements showing the amplification effect 140
5.10 Raw data showing correlation between measurements 140
5.11 Amplification factors 142
5.12 Simulation of the amplification factor 145
5.13 Modified measurement scheme that circumvent the amplification effect 147

A.1 Noise estimation for two photodiodes 152

Bibliography

[1] T. C. Liebisch, J. Stenger & J. Ullrich; "Understanding the Revised SI: Background, Consequences, and Perspectives"; Annalen der Physik **531**, p. 1800339 (2019). ix

[2] C. J. Bordé; "A consistent unified framework for the new system of units: Matter–wave optics"; Comptes Rendus Physique **20**, pp. 22–32 (2019). ix

[3] BIPM, CGPM; "Resolution 5 of the 12th CGPM"; (1964). https://www.bipm.org/en/CGPM/db/12/5/. ix

[4] P. Gill; "When should we change the definition of the second?" Philosophical Transactions of the Royal Society A: Mathematical, Physical and Engineering Sciences **369**, pp. 4109–4130 (2011). ix

[5] N. Hinkley, J. A. Sherman, N. B. Phillips, M. Schioppo, N. D. Lemke, K. Beloy, M. Pizzocaro, C. W. Oates & A. D. Ludlow; "An Atomic Clock with 10-18 Instability"; Science **341**, pp. 1215–1218 (2013). ix

[6] B. J. Bloom, T. L. Nicholson, J. R. Williams, S. L. Campbell, M. Bishof, X. Zhang, W. Zhang, S. L. Bromley & J. Ye; "An optical lattice clock with accuracy and stability at the 10-18 level"; Nature **506**, pp. 71–75 (2014). ix, x

[7] T. E. Mehlstäubler, G. Grosche, C. Lisdat, P. O. Schmidt & H. Denker; "Atomic clocks for geodesy"; Reports on Progress in Physics **81**, p. 064401 (2018). ix

[8] M. Safronova, D. Budker, D. DeMille, D. F. J. Kimball, A. Derevianko & C. W. Clark; "Search for new physics with atoms and molecules"; Reviews of Modern Physics **90** (2018). ix

[9] W. F. SNYDER; "Lord Kelvin on Atoms as Fundamental Natural Standards (for Base Units)"; IEEE Transactions on Instrumentation and Measurement **22**, pp. 99–99 (1973). ix

[10] D. Budker & M. Romalis; "Optical magnetometry"; Nature Physics **3**, pp. 227–234 (2007). ix

[11] H. Fan, S. Kumar, J. Sedlacek, H. Kübler, S. Karimkashi & J. P. Shaffer; "Atom based RF electric field sensing"; Journal of Physics B: Atomic, Molecular and Optical Physics **48**, p. 202001 (2015). ix

[12] R. Karcher, A. Imanaliev, S. Merlet & F. P. D. Santos; "Improving the accuracy of atom interferometers with ultracold sources"; New Journal of Physics **20**, p. 113041 (2018). ix

[13] G. D'Amico, G. Rosi, S. Zhan, L. Cacciapuoti, M. Fattori & G. Tino; "Canceling the Gravity Gradient Phase Shift in Atom Interferometry"; Physical Review Letters **119** (2017). ix

[14] D. Savoie, M. Altorio, B. Fang, L. A. Sidorenkov, R. Geiger & A. Landragin; "Interleaved atom interferometry for high-sensitivity inertial measurements"; Science Advances **4**, p. eaau7948 (2018). ix

[15] C. Overstreet, P. Asenbaum, T. Kovachy, R. Notermans, J. M. Hogan & M. A. Kasevich; "Effective Inertial Frame in an Atom Interferometric Test of the Equivalence Principle"; Physical Review Letters **120** (2018). ix

[16] T. Bandi, C. Affolderbach, C. Stefanucci, F. Merli, A. K. Skrivervik & G. Mileti; "Compact high-performance continuous-wave double-resonance rubidium standard with $1.4 \times 10^{-13}\tau^{-1/2}$ stability"; IEEE Transactions on Ultrasonics, Ferroelectrics, and Frequency Control **61**, pp. 1769–1778 (2014). x

[17] M. A. Hafiz, G. Coget, M. Petersen, C. Rocher, S. Guérandel, T. Zanon-Willette, E. de Clercq & R. Boudot; "Toward a High-Stability Coherent Population Trapping Cs Vapor-Cell Atomic Clock Using Autobalanced Ramsey Spectroscopy"; Physical Review Applied **9** (2018). x

[18] F. Esnault, N. Rossetto, D. Holleville, J. Delporte & N. Dimarcq; "HORACE: A compact cold atom clock for Galileo"; Advances in Space Research **47**, pp. 854–858 (2011). x

[19] R. L. Tjoelker, J. D. Prestage, E. A. Burt, P. Chen, Y. J. Chong, S. K. Chung, W. Diener, T. Ely, D. G. Enzer, H. Mojaradi, C. Okino, M. Pauken, D. Robison, B. L. Swenson, B. Tucker & R. Wang; "Mercury Ion Clock for a NASA Technology Demonstration Mission"; IEEE Transactions on Ultrasonics, Ferroelectrics, and Frequency Control **63**, pp. 1034–1043 (2016). x

[20] J. Kitching; "Chip-scale atomic devices"; Applied Physics Reviews **5**, p. 031302 (2018). x

[21] Muquans; "MuClock Data sheet"; (2019). https://www.muquans.com/product/muclock/. x

[22] V. Ménoret, P. Vermeulen, N. L. Moigne, S. Bonvalot, P. Bouyer, A. Landragin & B. Desruelle; "Gravity measurements below 10-9 g with a transportable absolute quantum gravimeter"; Scientific Reports **8** (2018). x

[23] G. Santarelli, P. Laurent, P. Lemonde, A. Clairon, A. G. Mann, S. Chang, A. N. Luiten & C. Salomon; "Quantum Projection Noise in an Atomic Fountain: A High Stability Cesium Frequency Standard"; Physical Review Letters **82**, pp. 4619–4622 (1999). x, 14

[24] W. Wasilewski, K. Jensen, H. Krauter, J. J. Renema, M. V. Balabas & E. S. Polzik; "Quantum Noise Limited and Entanglement-Assisted Magnetometry"; Physical Review Letters **104** (2010). x, xi

[25] L. Pezzè, A. Smerzi, M. K. Oberthaler, R. Schmied & P. Treutlein; "Quantum metrology with nonclassical states of atomic ensembles"; Reviews of Modern Physics **90** (2018). x, 13, 14

[26] D. Braun, G. Adesso, F. Benatti, R. Floreanini, U. Marzolino, M. W. Mitchell & S. Pirandola; "Quantum-enhanced measurements without entanglement"; Reviews of Modern Physics **90** (2018). x

[27] A. Acín, I. Bloch, H. Buhrman, T. Calarco, C. Eichler, J. Eisert, D. Esteve, N. Gisin, S. J. Glaser, F. Jelezko, S. Kuhr, M. Lewenstein, M. F. Riedel, P. O. Schmidt, R. Thew, A. Wallraff, I. Walmsley & F. K. Wilhelm; "The quantum technologies roadmap: a European community view"; New Journal of Physics **20**, p. 080201 (2018). x

[28] M. Kitagawa & M. Ueda; "Squeezed spin states"; Physical Review A **47**, pp. 5138–5143 (1993). x, 13, 14, 15

[29] D. J. Wineland, J. J. Bollinger, W. M. Itano & D. J. Heinzen; "Squeezed atomic states and projection noise in spectroscopy"; Physical Review A **50**, pp. 67–88 (1994). x, 13

[30] L. Barsotti, J. Harms & R. Schnabel; "Squeezed vacuum states of light for gravitational wave detectors"; Reports on Progress in Physics **82**, p. 016905 (2018). x

[31] M. A. Taylor, J. Janousek, V. Daria, J. Knittel, B. Hage, H.-A. Bachor & W. P. Bowen; "Biological measurement beyond the quantum limit"; Nature Photonics **7**, pp. 229–233 (2013). x

[32] J. G. Bohnet, B. C. Sawyer, J. W. Britton, M. L. Wall, A. M. Rey, M. Foss-Feig & J. J. Bollinger; "Quantum spin dynamics and entanglement generation with hundreds of trapped ions"; Science **352**, pp. 1297–1301 (2016). x

[33] C. Gross, T. Zibold, E. Nicklas, J. Estève & M. K. Oberthaler; "Nonlinear atom interferometer surpasses classical precision limit"; Nature **464**, pp. 1165–1169 (2010). x, 15, 121

[34] M. F. Riedel, P. Böhi, Y. Li, T. W. Hänsch, A. Sinatra & P. Treutlein; "Atom-chip-based generation of entanglement for quantum metrology"; Nature **464**, pp. 1170–1173 (2010). x, 15, 121

[35] C. F. Ockeloen, R. Schmied, M. F. Riedel & P. Treutlein; "Quantum Metrology with a Scanning Probe Atom Interferometer"; Physical Review Letters **111** (2013). x, 15, 122

[36] W. Muessel, H. Strobel, D. Linnemann, D. Hume & M. Oberthaler; "Scalable Spin Squeezing for Quantum-Enhanced Magnetometry with Bose-Einstein Condensates"; Physical Review Letters **113** (2014). x, 15

[37] A. Kuzmich, N. P. Bigelow & L. Mandel; "Atomic quantum non-demolition measurements and squeezing"; Europhysics Letters (EPL) **42**, pp. 481–486 (1998). x

[38] R. J. Sewell, M. Koschorreck, M. Napolitano, B. Dubost, N. Behbood & M. W. Mitchell; "Magnetic Sensitivity Beyond the Projection Noise Limit by Spin Squeezing"; Physical Review Letters **109** (2012). xi, 16

[39] J. Appel, P. J. Windpassinger, D. Oblak, U. B. Hoff, N. Kjaergaard & E. S. Polzik; "Mesoscopic atomic entanglement for precision measurements beyond the standard quantum limit"; Proceedings of the National Academy of Sciences **106**, pp. 10960–10965 (2009). xi, 16

[40] S. Haroche & J.-M. Raimond; *Exploring the Quantum* (Oxford University Press) (2006). xi

[41] M. H. Schleier-Smith, I. D. Leroux & V. Vuletić; "States of an Ensemble of Two-Level Atoms with Reduced Quantum Uncertainty"; Physical Review Letters **104** (2010). xi, 16, 109

[42] O. Hosten, N. J. Engelsen, R. Krishnakumar & M. A. Kasevich; "Measurement noise 100 times lower than the quantum-projection limit using entangled atoms"; Nature **529**, pp. 505–508 (2016). xi, 16, 122

[43] M. H. Schleier-Smith, I. D. Leroux & V. Vuletić; "Squeezing the collective spin of a dilute atomic ensemble by cavity feedback"; Physical Review A **81** (2010). xi, 15, 26, 27, 122

[44] I. D. Leroux, M. H. Schleier-Smith & V. Vuletić; "Implementation of Cavity Squeezing of a Collective Atomic Spin"; Physical Review Letters **104** (2010). xi, 15, 121, 122

[45] B. Braverman, A. Kawasaki, E. Pedrozo-Peñafiel, S. Colombo, C. Shu, Z. Li, E. Mendez, M. Yamoah, L. Salvi, D. Akamatsu, Y. Xiao & V. Vuletić; "Near-Unitary Spin Squeezing in Yb171"; Physical Review Letters **122** (2019). xi, 15

[46] I. D. Leroux, M. H. Schleier-Smith & V. Vuletić; "Orientation-Dependent Entanglement Lifetime in a Squeezed Atomic Clock"; Physical Review Letters **104** (2010). xi, 122

[47] P. Rosenbusch; "Magnetically trapped atoms for compact atomic clocks"; Applied Physics B **95**, pp. 227–235 (2009). xi, 7, 8

[48] C. Deutsch, F. Ramirez-Martinez, C. Lacroûte, F. Reinhard, T. Schneider, J. N. Fuchs, F. Piéchon, F. Laloë, J. Reichel & P. Rosenbusch; "Spin Self-Rephasing and Very Long Coherence Times in a Trapped Atomic Ensemble"; Physical Review Letters **105** (2010). xi, 81, 116, 129, 130, 133

[49] W. Maineult, C. Deutsch, K. Gibble, J. Reichel & P. Rosenbusch; "Spin Waves and Collisional Frequency Shifts of a Trapped-Atom Clock"; Physical Review Letters **109** (2012). xi, 52

[50] R. Szmuk, V. Dugrain, W. Maineult, J. Reichel & P. Rosenbusch; "Stability of a trapped-atom clock on a chip"; Physical Review A **92** (2015). xi, 49, 79, 82, 83, 85, 87

[51] J. N. Fuchs, D. M. Gangardt & F. Laloë; "Internal State Conversion in Ultracold Gases"; Physical Review Letters **88** (2002). xi, 126, 128

[52] M. J. Martin, M. Bishof, M. D. Swallows, X. Zhang, C. Benko, J. von Stecher, A. V. Gorshkov, A. M. Rey & J. Ye; "A Quantum Many-Body Spin System in an Optical Lattice Clock"; Science **341**, pp. 632–636 (2013). xi, 126, 127

[53] S. L. Bromley, S. Kolkowitz, T. Bothwell, D. Kedar, A. Safavi-Naini, M. L. Wall, C. Salomon, A. M. Rey & J. Ye; "Dynamics of interacting fermions under spin–orbit coupling in an optical lattice clock"; Nature Physics **14**, pp. 399–404 (2018). xi, 125, 127, 129, 150

[54] E. Davis, G. Bentsen & M. Schleier-Smith; "Approaching the Heisenberg Limit without Single-Particle Detection"; Physical Review Letters **116** (2016). xi, 125

[55] O. Hosten, R. Krishnakumar, N. J. Engelsen & M. A. Kasevich; "Quantum phase magnification"; Science **352**, pp. 1552–1555 (2016). xi, 125

[56] R. Kohlhaas, A. Bertoldi, E. Cantin, A. Aspect, A. Landragin & P. Bouyer; "Phase Locking a Clock Oscillator to a Coherent Atomic Ensemble"; Physical Review X **5** (2015). xii, 11, 16, 90, 149

[57] N. F. Ramsey; "Experiments with separated oscillatory fields and hydrogen masers"; Reviews of Modern Physics **62**, pp. 541–552 (1990). 1, 4

[58] F. T. Arecchi, E. Courtens, R. Gilmore & H. Thomas; "Atomic Coherent States in Quantum Optics"; Physical Review A **6**, pp. 2211–2237 (1972). 3

[59] A. Peters, K. Y. Chung & S. Chu; "High-precision gravity measurements using atom interferometry"; Metrologia **38**, pp. 25–61 (2001). 5

[60] T. Kovachy, P. Asenbaum, C. Overstreet, C. A. Donnelly, S. M. Dickerson, A. Sugarbaker, J. M. Hogan & M. A. Kasevich; "Quantum superposition at the half-metre scale"; Nature **528**, pp. 530–533 (2015). 5

[61] C. L. Garrido Alzar; "Compact cold-guided-atom gyrometers for inertial navigation: Enabling technologies and design study"; In press (2019). 5

[62] A. D. Ludlow, M. M. Boyd, J. Ye, E. Peik & P. Schmidt; "Optical atomic clocks"; Reviews of Modern Physics **87**, pp. 637–701 (2015). 6

[63] M. Abgrall, B. Chupin, L. D. Sarlo, J. Guéna, P. Laurent, Y. L. Coq, R. L. Targat, J. Lodewyck, M. Lours, P. Rosenbusch, G. D. Rovera & S. Bize; "Atomic fountains and optical clocks at SYRTE: Status and perspectives"; Comptes Rendus Physique **16**, pp. 461–470 (2015). 6

[64] M. D. Swallows, M. Bishof, Y. Lin, S. Blatt, M. J. Martin, A. M. Rey & J. Ye; "Suppression of Collisional Shifts in a Strongly Interacting Lattice Clock"; Science **331**, pp. 1043–1046 (2011). 6

[65] S. L. Campbell, R. B. Hutson, G. E. Marti, A. Goban, N. D. Oppong, R. L. McNally, L. Sonderhouse, J. M. Robinson, W. Zhang, B. J. Bloom & J. Ye; "A Fermi-degenerate three-dimensional optical lattice clock"; Science **358**, pp. 90–94 (2017). 6, 14

[66] J. Reichel & V. Vuletić (Editors); *Atom Chips* (Wiley-VCH Verlag GmbH & Co. KGaA) (2011). 6

[67] T. van Zoest, N. Gaaloul, Y. Singh, H. Ahlers, W. Herr, S. T. Seidel, W. Ertmer, E. Rasel, M. Eckart, E. Kajari, S. Arnold, G. Nandi, W. P. Schleich, R. Walser, A. Vogel, K. Sengstock, K. Bongs, W. Lewoczko-Adamczyk, M. Schiemangk, T. Schuldt, A. Peters, T. Konemann, H. Muntinga, C. Lammerzahl, H. Dittus, T. Steinmetz, T. W. Hansch & J. Reichel; "Bose-Einstein Condensation in Microgravity"; Science **328**, pp. 1540–1543 (2010). 6

[68] M. Keil, O. Amit, S. Zhou, D. Groswasser, Y. Japha & R. Folman; "Fifteen years of cold matter on the atom chip: promise, realizations, and prospects"; Journal of Modern Optics **63**, pp. 1840–1885 (2016). 6

[69] W. Petrich, M. H. Anderson, J. R. Ensher & E. A. Cornell; "Stable, Tightly Confining Magnetic Trap for Evaporative Cooling of Neutral Atoms"; Physical Review Letters **74**, pp. 3352–3355 (1995). 6

[70] F. Reinhard; *Design and construction of an atomic clock on an atom chip*; Ph.D. thesis; Université Pierre et Marie Curie - Paris VI (2009). https://tel.archives-ouvertes.fr/tel-00414386. 6, 9, 29, 30, 38, 39, 40, 55

[71] D. M. Harber, H. J. Lewandowski, J. M. McGuirk & E. A. Cornell; "Effect of cold collisions on spin coherence and resonance shifts in a magnetically trapped ultracold gas"; Physical Review A **66** (2002). 7

[72] C. Deutsch; *Trapped atom clock on a chip : identical spin rotation effects in an ultracold trapped atomic clock*; Ph.D. thesis; Université Pierre et Marie Curie - Paris VI (2011). http://www.theses.fr/2011PA066742. 8, 9, 57, 129, 130

[73] D. A. Steck; "Rubidium 87 D Line Data"; Technical report (2015). http://steck.us/alkalidata; (revision 2.1.5, 13 January 2015). 8, 61, 93, 107

[74] W. Riley & D. A. Howe; "Handbook of Frequency Stability Analysis"; Special Publication (NIST SP) 1065; NIST (2008). https://www.nist.gov/publications/handbook-frequency-stability-analysis. 9, 10

[75] E. Rubiola; *Phase Noise and Frequency Stability in Oscillators* (Cambridge University Press) (2008). 10

[76] G. Santarelli, C. Audoin, A. Makdissi, P. Laurent, G. Dick & A. Clairon; "Frequency stability degradation of an oscillator slaved to a periodically interrogated atomic resonator"; IEEE Transactions on Ultrasonics, Ferroelectrics and Frequency Control **45**, pp. 887–894 (1998). 10, 81

[77] K. Gibble; "Decoherence and Collisional Frequency Shifts of Trapped Bosons and Fermions"; Physical Review Letters **103** (2009). 11

[78] F. P. D. Santos, H. Marion, S. Bize, Y. Sortais, A. Clairon & C. Salomon; "Controlling the Cold Collision Shift in High Precision Atomic Interferometry"; Physical Review Letters **89** (2002). 12

[79] J. Guéna, M. Abgrall, A. Clairon & S. Bize; "Contributing to TAI with a secondary representation of the SI second"; Metrologia **51**, pp. 108–120 (2014). 12

[80] A. S. Sørensen & K. Mølmer; "Entanglement and Extreme Spin Squeezing"; Physical Review Letters **86**, pp. 4431–4434 (2001). 13

[81] J. Ma, X. Wang, C. P. Sun & F. Nori; "Quantum spin squeezing"; Physics Reports **509**, pp. 89–165 (2011). 14

[82] M. Gessner, A. Smerzi & L. Pezzè; "Metrological Nonlinear Squeezing Parameter"; Physical Review Letters **122** (2019). 14

[83] B. Braverman, A. Kawasaki & V. Vuletić; "Impact of non-unitary spin squeezing on atomic clock performance"; New Journal of Physics **20**, p. 103019 (2018). 15, 25

[84] Y.-L. Zhang, C.-L. Zou, X.-B. Zou, L. Jiang & G.-C. Guo; "Detuning-enhanced cavity spin squeezing"; Physical Review A **91** (2015). 15, 27

[85] C. K. Law, H. T. Ng & P. T. Leung; "Coherent control of spin squeezing"; Physical Review A **63** (2001). 15

[86] H. Strobel, W. Muessel, D. Linnemann, T. Zibold, D. B. Hume, L. Pezze, A. Smerzi & M. K. Oberthaler; "Fisher information and entanglement of non-Gaussian spin states"; Science **345**, pp. 424–427 (2014). 15

[87] J. Borregaard, E. J. Davis, G. S. Bentsen, M. H. Schleier-Smith & A. S. Sørensen; "One- and two-axis squeezing of atomic ensembles in optical cavities"; New Journal of Physics **19**, p. 093021 (2017). 15

[88] R. Inoue, S.-I.-R. Tanaka, R. Namiki, T. Sagawa & Y. Takahashi; "Unconditional Quantum-Noise Suppression via Measurement-Based Quantum Feedback"; Physical Review Letters **110** (2013). 16

[89] K. C. Cox, G. P. Greve, J. M. Weiner & J. K. Thompson; "Deterministic Squeezed States with Collective Measurements and Feedback"; Physical Review Letters **116** (2016). 16, 20, 122

[90] A. Kuzmich, L. Mandel, J. Janis, Y. E. Young, R. Ejnisman & N. P. Bigelow; "Quantum nondemolition measurements of collective atomic spin"; Physical Review A **60**, pp. 2346–2350 (1999). 16

[91] G. Vasilakis, H. Shen, K. Jensen, M. Balabas, D. Salart, B. Chen & E. S. Polzik; "Generation of a squeezed state of an oscillator by stroboscopic back-action-evading measurement"; Nature Physics **11**, pp. 389–392 (2015). 16

[92] J. G. Bohnet, K. C. Cox, M. A. Norcia, J. M. Weiner, Z. Chen & J. K. Thompson; "Reduced spin measurement back-action for a phase sensitivity ten times beyond the standard quantum limit"; Nature Photonics **8**, pp. 731–736 (2014). 16, 109

[93] Z. Chen, J. G. Bohnet, S. R. Sankar, J. Dai & J. K. Thompson; "Conditional Spin Squeezing of a Large Ensemble via the Vacuum Rabi Splitting"; Physical Review Letters **106** (2011). 16

[94] J. Lodewyck, P. G. Westergaard & P. Lemonde; "Nondestructive measurement of the transition probability in a Sr optical lattice clock"; Physical Review A **79** (2009). 16

[95] G. Vallet, E. Bookjans, U. Eismann, S. Bilicki, R. L. Targat & J. Lodewyck; "A noise-immune cavity-assisted non-destructive detection for an optical lattice clock in the quantum regime"; New Journal of Physics **19**, p. 083002 (2017). 16

[96] T. Vanderbruggen, R. Kohlhaas, A. Bertoldi, E. Cantin, A. Landragin & P. Bouyer; "Feedback control of coherent spin states using weak nondestructive measurements"; Physical Review A **89** (2014). 16

[97] Z. Chen, J. G. Bohnet, J. M. Weiner, K. C. Cox & J. K. Thompson; "Cavity-aided nondemolition measurements for atom counting and spin squeezing"; Physical Review A **89** (2014). 18, 20, 24

[98] E. Jaynes & F. Cummings; "Comparison of quantum and semiclassical radiation theories with application to the beam maser"; Proceedings of the IEEE **51**, pp. 89–109 (1963). 18

[99] M. Tavis & F. W. Cummings; "Exact Solution for anN-Molecule—Radiation-Field Hamiltonian"; Physical Review **170**, pp. 379–384 (1968). 18

[100] D. Hunger, T. Steinmetz, Y. Colombe, C. Deutsch, T. W. Hänsch & J. Reichel; "A fiber Fabry–Perot cavity with high finesse"; New Journal of Physics **12**, p. 065038 (2010). 20

[101] Z. Chen; *Breaking Quantum Limits with Collective Cavity-QED: Generation of Spin Squeezed States viaQuantum Non-Demolition Measurements*; Ph.D. thesis; University of Colorado, Boulder (2013). https://scholar.colorado.edu/phys_gradetds/92. 20, 110

[102] E. Brion, L. H. Pedersen & K. Mølmer; "Adiabatic elimination in a lambda system"; Journal of Physics A: Mathematical and Theoretical **40**, pp. 1033–1043 (2007). 20

[103] J. Hu, W. Chen, Z. Vendeiro, H. Zhang & V. Vuletić; "Entangled collective-spin states of atomic ensembles under nonuniform atom-light interaction"; Physical Review A **92** (2015). 21, 92

[104] M. H. Schleier-Smith; *Cavity-Enabled Spin Squeezing for a Quantum-Enhanced Atomic Clock*; Ph.D. thesis; Massachusetts Institute of Technology (2011). http://hdl.handle.net/1721.1/68878. 23, 27, 90, 110, 112, 113

[105] N. J. Engelsen; *Quantum metrology using large ensembles of entangled atoms*; Ph.D. thesis; Stanford University (2016). https://purl.stanford.edu/th219jv5647. 25

[106] K. Pawłowski, J. Estève, J. Reichel & A. Sinatra; "Limits of atomic entanglement by cavity feedback: From weak to strong coupling"; EPL (Europhysics Letters) **113**, p. 34005 (2016). 27

[107] C. Lacroûte; *Développement d'une horloge atomique sur puce à atomes : Optimisation de la durée de cohérence et caractérisation préliminaire*; Ph.D. thesis; Université Pierre et Marie Curie - Paris VI (2010). https://tel.archives-ouvertes.fr/tel-00528925. 29, 34

[108] K. Ott; *Towards a squeezing-enhanced atomic clock on a chip*; Ph.D. thesis; Université Pierre et Marie Curie - Paris VI (2016). https://tel.archives-ouvertes.fr/tel-01452767. 29, 30, 44, 60, 61, 97

[109] J. Reichel, W. Hänsel & T. W. Hänsch; "Atomic Micromanipulation with Magnetic Surface Traps"; Physical Review Letters **83**, pp. 3398–3401 (1999). 29

[110] K. Dieckmann, R. J. C. Spreeuw, M. Weidemüller & J. T. M. Walraven; "Two-dimensional magneto-optical trap as a source of slow atoms"; Physical Review A **58**, pp. 3891–3895 (1998). 31

[111] M. Gilowski, C. Schubert, M. Zaiser, W. Herr, T. Wübbena, T. Wendrich, T. Müller, E. Rasel & W. Ertmer; "Narrow bandwidth interference filter-stabilized diode laser systems for the manipulation of neutral atoms"; Optics Communications **280**, pp. 443–447 (2007). 35

[112] S. J. Park, J. Noh & J. Mun; "Cold atomic beam from a two-dimensional magneto-optical trap with two-color pushing laser beams"; Optics Communications **285**, pp. 3950–3954 (2012). 35

[113] L. J. LeBlanc; *Evaporative Cooling in a Strongly Confining Microchip Trap*; Master's thesis; University of Toronto (2005). 45

[114] X. Chen, A. Ruschhaupt, S. Schmidt, S. Ibáñez & J. G. Muga; "Shortcut to adiabaticity in harmonic traps"; Journal of Atomic and Molecular Sciences **1**, pp. 1–17 (2010). 47

[115] V. Dugrain; *Metrology with trapped atoms on a chip using non-degenerate and degenerate quantum gases*; Ph.D. thesis; Université Pierre et Marie Curie - Paris VI (2012). http://www.theses.fr/2012PA066670. 48

[116] M. Kasevich & S. Chu; "Laser cooling below a photon recoil with three-level atoms"; Physical Review Letters **69**, pp. 1741–1744 (1992). 48

[117] F. Ramirez-Martinez, M. Lours, P. Rosenbusch, F. Reinhard & J. Reichel; "Low-phase-noise frequency synthesizer for the trapped atom clock on a chip"; IEEE Transactions on Ultrasonics, Ferroelectrics and Frequency Control **57**, pp. 88–93 (2010). 48

[118] G. Reinaudi, T. Lahaye, Z. Wang & D. Guéry-Odelin; "Strong saturation absorption imaging of dense clouds of ultracold atoms"; Optics Letters **32**, p. 3143 (2007). 56

[119] T. Laudat; *Spontaneous spin squeezing in a spinor Bose-Einstein condensate trapped on an atom chip*; Theses; PSL Research University (2017). https://tel.archives-ouvertes.fr/tel-01688752. 57, 58, 59

[120] K. Ott, S. Garcia, R. Kohlhaas, K. Schüppert, P. Rosenbusch, R. Long & J. Reichel; "Millimeter-long fiber Fabry-Perot cavities"; Optics Express **24**, p. 9839 (2016). 60

[121] S. Garcia; *Interfaces fibrées entre atomes uniques et photons uniques*; Theses; Ecole normale supérieure - ENS PARIS (2015). https://tel.archives-ouvertes.fr/tel-01382230. 60, 62

[122] G. K. Gulati, H. Takahashi, N. Podoliak, P. Horak & M. Keller; "Fiber cavities with integrated mode matching optics"; Scientific Reports **7** (2017). 60

[123] J. P. Brantut, J. F. Clément, M. R. de Saint Vincent, G. Varoquaux, R. A. Nyman, A. Aspect, T. Bourdel & P. Bouyer; "Light-shift tomography in an optical-dipole trap for neutral atoms"; Physical Review A **78** (2008). 60

[124] F. Ferri; *Strong coupling between a fiber-cavity mode and a commensurate atomic lattice*; Ph.D. thesis; PSL Research University (2018). 60, 92

[125] J. Gallego, S. Ghosh, S. K. Alavi, W. Alt, M. Martinez-Dorantes, D. Meschede & L. Ratschbacher; "High-finesse fiber Fabry–Perot cavities: stabilization and mode matching analysis"; Applied Physics B **122** (2016). 62

[126] J. H. Shirley; "Modulation transfer processes in optical heterodyne saturation spectroscopy"; Optics Letters **7**, p. 537 (1982). 63

[127] D. J. McCarron, S. A. King & S. L. Cornish; "Modulation transfer spectroscopy in atomic rubidium"; Measurement Science and Technology **19**, p. 105601 (2008). 63

[128] N. C. Wong & J. L. Hall; "Servo control of amplitude modulation in frequency-modulation spectroscopy: demonstration of shot-noise-limited detection"; Journal of the Optical Society of America B **2**, p. 1527 (1985). 65, 66

[129] Z. Li, L. Zhao, W. Tan, W. Ma, G. Zhao, X. Fu, L. Dong, L. Zhang, W. Yin & S. Jia; "Investigation and cancellation of residual amplitude modulation in fiber electro-optic modulator based frequency modulation gas sensing technique"; Sensors and Actuators B: Chemical **196**, pp. 23–30 (2014). 66

[130] E. D. Black; "An introduction to Pound–Drever–Hall laser frequency stabilization"; American Journal of Physics **69**, pp. 79–87 (2001). 67, 151

[131] L. Neuhaus; *Cooling a macroscopic mechanical oscillator close to its quantum ground state*; Ph.D. thesis; Université Pierre et Marie Curie - Paris VI (2016). https://tel.archives-ouvertes.fr/tel-01467924. 73

[132] A. Ryou & J. Simon; "Active cancellation of acoustical resonances with an FPGA FIR filter"; Review of Scientific Instruments **88**, p. 013101 (2017). 73

[133] H. Carmichael; *An Open Systems Approach to Quantum Optics* (Springer Berlin Heidelberg) (1993). 93

[134] J. Benedikter, T. Hümmer, M. Mader, B. Schlederer, J. Reichel, T. W. Hänsch & D. Hunger; "Transverse-mode coupling and diffraction loss in tunable Fabry–Pérot microcavities"; New Journal of Physics **17**, p. 053051 (2015). 97

[135] E. L. Hahn; "Spin Echoes"; Physical Review **80**, pp. 580–594 (1950). 109

[136] L. M. K. Vandersypen & I. L. Chuang; "NMR techniques for quantum control and computation"; Reviews of Modern Physics **76**, pp. 1037–1069 (2005). 112

[137] K. C. Cox, M. A. Norcia, J. M. Weiner, J. G. Bohnet & J. K. Thompson; "Reducing collective quantum state rotation errors with reversible dephasing"; Applied Physics Letters **105**, p. 261102 (2014). 113

[138] H. K. Cummins, G. Llewellyn & J. A. Jones; "Tackling systematic errors in quantum logic gates with composite rotations"; Physical Review A **67** (2003). 114

[139] A. Dunning, R. Gregory, J. Bateman, N. Cooper, M. Himsworth, J. A. Jones & T. Freegarde; "Composite pulses for interferometry in a thermal cold atom cloud"; Physical Review A **90** (2014). 114

[140] P. Kunkel, M. Prüfer, H. Strobel, D. Linnemann, A. Frölian, T. Gasenzer, M. Gärttner & M. K. Oberthaler; "Spatially distributed multipartite entanglement enables EPR steering of atomic clouds"; Science **360**, pp. 413–416 (2018). 125

[141] M. Fadel, T. Zibold, B. Décamps & P. Treutlein; "Spatial entanglement patterns and Einstein-Podolsky-Rosen steering in Bose-Einstein condensates"; Science **360**, pp. 409–413 (2018). 125, 147

[142] K. Lange, J. Peise, B. Lücke, I. Kruse, G. Vitagliano, I. Apellaniz, M. Kleinmann, G. Tóth & C. Klempt; "Entanglement between two spatially separated atomic modes"; Science **360**, pp. 416–418 (2018). 125

[143] E. P. Bashkin; "Spin waves in polarized paramagnetic gases"; JETP Lett. **33**, p. 8 (1981). 125

[144] C. Lhuillier & F. Laloë; "Transport properties in a spin polarized gas, I"; Journal de Physique **43**, pp. 197–224 (1982). 125, 126

[145] K. Gibble; "Keeping atoms synchronized for better timekeeping"; Physics **3** (2010). 126

[146] A. M. Rey, A. V. Gorshkov & C. Rubbo; "Many-Body Treatment of the Collisional Frequency Shift in Fermionic Atoms"; Physical Review Letters **103** (2009). 126

[147] A. Rey, A. Gorshkov, C. Kraus, M. Martin, M. Bishof, M. Swallows, X. Zhang, C. Benko, J. Ye, N. Lemke & A. Ludlow; "Probing many-body interactions in an optical lattice clock"; Annals of Physics **340**, pp. 311–351 (2014). 126

[148] P. He, M. A. Perlin, S. R. Muleady, R. J. Lewis-Swan, R. B. Hutson, J. Ye & A. M. Rey; "Engineering spin squeezing in a 3D optical lattice with interacting spin-orbit-coupled fermions"; Preprint 1904.07866 (2019). https://arxiv.org/abs/1904.07866. 127

[149] H. J. Lewandowski, D. M. Harber, D. L. Whitaker & E. A. Cornell; "Observation of Anomalous Spin-State Segregation in a Trapped Ultracold Vapor"; Physical Review Letters **88** (2002). 128

[150] J. M. McGuirk, H. J. Lewandowski, D. M. Harber, T. Nikuni, J. E. Williams & E. A. Cornell; "Spatial Resolution of Spin Waves in an Ultracold Gas"; Physical Review Letters **89** (2002). 128

[151] M. . Oktel & L. S. Levitov; "Internal Waves and Synchronized Precession in a Cold Vapor"; Physical Review Letters **88** (2002). 128

[152] X. Du, L. Luo, B. Clancy & J. E. Thomas; "Observation of Anomalous Spin Segregation in a Trapped Fermi Gas"; Physical Review Letters **101** (2008). 128

[153] F. Piéchon, J. N. Fuchs & F. Laloë; "Cumulative Identical Spin Rotation Effects in Collisionless Trapped Atomic Gases"; Physical Review Letters **102** (2009). 128, 129

[154] S. Pegahan, J. Kangara, I. Arakelyan & J. E. Thomas; "Spin-Energy Correlation in Degenerate Weakly-Interacting Fermi Gases"; Physical Review A **99** (2018). 128

[155] C. Solaro, A. Bonnin, F. Combes, M. Lopez, X. Alauze, J.-N. Fuchs, F. Piéchon & F. P. D. Santos; "Competition between Spin Echo and Spin Self-Rephasing in a Trapped Atom Interferometer"; Physical Review Letters **117** (2016). 129

[156] F. Combes; *Thermodynamique de la réponse électrique dans les isolants de bande - Synchronisation et écho de spin dans une horloge atomique*; Phd thesis; Université Paris-Saclay (2018). https://tel.archives-ouvertes.fr/tel-02137505. 130

HUANG Meng-Zi **17 septembre 2019**

Sujet : Compression et dynamique de spin dans une horloge à atomes piégés

Résumé : Les capteurs atomiques sont un outil de référence pour les mesures de précision du temps, des champs électriques et magnétiques et des forces d'inertie. Cependant, en absence d'une corrélation quantique entre atomes, le bruit de projection quantique constitue une limite fondamentale pour ces capteurs, appelée la limite quantique standard (SQL). Les meilleures horloges actuelles ont déjà atteint cette limite. Cependant, elle peut être surmonté en utilisant l'intrication quantique, dans un état comprimés de spin notamment. Ce dernier peut être crée par mesure quantique non-destructive (QND), en particulier dans le cadre de l'électrodynamique quantique en cavité (cQED).
Dans cette thèse, je présente la deuxième génération de l'horloge à atomes piégés sur puce (TACC), dans laquelle nous combinons une horloge atomique compacte avec une plateforme cQED miniature pour tester les protocoles de métrologie quantique à un niveau de précision métrologique. Dans une mesure Ramsey standard, nous mesurons une stabilité de 6×10^{-13} à 1 s. Nous démontrons la compression de spin par mesure QND, atteignant 8(1) dB pour 1.7×10^4 atomes, limitée actuellement par la décohérence due au bruit technique.
Les collisions entre atomes froids jouent un rôle important à ce niveau de précision, donnant lieu à une riche dynamique de spin. Nous constatons que l'interaction entre mesures par la cavité et dynamique collisionnelle de spin se manifeste dans un effet d'amplification du signal de la cavité. Un modèle simple est proposé et confirmé par des mesures préliminaires. De nouvelles expériences sont proposés pour éclairer davantage la physique à N corps surprenante dans ce système d'atomes froids.

Mots clés : Horloge atomique, états comprimés de spin, electrodynamique quantique en cavité, dynamique de spin, métrologie quantique, microcircuit à atomes

Subject : Spin squeezing and spin dynamics in a trapped-atom clock

Abstract: Atomic sensors are among the best devices for precision measurements of time, electric and magnetic fields, and inertial forces. However, all atomic sensors that utilise uncorrelated particles are ultimately limited by quantum projection noise, as is already the case for state-of-the-art atomic clocks. This so-called standard quantum limit (SQL) can be overcome by employing entanglement, a prime example being the spin-squeezed states. Spin squeezing can be produced in a quantum non-demolition (QND) measurement of the collective spin, particularly with cavity quantum electrodynamical (cQED) interactions.
In this thesis, I present the second-generation trapped-atom clock on a chip (TACC) experiment, where we combine a metrology-grade compact clock with a miniature cQED platform to test quantum metrology protocols at a metrologically-relevant precision level. In a standard Ramsey spectroscopy, the stability of the apparatus is confirmed by a fractional frequency Allan deviation of 6×10^{-13} at 1 s. We demonstrate spin squeezing by cavity QND measurement, reaching 8(1) dB for 1.7×10^4 atoms, currently limited by decoherence due to technical noise.
Cold collisions between atoms play an important role at this level of precision, leading to rich spin dynamics. Here we find that the interplay between cavity measurements and collisional spin dynamics manifests itself in a quantum amplification effect of the cavity measurement. A simple model is proposed, and is confirmed by initial measurements. New experiments in this direction may shed light on the surprising many-body physics in this sytem of interacting cold atoms.

Keywords: Atomic clock, spin-squeezed states, cavity quantum electrodynamics, spin dynamics, quantum metrology, atom chip